2018

Electron Microscopy Studies of Quantum Dot and Catalyst Nanomaterials

Li Lu
Lehigh University

Electron Microscopy Studies of Quantum Dot and Catalyst Nanomaterials

by

Li Lu

A Dissertation
Presented to the Graduate Committee
of Lehigh University
in Candidacy for the Degree of
Doctor of Philosophy

in

Materials Science and Engineering

Lehigh University

May 2018

Approved and recommended for acceptance as a dissertation in partial fulfillment of the requirements for the degree of Doctor of Philosophy.

Li Lu
Electron Microscopy Studies of Quantum Dot and Catalyst Nanomaterials

_____
Date

_____
Dissertation Director

_____
Accepted Date

Committee Members:

_____
Dr. Christopher J. Kiely

_____
Dr. Bryan W. Berger

_____
Dr. Steven McIntosh

_____
Dr. Masashi Watanabe

Acknowledgements

I would like to express my utmost appreciation and sincere gratitude to my Ph.D. advisor, Professor Christopher J. Kiely, who offered me this great opportunity to work in his group on so many exciting research projects. It is the tremendous support, inspiration, encouragement and patience of Professor Christopher J. Kiely that have guided me through my graduate study at Lehigh. I feel very fortunate to have him as my advisor over the past five years and cannot imagine having a better one.

I want to extend my thanks to Professor Steven McIntosh and Professor Bryan W. Berger, for their insightful mentoring in our fruitful collaboration. I am also very grateful to Professor Masashi Watanabe; I have learned a lot on electron microscopy from his lectures and through the discussions I had with him. In particular, I really appreciate the generous participation and expert supervision of these three professors as my Ph.D. committee members.

My work could never be accomplished without the tremendous teamwork with my collaborators, who provided me with not only interesting samples but also enormous help in my research. Among them are Professor Graham J. Hutchings and his research team at Cardiff University, UK. These include Grazia Malta, Dr. Simon A. Kondrat, Dr. Simon J. Freakley, Dr. Catherine J. Davies, Simon Dawson, Professor David J. Morgan, Professor C. Richard A. Catlow, Dr. Xi Liu, Dr. Marco Conte, and David Elias. I am also thankful to Professor Bert M. Weckhuysen and his group members Charlotte Vogt and Dr. Florian Meirer at Utrecht University, Netherlands. Another group of people I owe thanks to is the biomineralization team led by Professor Steven McIntosh and Professor Bryan W. Berger in the Department of Chemical

Engineering at Lehigh University, which includes Dr. Zhou Yang, Leah, C. Spangler, Christopher D. Curran, Robert Dunleavy, Yue Jia, Roxanne Chu, Abdolhamid Sadeghnejad, and Siavash Rajabpour. The various significant contributions of all my collaborators are fully acknowledged.

Dozens of people have helped and taught me in one way or another during my years at Lehigh. I am indebted to the former and current members in our group, Dr. Qian He, Dr. Wu Zhou, Dr. Weihao Weng, Dr. Ram Chandra Tiruvalam, and Sultan Althahban, for their generous sharing of useful suggestions. Especially I would like to thank Dr. Qian He and Sultan Althahban for exchanging ideas with me on numerous projects. Dr. Robert Keyse, Mr. William Mushock and Dr. Carol Kiely offered me invaluable training and assistance in the use of various electron microscopes, and I send my grateful thanks to them.

Lastly, my deepest thanks go to my parents for their continuous love and unconditional support from the other side of the Pacific. Above all, I am extremely thankful to my fantastic wife Yi, who has been a constant source of strength and hope.

Contents

List of Tables

List of Figures

Abstract

Materials with nanoscale dimensions often display unique optical, electronic and chemical properties that depend on their size, structure and composition. For instance, semiconductor nanocrystals, or quantum dots (QDs), exhibit quantum confinement effects which can lead to tunable electronic and optical properties. Similarly, nanoscopic metal structures ranging from nanoparticles to sub-nm clusters and even individual atoms can display excellent catalytic properties when dispersed on a suitable support, due to their high surface area-to-volume ratio and modified electronic properties. In order to develop meaningful structure-property correlations and optimize the performance of such nanomaterials, their structural and compositional features need to be carefully characterized by state-of-the-art aberration corrected analytical electron microscopy (AC-AEM).

The first half of this dissertation concerns the study of semiconductor QDs prepared via a novel aqueous-phase biomineralization route that offers lower environmental impact and decreased economic costs compared to more traditional chemical synthesis routes. In particular, we show how the optical properties of these biosynthesized QDs have been understood and improved by a process of 'microscopy informed nanomaterial design'. Firstly, cadmium sulfide QDs biosynthesized using an engineered bacterial strain of *Stenotrophomonas maltophilia* have been structurally and chemically analyzed by aberration corrected STEM. This has allowed us to establish a direct correlation between mean nanocrystal size and the particle growth time, which in turn affords us good control and tunability over the band gap energy and absorption/fluorescence behavior of the resultant QDs. Next, a single enzyme produced by the bacterium, namely cystathionine γ-lyase (smCSE), is shown to be responsible for both inducing

CdS mineralization and templating nanocrystal growth. The production of size- and structure-controlled CdSe and CdSe-CdS core-shell QDs is also shown to be possible using this same enzyme. The palette of QD materials available from this biomineralization approach is then further expanded to cover other metal sulfide nanocrystals, such as PbS and PbS-CdS core-shell QDs, and $CuInS_2$ (ternary) and $(CuInZn)S_2$ (quaternary) alloy QDs. Detailed HR-TEM, STEM and XEDS measurements on these PbS- and $CuInS_2$-based QD systems are described and then correlated to their functional properties. Finally, it is shown that this aqueous, room temperature biomineralization strategy can also be adapted to produce cerium-based oxide materials by employing a modified form of silicatein as the biosynthesis agent. In particular, AC-AEM analysis is used to validate the successful biomineralization of sub-3 nm fluorite-type CeO_2 and CeO_2-ZrO_2 nanocrystals, which are amongst the smallest reported to date. Their catalytic properties and thermal stability are also explored in relation to the CO oxidation reaction.

The second half of this dissertation presents three case studies which serve to demonstrate how the ability to visualize the structure and dispersion of metallic nano-catalysts by AC-AEM, when coupled with spectroscopic information obtained from other complementary techniques, can be used to advance our mechanistic understanding of how these catalysts operate. In the first example, HAADF-STEM analysis is coupled with *in-situ* X-ray absorption fine structure (XAFS) analysis to study a gold-on-carbon catalyst which is commercially used for the hydrochlorination of acetylene to produce vinyl chloride monomer. We unequivocally demonstrate that a mixture of atomically dispersed Au^+ and Au^{3+} cations constitute the active centers in this Au/C catalyst system. In a second example, physically separate cobalt and platinum nanoparticles supported on either γ-Al_2O_3 or $BaZrO_3$ are examined as CO_2 methanation catalysts. Detailed HAADF-STEM

analysis is employed to show how the Pt re-distributes during catalyst activation and ends up atomically decorating the more strongly anchored Co particles. Finally, structure sensitivity is demonstrated for nickel nanoparticles supported on SiO_2 which were designed as catalysts for CO_2 hydrogenation. A systematic series of Ni/SiO_2 catalysts with different Ni loadings has been carefully characterized by HAADF-STEM imaging to obtain reliable Ni particle size distribution data which take into account corrections for metal oxidation effects. The same set of Ni/SiO_2 materials were then also characterized by operando FT-IR and quick X-ray absorption spectroscopy. By correlating the complementary data obtained from these three techniques two distinct, particle size dependent pathways are identified for this CO_2 hydrogenation reaction.

Chapter 1

Electron microscopy techniques and their application to studies of semiconductor nanocrystals and supported metal catalysts

1.1 Introduction

Materials at the nanoscale are the subject of considerable interest for their unique optical, electronic and chemical properties which are dictated by their size, structure and composition. In particular, semiconductor nanoparticles, or quantum dots (QDs), exhibit tunable optical behavior by varying their size and shape within the quantum confinement regime. On the other hand, metal nanostructures in various forms including discrete nanoparticles, sub-nm clusters and even single atoms can exhibit excellent catalytic performance in supported heterogeneous catalyst systems due to their high surface area to volume ratio. It is critically important to have the ability to characterize the structure and composition of these nanomaterials in order to establish structure-property correlations and to develop optimization strategies for improved material performance.

Electron microscopy has played a significant role in the study of semiconductor and metal nanostructures by revealing their nanoscopic features. Conventionally nanomaterials are characterized by light spectroscopy techniques (*e.g.*, ultra violet-visible (UV-vis), Raman, infra-red (IR)) and X-ray techniques (*e.g.*, X-ray diffraction (XRD), X-ray photoelectron spectroscopy

(XPS), X-ray absorption spectroscopy (XAS)). All of these methods simultaneously probe a very large number of the nanoscale species and provide global or 'averaged' information about the sample. In addition, despite being a surface sensitive technique, XPS with a detection depth of ~10 nm becomes a bulk technique for nanostructures smaller than 10 nm. By comparison, electron microscopy, especially transmission electron microscopy, can provide highly localized structural and chemical information on the sample in question at the nanoscale. The more recent advent of advanced aberration corrected electron microscopes has further pushed the resolution limit of the technique into the sub-angstrom regime. Herein, several electron microscopy techniques will be discussed that are applicable to the specific nanomaterial research problems detailed in the subsequent chapters of this dissertation.

1.2 Transmission electron microscopy

In conventional transmission electron microscopy (TEM), a near parallel electron beam passes through an ultra-thin specimen and gets projected onto a screen or a camera after magnification by electromagnetic lenses. The use of electrons for imaging rather than visible photons in light microscopes greatly improves the resolution limit due to the much shorter wavelengths of high-speed electrons.

Through interaction with the specimen, the electron wave can have both its amplitude and its phase modified, giving rise to image contrast. Thus, a fundamental distinction that needs to be made in TEM is between amplitude contrast and phase contrast. Amplitude contrast includes two common contrast mechanisms, namely, mass-thickness contrast and diffraction contrast. Mass-thickness contrast occurs when thicker or higher-mass (Z) regions of the specimen absorb

or scatter more electrons off the optic axis, leading to lower intensities in the bright field (BF) image. Diffraction contrast depends on the crystal orientation and arises from coherent elastic scattering at specific Bragg angles. Phase contrast, which is usually associated with high-resolution (HR-)TEM, is formed by the interference of two or more electron beams with different phases.

1.2.1 High-resolution TEM imaging

HR-TEM generally refers to the phase contrast imaging of lattice fringes in order to reveal the atomic structure of crystalline specimens. As described above, a phase contrast image needs to include contributions from more than one beam (Figure 1.1 (a)). When the beam is aligned along a low-index zone axis, an array of spots representing different sets of lattice planes will appear in the diffraction pattern (Figure 1.1 (b)), which will then interfere with each other to give crossed fringes in the image plane which can be related to the periodicities in the crystal lattice (Figure 1.1 (c)).

To better understand this contrast mechanism, we must first consider electrons in vacuum with a wavelength of λ. In the non-relativistic approximation, the correlation between λ and acceleration voltage U_0 is given by:

$$\lambda = \frac{h}{\sqrt{2meU_0}} \qquad \textbf{Eq. 1.1}$$

where h is Planck's constant, m is electron mass, e is the elementary electric charge. When the electron wave is within a solid having a potential of $\Phi(x, y, z)$, λ is modified to become λ':

$$\lambda' = \frac{h}{\sqrt{2me\left(U_0+\Phi(x,y,z)\right)}} \qquad \textbf{Eq. 1.2}$$

As they penetrate through a thin crystalline slab of thickness dz, the electrons undergo a phase

shift given by:

$$\mathrm{d}\phi = 2\pi\left(\frac{\mathrm{d}z}{\lambda'} - \frac{\mathrm{d}z}{\lambda}\right) = 2\pi\frac{\mathrm{d}z}{\lambda}\left(\frac{\lambda}{\lambda'} - 1\right) \qquad \textbf{Eq. 1.3}$$

Further manipulations of Eqs. 1.2 and 1.3 lead to:

$$\mathrm{d}\phi = 2\pi\frac{\mathrm{d}z}{\lambda}\left(\sqrt{\frac{2me\left(U_0+\Phi(x,y,z)\right)}{2meU_0}} - 1\right) = 2\pi\frac{\mathrm{d}z}{\lambda}\left(\sqrt{1+\frac{\Phi(x,y,z)}{U_0}} - 1\right) \qquad \textbf{Eq. 1.4}$$

The accelerating voltage in a TEM usually satisfies the condition that $U_0 >> \Phi(x, y, z)$. We can therefore expand the radical term in Eq. 1.4 as a Taylor series at $\frac{\Phi(x,y,z)}{U_0} = 0$ up to the second term, and get:

$$\mathrm{d}\phi = 2\pi\frac{\mathrm{d}z}{\lambda}\left(1 + \frac{1}{2}\frac{\Phi(x,y,z)}{U_0} - 1\right) = \frac{\pi}{\lambda U_0}\Phi(x,y,z)\cdot\mathrm{d}z \qquad \textbf{Eq. 1.5}$$

Hence, the total phase shift in a thin specimen can be obtained by integration:

$$\phi = \frac{\pi}{\lambda U_0}\int_0^t \Phi(x,y,z)\cdot\mathrm{d}z \qquad \textbf{Eq. 1.6}$$

where t is the specimen thickness. Assuming the potential depends only on x and y and is constant through the projected thickness of the sample it follows that:

$$\phi(x,y) = \frac{\pi t}{\lambda U_0}\Phi(x,y) \qquad \textbf{Eq. 1.7}$$

This indicates the phase shift generated reflects the periodicity of the crystal. The plane wave entering the crystal therefore gets phase-modulated by the periodicity of the crystal lattice to form the periodic exit wave.

The lattice fringes shown in HR-TEM imaging are interference fringes rather than direct images of atomic columns. Full interpretation via computer simulation of HR-TEM images usually requires a detailed knowledge of the specimen thickness, objective lens defocus and other lens and beam parameters. However, some very useful information can be reliably extracted from such images just by analyzing the spacings and interplanar angles of the fringes present in the illuminated area. Such HR-TEM images, if analyzed appropriately, can reveal crystallographic

information from nanoscale regions of interest and help to identify the crystal structures of unknown phases.

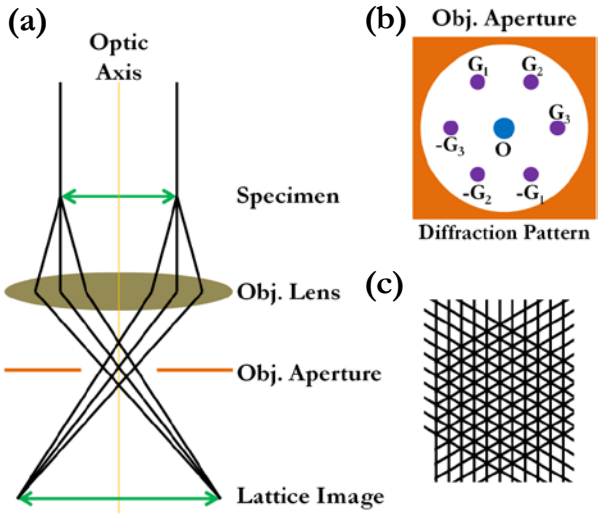

Figure 1.1: Phase contrast mechanism in HR-TEM. (a) Ray diagram for producing a phase contrast lattice image. (b) The diffraction pattern showing inclusion of multiple electron waves with different phases in the objective aperture. (c) Many-beam image displaying crossed lattice fringes. Adapted from Ref. 1.

1.2.2 Fourier transforms of lattice images

The periodicities present in HR-TEM lattice images can be best interpreted and measured via Fourier transform analysis. A Fourier transform decomposes a signal into its component frequencies. In the case of high resolution electron micrographs showing parallel lattice fringe stripes, a Fourier transform converts brightness fluctuations in real space into frequencies in reciprocal space.

Let us consider a 2-D image with N_x pixels horizontally and N_y pixels vertically. The pixel brightness at position (x, y) is $I(x, y)$. Then the brightness of the pixel (q_x, q_y) in the Fourier transform (reciprocal space) representation can be calculated by:

$$I(q_x, q_y) = \sum_{x=0}^{N_x-1} \sum_{y=0}^{N_y-1} I(x,y) \cdot \cos(2\pi q_x x) \cdot \cos(2\pi q_y y) \qquad \textbf{Eq. 1.8}$$

This process presents an inverse proportionality: a larger periodic length of the brightness modulation corresponds to a smaller distance between the brightness maxima in the Fourier transform, which is analogous to the diffraction pattern.

In practical analysis of lattice fringe spacings and interplanar angles, however, a fast Fourier transform (FFT) is more often used. The FFT is a special algorithm for quick calculation of a Fourier transform on a source image having x and y dimensions that are simple powers of two (*i.e.*, 2×2, 4×4, 8×8, 16×16, 32×32, 64×64, *etc.*). Armed with this size requirement, the FFT method is faster and more efficient than straightforward calculation of the discrete Fourier transform.

1.3 Scanning transmission electron microscopy imaging and spectroscopy

Scanning transmission electron microscopy (STEM) is a special type of TEM, in which the electron beam can be focused to a small probe and scanned over the specimen in a raster (Figure 1.2), in a manner analogous to that used in scanning electron microscopy (SEM). However, it should be noted that the scanned beam in the STEM always travels parallel to the optic axis during the scanning process, whereas the beam is tilted in the SEM during the scan.

Two major imaging modes can be employed in STEM, namely, bright-field (BF) and annular dark-field (ADF) imaging (Figure 1.2). The BF detector collects transmitted electrons exiting the specimen at relatively low angles with respect to the optic axis; in contrast, electrons scattered at relatively high angles, usually several times the incident beam convergence angle, contribute to ADF imaging. Based on the scattering angle range, ADF can be sub-divided into high-angle ADF

(HAADF), medium-angle ADF (MAADF) and low-angle ADF (LAADF), with typical inner collection angles of 25, 56 and 150 mrad respectively.[3] The most popular imaging mode in STEM is HAADF imaging, which utilizes incoherently scattered electrons and is highly sensitive to the atomic number of atoms in the sample. Apart from the different imaging modes, STEM also provides highly localized chemical analysis capabilities. X-rays generated from electronic excitations in the sample can be used for elemental identification by forming characteristic X-ray energy peaks in X-ray energy dispersive spectroscopy (XEDS). Another chemical analysis technique available on many STEMs is electron energy loss spectroscopy (EELS), which measures the amount of energy loss incurred from inelastic scattering of electrons. EELS can be used to detect inner-shell ionization events which can yield the elemental identity and oxidation states of atoms in a material with very high spatial resolution.

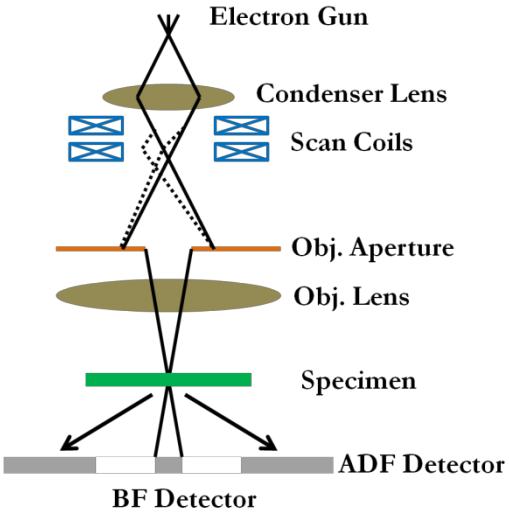

Figure 1.2: A schematic diagram of a STEM instrument. Adapted from Ref. 2.

1.3.1 Aberration correction in STEM

In an ideal optical system, every point on the object will be reproduced perfectly in the image.

However, electromagnetic lenses used in electron microscopes inevitably have optical imperfections, leading to the presence of aberrations that will degrade the spatial resolution. The dominant aberration type that controls the probe size in STEM (and TEM) is the 3rd order spherical aberration in the objective lens. Spherical aberration arises from the inhomogeneity in rotationally symmetric lenses, whereby electrons further off-axis are more strongly bent back toward the axis (Figure 1.3 (a)). This lens defect gives a positive spherical aberration coefficient C_s, and results in a point object being imaged as a disk with a minimum diameter in the plane of least confusion. The diameter of this disk of least confusion is given by: $d_s = 0.5C_s\alpha^3$, where α is the collection semi-angle.

The geometrical blur from spherical aberration limits our ability to magnify detail and cannot be refined by round lenses, where the large axial component of the magnetic field merely rotates the electron trajectories. To neutralize the positive C_s, the notion of non-round multipole lenses was first introduced by Scherzer[4] to break the rotational symmetry of the electromagnetic lenses. A multipole usually consists of several magnetic poles that diverge off-axis electrons such that they re-converge with near-axis electrons to a point (Figure 1.3 (b)). Multipole lenses usually come in a series with 4, 6 or 8 poles alternating North and South around the optical axis (Figure 1.4). These are termed quadrupole, hexapole, and octupole lenses respectively. The Lorentz force of these multipoles deflects the rays differently: a quadrupole squeezes the beam into a line; a hexapole imparts a triangular distortion to the beam; and an octupole transforms the beam into a square-like shape.

Current commercially available spherical aberration correctors with multipoles are classified into two types: the quadrupole-octupole (QO) corrector from Nion[6-7] and the hexapole corrector

from CEOS[8]. Nion's QO corrector consists of four quadrupoles and three octupoles, and was designed for a dedicated STEM, whereas CEOS's corrector is composed of a pair of hexapoles and additional transfer lenses, and can fit into most (S)TEM instruments.

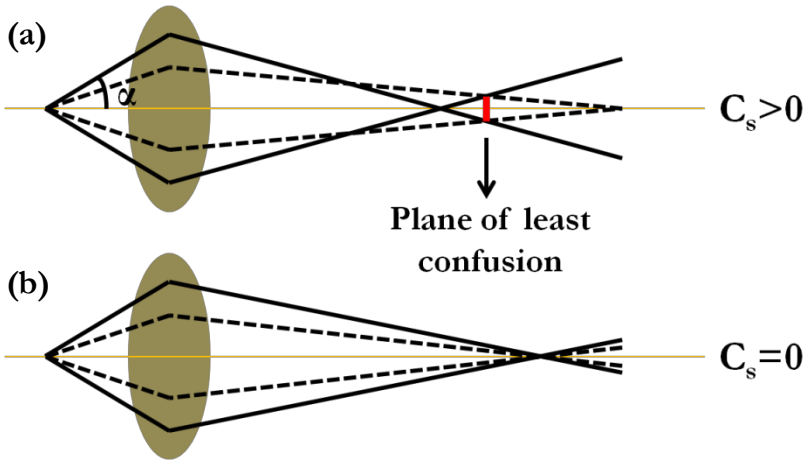

Figure 1.3: Schematic diagrams showing an electron lens (a) with spherical aberration (C_s) and (b) without spherical aberration (C_s).

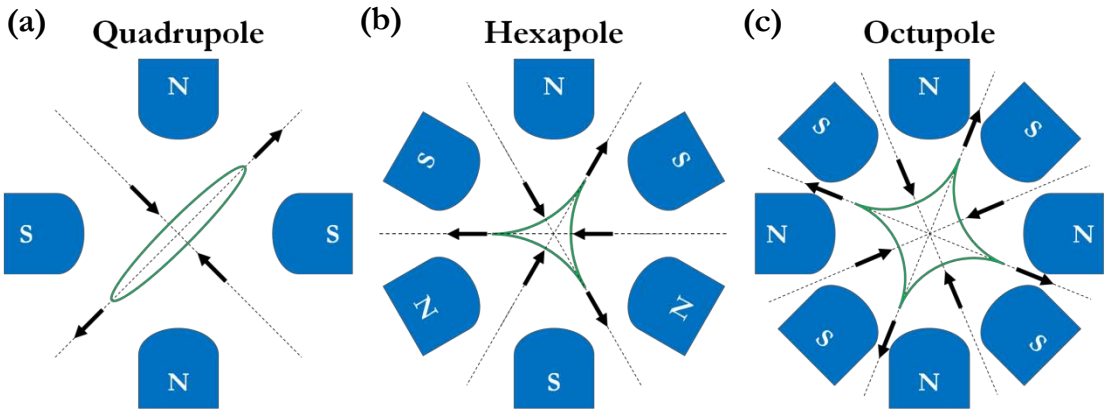

Figure 1.4: Schematic representation of multipole lenses of orders 4, 6 and 8 in aberration correctors (a) quadrupole, (b) hexapole and (c) octupole. Arrows indicate the resulting forces on electrons traveling down the optical axis (into the page). Adapted from Ref. 5.

It should be noted that modern instruments can now be corrected up to the 5th order aberrations, removing spherical aberration as the dominating factor in limiting the (S)TEM resolution. Emerging restrictions on microscope performances come from one or more of the following, namely, chromatic aberration, higher-order geometric aberrations, instrumental

instabilities, and statistical noise in the images.

1.3.2 HAADF-STEM imaging

As mentioned above, HAADF imaging is the most frequently used imaging technique in STEM. In this mode, an annular detector with a hole in the center collects electrons scattered out to high angles (>50 mrad). At large scattering angles, the atomic scattering factor from an atom tends towards that for Rutherford scattering from the nucleus. Meanwhile, Bragg reflections (diffraction contrast) would be suppressed as the phase shifts incurred by small random changes in the atom position due to thermal vibrations become significant, so that the coherent interference of the elastic scattering from the ideal crystal is lost. To a first approximation, the HAADF signal is the incoherent sum of the intensities of the Rutherford scattering from all the atoms irradiated by the beam. Apart from the transverse momentum imparted by the elastic scattering from the crystal, additional momentum is induced by inelastic scattering from phonons, namely, thermal diffuse scattering (TDS).

Free from wave interference, incoherent imaging in HAADF-STEM generates easily interpretable data. Atoms and projected atomic columns are identified as bright spots, regardless of the defocus value of a probe-forming lens and specimen thickness under all conditions. This is in stark contrast to the situation for HR-TEM imaging where computation is needed to unequivocally determine atom positions. Unscreened Rutherford scattering from a nucleus with an atomic number of Z will give rise to a Z^2-dependence of HAADF image intensity. Thus, HAADF imaging is also referred to as Z-contrast imaging. Due to the TDS effects, the HAADF image contrast deviates from Z^2 into Z^{2-x} (x = 0.3-0.7).[9] This strong Z-contrast feature of

HAADF-STEM leads to a straightforward chemically sensitive imaging mode that can be exploited in many circumstances to discriminate different atom types in structures without resorting to image simulation or spectroscopy.

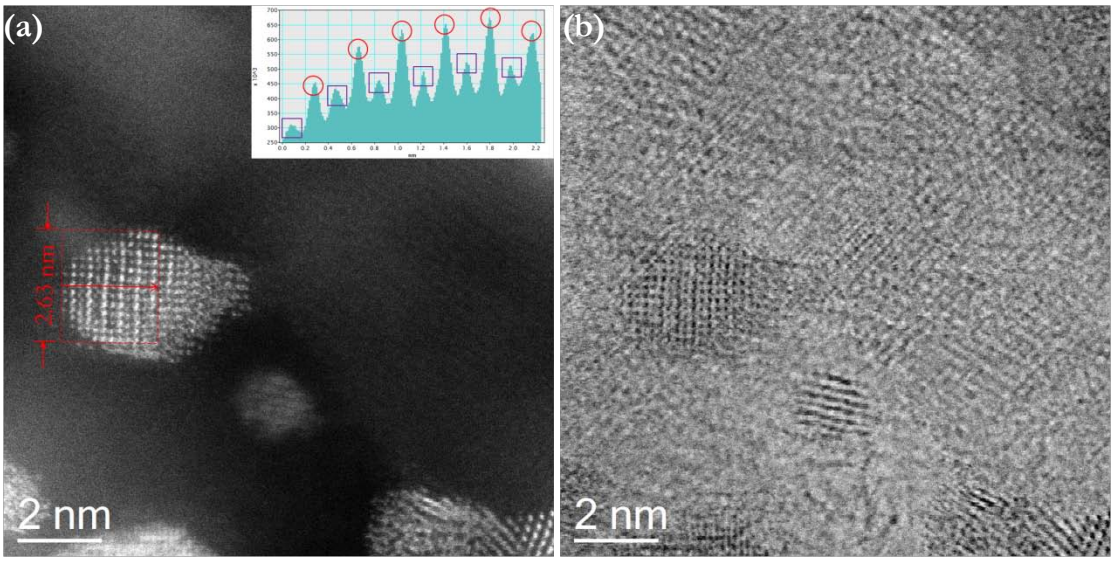

Figure 1.5: A pair of HAADF- (a) and BF-STEM (b) images of a Pt-Fe/Al_2O_3 catalyst. The inset in (a) is the intensity profile of a Pt-Fe nanoparticle with an integration width of 2.63 nm; red circles indicate high intensity (Pt-rich) planes, while purple squares indicate lower intensity (Fe-rich) planes.

Figure 1.5 shows a pair of HAADF- and BF-STEM images of a Pt-Fe/Al_2O_3 catalyst containing ordered Pt-Fe alloy nanoparticles. The intensity profile along the Pt-Fe particle oriented along the <110> zone axis in the HAADF-STEM image (Figure 1.5 (a) and inset) displays periodic intensity variations illustrating alternating Pt-rich and Fe-rich crystal planes. Because Pt (Z = 78) is much heavier than Fe (Z = 26), we are able to easily visualize Z-contrast differences between Pt-rich and Fe-rich planes within the same particle. In comparison, the Al_2O_3 support consisting of lighter elements exhibits an even lower intensity in the HAADF image. On the other hand, the same particle in the BF-STEM image (Figure 1.5 (b)), which is essentially equivalent to a phase contrast image in HR-TEM, does not show such intensity variation within

itself, and does not greatly stand out in contrast from the support background. This example demonstrates the strong chemical diagnostic capabilities of the *Z*-contrast imaging mode in STEM.

1.3.3 STEM-X-ray energy dispersive spectroscopy

Inelastic scattering of the incident electrons from the specimen may promote atoms into higher energy excited states via inner shell ionization, which can then be restored to their ground state by demotion of electrons from higher energy levels to fill the hole created in the vacant inner shell. This relaxation process releases excess energy that leads to the generation of X-rays and/or Auger electrons. The Auger yield is usually low, except for light elements, whilst the alternative de-excitation pathway favored by heavier elements entails the emission of an X-ray. The energy of the emitted characteristic X-ray when a single outer electron drops into the inner shell hole is equal to the difference between the energies of the two excited states involved. This energy difference is characteristic of the atom and can be traced to its chemical nature, while the X-ray intensity can be quantified to measure the elemental concentration. This secondary emission process provides the basis for X-ray energy dispersive spectroscopy (XEDS), which monitors the energy of emitted X-rays produced through interaction of the incident beam with the sample.

Compared to XEDS in a conventional TEM instrument, XEDS in the STEM has more analytical flexibility as it can analyze individual points or measure composition variations along line profiles spanning specific regions of interest. Moreover, spectral imaging in STEM enables mapping of the elemental distributions over an area. The advent of aberration correction in STEM not only dramatically improves the XEDS spatial resolution with the refined probe,[10] but

also enhances analytical sensitivity as more probe current can be packed into a smaller probe footprint after aberration correction.

As pointed out above, the measured characteristic X-ray signals can be quantified to determine local compositions of thin specimens. The Cliff-Lorimer ratio method[11] is widely used for quantitative X-ray analysis, and the compositions of constituent elements can be determined from the measured integrated intensities of characteristic X-ray counts above background:

$$\frac{C_{\mathrm{A}}}{C_{\mathrm{B}}} = k_{\mathrm{AB}}\left(\frac{I_{\mathrm{A}}}{I_{\mathrm{B}}}\right) \qquad \textbf{Eq. 1.9}$$

where C_A and C_B are the weight (or atomic) fractions of elements A and B, respectively, I_A and I_B are the respective integrated X-ray intensities, and k_{AB} represents the Cliff-Lorimer k factor, which may either be calculated from first principles or measured experimentally. The experimental method requires analysis of a thin foil of known composition with homogeneous distributions of elements A and B. Most XEDS software packages nowadays offer a much more rapid approach, whereby they can commonly calculate a set of k-factors for a specific detector system at a given accelerating voltage.

1.4 Environmental TEM

In the study of materials involved in chemical processes such as catalysis, it is highly desirable to monitor the response of the material to the surrounding environment (gas exposure, heat, *etc.*) real time while maintaining high spatial resolution. An environmental TEM (ETEM) is a TEM that enables the dynamic observation of catalyst specimens under a controlled gas and temperature environment. The specimen is exposed to gases so that the pressure of the volume around the specimen is kept higher than that of the TEM column. Two viable approaches have

been developed to conduct *in-situ* observations in the ETEM: namely the differential pumping approach (Figure 1.6 (a)), and the windowed cell approach (Figure 1.6 (b)).

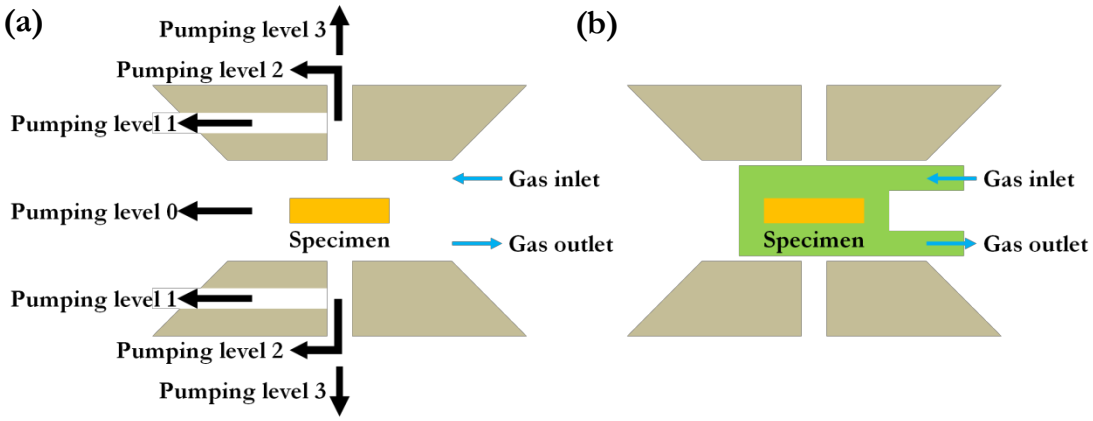

Figure 1.6: Schematics of the two main types of ETEM systems for imaging under gas environments. (a) The differential pumping system. (b) The windowed cell system. Adapted from Ref. 12.

In a basic design of the differential pumping system, several pressure limiting apertures in the TEM column are inserted in the bores of the polepieces to isolate regions with different gas pressures, which are pumped separately to maintain high vacuum in the electron gun area. A dedicated ETEM instrument needs to be built to accommodate the differential pumping system. The gas pressure, which usually has to be kept lower than 3000 Pa, is controlled by a flow directly into the polepiece gap. No other objects interact with the electron beam except the gas molecules. Therefore, materials composed of light elements, even graphene, can be observed with high resolution and good contrast under low gas pressure.[13] The differential pumping apertures, however, block the high-angle scattered electrons, limiting the use of ADF-STEM imaging in the low-angle regime. Furthermore, the low pressure in the differential pumping system makes it difficult to analyze the product gases due to their low yields, which is an unavoidable consequence of the extremely small amounts of gases flowing through and reacting on the

sample surface.

In contrast to the open system in the differential pumping ETEM, the windowed cell system creates an enclosed gas environment connected to passages for gas introduction and evacuation. The windowed cell is incorporated into the tip of a dedicated TEM holder (Figure 1.6 (b)). Above and below the cell along the optic axis there are holes sealed with thin films of carbon or silicon nitride in order to allow electron transmission while preventing gas leakage. By confining the volume to a small, closed layer around the specimen, the gaseous phase can reach pressures above one atmosphere,[14-15] which constitutes a more realistic reaction condition for most chemical processes. This set-up can be installed in different TEMs with no modification to the column or vacuum system required and the preferred HAADF-STEM imaging mode can be accessed. Nevertheless, additional scattering information from the window material is superimposed onto the image and diffraction pattern of the specimen, causing resolution degradation. This interaction also impedes reliable XEDS analysis.

1.5 Applications of these electron microscopy techniques in studies of semiconductor nanocrystals

1.5.1 Nanoscopic analysis of semiconductor nanocrystals

Reducing the size of inorganic materials down to the nanometer regime has been one of the most active fields of research in materials science over the past two decades. The ultra-small size of nanomaterials endows them with size- and shape-dependent physical and chemical properties owing to their high surface/volume ratio and associated quantum effects. Semiconductor nanocrystals, also known as quantum dots (QDs), have been particularly well studied in the

nascent nanotechnology field. In these materials, quantum confinement effects arise below a critical threshold size, usually referred to as the Bohr radius, due to the restriction of charge carrier motion by the small physical volume of the QD. This causes a widening of the band gap, and manifests itself as a blue shift in optical absorption spectra.

As the optical, electronic and chemical properties of semiconductor nanocrystals are size-dependent, it is desirable to determine the particle size distribution (PSD) of these nanocrystals. (S)TEM imaging is capable of directly visualizing the 2-D projected area of a particle, from which the equivalent spherical diameter can be deduced. More details concerning the PSD determination of nanomaterials in general will be discussed in Section 1.6.1.

The shape of semiconductor nanocrystals is another factor affecting their properties.[16] The synthesis of nanocrystals with various well-defined exposed surface facet planes has been an area of exciting development[17-18] as it paves the way to materials with tailored, geometry-dependent properties. TEM-based techniques are essential for studying the morphologies of nanocrystals and unveiling their underlying synthesis-shape-property correlations. Perhaps the most convenient way to study nanocrystal shapes is to image their 2-D projections. If one intends to extract information on 3-D morphologies for 2-D projections, analysis by image simulation can be of great help. For example, Cordeiro *et al.*[19] reported a two-phase hydrothermal synthesis method capable of controlling the shape of CeO_2 nanocrystals by varying the oleic acid (OLA) to cerium (Ce^{3+}) ratio. To obtain detailed analysis of the resulting nanocrystal morphologies, they applied HR-TEM multi-slice image simulations wherein the specimen is sectioned into many thin slices normal to the incident beam direction and compared to the experimental data, from which 3-D model structures were proposed (Figure 1.7). The reconstructed 3-D images (Figure 1.7 (d,

h)) demonstrate the tendency for a low [OLA]:[Ce^{3+}] ratio of 4:1 to generate polyhedral CeO_2 nanocrystals exposing {111} and {200} facets, whereas a higher [OLA]:[Ce^{3+}] ratio of 8:1 led to the formation of CeO_2 nanocubes exposing {220}, {111} and {200} facets.

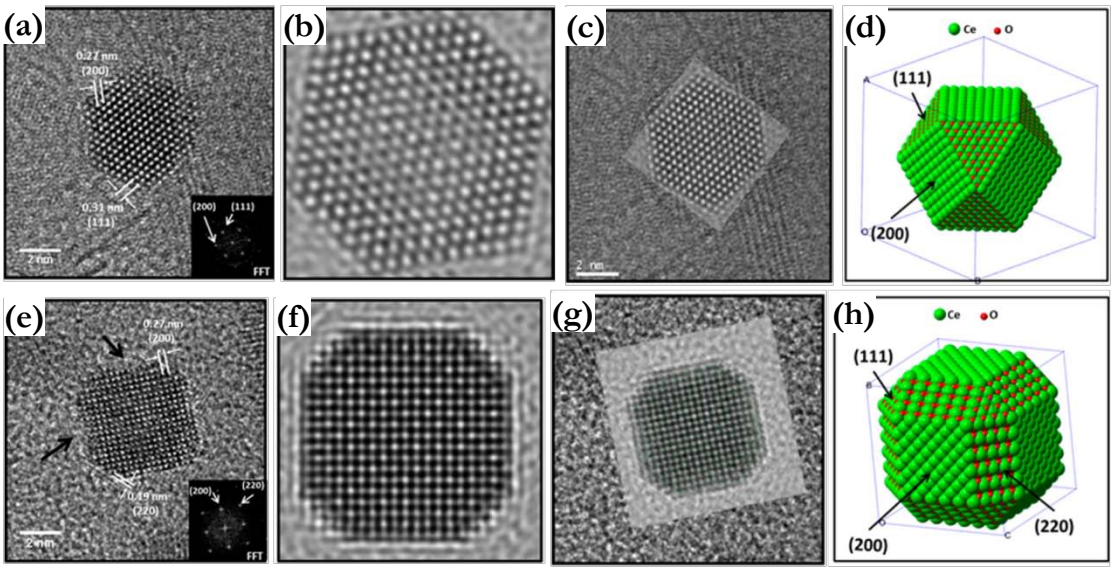

Figure 1.7: HR-TEM simulations of CeO_2 nanocrystals prepared with a two-phase hydrothermal method using different [OLA]:[Ce^{3+}] ratios. (a-d) [OLA]:[Ce^{3+}] = 4:1; (e-h) [OLA]:[Ce^{3+}] =8:1. (a, e) HR-TEM images of a polyhedral (a) and a cubic (e) CeO_2 nanocrystal respectively. (b, f) Simulated CeO_2 nanocrystal images oriented along the [110] (b) and [100] (f) zone axes respectively. (c, g) Superpositions of the simulated images with the experimental ones. (d, h) 3-D image reconstructions. Insets in (a) and (e) are the FFTs of the respective nanocrystals.[19]

Electron tomography is another useful tool for the recovery of nanoparticles shapes, in which a systematic sequence of images collected at different tilt angles are reconstructed into a 3-D representation of the object. However, electron tomography in most cases is only applied to relatively large (>5 nm) nanoparticles. Reports have been very rare[20] of electron tomography performed at atomic resolution on sub-5 nm nanocrystals, due to the beam sensitivity of small nanoparticles under extended electron beam illumination. In addition, electron tomography is especially challenging on semiconductor QDs because they have more complex structures and are considerably more vulnerable to beam damage than their more robust metal nanoparticle

counterparts.

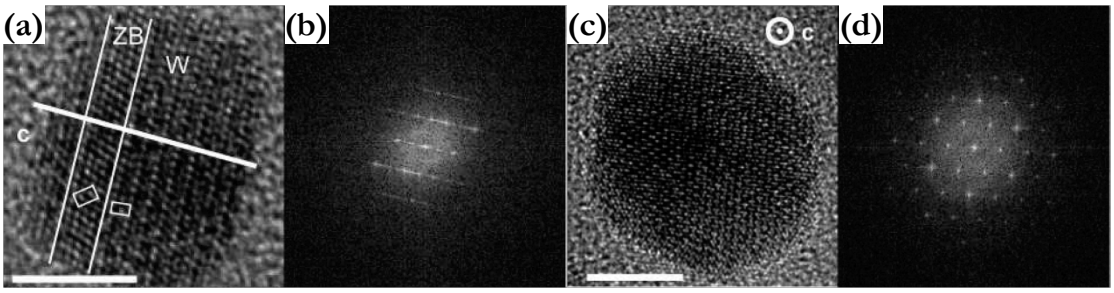

Figure 1.8: Polytypic CdSe (3 nm diameter)-CdS (4 nm thick) core-shell nanocrystals. (a) HR-TEM image highlighting the presence of wurtzite $[2\bar{1}0]$ and zinc-blende $[01\bar{1}]$ domains observed from the direction normal to the wurtzite *c*-axis. Unit cells are indicated by white rectangles. (b) The FFT of (a) showing polytypism as blurred lines. (c) HR-TEM image viewed along the wurtzite *c*-axis. (d) The FFT of (c). Scale bars in (a) and (c) represent 5 nm.[21]

Polytypism exists in many semiconductor nanocrystal systems. For instance, II-VI compound semiconductors generally crystallize in either face-centered cubic (zinc-blende) and hexagonal (wurtzite) crystal structures, both of which are four-coordinate and vary in the layer stacking along the <111> zone axis for zinc-blende or <001> for wurtzite, displaying an ABCABC or an ABABAB sequence, respectively. While XRD can identify the co-existence of both polymorphs provided the nanocrystals are not too small, it cannot distinguish whether the sample consists of a mixture of purely wurtzite and zinc-blende nanocrystals or if individual nanocrystals contain both polytypic domains. Such highly localized information can however be obtained from high resolution lattice images complemented by FFT analysis. For example, in a study conducted by Dubertret *et al.*[21], they attempted to grow a CdS shell on a zinc-blende CdSe core using primary amines as the ligand during shell formation. HR-TEM imaging and the corresponding FFT analysis demonstrated the co-existence of wurtzite and zinc-blende domains within single particles (Figure 1.8 (a, b)). However, when the nanocrystal was oriented along the wurtzite *c*-axis, it was not possible to distinguish between wurtzite or zinc-blende, and the overall

structure appears wurtzite in the FFT (Figure 1.8 (c, d)). In light of this possible ambiguity, it is often necessary to examine multiple nanocrystals along a variety of interpretable orientations to more confidently draw conclusions about their polymorphic crystal structures.

Surface engineering is an important tool to manipulate the properties of semiconductor nanocrystals. One major strategy is to grow a shell of a second semiconductor with a different band gap onto the nanocrystals, forming a core-shell system. This method has been applied to improve the fluorescence quantum yield in QD systems, to stabilize them against photo-oxidation, and to tune their emission wavelength range. Several electron microscopy approaches have been employed to visualize and validate the formation of the core-shell heterostructure.

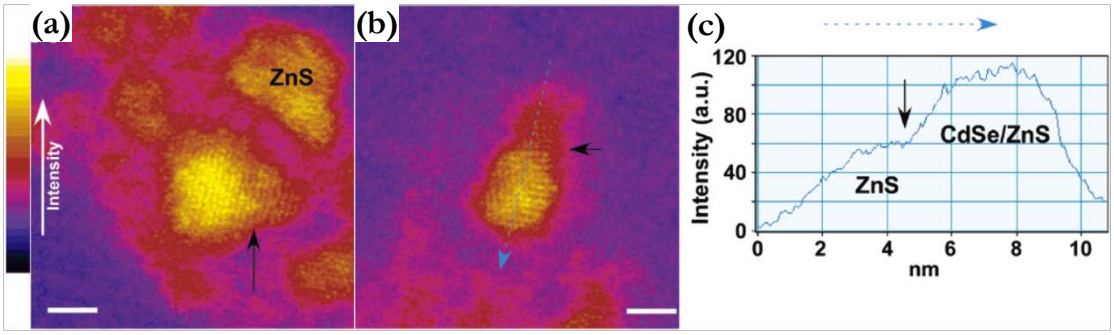

Figure 1.9: HAADF-STEM imaging of CdSe-ZnS core-shell nanocrystals. (a, b) False colored HAADF images. The black arrows in (a) and (b) indicate the ZnS shells. (c) The line intensity profile of the nanocrystal in (b) showing the core-shell interface. The black arrow in (c) indicates the core-shell interface. Scale bars in (a) and (b) represent 3 nm.[22]

In some cases, the different atomic numbers of the constituent elements in the core and shell materials can give rise to significant *Z*-contrast. For example, Rosenthal *et al.*[22] used HAADF-STEM to image CdSe-ZnS core-shell nanocrystals, where bright cores were observed with fainter shells encircling them (Figure 1.9 (a, b)). For comparison, the existence of coreless particles, presumably secondary ZnS particles that nucleated during shell growth, could be

confirmed by the presence of fainter particles showing uniform intensity (Figure 1.9 (a), top right corner). The line profile shown in Figure 1.9 (c) along the *c*-axis of the core-shell nanocrystal in Figure 1.9 (b) displays the intensity variation across the core-shell interface.

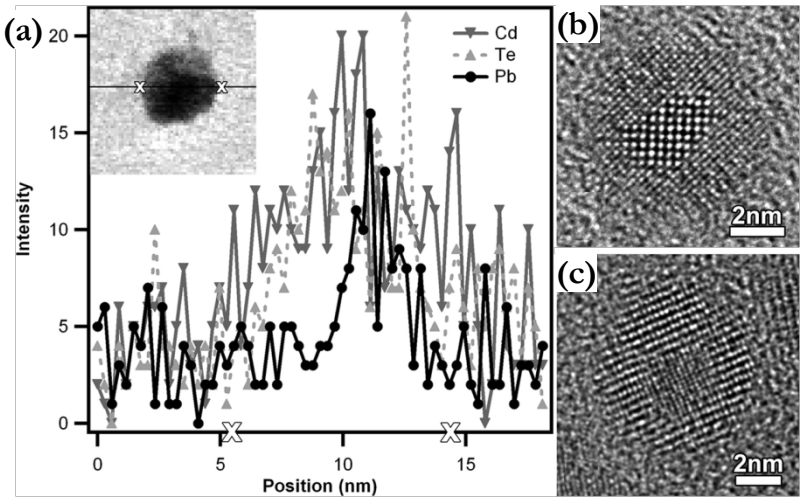

Figure 1.10: Electron microscopy characterization of PbTe-CdTe core-shell nanocrystals. (a) STEM-XEDS line scan along a core-shell particle. The particle edges are marked with X. (b, c) HR-TEM images of core-shell nanocrystals along the <100> (b) and <211> (c) projections.[23]

STEM-XEDS analysis provides another tool for identifying core-shell structures. This is performed by comparing XEDS signals from the center and edge regions of a nanocrystal. For example, from an STEM-XEDS line-scan through the center of a single PbTe-CdTe core-shell nanocrystal, Hens *et al.*[23] concluded that Cd and Te were present over the entire diameter of the particle, whereas Pb was limited to a narrow region near the particle center (Figure 1.10 (a)). However, due to the inherently poor signal-to-noise ratio of the line-scan, this claim does not seem entirely convincing. Further confirmation comes from phase contrast imaging along specific zone axes. While both PbTe and CdTe adopt a rock-salt structure with minimal lattice mismatch,[24] they may display distinct lattice patterns in HR-TEM even along the same orientation. This is because the electron beam can interfere differently with the two cations,

resulting in different phases and amplitudes in the image plane. An appropriate defocus value can manifest the difference in the lattice patterns of PbTe and CdTe. Figure 1.10 (b, c) shows two excellent examples of such effects. Under the same orientation, the core and shell regions of a nanocrystal exhibit different patterns, unequivocally proving the formation of an epitaxial core-shell structure. Besides XEDS, EELS and the associated energy filtered TEM (EF-TEM) techniques have also been applied to the characterization of core-shell nanostructures.[25-26]

1.5.2 Scope of semiconductor nanocrystal studies presented in this dissertation

Conventionally, semiconductor nanocrystal materials are largely synthesized via chemical routes (*e.g.*, hot-injection method), which usually require harsh reaction conditions and toxic organic solvents. Alternatively, biomineralization offers a greener synthesis approach by allowing naturally evolved systems such as diatoms[27] and mollusks[28] to immobilize metal ions to grow structurally controllable solid-phase materials in aqueous media under ambient conditions. This new strategy is of great potential interest because of its lower environmental and economic costs.

In Chapters 2, 3 and 4 of this dissertation, I will describe the application of advanced electron microscopy techniques to various semiconductor and insulator nanocrystal systems prepared using the biomineralization method. Chapter 2 will discuss the preparation and physical characterization of several biomineralized cadmium chalcogenide nanocrystal systems. The extracellular production of CdS QDs via an engineered bacterial strain of *Stenotrophomonas maltophilia* (SMCD1) will first be demonstrated. The cadmium-tolerant colonies of this bacterium are shown to be capable of manufacturing luminescent CdS QDs in the presence of cadmium

acetate and L-cysteine in M9 minimal media. The combination of (S)TEM and optical characterization techniques establishes a positive correlation between the mean nanocrystal size and the growth time, illustrating good control and tunability over a range of quantum confined particle sizes and band gap energies. Next we show that it is a particular enzyme, a recombinant putative cystathionine γ-lyase (smCSE) that is secreted by the bacterium which is responsible for generating H_2S from L-cysteine. This single enzyme is demonstrated to play a dual role in both inducing CdS mineralization and templating nanocrystal growth. The smCSE-mineralized nanocrystals library is then expanded beyond CdS, to create CdSe QDs with controlled size and structure. Biomineralization of CdSe-CdS core-shell morphology QDs with considerably improved optical properties is then demonstrated. In this work TEM and STEM imaging as well as XEDS analysis have been utilized to correlate the structural features of the cadmium chalcogenide QDs to their optical properties and the growth parameters of the biomineralization processes. In particular, to better characterize the particle size distribution (PSD) of the irregularly shaped CdSe-based nanocrystals produced, a useful measurement protocol has been devised which allows us to associate the shortest dimension within a particle to the measured band gap of the QDs.

Chapter 3 further expands the material palette of this biomineralization strategy to other metal sulfide nanocrystals. In common with the bacteria-mediated production of CdS QDs, the SMCD1 strain is shown to be capable of biomineralizing PbS-based QDs. Furthermore, subsequent biomineralization of a CdS overlayer onto the PbS QDs is demonstrated to form a PbS-CdS core-shell configuration that possesses blue-shifted optical properties relative to the PbS core. In addition, the biomineralization of $CuInS_2$ (ternary) and $(CuInZn)S_2$ (quaternary)

alloy nanocrystals is then developed which involves a two-step nucleation pathway. Detailed HR-TEM, HAADF-STEM and XEDS investigations of both the PbS-based and $CuInS_2$-based QDs are used to characterize the structural and compositional characteristics of these novel biomineralized nanomaterials.

In additions to II-VI compound semiconductor nanocrystals, we have also explored if metal oxide nanocrystals can be biosynthesized. The aqueous biomineralization of CeO_2 and alloyed CeO_2-ZrO_2 nanocrystals is demonstrated in Chapter 4 using another enzyme, namely a modified form of silicatein (rCeSi). This enzyme not only catalyzes the formation of ceria and ceria-zirconia mixed oxide nanocrystals at room temperature, but also templates their morphological structure without needing to add a base or an explicit chemical structure directing agent. Analytical electron microscopy analysis is applied to validate the successful biomineralization of sub-3 nm fluorite-type CeO_2 and CeO_2-ZrO_2 nanocrystals, which are amongst the smallest reported to date. Their catalytic properties are also explored in relation to the CO oxidation reaction.

1.6 Applications of these electron microscopy techniques in studies of supported metal catalysts

1.6.1 Electron microscopy investigations of catalyst size and dispersion

Highly dispersed supported metal catalysts have a large proportion of metal atoms available for chemisorption of gases and subsequent catalytic reactions. Dispersion and the mean catalyst size are two important parameters used to characterize the catalyst. Dispersion refers to the fraction of metal atoms directly exposed to the reactants and is used to calculate the activity of the

catalyst per surface metal atom. A high dispersion is usually associated with a small mean particle size in a catalyst, which ensures a high proportion of exposed surface atoms. Metal dispersion is typically determined from gas chemisorption measurements. If the chemisorption stoichiometry is known, dispersion can be calculated from the metal surface area given by the measurement of the quantity of a gas adsorbed selectively on the metal at monolayer coverage.

The size of a particle is usually defined as its equivalent spherical diameter. If we consider a collection of n_i spherical particles of diameter d_i, we can produce two types of size distribution. The first is the *number distribution*, which is a plot of n_i as a function of d_i; the second is the *area distribution,* which is a plot of $n_i d_i^2$ as a function of d_i. The latter gives more weight to larger particles and thus is more representative of the metal surface. Accordingly, two mean particle sizes are usually considered, the length-number mean diameter,

$$d_{\mathrm{LN}} = \sum n_i d_i / \sum n_i \qquad \textbf{Eq. 1.10}$$

and the volume-area mean diameter,

$$d_{\mathrm{VA}} = \sum n_i d_i^3 / \sum n_i d_i^2 \qquad \textbf{Eq. 1.11}$$

The latter can be associated with surface area and dispersion measurements by chemisorption. Assuming spherical shapes for all particles, the relationship between specific surface area S_{sp} and the length-number mean diameter d_{VA} is given by:

$$S_{\mathrm{sp}} = \frac{6}{\rho d_{\mathrm{VA}}} \qquad \textbf{Eq. 1.12}$$

where ϱ represents the mass density. Similarly, the relationship between metal dispersion D and mean particle size d_{VA} is:

$$D = 6\frac{v_{\mathrm{m}}/a_{\mathrm{m}}}{d_{\mathrm{VA}}} \qquad \textbf{Eq. 1.13}$$

where v_{m} is the volume occupied by an atom m in the bulk of metal, and a_{m} is the surface area

occupied by a surface atom *m*. Therefore, the volume-area mean diameter can be correlated to the diameter deduced from gas chemisorption experiments.

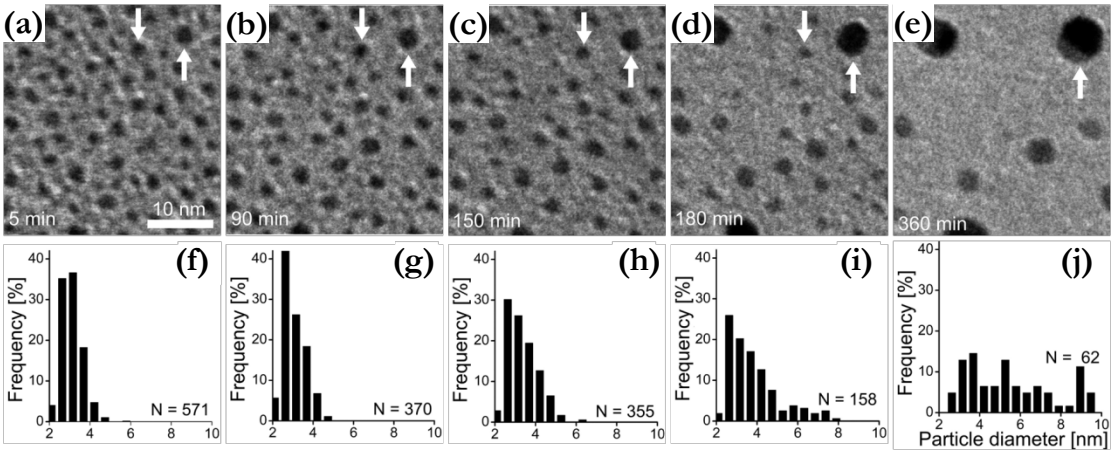

Figure 1.11: *In-situ* TEM images (the 40 × 40 nm² part selected from 130 × 130 nm² area) of Pt supported on Al_2O_3 catalyst in 10 mbar at 650 °C (a-e), and the histogram of the size distribution measured from the full image (f-j).[29]

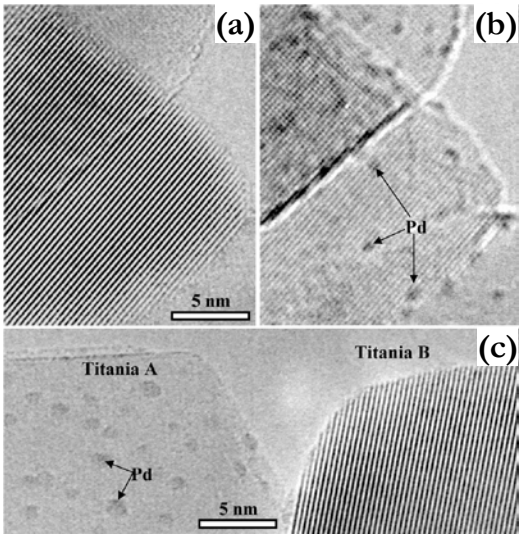

Figure 1.12: HR-TEM images of a TiO_2-supported Pd catalyst illustrating the variations of the visibility of small particles when the defocus changes.[30]

Particle size can be determined directly from granulometry measurements by electron microscopy. For instance, Helveg's group[29] carried out a dynamic PSD study of Pt nanoparticles in an environmental TEM under 10 mbar air at 650 °C. The Pt nanoparticles supported on Al_2O_3

were found to increase in diameter with an increasing sintering time, following an Oswald ripening process (Figure 1.11 (a-e)). Such size changes were more comprehensively reflected by the corresponding PSDs (Figure 1.11 (f-j)). Detailed analysis suggested that the sintering rate of Pt nanoparticles depended on (i) the size and (ii) the distance to the neighboring nanoparticles.

The pre-requisite for obtaining a useful PSD is the need to consider a large number of particles that can give a statistically reliable result. Failure to detect particles is the major factor compromising the accuracy of PSD measurements by TEM. The usual cause is the weak contrast of the particles with respect to the support. Thick and/or highly-scattering supports will overshadow the contrast from many small particles except those located near support edges. The imaging conditions of the microscope also affects the visibility of small particles.[31] For example, when supported on amorphous carbon, sub-1 nm particles cannot be discerned from the phase contrast background of the support, leading to distorted PSDs, especially if the focus, astigmatism and specimen drift are not optimally controlled. For the situation when crystalline oxides constitute the support, depending on the space frequency transferred by the objective lens, either only the lattice fringes of the oxide support are visible, obscuring any contrast from small particles (Figure 1.12 (a)), or the weak mass contrast of the particles vanishes in or are overshadowed by the defocused lattice fringes of the oxide support (Figure 1.12 (b)), again impeding the accuracy of the size measurements.[30] Examination of Figure 1.12 (c) may lead one to conclude preferential dispersion of Pd nanoclusters on the left crystallite (Titania A) but not on the right one (Titania B), which is actually a false impression caused by the different heights and orientations of the two support crystallites.[30] To clarify and overcome this confusion several micrographs must be taken from the same area using different imaging conditions.[31]

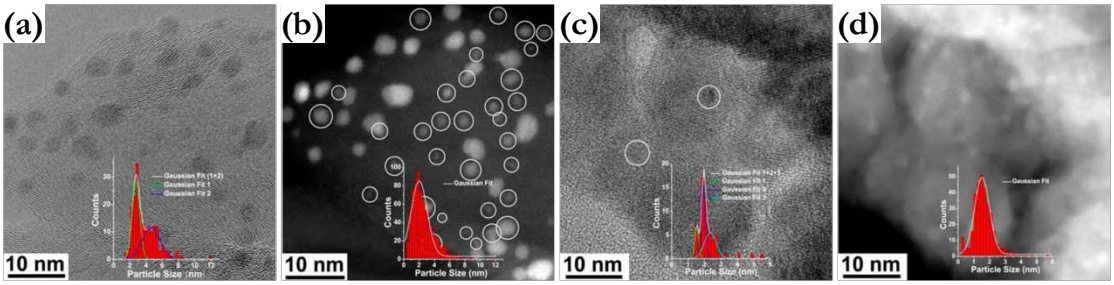

Figure 1.13: HR-TEM (a) and HAADF-STEM (b) images of Ru/CNTs, and HR-TEM (c) and HAADF-STEM (d) images of a Pd/FeO_x catalyst, respectively, showing different visibilities of small particles when imaged with these two methods. The insets are the corresponding PSDs. Some small particles (circled in (b)) are not visible in (a). Most of the Pd nanoparticles in (d) are invisible in (c), except for the two circled particles.[32]

HAADF-STEM imaging greatly facilitates our ability to resolve ultra-small metal nanoparticles consisting of high *Z* atoms on lower mass supports. As illustrated in Figure 1.13, numerous small Ru/Pd particles are clearly observed on both for carbon nanotube (CNT) and iron oxide supports in HAADF-STEM imaging, but not in the corresponding HR-TEM images, resulting in significant differences in the total numbers of particles counted and the resultant PSDs derived from each imaging technique.[32]

Special care must be taken when examining the particle size of first-row transition metals, as they are prone to oxidation in air before transfer into the microscope. For larger particles, oxide layers can form surrounding the metallic cores, whereas complete oxidation usually takes place in the case of smaller particles. In both cases the observed particles by *ex-situ* microscopy are larger than those in the metallic state. Lattice fringe analysis offers a useful tool to discriminate the metallic phase from its oxidized form. To produce a PSD that is truly representative of the supported metal catalyst in reaction conditions (often under a reducing atmosphere), one can sometimes deduce the original particle size from the size measured from the oxidized particles, given the volume that each metal atom occupies in the reduced and oxidized states respectively.

If partial oxidation occurs forming an oxide shell, statistical measurements of the shell thickness need to be conducted to obtain the original metal particle size.

Another possible scenario where particles escape detection is via the build-up of a carbonaceous deposit on the catalyst surface by electron beam-induced decomposition of organic contaminants present in (i) the microscope column, (ii) on the TEM support grid or (iii) intrinsic to the sample itself. Clean preparation of grids and specimens and a high vacuum in the column are imperative to keep (S)TEM observation free from contamination effects obscuring the visibility of particles. Typical methods to mitigate specimen borne contamination include baking, plasma cleaning, and beam showering. By raising the temperature of the sample to ~110 °C, baking aids in the desorption of water and light organic fractions from the specimen. Plasma cleaning utilizes ionized gases (*e.g.*, O_2, Ar) to chemically interact with the hydrocarbon material on the sample, converting it to volatile species. Beam showering, carried out in the TEM instrument, floods a very large area on the specimen with a high electron flux to immobilize the hydrocarbon species.

When the size of the metal species in catalysts is reduced from the nanoscale to their ultimate limit, forming atomically dispersed supported metal catalysts, the metal dispersion reaches 100%. The topic of single-atom catalysts (SACs), containing isolated single atoms dispersed on the support, has attracted increasing attention in the field of heterogeneous catalysis in recent years.[33] To identify the single atoms and determine their spatial distribution, the most convincing and intuitive evidence is usually obtained from aberration-corrected HAADF-STEM imaging which shows bright spots against the background support that can often be directly interpreted as single heavy atoms. For example, the HAADF-STEM images in Figure 1.14

unambiguously shows a dispersion of Pt, Ir and Au single atoms that occupy the positions of Fe atoms on the FeO_x support.[34-36] Compositional analysis of individual metal atoms is still not routinely available by XEDS[37-38] and EELS[39], which is hindered by the electron beam induced effects and the detection sensitivity limitation.[40]

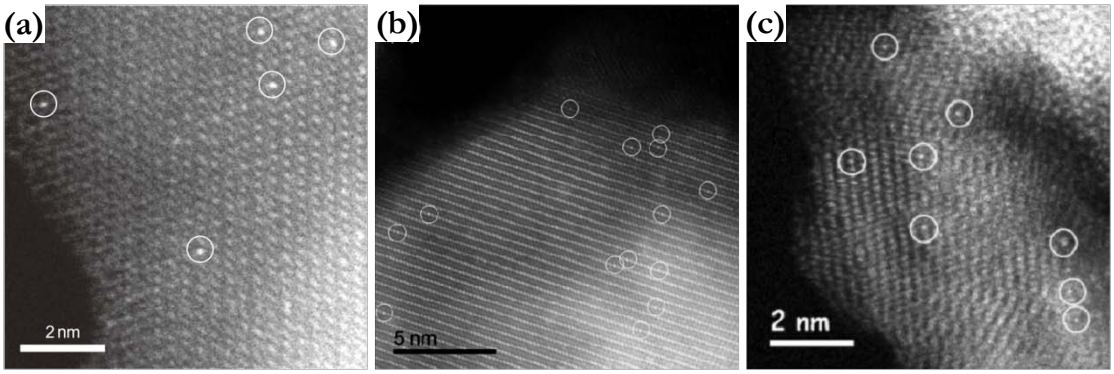

Figure 1.14: Aberration-corrected HAADF-STEM images of various metal catalysts on the FeO_x support showing the presence of isolated metal atoms. (a) 0.17 wt% Pt/FeO_x. (b) 0.22 wt% Ir/FeO_x. (c) 0.03 wt% Au/FeO_x. Single metal atoms are indicated by white circles.[34-36]

Besides (S)TEM, many bulk spectroscopic techniques are also often applied to the study of heterogeneous catalyst systems, which give 'averaged' information on the structural, chemical and catalytic properties of the samples. These techniques serve as complementary tools to the highly localized, ands statistically more sparse information derived from the (S)TEM methods. For instance, extended X-ray absorption fine structure (EXAFS) spectroscopy can be used to determine metal–metal coordination numbers. For instance, the lack of signal corresponding to metal–metal bonding in the active catalytic species can be sometimes be associated with the formation of atomically dispersed catalysts. Infra-red (IR) based techniques such as Fourier transform IR (FTIR) spectroscopy and diffuse reflectance IR Fourier transform spectroscopy (DRIFTS) may also be employed to identify the presence of isolated metal atoms in a supported catalyst. If the IR-related techniques and EXAFS methods can be coupled with HAADF-STEM

they collectively provide a powerful tool box for the investigation of metal SACs. Furthermore, the white-line intensity in the X-ray absorption near edge structure (XANES) and X-ray photoelectron spectroscopy (XPS) analysis can be used to monitor the oxidation state of the metal species, and can be correlated to the STEM-EELS data derived from nanoscale features in the catalyst.

1.6.2 Scope of catalyst nanocrystal and dispersion studies presented in this dissertation

In Chapters 5, 6 and 7, the application of analytical electron microscopy tools to the study of catalyst dispersion and size in three specific heterogeneous catalyst systems of current technological interest will be described. Chapter 5 focuses on developing an atomically dispersed Au catalyst supported on amorphous carbon for the acetylene hydrochlorination reaction. Correlations of *in-situ* X-ray absorption fine structure (XAFS) data with our *ex-situ* HAADF-STEM analysis indicate that by choosing the appropriate combination of solvent and gold precursor in the preparation method, isolated cationic Au^{+} and Au^{3+} species can be stabilized at ~100% dispersion. These studies also provide fundamental insight into the catalytic mechanism at play in this reaction.

In Chapter 6, studies on a set of co-supported Co and Pt nanoparticles designed for CO_2 methanation are described, in which a $BaZrO_3$ support is found to considerably improve the catalyst performance relative to a more conventional γ-Al_2O_3 support. Aberration-corrected STEM identifies the active form in the catalysts as Co nanoparticles decorated with atomically dispersed Pt, which are formed by surface Pt migration under high temperature treatments. The

disparity in catalyst performance afforded by the two supports is rationalized in terms of the different strengths of metal-support interaction that are characterized by a comparison of the contact angle and wettability of Co nanoparticles on the supports.

Chapter 7 will showcase a study in the structure sensitivity of Ni/SiO_2 catalysts for the CO_2 hydrogenation reaction. Catalyst samples with different mean Ni particle sizes are prepared and examined by HAADF-STEM, which produces reliable PSD data after suitable correction for the metal oxidation effects. Two distinct, particle size dependent reaction pathways are identified by complementary operando Fourier transform infrared (FT-IR) spectroscopy and quick-XAS experiments, shedding light upon the mechanism of CO_2 hydrogenation over Ni.

1.7 (S)TEM experimental information

Throughout this dissertation, all the semiconductor nanocrystal and catalyst samples were analyzed in a JEOL ARM 200CF analytical electron microscope equipped with a 4th order ASCOR probe corrector and a JEOL Centurio silicon drift detector XEDS system operating at 200 kV. Images were collected in the HAADF-STEM, BF-STEM and HR-TEM modes. (S)TEM image acquisition and interpretation were performed in DigitalMicrograph; crystal structure visualization was realized in the VESTA program. XEDS data were acquired and analyzed using Thermo Scientific NSS software. During XEDS data acquisition, the specimen was usually tilted 15° towards the X-ray detector to maximize the collection efficiency.

Prior to (S)TEM examination of the biomineralized semiconductor and insulator nanocrystals that will be discussed in Chapters 2, 3 and 4, the TEM specimens were usually prepared by drop casting the aqueous sol onto holey carbon copper mesh TEM grids. For the

solid catalyst samples, the materials for (S)TEM analysis were ground to finer powders using an agate mortar and pestle and then dry dispersed onto TEM grids.

Hydrocarbon contamination of the specimens was often encountered during (S)TEM analysis, particularly for the aqueous-phase biomineralized nanocrystals under STEM imaging mode at high magnifications. To alleviate the contamination problem, the specimens would undergo air-plasma treatments for ~10 s at 1 W power. Extended exposure to the plasma with a high input power was found to be detrimental to the carbon film of the TEM grid. Another approach to tackle specimen contamination was to conduct an electron beam shower in the microscope column. However, due to the beam sensitivity of some of the biomineralized nanocrystal systems, great caution needed to be taken during the beam showering process to prevent structure modification and destruction of the delicate nanocrystals. A tentative 1-2 min beam showering period was often applied first to test the robustness of the particles.

1.8 References

1. Williams, D. B.; Carter, C. B. *Transmission electron microscopy: a textbook for materials science*; Springer-Verlag: New York, 2009.

2. Pennycook, S. J.; Nellist, P. D., Eds.; *Scanning transmission electron microscopy: imaging and analysis*; Springer-Verlag: New York, 2011.

3. Jones, L.; Yang, H.; MacArthur, K. E.; Ryll, H.; Simson, M.; Soltau, H.; Kondo, Y.; Sagawa, R.; Banba, H.; Nellist, P. D., Opportunities in angularly resolved dark-field STEM using pixelated detectors. *Microsc. Microanal.* **2015**, 21, 2411-2412.

4. Scherzer, O., Spharische und chromatische Korrektur von Elektronen-Linsen. *Optik* **1947**, 2, 114-132.

5. Brydson, R., Ed.; *Aberration-corrected analytical transmission electron microscopy*; John Wiley & Sons: Chichester, 2011.

6. Krivanek, O. L.; Dellby, N.; Lupini, A. R., Towards sub-Å electron beams. *Ultramicroscopy* **1999**, 78, 1-11.

7. Krivanek, O. L.; Nellist, P. D.; Dellby, N.; Murfitt, M. F.; Szilagyi, Z., Towards sub-0.5 Å electron beams. *Ultramicroscopy* **2003**, 96, 229-237.

8. Rose, H., Outline of a spherically corrected semiaplanatic medium-voltage transmission electron-microscope. *Optik* **1990**, 85, 19-24.

9. Treacy, M. M. J., Z dependence of electron scattering by single atoms into annular dark-field detectors. *Microsc. Microanal.* **2011**, 17, 847-858.

10. Watanabe, M.; Ackland, D. W.; Burrows, A.; Kiely, C. J.; Williams, D. B.; Krivanek, O. L.; Dellby, N.; Murfitt, M. F.; Szilagyi, Z., Improvements in the X-ray analytical capabilities of a scanning transmission electron microscope by spherical-aberration correction. *Microsc. Microanal.* **2006**, 12, 515-526.

11. Cliff, G.; Lorimer, G. W., The quantitative analysis of thin specimens. *J. Microsc.* **1975**, 103, 203-207.

12. Yoshida, K.; Tominaga, T.; Hanatani, T.; Tagami, A.; Sasaki, Y.; Yamasaki, J.; Saitoh, K.; Tanaka, N., Key factors for the dynamic ETEM observation of single atoms. *Microscopy* **2013**, 62, 571-582.

13. Hansen, T. W.; Wagner, J. B., Environmental transmission electron microscopy in an aberration-corrected environment. *Microsc. Microanal.* **2012**, 18, 684-690.

14. Creemer, J. F.; Helveg, S.; Hoveling, G. H.; Ullmann, S.; Molenbroek, A. M.; Sarro, P. M.; Zandbergen, H. W., Atomic-scale electron microscopy at ambient pressure. *Ultramicroscopy* **2008**, 108, 993-998.

15. Klein, K. L.; Anderson, I. M.; De Jonge, N., Transmission electron microscopy with a liquid flow cell. *J. Microsc.* **2011**, 242, 117-123.

16. El-Sayed, M. A., Small is different: shape-, size-, and composition-dependent properties of some colloidal semiconductor nanocrystals. *Acc. Chem. Res.* **2004**, 37, 326-333.

17. Haldar, K. K.; Sinha, G.; Lahtinen, J.; Patra, A., Hybrid colloidal Au-CdSe pentapod heterostructures synthesis and their photocatalytic properties. *ACS Appl. Mater. Interfaces* **2012**, 4, 6266-6272.

18. Burda, C.; Chen, X.; Narayanan, R.; El-Sayed, M. A., Chemistry and properties of

nanocrystals of different shapes. *Chem. Rev.* **2005**, 105, 1025-1102.

19. Cordeiro, M. A. L.; Weng, W.; Stroppa, D. G.; Kiely, C. J.; Leite, E. R., High resolution electron microscopy study of nanocubes and polyhedral nanocrystals of cerium (IV) oxide. *Chem. Mater.* **2013**, 25, 2028-2034.

20. Van Aert, S.; Batenburg, K. J.; Rossell, M. D.; Erni, R.; Van Tendeloo, G., Three-dimensional atomic imaging of crystalline nanoparticles. *Nature* **2011**, 470, 374-377.

21. Mahler, B.; Lequeux, N.; Dubertret, B., Ligand-controlled polytypism of thick-shell CdSe/CdS nanocrystals. *J. Am. Chem. Soc.* **2009**, 132, 953-959.

22. McBride, J.; Treadway, J.; Feldman, L. C.; Pennycook, S. J.; Rosenthal, S. J., Structural basis for near unity quantum yield core/shell nanostructures. *Nano Lett.* **2006**, 6, 1496-1501.

23. Lambert, K.; De Geyter, B.; Moreels, I.; Hens, Z., PbTe|CdTe core|shell particles by cation exchange, a HR-TEM study. *Chem. Mater.* **2009**, 21, 778-780.

24. Koike, K.; Honden, T.; Makabe, I.; Yan, F. P.; Yano, M., PbTe/CdTe single quantum wells grown on GaAs (100) substrates by molecular beam epitaxy. *J. Cryst. Growth* **2003**, 257, 212-217.

25. Wang, F.; Deng, R.; Wang, J.; Wang, Q.; Han, Y.; Zhu, H.; Chen, X.; Liu, X., Tuning upconversion through energy migration in core-shell nanoparticles. *Nat. Mater.* **2011**, 10, 968-973.

26. Langlois, C. T.; Oikawa, T.; Bayle-Guillemaud, P.; Ricolleau, C., Energy-filtered electron microscopy for imaging core–shell nanostructures. *J. Nanopart. Res.* **2008**, 10, 997-1007.

27. Hildebrand, M., Diatoms, biomineralization processes, and genomics. *Chem. Rev.* **2008**, 108, 4855-4874.

28. Lowenstam, H. A.; Weiner, S. *On Biomineralization*; Oxford University Press: New York, 1989.

29. Simonsen, S. B.; Chorkendorff, I.; Dahl, S.; Skoglundh, M.; Sehested, J.; Helveg, S., Direct observations of oxygen-induced platinum nanoparticle ripening studied by in situ TEM. *J. Am. Chem. Soc.* **2010**, 132, 7968-7975.

30. Liu, J., Advanced electron microscopy characterization of nanostructured heterogeneous catalysts. *Microsc. Microanal.* **2004**, 10, 55-76.

31. Heinemann, K.; Soria, F., On the detection and size classification of nanometer-size metal particles on amorphous substrates. *Ultramicroscopy* **1986**, 20, 1-14.

32. Zhang, B.; Zhang, W.; Su, D. S., Towards a more accurateparticle size distribution of supported catalyst by using HAADF - STEM. *ChemCatChem* **2011**, 3, 965-968.

33. Yang, X.-F.; Wang, A.; Qiao, B.; Li, J.; Liu, J.; Zhang, T., Single-atom catalysts: a new frontier in heterogeneous catalysis. *Acc. Chem. Res.* **2013**, 46, 1740-1748.

34. Qiao, B.; Wang, A.; Yang, X.; Allard, L. F.; Jiang, Z.; Cui, Y.; Liu, J.; Li, J.; Zhang, T., Single-atom catalysis of CO oxidation using Pt_1/FeO_x. *Nature chemistry* **2011**, 3, 634-641.

35. Liang, J.-X.; Lin, J.; Yang, X.-F.; Wang, A.-Q.; Qiao, B.-T.; Liu, J.; Zhang, T.; Li, J., Theoretical and experimental investigations on single-atom catalysis: Ir_1/FeO_x for CO oxidation. *J. Phys. Chem. C* **2014**, 118, 21945-21951.

36. Qiao, B.; Liang, J.-X.; Wang, A.; Xu, C.-Q.; Li, J.; Zhang, T.; Liu, J. J., Ultrastable single-atom gold catalysts with strong covalent metal-support interaction (CMSI). *Nano Res.* **2015**, 8, 2913-2924.

37. Stroud, R. M.; Lovejoy, T. C.; Falke, M.; Bassim, N. D.; Corbin, G. J.; Dellby, N.; Hrncirik, P.; Kaeppel, A.; Noack, M.; Hahn, W., Individual heteroatom identification with X-ray spectroscopy. *Appl. Phys. Lett.* **2016**, 108, 163101.

38. Suenaga, K.; Okazaki, T.; Okunishi, E.; Matsumura, S., Detection of photons emitted from single erbium atoms in energy-dispersive X-ray spectroscopy. *Nat. Photonics* **2012**, 6, 545-548.

39. Zhu, Y.; Ramasse, Q. M.; Brorson, M.; Moses, P. G.; Hansen, L. P.; Kisielowski, C. F.; Helveg, S., Visualizing the stoichiometry of industrial - style Co - Mo - S catalysts with single - atom sensitivity. *Angew. Chem. Int. Ed.* **2014**, 53, 10723-10727.

40. Liu, J., Catalysis by Supported Single Metal Atoms. *ACS Catal.* **2017**, 7, 33-59.

Chapter 2

Biomineralized cadmium chalcogenide nanocrystals

2.1 Introduction

Cadmium chalcogenides (CdE, E = S, Se, Te), an important class of II-VI semiconductor nanocrystals (quantum dots, QDs), have attracted intense interest because of their size-dependent optical properties and high quantum efficiencies in the visible range. Their tunable optical properties have found myriad of applications, including light-emitting diodes,[1-2] lasers,[3] and biolabeling agents.[4]

Just as in other semiconductor nanocrystal systems, the most widely used strategies to synthesize cadmium chalcogenide nanocrystals require elevated temperature and the use of organic solvent. For instance, Bawendi *et al.*[5] initiated the formation of monodisperse CdS QDs by rapid injection of dimethylcadmium (Me_2Cd) into an anhydrous coordinating solvent containing bis(trimethylsilyl)sulfide ($(tms)_2S$) at ~300 °C. Peng's group[6] recently developed a synthetic approach towards CdSe hexahedral nanocrystals, which involved swift injection of a Se powder suspension into a mixture of CdO and myristic acid in octadecene (ODE) at 250 °C. Particular drawbacks of the organometallic route for producing CdE QDs include the high cost of reagents, lack of biocompatibility, and difficulty in scaling-up production.

Aqueous based biomineralization methods offer potential as an advantageous alternative. While several biological approaches have shown successful biomanufacturing of cadmium

chalcogenide QDs,[7-9] these previous reports demonstrated only limited control over particle size or production of particles within a limited range of size distribution. Given the strong size dependence of the band gaps of such QDs, which enables their opto-electronic functionality, any application related production route would require reproducible control over the nanocrystal size within the quantum confinement regime.

Cell-based biomineralization can be realized by either intracellular or extracellular nanocrystal production. The latter is more desirable as it circumvents the need for cell lysis during harvesting, and thus minimizes biomacromolecule contamination of the product QDs. Cell-based biomineralization could be further simplified by extracting the active species within cells that are responsible for the biomineralization process. Such active species, usually enzymes, could induce and control the growth of QDs.

In this chapter, we first describe a bacteria-mediated, biosynthetic procedure for CdS QD manufacture at 37 °C. The extracellular synthesis of CdS nanocrystals, based on an engineered strain of *Stenotrophomonas maltophilia* (SMCD1), exhibits good control over the mean particle size, largely within the 2-4 nm range, offering good tunability over a wide range of quantum confined band gap energies. Then we demonstrate that a recombinant putative cystathionine γ-lyase (smCSE) associated with SMCD1 is capable of *both* catalyzing CdS mineralization *and* directing nanocrystal growth in aqueous solution. The versatility of the single engineered enzyme smCSE has been further attested by its successful mineralization of CdSe QDs through biological generation of reactive precursors and nanocrystal templating, which allows modulation of nanocrystal size and structure. The enzyme smCSE is also shown to be effective in subsequent immobilization of a CdS overlayer onto the CdSe nanocrystals, forming a CdSe-CdS core-shell

heterostructure. Advanced electron microscopy techniques have been applied to assess the structure, composition and size of these biomineralized cadmium chalcogenide nanocrystals derived from SMCD1.

2.2 CdS nanocrystals synthesized by SMCD1

In this work, a strain of cadmium-tolerant bacteria SMCD1 has been engineered via directed evolution. The iteratively selected colonies were cultured at 37 °C in M9 minimal media containing cadmium acetate as the Cd source and L-cysteine as the S source and capping agent. We have successfully demonstrated reproducible, extracellular biomineralization of CdS QDs. The nanocrystals were incubated for different lengths of time to alter the particle size. The optical and structural properties of the harvested QD materials have been characterized and analyzed, and the growth mechanism of CdS QDs has been probed.

2.2.1 Synthetic protocols for SMCD1 mineralized CdS nanocrystals

SMCD1 was isolated from soil using previously reported methods and iteratively selected for variants in culture that were tolerant to cadmium acetate at concentrations above 1 mmol.[10] Lysogeny broth (LB) and M9 minimal media were used for the growth of the bacterial strain. Selection of cadmium resistant strains was performed iteratively by increasing the concentration of cadmium acetate from 0.1 mM to 5 mM. After isolation of individual colonies, cell growth rate in culture was measured by monitoring the change in optical density at 600 nm (OD_{600}). Colonies that survived in cadmium acetate at concentrations in excess of 1 mM were selected from Cd-containing plates.

After the selection procedure, the SMCD1 culture were grown in LB broth (100 mL) for 12 h at 37 °C with shaking, followed by centrifugation and resuspension in M9 minimal media for cell isolation. The bacterial strain was mixed with cadmium acetate (1 mM) and L-cysteine (8 mM), and then placed in an incubator at 37 °C with shaking to initiate nanocrystal nucleation. Sample aliquots were gathered every 30 min, and subjected to subsequent separation and purification processes, namely centrifugation, dialysis and gravity-feed size exclusion chromatography.

2.2.2 Optical and structural characterization of CdS nanocrystals

The observed photoluminescence (Table 2.1) and absorption spectra (Figure 2.1 (a)) evidently establish the indispensability of any of the four components, *i.e.*, SMCD1 cells, cadmium acetate, L-cysteine, and M9 minimal media, for successful production of luminescent CdS nanocrystals with a well-defined first excitonic peak. On the other hand, combinations of ingredients with any of the four components absent showed no fluorescence. The reproducibility of the procedure was validated, with essentially identical QD optical properties observed from independent cultures using optimized growth media and the same growth time (Figure 2.1 (b)).

After removal of the bacteria by centrifugation, the culture supernatants remained photoluminescent (Figure 2.2 (a)), confirming the extracellular nature of QD biomanufacturing. Also noticeable are the systematic shifts of both absorption and fluorescence maxima with longer growth time in culture. The absorption spectra of CdS QDs show well-defined first excitonic peaks with maxima that become progressively more red-shifted with increasing growth time (Figure 2.2 (b)). Similarly, continuous shifts to longer wavelengths in the fluorescence

emission spectra are also observed as growth time increases (Figure 2.2 (c)). Specifically, the absorption peak wavelength moves from 312 nm at 30 min to 378 nm at 360 min, indicative of a blue-shift in the absorption onset with reference to that of bulk CdS (495 nm)[11-12]. Meanwhile, the corresponding emission spectra peak wavelength shifts from 460 nm to 562 nm. The relatively large Stokes shift is characteristic of CdS nanocrystals with L-cysteine capping in aqueous solution as reported previously.[13-14]

Table 2.1: Comparison of different growth conditions for CdS QD formation. *Courtesy of Dr. Zhou Yang.*

Ingredient	Sample 1	Sample 2	Sample 3	Sample 4	Sample 5	Sample 6
SMCD1 (OD_{600})	0.5	0.5	0.5	0.5	-	-
$Cd(Ac)_2$ (mmol)	1	-	1	1	1	1
L-cysteine (mmol)	8	8	-	8	8	8
Growth media	M9 media	M9 media	M9 media	DI water†	M9 media	DI water
Photoluminescence under UV light	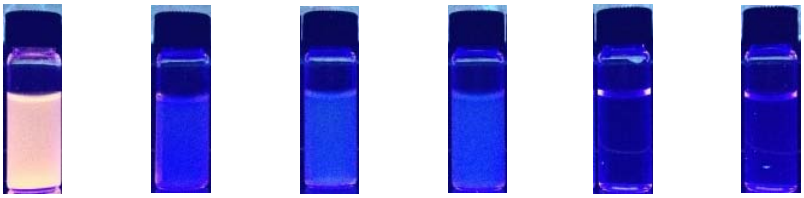					

† Deionized water.

TEM and STEM techniques have been applied to further corroborate the effectiveness of this biomineralization route in CdS nanocrystal generation. Well dispersed nanocrystals are clearly observable (Figure 2.3 (a, b)). Electron diffraction of the nanocrystals (inset in Figure 2.3 (a)) presents two broad but distinct rings corresponding to interplanar spacings of 0.33 nm and 0.21 nm, consistent with expected lattice spacings of CdS. However, the diffraction pattern could not adequately differentiate between the two polymorphs of the CdS crystal, *i.e.*, zinc-blende and

wurtzite crystal type, as they both have lattice spacings close to those measured within the limits of experimental error. X-ray powder diffraction (Figure 2.4) also implies CdS formation, but fails to determine the exact crystal structure of CdS due to severe peak broadening which originates from the nanoscopic nature of the particles.

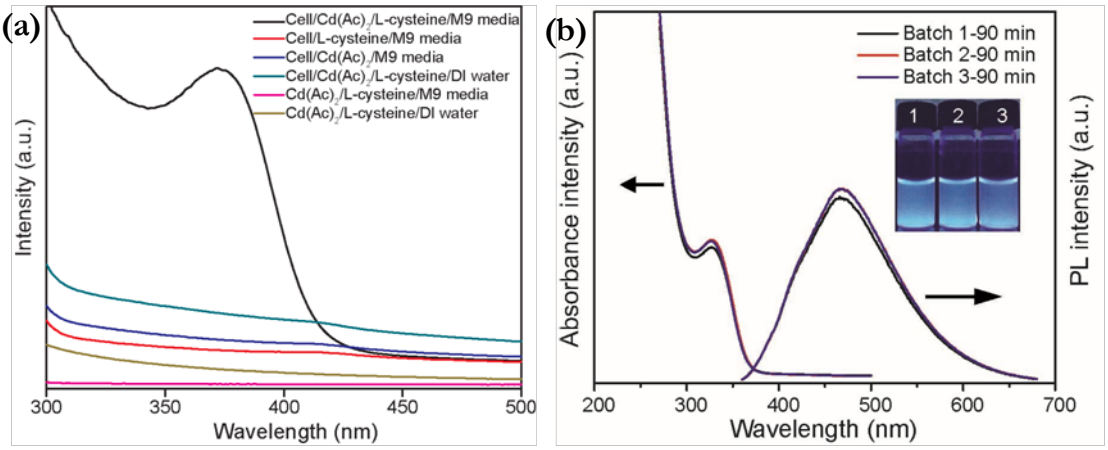

Figure 2.1: Absorption and emission spectra of the as-grown cultures. (a) Absorption spectra of a series of samples grown under different conditions for 6 h, showing that only SMCD1 cells incubated in the presence of both cadmium acetate and L-cysteine in M9 minimal media lead to the formation of CdS QDs with a well-defined first excitonic peak. (b) Optical properties of three different batches of CdS QDs prepared using identical growth conditions indicating good reproducibility. Inset is a photograph of the culture supernatants under UV illumination. The emission spectra were recorded using a 350 nm excitation wavelength. *Courtesy of Dr. Zhou Yang.*

The ambiguity in nanocrystal structure identification could be resolved by resorting to high resolution HAADF-STEM imaging. Lattice fringe analysis of HAADF-STEM micrographs of individual nanocrystals demonstrates that some particles have d-spacing values and intersection angles that can be uniquely assigned to zinc-blende type CdS, while others are measured to fit exclusively with wurtzite type CdS. For example, Figure 2.3 (c) showcases a nanocrystal with measured d-spacings of 0.30 nm for two planes and an interplanar angle of 89°, perfectly matching those of the two perpendicular planes of (002) and (020) in zinc-blende type CdS viewed along the [100] projection; the nanocrystal in Figure 2.3 (d) displays two planes having

0.19 nm and 0.32 nm lattice spacings intersecting at 83°, which correspond to the $(2\bar{1}1)$ and (011) planes of wurtzite type CdS that intersect at 82.0° along $[1\bar{1}1]$. Herein, the lattice fringe analysis proves the co-existence of zinc-blende and wurtzite CdS polymorphs in the biomineralized QDs. In addition, XEDS analysis (Figure 2.3 (e)) revealed both Cd and S signals in the sample.

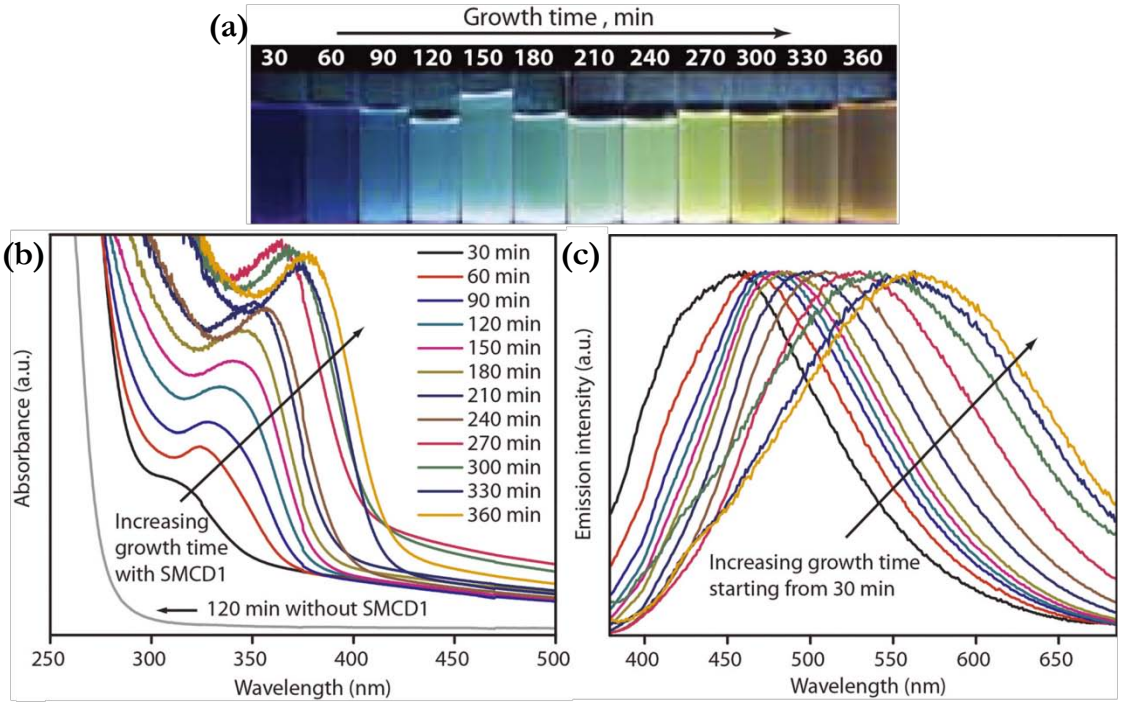

Figure 2.2: Optical properties of the as-grown CdS nanocrystals with different growth times. (a) Photograph of the culture supernatants from strain SMCD1 collected at various growth times when illuminated under UV light. (b) UV-vis absorption spectra of CdS QDs as a function of growth time. (c) Fluorescence emission spectra using a 350 nm excitation wavelength as a function of growth time. *Courtesy of Dr. Zhou Yang.*

In order to evaluate the influence of growth time on CdS nanocrystal dimension, particle size distribution (PSD) histograms for different growth times (Figure 2.5 (a-c)) were constructed from HR-TEM images. A progressive increase of the mean particle size from 2.75 to 3.04 to 3.36 nm was noted after growth times of 60, 180 and 300 min, respectively. Correlation of the measured size and absorption peak position is consistent with prior reports for L-cysteine capped CdS nanocrystals.[13, 15] There is also an incremental broadening trend in the PSD width with

longer growth time as reflected by the standard deviation variation from 0.68 nm at 60 min to 0.95 nm at 300 min, while the relative standard deviation remains roughly constant at ~25%.

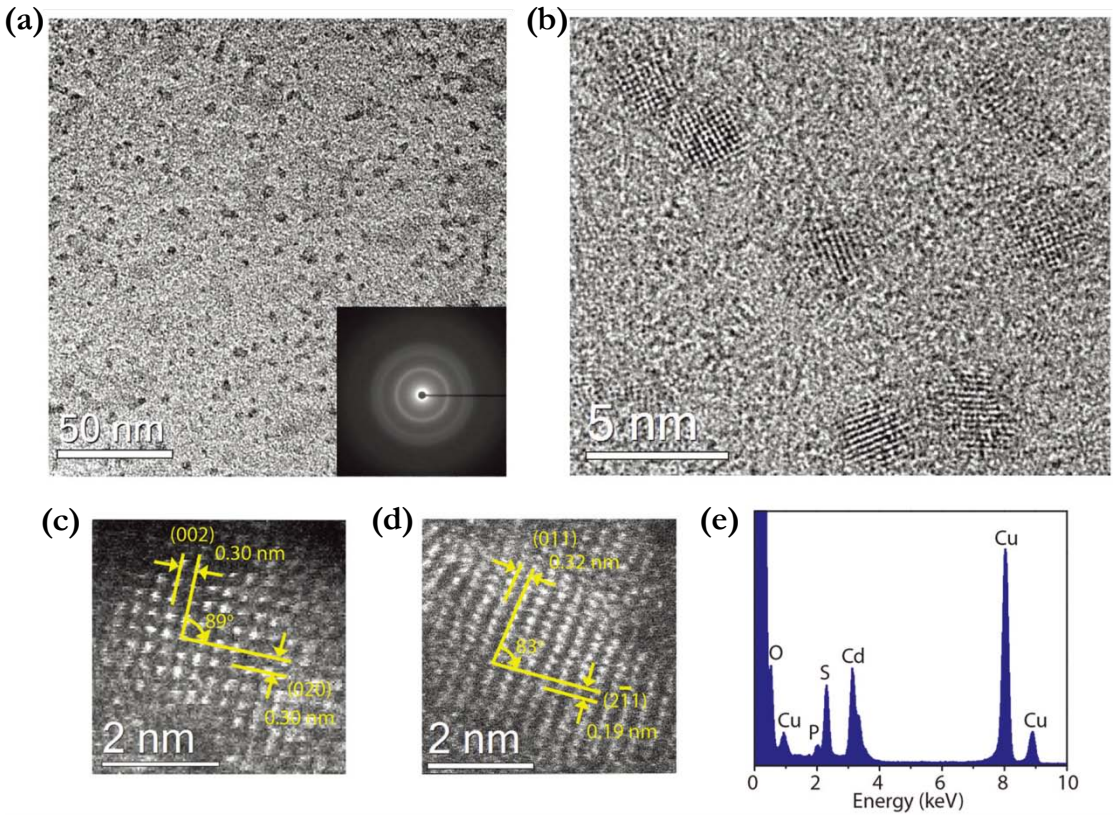

Figure 2.3: Electron microscopy characterization of purified CdS QDs after 60 min growth. (a) BF-TEM image of CdS nanocrystals displaying the typical particle dispersion. Inset in (a) is the corresponding selected area electron diffraction (SAED) pattern. (b) Representative HR-TEM image of CdS QDs. (c, d) HAADF-STEM images of nanocrystals exhibiting zinc-blende (c) and wurtzite (d) type polymorph of CdS respectively. (e) XEDS spectrum showing the co-existence of Cd and S in the QDs.

The quantum yield (QY) of the biomineralized CdS nanocrystals was found to increase linearly with growth time from 0.30% at 30 min to 2.08% at 180 min. Inaccuracies occurred in QY measurement at longer growth times, which most likely arose from aggregation of the larger particles. This range of QY is about three orders of magnitude higher than the QY (0.007%) reported for previously biosynthesized CdS QDs.[16] However, it should be pointed out that our biomineralized QDs still have a relatively low QY as compared to chemically prepared CdS

QDs,[17-18] which might be ascribed to quenching by L-cysteine or dimer cysteine ligands.[19-20] Considering the observed systematic variation in PSD with growth time, we can infer a positive correlation of the QY with mean nanocrystal size in the 30-180 min growth time range. Such size-dependent trends for the photoluminescence QY of semiconductor nanocrystals have been noted elsewhere.[21-25] Smaller particles would have higher surface-to-volume ratios, leading to higher proportions of surface defects. Therefore, non-radiative relaxation at surface traps are expected to become more prominent with decreasing particle size.

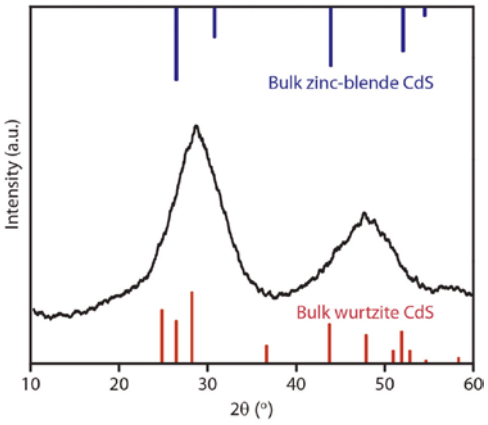

Figure 2.4: X-ray powder diffraction pattern of the precipitated CdS QD powder after 360 min of growth. The stick patterns indicate the expected standard peak positions from bulk wurtzite (*bottom*, PDF card no. 00-006-0314) and from zinc-blende (*top*, PDF card no. 00-010-0454) type CdS polymorphs. *Courtesy of Dr. Zhou Yang.*

2.2.3 Investigation of CdS growth mechanism

CdS nanocrystals produced from SMCD1 exhibit an extracellular growth period following cluster nucleation. In yeast, intracellular cadmium is extracted through a glutathione-dependent mechanism, wherein up-regulation of glutathione monomer, oligomer and cysteine-rich binding peptide biosynthesis occurs to neutralize cadmium via metal-thiol complexation.[26] Decomposition of bound thiol ligands, in this case the thiol group on L-cysteine, is considered to

supply sulfur for CdS nanocrystal nucleation and growth. L-cysteine is one of three amino acids required for glutathione biosynthesis, and L-cysteine biosynthesis is usually the rate-determining step during the overall cellular glutathione biosynthesis process.[27]

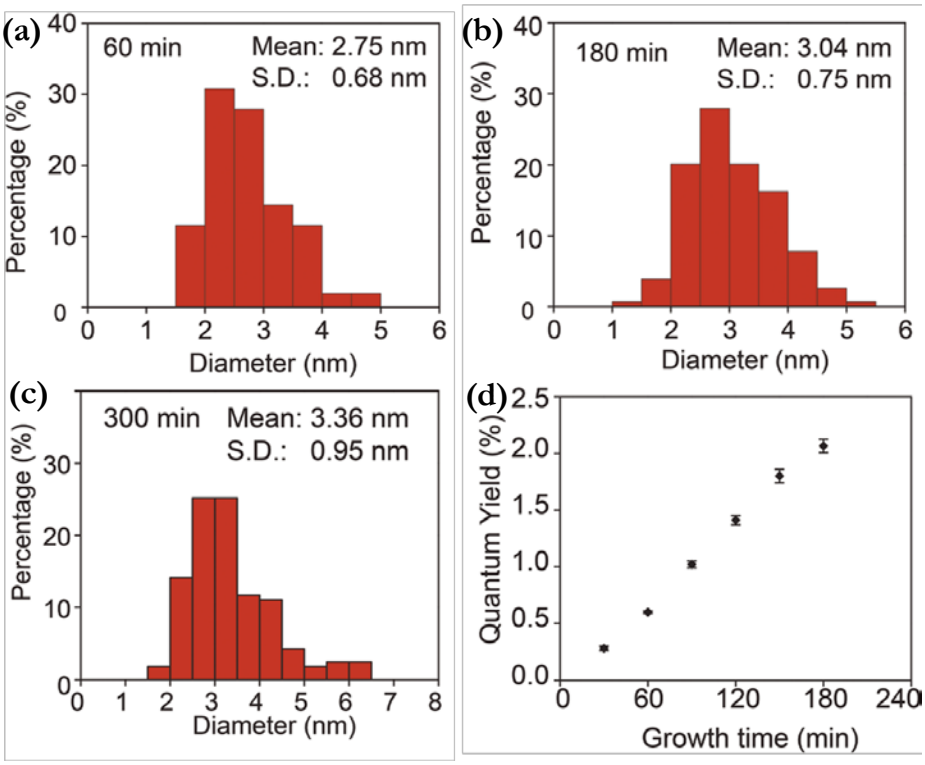

Figure 2.5: Particle size distribution and quantum yields of CdS QDs as a function of growth time. (a-c) Particle size distribution histograms with 60 (a), 180 (b), and 300 min (c) growth time respectively. (d) Quantum yield values of CdS QDs with various growth times (*courtesy of Dr. Zhou Yang*).

To better understand the growth mechanism of our biomineralized CdS nanocrystals, we investigated particle growth after the elimination of SMCD1 cells from culture via centrifugation. The optical density at 600 nm (OD_{600}) of the supernatant, a measure of bacteria concentration, dropped below 2% of the initial value, confirming the absence of the cells. The growth of CdS QDs in the supernatant persisted without the cells, yet at a slower rate as evidenced by smaller red-shifts in both absorption and fluorescence peak maxima with longer growth time (Figure 2.6).

For comparison, after 360 min the absorbance and photoluminescence spectra without cells reached maxima at 343 and 469 nm, respectively, shorter in wavelength than the corresponding peak positions at 378 and 562 nm respectively attained with cells. This result reaffirms the extracellular production of CdS QDs, and also reveals that continuous presence of bacteria cells is not a prerequisite for QD growth. We propose that the presence of SMCD1 cells promotes the biosynthesis rate by continuously generating the extracellular components responsible for nanocrystal biosynthesis. Removal of the cells after an initial period slowed down the biomineralization process by lowering the concentration of extracellular components needed for QD biomanufacturing.

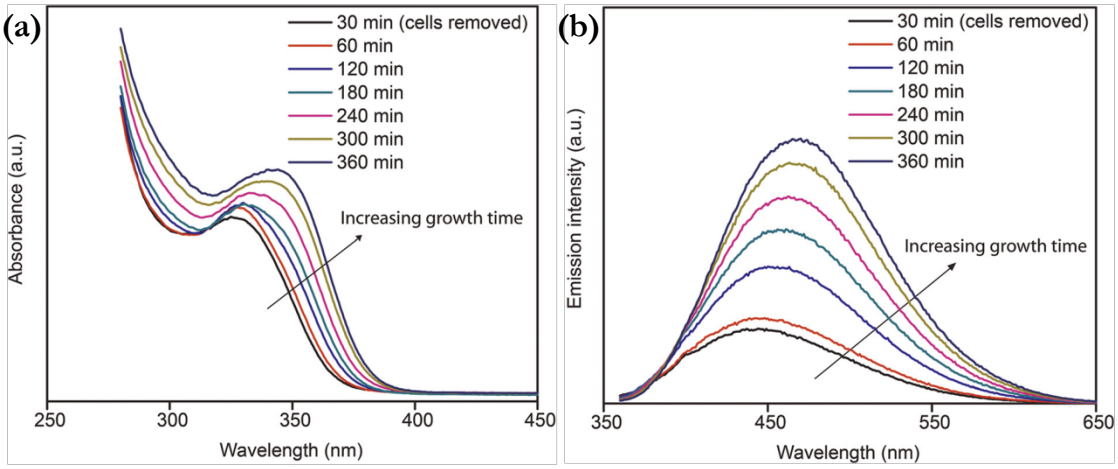

Figure 2.6: Optical properties of the as-grown CdS nanocrystals as a function of incubation time in the supernatant following removal of cells via centrifugation for 30 min. (a) UV-vis absorption spectra, and (b) fluorescence emission spectra using a 350 nm excitation wavelength as a function of growth time. *Courtesy of Dr. Zhou Yang.*

In order to investigate the driving force for nanocrystal growth after withdrawal of SMCD1 cells, the QD containing supernatant underwent dialysis against distilled water to extract the free cadmium salt and L-cysteine. After lyophilization the sample was analyzed by electrospray ionization mass spectrometry (ESI-MS), which could identify the proteins associated with the

nanocrystals that might contribute to the extracellular CdS QD synthesis. As a result, a putative cystathionine γ-lyase (CSE, NCBI Accession Number WP_012509966) was determined from independent QD samples analyzed by ESI-MS. The CSE is an enzyme that catalyzes the generation of H_2S from L-cysteine. It has been previously shown that over-expression of a highly active CSE in *E. coli* could detoxify an aqueous solution of cadmium chloride (0.1-0.4 mM) by precipitating a CdS complex on the cell wall through H_2S generation from 1 mM L-cysteine.[28] In accordance with these results, L-cysteine proves to be an essential ingredient for QD biomineralization from strain SMCD1 (Table 2.1 and Figure 2.1 (a)).

In conclusion, all of our results suggest a mechanism wherein CdS nanocrystal biomineralization occurs extracellularly via a CSE catalyzed conversion of L-cysteine to H_2S. This enzyme is secreted by strain SMCD1 and is found to be associated with the CdS QDs.

2.3 CdS nanocrystals synthesized by smCSE

From the bacterial strain SMCD1 used in Section 2.2, a putative CSE has been identified as responsible for CdS nanocrystal biomineralization. Herein, we distill the potential complexity to its simplest form: a single enzyme. A recombinant putative cystathionine γ-lyase (smCSE) mineralizes CdS QDs from an aqueous cadmium acetate solution via reactive H_2S generation from L-cysteine and controls nanocrystal growth within the quantum confined size regime. By introducing reactive Na_2S to replace the substrate L-cysteine, smCSE could serve as a template for CdS nanocrystal formation. Without smCSE, bulk CdS would precipitate in solution, demonstrating a role for smCSE not only in H_2S generation, but also in directing or templating QD growth.

2.3.1 CdS nanocrystal growth driven by smCSE

As mentioned in Section 2.2, H_2S formation catalyzed by CSE could cause CdS precipitation. To clarify the ability of the putative CSE to convert L-cysteine to H_2S, the enzyme was heterologously over-expressed and purified from *E. coli* and the intrinsic kinetics of L-cysteine turnover to H_2S measured. Expression and purification using immobilized metal affinity chromatography (IMAC) eluted a single protein of 42 kDa (Figure 2.7, inset), consistent with the expected size of smCSE. A strong absorbance peak emerges at 430 nm for the purified smCSE (Figure 2.7), suggesting smCSE binds a pyridoxal phosphate (PLP) cofactor, an obligate cofactor necessary for CSE catalysis.[29] The Michaelis-Menten rate parameters for L-cysteine conversion measured for smCSE are comparable to reported values for other well-studied CSEs (Table 2.2).[30-31]

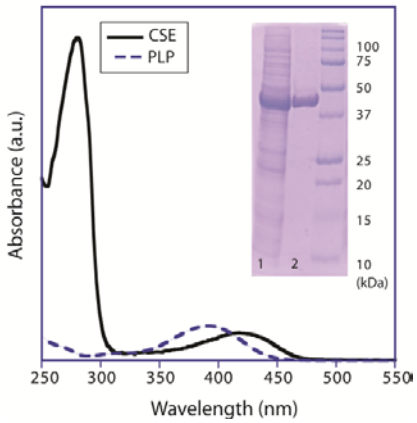

Figure 2.7: Absorbance spectra of purified smCSE (2.5 mg mL^{-1}). *Solid black line*: in 500 mM imidazole (pH = 8.6); *dotted blue line*: in unbound PLP (5 μM). *Inset* is the sodium dodecyl sulfate polyacrylamide gel electrophoresis (SDS-PAGE) of cell lysate (Lane 1) and IMAC purified smCSE (Lane 2) showing a molecular mass of 42 kDa. *Courtesy of Robert Dunleavy.*

With the role of smCSE validated in the generation of reactive sulfur, it was further postulated that the introduction of a cadmium salt to the solution would yield CdS. To assess this

hypothesis, L-cysteine (4 mM) and cadmium acetate (0.5 mM) were mixed in an aqueous solution of smCSE (0.1 mg mL^{-1} in Tris buffer, pH = 7.5). UV-vis and fluorescence spectra were recorded from the mixture as a function of time at ambient conditions (Figure 2.8). A distinct absorption peak appeared at 333 nm after 90 min (Figure 2.8 (a)); meanwhile, a corresponding emission peak at 464 nm was also observed (Figure 2.8 (b)). The maxima in both the absorbance and fluorescence spectra move gradually to longer wavelengths with increasing growth times up to 195 min with visible photoluminescence observed in solution under UV light for each time interval measured (Figure 2.8 (c)). In common with the case of SMCD1-mediated biomineralization, smCSE, cadmium acetate and L-cysteine were all necessary here for CdS QD formation. In the absence of any of the three 'growth' components, the absorbance and fluorescence peaks completely disappeared (Figure 2.9) and no photoluminescence under UV light could be observed under UV radiation (Table 2.3). Chilling the reactant mixture on ice essentially inhibits smCSE activity, allowing collection of a specific population of particles with a given set of photoluminescence properties.

Table 2.2: Measured Michaelis-Menten kinetic parameters of smCSE with respect to L-cysteine, in comparison to kinetic parameters of human CSE and *Prevotella intermedia* (*P. intermedia*) CSE. *Courtesy of Robert Dunleavy.*

	L-cysteine		
	V_{max}† **(U mg^{-1})**	K_m‡ **(mM)**	K_{cat}§ **(s^{-1})**
smCSE	0.68 ± 0.20	87 ± 25	1.81
Human CSE[30]	0.14	2.75	0.4
***P. intermedia* CSE**[31]	4.2	0.7	-

† The maximum rate achieved by the system at saturating substrate concentration.
‡ Michaelis constant, the substrate concentration at which the reaction rate is half of V_{max}.
§ Catalytic rate constant.

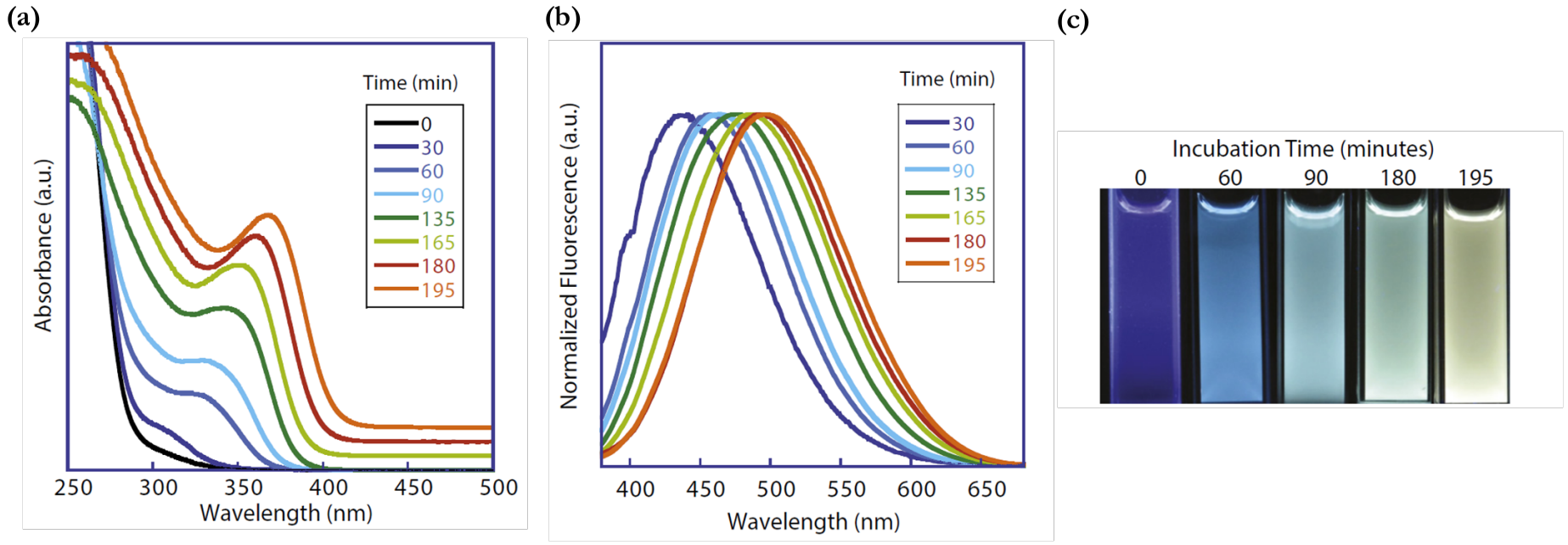

Figure 2.8: Optical properties of CdS versus synthesis time. (a) Absorbance spectra of smCSE (0.1 mg mL^{-1}) incubated with 4 mM L-cysteine and 0.5 mM cadmium acetate for various time intervals. (b) Corresponding fluorescence spectra at selected time intervals using an excitation wavelength of 350 nm. (c) Photographs of photoluminescence under UV illumination at various growth times. *Courtesy of Robert Dunleavy.*

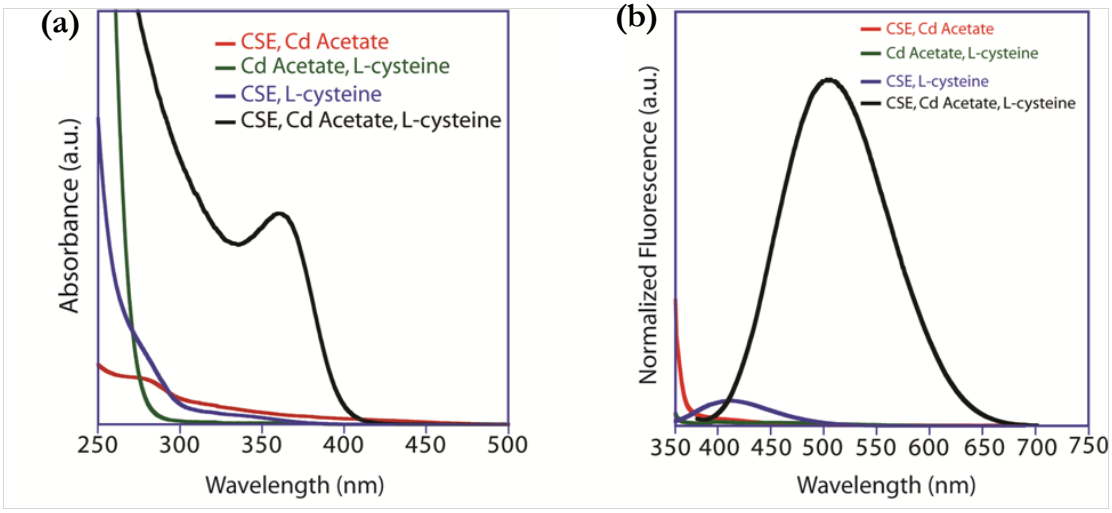

Figure 2.9: Optical spectra for the different combinations of smCSE, L-cysteine and cadmium acetate. (a) UV-vis absorption spectra. (b) Photoluminescence spectra using an excitation wavelength of 360 nm. *Courtesy of Robert Dunleavy.*

Table 2.3: Concentrations of the reagents for the solutions in Figure 2.9 and corresponding photoluminescence under UV light. *Courtesy of Robert Dunleavy.*

CSE (mg mL^{-1})	0.1	-	0.1	0.1
Cadmium acetate (mM)	0.5	0.5	-	0.5
L-cysteine (mM)	-	4	4	4
Fluorescence under UV light	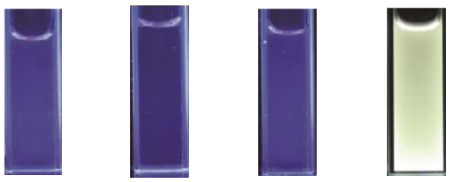			

STEM characterization was carried out to analyze the CdS crystallites harvested from solution after 180 min growth (displaying an absorbance peak at 350 nm). Discrete but irregularly shaped and partially overlapping nanocrystals of 2-4 nm in size could be visualized via HAADF-STEM (Figure 2.10 (a)). Significant Cd and S signals were detected by XEDS (Figure 2.10 (b)). Higher magnification HAADF-STEM imaging of individual particles illustrates the nanocrystal size and confirms the presence of both wurtzite and zinc-blende polymorphs of CdS

crystallites by measuring and examining lattice d-spacings and interplanar angles (Figure 2.10 (c-f), Table 2.4). The formation and co-existence of both CdS polymorphs probably emanates from the very small energy difference (69 meV) between the two crystal structures.[32]

Although the irregular shapes of the enzyme-mineralized QDs might distort a fair comparison of size-dependent optical properties with previously reported correlations,[21] the absorbance maxima for all reported growth times (Figure 2.8 (a)) remain well below the absorbance maximum corresponding to the band gap of bulk CdS (2.5 eV, 495 nm)[11-12] and the apparent dimensions of the CdS nanocrystals are well within the quantum confined regime for CdS.[11] In addition, the smCSE-synthesized CdS QDs possessed a similar QY value (1.8%) to that displayed by our SMCD1-derived CdS QDs (2%).

2.3.2 Role of smCSE in nanocrystal templating

L-cysteine, being a substrate for smCSE to generate H_2S, can also attach itself to the CdS surface.[33] To ascertain the dual role of L-cysteine as the sulfur source and capping agent, the influence of L-cysteine concentration on CdS biomineralization was evaluated. At a concentration of 4 mM L-cysteine, below which no nanocrystal formation occurred at 0.1 mg mL^{-1} smCSE and 0.5 mM cadmium acetate, the observed absorbance peak red-shifted with time, reaching 370 nm after 4 h of growth (Figure 2.11 (a)). Further extension of growth time resulted in bulk CdS formation, which was not encountered in the cases of higher L-cysteine concentrations. This suggests improved stabilization of the CdS nanocrystals in solution with increased availability of capping L-cysteine ligands. Higher L-cysteine concentrations of 10 and 20 mM led absorbance and photoluminescence maxima to move to longer wavelengths during

incubation (Figure 2.11 (a, b)). This red shift points to increased CdS growth rates with increasing L-cysteine concentration for nanocrystals within the quantum confined size range and is particularly conspicuous for the 20 mM L-cysteine data. It is worth noting that all of the growth curves attain similar maxima after 4 h: 370, 375, and 380 nm at 4, 10, and 20 mM L-cysteine, respectively. The solutions turn slurry-like after longer growth times (Figure 2.11 (b)), suggesting that nanocrystals capped with L-cysteine have reached saturation.

To elucidate the stabilization effect of thiol-mediated capping on the nanocrystals, glutathione was added into the enzymatic synthesis solution. Glutathione is a capping agent derived from L-cysteine and L-glutamine that has been reported to bind to water-soluble CdS nanocrystals.[34-35] However, unlike L-cysteine, glutathione functions solely as a capping agent as it is not a substrate for CSEs.[36] Addition of 1 and 4 mM glutathione in the presence of 4 mM L-cysteine gave rise to absorbance maxima at 375 and 385 nm, respectively, after 4 h of growth, similar to those with elevated L-cysteine concentrations, yet the solutions remained optically clear after 5 h (Figure 2.11 (c, d)). The persistent optical clarity suggests enhanced stabilization of the aqueous nanocrystal suspension with glutathione capping relative to L-cysteine capping. With 4 mM glutathione already showing a tendency to lower the growth rate, such a suppression effect on particle growth becomes more significant at a glutathione concentration of 10 mM, which with respect to lower glutathione concentrations causes a blue shift in absorbance maximum at all incubation times. Optical clarity was maintained after 24 h of growth by inclusion of 10 mM glutathione, with absorbance maximum positioned at 400 nm (Figure 2.11 (c, d)).

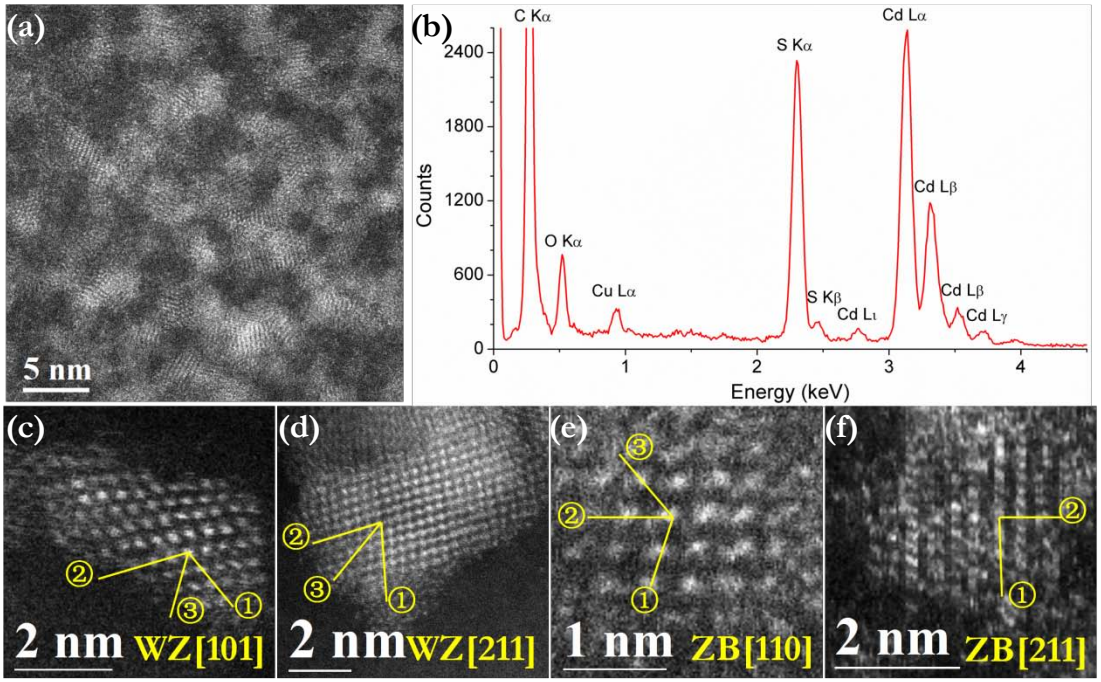

Figure 2.10: STEM characterization of smCSE-synthesized CdS QDs. (a) Representative HAADF-STEM image showing numerous partially overlapping nanocrystals. (b) XEDS spectrum confirming the co-existence of Cd and S in the nanocrystals. (c, d) Example images from wurtzite CdS nanocrystals viewed along [101] and [211] projections, respectively. (e, f) Example images from zinc-blende CdS nanocrystals viewed along [110] and [211] projections, respectively.

Table 2.4: Lattice fringe analysis of the CdS nanocrystals in Figure 2.10 (c-f).

	QDs identified as wurtzite CdS				**QDs identified as zinc-blende CdS**			
	Fig. 2.10 (c): [101]		Fig. 2.10 (d): [211]		Fig. 2.10 (e): [110]		Fig. 2.10 (f): [211]	
	Measured	Matching	Measured	Matching	Measured	Matching	Measured	Matching
Plane 1	3.1 Å	3.2 Å ($1\bar{1}\bar{1}$)	3.3 Å	3.2 Å ($1\bar{1}\bar{1}$)	3.6 Å	3.4 Å ($1\bar{1}1$)	3.5 Å	3.4 Å ($1\bar{1}\bar{1}$)
Plane 2	3.6 Å	3.6 Å (010)	2.6 Å	2.5 Å ($10\bar{2}$)	3.4 Å	3.4 Å ($1\bar{1}\bar{1}$)	2.0 Å	2.1 Å ($02\bar{2}$)
Plane 3	3.2 Å	3.2 Å ($10\bar{1}$)	3.3 Å	3.2 Å ($01\bar{1}$)	3.0 Å	2.9 Å (002)	-	-
<1, 2>	61.7°	63.8°	50.0°	49.8°	72.8°	70.5°	90.0°	90.0°
<2, 3>	64.2°	63.8°	49.2°	49.8°	54.8°	54.7°	-	-
<3, 1>	54.1°	52.4°	80.9°	80.3°	52.3°	54.7°	-	-

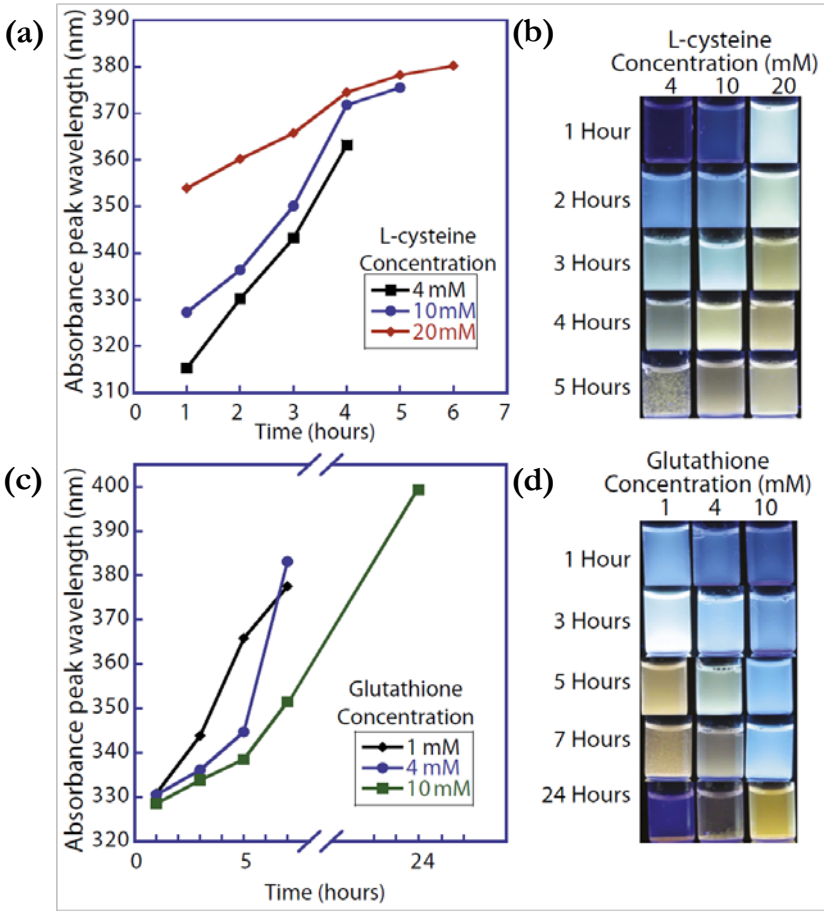

Figure 2.11: Control of nanocrystal size by the co-addition of L-cysteine and glutathione. (a) Absorbance maximum versus reaction time for preparations containing 4, 10, and 20 mM of L-cysteine. (b) Corresponding photographs of the solutions in (a) under UV illumination. (c) Absorbance maximum versus reaction time for 4 mM L-cysteine supplemented with 1, 4, and 10 mM of glutathione. (d) Corresponding photographs of the solutions in (c) under UV illumination. For all syntheses, smCSE and cadmium acetate concentration were kept constant at 0.1 mg mL^{-1} and 0.5 mM, respectively. *Courtesy of Robert Dunleavy.*

To reinforce the role of glutathione as a stabilizer, we measured the temporal evolution of absorbance maximum and L-cysteine concentration with glutathione present and absent (Figure 2.12). While L-cysteine consumption is hardly affected by glutathione addition, the absorbance peak emerges at a shorter wavelength, corresponding to a smaller mean particle size for the sample containing glutathione. The decrease in the average nanocrystal dimension could be rationalized by the participation of glutathione in capping CdS surface and curbing further growth of nanocrystals. Whereas with L-cysteine, the concentration-dependent stabilization and

growth of CdS nanocrystals is due to the dual role of L-cysteine as a capping agent and smCSE substrate; however, the thiolated ligand glutathione which is not a substrate for smCSE stabilizes the nanocrystal solution and decelerates crystal growth, yielding smaller CdS particles for any given growth time.

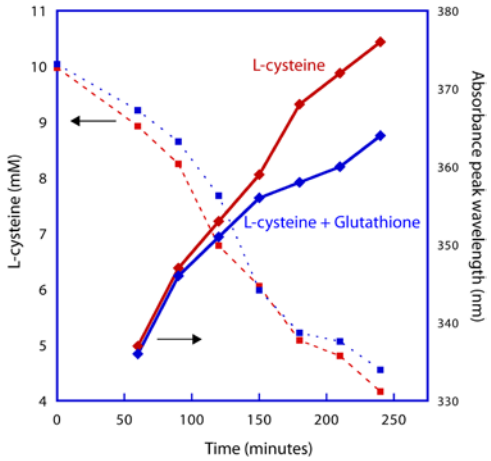

Figure 2.12: Temporal evolution of L-cysteine concentration and absorbance peak wavelength with and without 5 mM glutathione. *Amounts of other ingredients*: 10 mM L-cysteine, 0.5 mM cadmium acetate, and 0.1 mg mL^{-1} smCSE. The concentration of L-cysteine was quantified using Ellman's reagent (DTNB) by monitoring the absorbance at 412 nm with reference to a standard curve. *Courtesy of Robert Dunleavy.*

The function of smCSE is not limited to inducing biomineralization; it can also template the structure and size of CdS QDs. To verify this, L-cysteine was replaced with Na_2S as the sulfur source in the preparation. As a non-substrate for smCSE, Na_2S will not lead to H_2S formation with smCSE present, but Na_2S can supply sulfur for aqueous chemical synthesis of CdS nanocrystals aided by thiolated ligand capping agents.[37] Upon addition of Na_2S (4 mM) to an aqueous solution of cadmium acetate (0.5 mM) at room temperature, large CdS aggregates were immediately observed with no discernible absorption or fluorescence maxima (Figure 2.13), on account of lack of a capping agent to inhibit nanocrystal over-growth. Once smCSE (0.1 mg mL^{-1}) was mixed with the solution, a peak rose quickly in the absorbance spectrum centered at

360 nm (Figure 2.13 (a)), demonstrating that CdS nanocrystals can be produced with no additional capping agent involved.

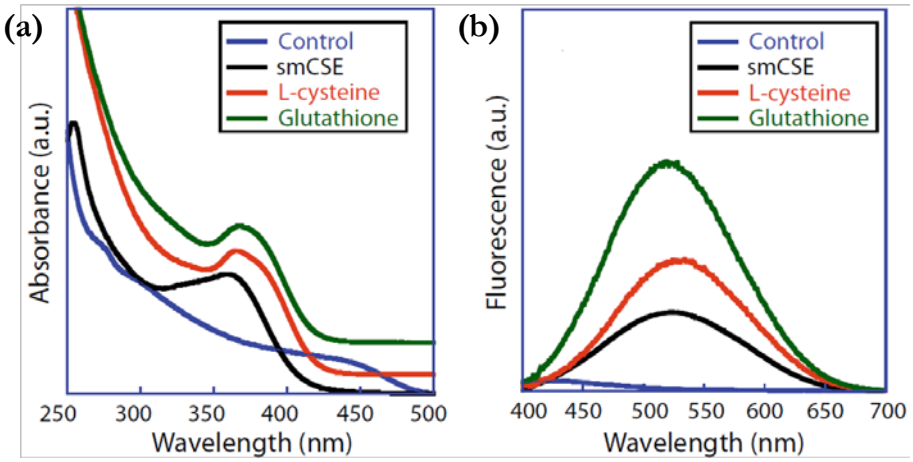

Figure 2.13: Nanocrystal formation by smCSE in the absence of L-cysteine or glutathione. (a) UV-vis absorbance spectra obtained upon addition of 4 mM Na_2S to a solution containing 0.5 mM cadmium acetate in the presence of smCSE, 4 mM L-cysteine, or 4 mM glutathione. A Na_2S solution added to 0.5 mM cadmium acetate is shown as a control. (b) Corresponding fluorescence spectra (excitation at 360 nm) of the solutions in (a). *Courtesy of Robert Dunleavy.*

If we introduce known capping agents L-cysteine and glutathione, nanocrystal formation could also occur as indicated by the appearance of absorbance and fluorescence maxima (Figure 2.13). L-cysteine and glutathione capping sharpens the absorption peaks, reflecting their higher binding affinity for the nanocrystal surface and their smaller size, both of which engender higher surface coverage of ligands during growth.[38-39] Thus, each of the three substances, smCSE, L-cysteine, and glutathione can enable controlled growth of CdS nanocrystals from Na_2S and cadmium acetate. Hence, the intrinsic ability of smCSE to *both* induce and template CdS nanocrystal growth has been unequivocally established.

2.4 CdSe and CdSe-CdS core-shell nanocrystals synthesized by smCSE

In this aspect of the work, we have been endeavoring to expand the smCSE-mineralized nanocrystal library beyond CdS. Biomineralization of CdSe nanocrystals was once again achieved using the single enzyme smCSE. The same enzyme also enabled the coating of a CdS shell over the purified CdSe nanocrystals in the presence of necessary precursors, yielding CdSe-CdS core-shell heterostructured particles with significantly improved QY values. Extensive electron microscopy characterization was conducted to assess the size, structure and composition of the CdSe and CdSe-CdS core-shell nanocrystals, and to reveal the underlying rationale of their microstructure-performance correlation.

2.4.1 CdSe nanocrystal formation via smCSE biomineralization

CdSe QDs were biosynthesized by 0.05 mg mL^{-1} smCSE at 37 °C from 8 mM seleno-L-cystine and 1 mM cadmium acetate in 0.05 M tris-HCl buffer (pH = 9.0) in an N_2 atmosphere. To stabilize the CdSe nanocrystals against photo-degradation, 20 mM of 3-mercaptopropionic acid (MPA) was also added.[40]

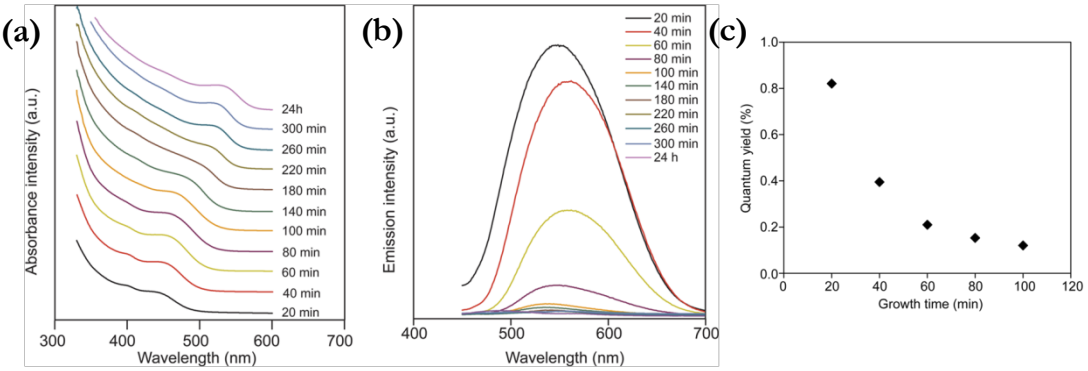

Figure 2.14: Optical properties of CdSe nanocrystals as a function of growth time in a buffered aqueous solution of smCSE, cadmium acetate, and seleno-L-cystine. (a) UV-vis absorption spectra. (b) Corresponding fluorescence emission spectra. (c) Corresponding QY values. *Courtesy of Dr. Zhou Yang.*

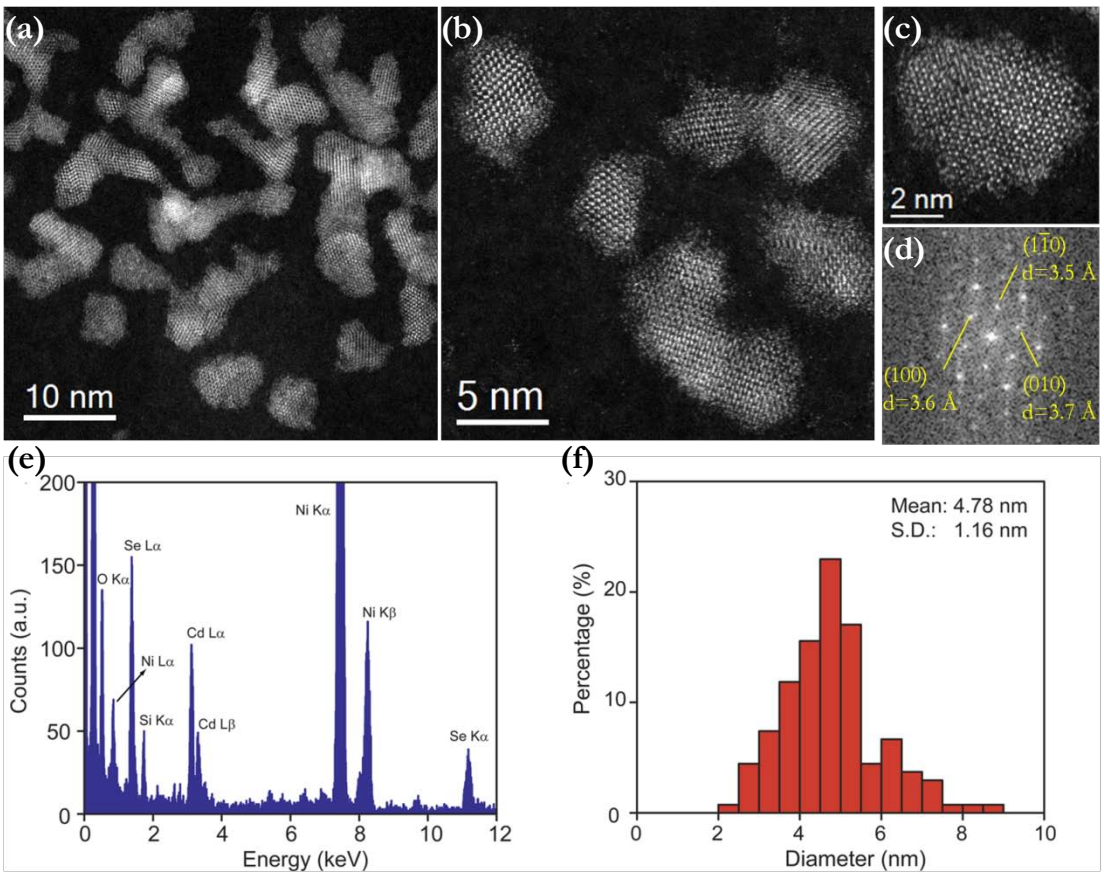

Figure 2.15: STEM characterization of biomineralized CdSe nanocrystals after 24 h of growth. (a-c) HAADF-STEM images. (d) The FFT diagram of the particle in (c). (e) The XEDS spectrum collected from a rectangular area of 130 nm × 160 nm. (f) Particle size distribution histogram measured from 138 particles.

A clear first excitonic peak red-shifts with increasing growth time in the UV-vis absorbance spectra of the buffered aqueous solution of smCSE enzyme, cadmium acetate, MPA and seleno-L-cystine (Figure 2.14 (a)). The absorbance maximum progressively moves from 438 nm at 20 min to 535 nm at 260 min, while longer incubation times caused minimal further peak shift. The observed absorption peak positions and red-shift with time are in accord with the expected progression for the nucleation and growth of CdSe quantum confined nanoparticles. In comparison, the corresponding photoluminescence peak maxima experienced a smaller shift, from 535 nm at 20 min to 559 nm at 260 min (Figure 2.14 (b)). The measured QY was found to be negatively impacted by longer incubation times, dropping from 0.8% at 20 min to 0.1% at 100

min (Figure 2.14 (c)). Beyond 100 min the QY fell below the detection limit of 0.1%. The relatively low QYs and large Stokes' shifts are both reflective of trap state photoluminescence, and are quite similar to that previously reported for CdSe chemically synthesized from cadmium acetate and NaHSe precursors.[41] This is probably a result of the formation of a relatively defective crystal structure with poor surface passivation. Despite the low QY values of these bare biomineralized CdSe QDs in aqueous solution, the QYs are still higher than some of those reported for purely chemically prepared CdSe nanocrystals in the aqueous phase.[41]

HAADF-STEM imaging and XEDS analysis provided direct evidence for the formation of CdSe nanocrystals. For electron microscopy sample preparation, the nanocrystals in aqueous suspension was phase transferred to 1-octodecene with oleylamine as a capping agent and further re-dispersed in chloroform. Well dispersed, yet irregularly shaped, nanoparticles with good crystallinity after 24 h incubation were observed (Figure 2.15 (a-c)). The measured lattice spacings and intersection angles from FFT diagrams of nanocrystal micrographs evidence the presence of wurtzite type CdSe. As an example illustrated in Figure 2.15 (c, d), the measured d-spacings of 3.5, 3.6 and 3.7 Å fit well with the reference value of 3.7 Å for the {100} plane of the hexagonal wurtzite polymorph of CdSe when viewed along the [001] zone axis. Meanwhile, the interplanar angles determined as 56.9°, 65.2°, and 57.9° are within experimental error compared to the expected value of 60°. Additional lattice fringe analysis further demonstrates the formation of wurtzite type CdSe (Figure 2.16, Table 2.5). It should be noted that none of the four examples shown in Figure 2.15 (c, d) and Figure 2.16 could be matched to the structure of the zinc-blende polymorph of CdSe. In fact, no particles measured in this sample after 24 h growth could be unambiguously assigned to zinc-blende CdSe. Compositional analysis using XEDS collected

signals from an assembly of ~200 particles identifies the presence of both Cd and Se (Figure 2.15 (e)).

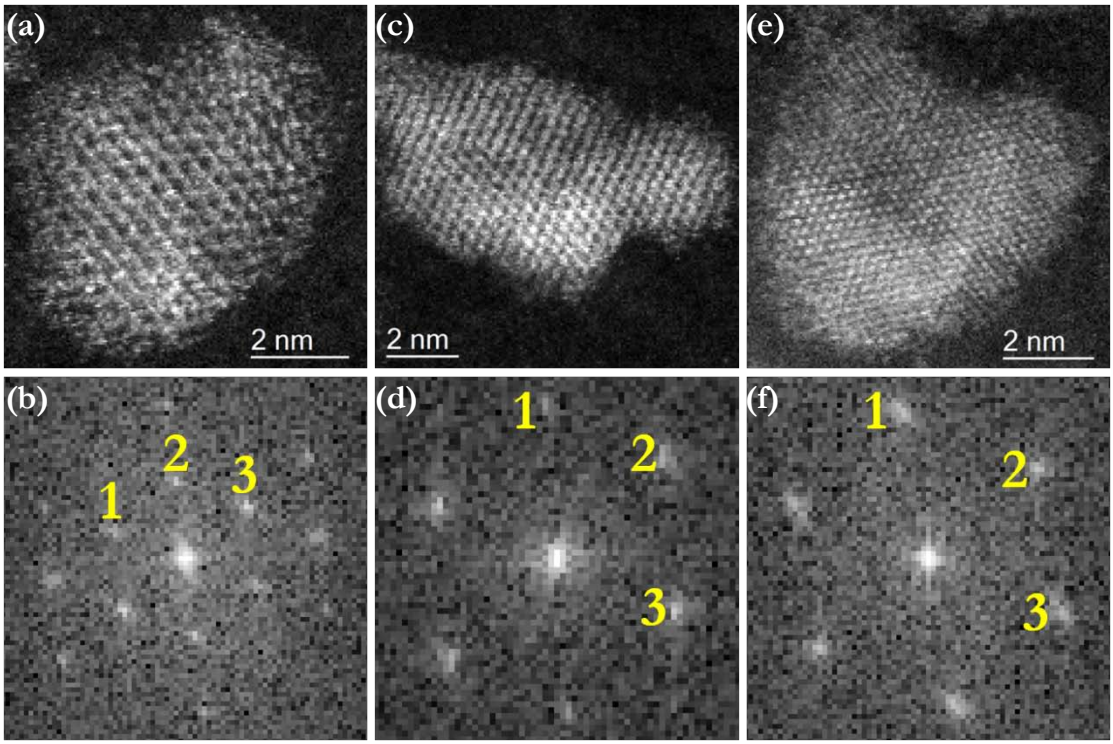

Figure 2.16: HAADF-STEM images (a, c, e) of individual CdSe nanocrystals after 24 h incubation with the corresponding FFT diagrams (b, d, f), demonstrating the formation of wurtzite type CdSe.

Table 2.5: Lattice fringe analysis based on HAADF-STEM images of CdSe nanocrystals after 24 h growth shown in Figure 2.16 demonstrating the formation of wurtzite CdSe.

Wurtzite CdSe	Fig. 2.16 (a): [001]		Fig. 2.16 (c): [$10\bar{1}$]		Fig. 2.16 (e): [$3\bar{3}\bar{1}$]	
	Measured	Matching	Measured	Matching	Measured	Matching
Plane 1	3.8 Å	3.7 Å (100)	3.2 Å	3.3 Å (101)	2.1 Å	2.0 Å (103)
Plane 2	3.8 Å	3.7 Å ($1\bar{1}0$)	3.3 Å	3.3 Å ($1\bar{1}1$)	2.2 Å	2.1 Å (110)
Plane 3	3.6 Å	3.7 Å (010)	3.8 Å	3.7 Å (010)	2.1 Å	2.0 Å ($01\bar{3}$)
<1, 2>	61.9°	60.0°	50.7°	52.4°	60.3°	62.6°
<2, 3>	56.6°	60.0°	68.0°	63.8°	62.0°	62.6°
<3, 1>	61.5°	60.0°	61.4°	63.8°	57.7°	54.8°

The irregular shape of the nanocrystals complicates the interpretation of the optical spectra. Instead of using the conventional size analysis method that calculates the spherical equivalent diameter from the 2-D projected area of a particle, in this study we chose the diameter of the largest circle enclosed by the projected outline of a particle as the particle size. Considerations for the choice of particle size measurement method will be discussed in more detail in Section 2.4.4. The mean nanocrystal size obtained employing this newly proposed method was 4.78 ± 1.16 nm for the sample incubated for 24 h. The absorption peak position of 535 nm indicates a band gap energy of ~2.3 eV, corresponding to an expected diameter of ~3 nm for CdSe QDs according to the CdSe sizing curves reported in prior publications.[21, 42] This is relatively consistent with the ~4 nm shortest dimension of the asymmetric nanoparticles, which did not undergo any post-synthesis size selection procedure.

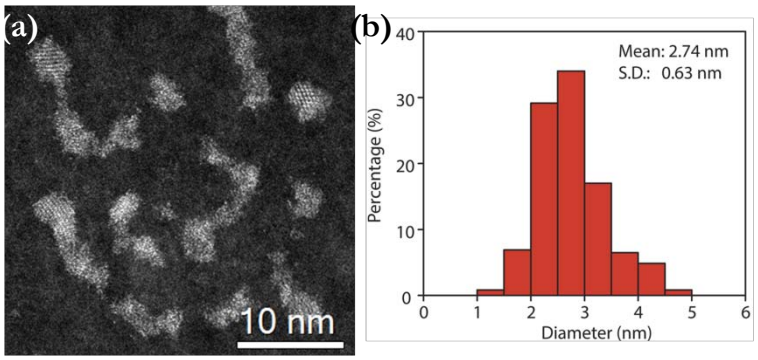

Figure 2.17: HAADF-STEM image (a) and corresponding particle size distribution histogram (b) from 247 particles of biomineralized CdSe nanocrystals after 20 min growth.

When the growth time was shortened to 20 min, the resultant nanoparticles remained fully crystalline but irregularly shaped (Figure 2.17 (a)). The average size of 2.74 ± 0.63 nm approximates the size of ~2 nm predicted for CdSe nanocrystals with strongest absorption at 438 nm.[21, 42] Lattice fringe analysis on this material identified the co-existence of both

zinc-blende and wurtzite polymorphs of CdSe nanocrystals after 20 min growth (Figure 2.18, Table 2.6).

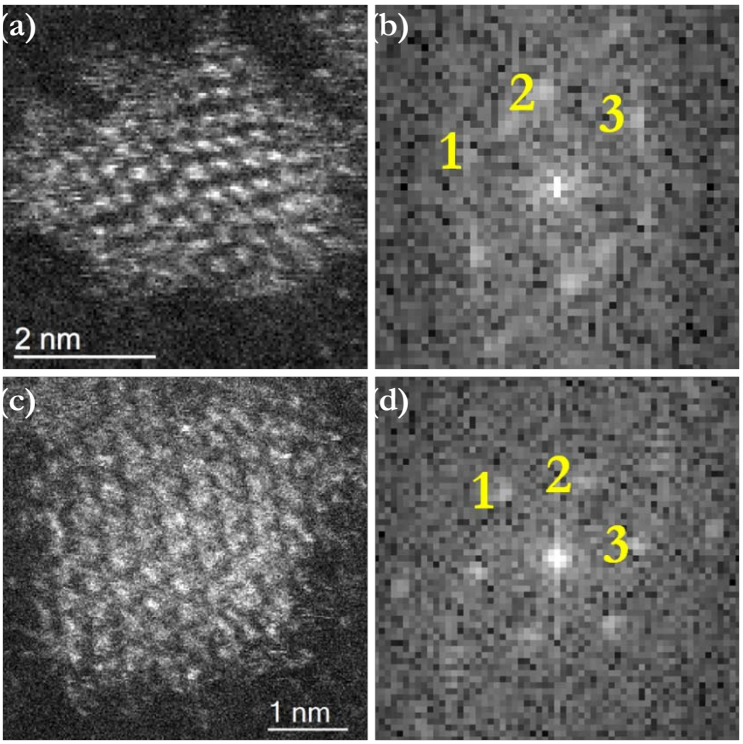

Figure 2.18: HAADF-STEM images (a, c)of CdSe nanocrystals after 20 min incubation with the corresponding FFT diagrams (b, d), demonstrating the formation of both zinc-blende (a) and wurtzite (c) type CdSe.

Table 2.6: Lattice fringe analysis based on HAADF-STEM images of CdSe nanocrystals after 20 min incubation shown in Figure 2.18 demonstrating the formation of both zinc-blende and wurtzite type CdSe.

	Fig. 2.18 (a): zinc-blende [$1\bar{1}0$]]		Fig. 2.18 (c): wurtzite [001]	
	Measured	Matching	Measured	Matching
Plane 1	3.7 Å	3.5 Å (111)	3.5 Å	3.7 Å (100)
Plane 2	3.6 Å	3.5 Å ($11\bar{1}$)	3.6 Å	3.7 Å ($1\bar{1}0$)
Plane 3	3.2 Å	3.0 Å (002)	3.7 Å	3.7 Å (010)
<1, 2>	66.2°	70.5°	57.5°	60.0°
<2, 3>	55.4°	54.7°	62.9°	60.0°
<3, 1>	58.5°	54.7°	59.6°	60.0°

As in the case of smCSE-mineralized formation of CdS nanocrystals described in Section 2.3, inclusion of all the components, *i.e.*, smCSE, cadmium acetate, and selenocystine, are necessary to ensure CdSe QD formation. Omission of any of the three components led to disappearance of any absorption peaks (Figure 2.19).

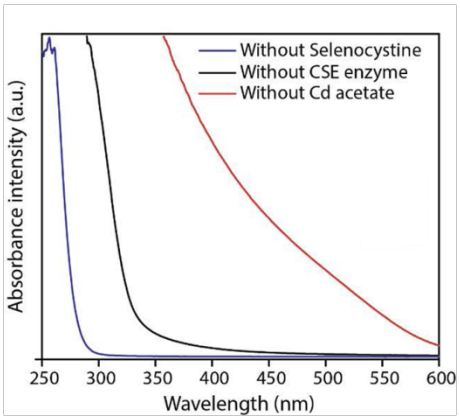

Figure 2.19: Absorbance spectra of samples prepared lacking one of the three key ingredients as measured after 24 h incubation. *Courtesy of Dr. Zhou Yang.*

2.4.2 CdSe-CdS core-shell nanocrystal formation via further smCSE biomineralization

As noted in Section 2.4.1, the as-prepared CdSe nanocrystals exhibited quite a low QY, especially at the larger end of the size spectrum, probably arising from the existence of deep surface traps. To boost the optical performance of these biosynthesized CdSe QDs, an additional shell of CdS was grown to passivate the defective surface of the CdSe QDs.[43] Herein, the shell growth onto two sets of previously formed core materials (*i.e.*, 2.74 ± 0.63 nm, 4.78 ± 1.16 nm CdSe QDs) was also accomplished by biomineralization utilizing the same enzyme smCSE. To initiate this second aqueous phase biomineralization step, fresh smCSE enzyme, cadmium acetate and L-cysteine were introduced to an aqueous suspension of purified CdSe nanocrystals. The mixture

was then incubated for 12 h for subsequent shell growth.

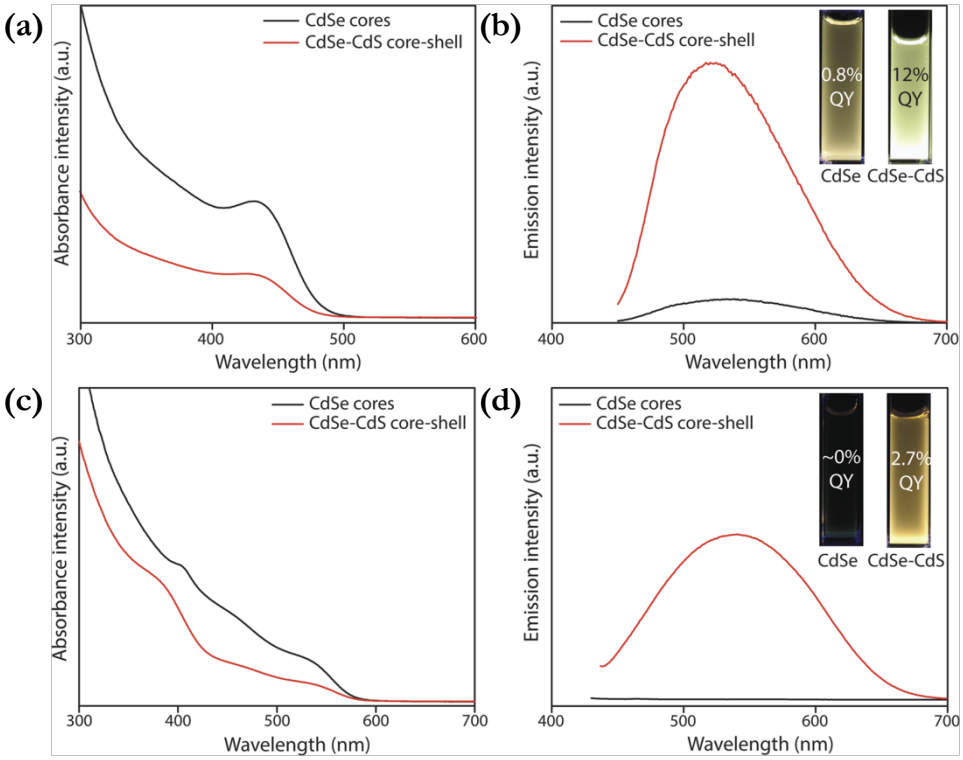

Figure 2.20: Optical spectra of aqueous phase biomineralized CdSe core and CdSe-CdS core-shell nanocrystals. (a, c) UV-vis absorption spectra. (b, d) Fluorescence emission spectra with insets showing photographs of the suspensions under UV light. Spectra in (a, b) are based on the 2.74 ± 0.63 nm CdSe cores (20 min CdSe growth), while spectra in (c, d) are based on the 4.78 ± 1.16 nm CdSe cores (24 h CdSe growth). *Courtesy of Dr. Zhou Yang.*

The QY improved remarkably upon shell growth for both sets of materials, as illustrated by the substantially enhanced photoluminescence of the core-shell materials compared to the respective core-only nanocrystals (Figure 2.20 (b, d)). This QY promotion becomes more impressive in consideration of the decreased absorption intensity (Figure 2.20 (a, c)) due to dilution of the nanocrystals upon addition of the enzyme, salt and buffer solutions required to initiate shell growth. The QY of the smaller 20 min growth time CdSe cores increases from 0.8% to 12%, while that of the larger 24 h growth time cores increased from almost 0 to 2.7% after being coated with the CdS layer. Little red-shift in the absorption maxima was noted and only a

small blue-shift in fluorescence emission maxima was observed upon shell coverage. For the 20 min grown CdSe core, the absorption and emission peaks located at 432 and 537 nm respectively shift to 433 and 522 nm respectively, after CdS passivation. It is noteworthy that these apparent spectral shifts are much smaller than the full width at half-maximum, ~125 nm, of the peaks, implying a very thin or even incomplete shell coverage. Further clarification of the cause of this shift is obscured by the irregularity of the nanocrystal morphology, the presence of L-cysteine capable of capping CdS surfaces, and the likely partial shell coverage.

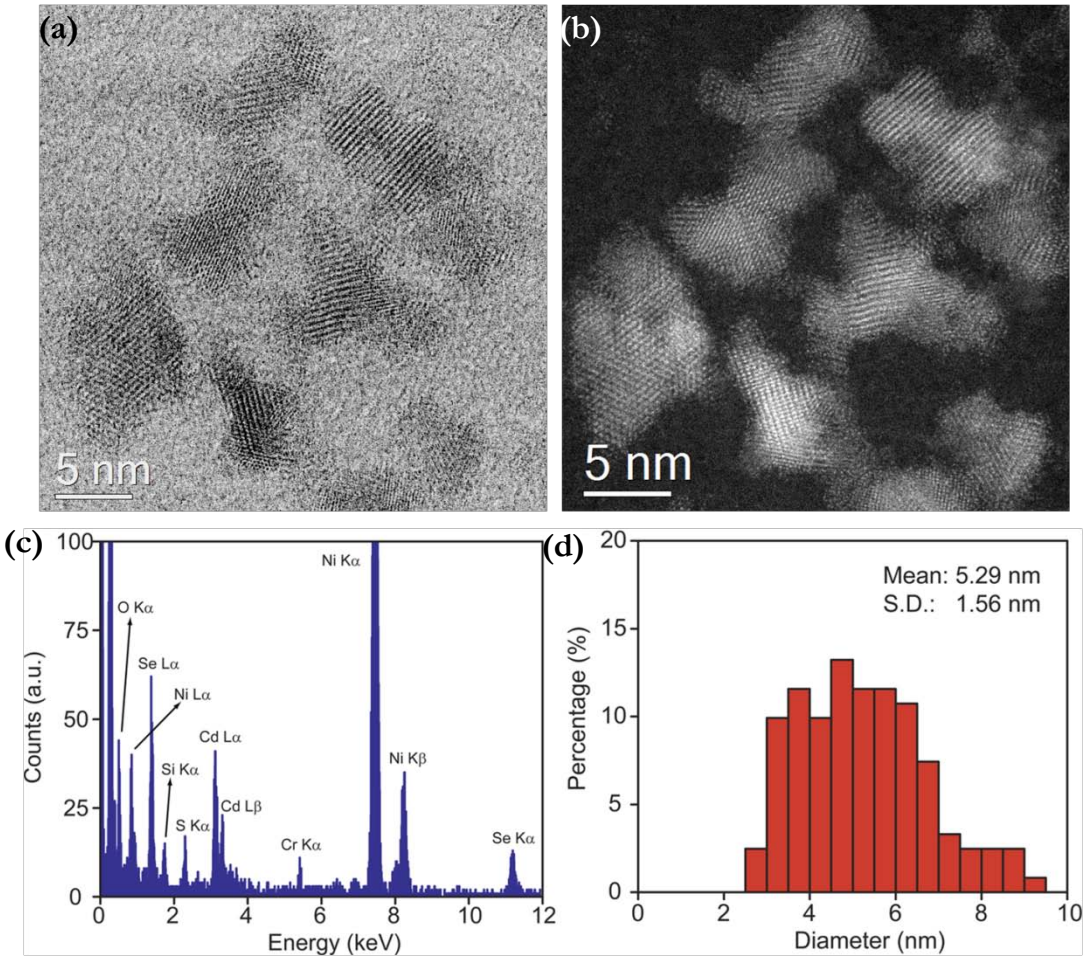

Figure 2.21: STEM characterization of the CdSe-CdS core-shell QDs grown using the larger CdSe cores incubated for 24 h. (a) BF-STEM and (b) HAADF-STEM images of the same area. (c) XEDS spectrum collected from a single particle. (d) Particle size distribution histogram derived from analysis of 122 particles.

BF- and HAADF-STEM imaging of the larger core-shell nanocrystals following phase transfer to chloroform with oleylamine as the capping agent shows nanocrystals with clear lattice fringes (Figure 2.21 (a, b)). As in the case of the larger core-only particles, the larger core-shell particles seem to be exclusively wurtzite type CdSe (Figure 2.22, Table 2.7), with no nanocrystals that could be uniquely fitted to zinc-blende type CdSe. The particles remain irregularly shaped. No recognizable core-shell boundary could be discerned, likely owing to the relatively thin shell, the small lattice mismatch between CdSe and CdS, and the distinction between S and Se sites being overshadowed by the strong contrast of Cd atomic columns in HAADF-STEM imaging. The average nanocrystal size of the larger core-shell particles increased from 4.78 ± 1.16 nm to 5.29 ± 1.56 nm (Figure 2.21 (d)), indicative of a shell thickness of 0.26 nm corresponding to ~0.7 monolayer of CdS crystal, provided that interdiffusion between Se and S is ignored. As a reference, Peng *et al.*[43] proposed that the 3.9% lattice mismatch between bulk CdSe and CdS is probably small enough to enable epitaxial growth but large enough to impede interdiffusion.

Every single particles from the larger core-shell material was found via XEDS analysis to contain Cd, Se and S (Figures 2.21 (c) and 2.23). In particular, it should be noted that the potential for interference of S-containing L-cysteine molecules in sulfur signal detection by XEDS was removed by phase transfer of the nanocrystals to the organic phase, accompanied by ligand exchange from L-cysteine to oleylamine. The determined atomic composition ratios of Cd/Se/S from three particles are quite close (Figure 2.23), and give an average Cd/Se/S ratio of 41.0/51.8/7.2, corresponding to an equivalent shell thickness of 0.4 monolayer, which is in good agreement with the measured increase in the mean particle size.

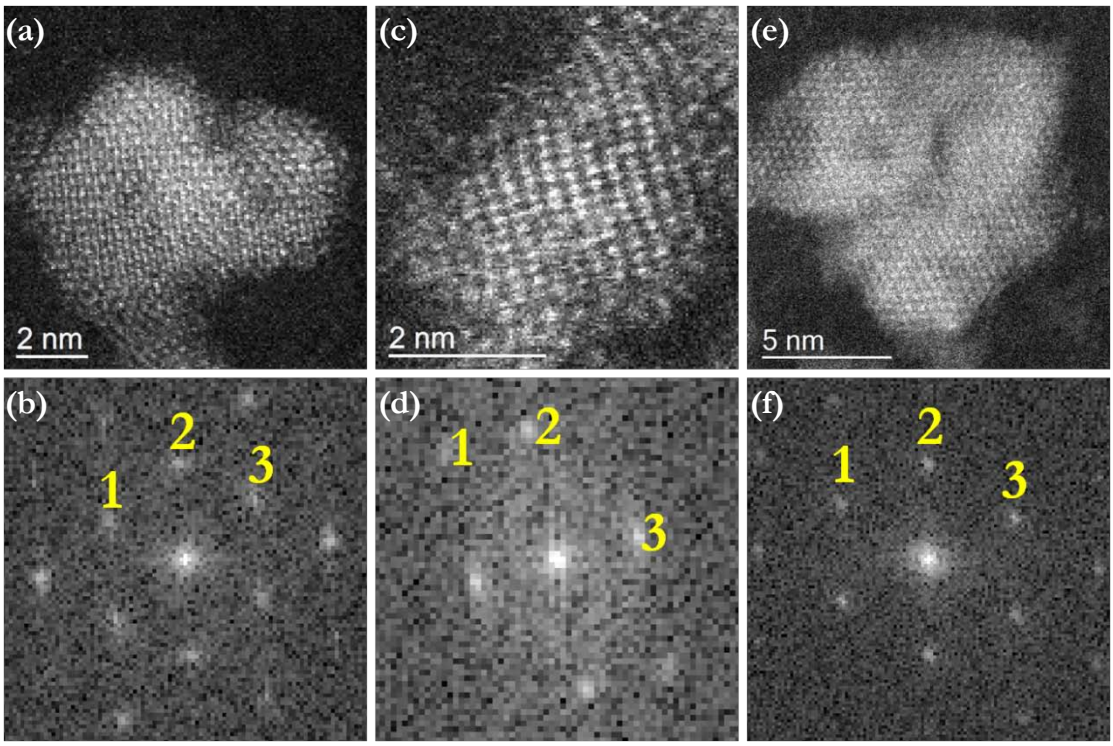

Figure 2.22: HAADF-STEM images (a, c, e) of individual CdSe-CdS core-shell nanocrystals after 24 h incubation of the CdSe cores with the corresponding FFT diagrams (b, d, f), demonstrating the formation of wurtzite type CdSe cores.

Table 2.7: Lattice fringe analysis based on HAADF-STEM images of CdSe-CdS core-shell nanocrystals after 24 h incubation of the CdSe cores shown in Figure 2.22 demonstrating the formation of wurtzite type CdSe cores.

Wurtzite CdSe	Fig. 2.22 (a): $[10\bar{1}]$		Fig. 2.22 (c): $[2\bar{4}1]$ or $[1\bar{4}\bar{2}]$			Fig. 2.22 (e): $[001]$	
	Measured	Matching	Measured	Matching	Matching	Measured	Matching
Plane 1	3.3 Å	3.3 Å (101)	1.5 Å	1.6 Å (014)	1.6 Å $(2\bar{1}3)$	3.6 Å	3.7 Å (100)
Plane 2	3.4 Å	3.3 Å $(1\bar{1}1)$	1.7 Å	1.8 Å (112)	1.8 Å (201)	3.8 Å	3.7 Å $(1\bar{1}0)$
Plane 3	3.7 Å	3.7 Å (010)	2.7 Å	2.6 Å $(10\bar{2})$	2.6 Å $(01\bar{2})$	3.9 Å	3.7 Å (010)
<1, 2>	53.5°	52.4°	33.0°	38.1°	37.8°	56.2°	60.0°
<2, 3>	67.4°	63.8°	87.2°	82.8°	81.7°	65.4°	60.0°
<3, 1>	59.1°	63.8°	59.8°	59.2°	60.5°	58.4°	60.0°

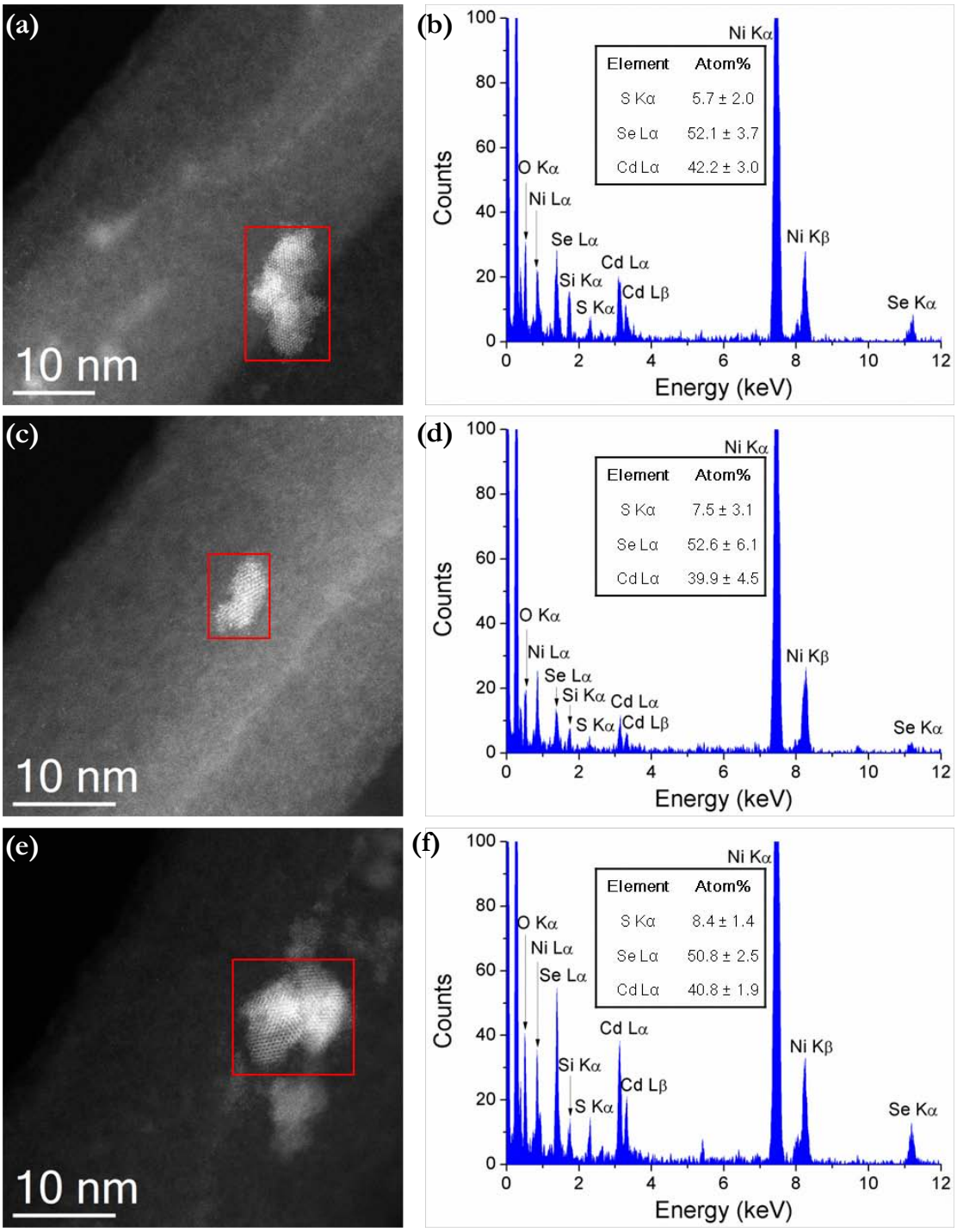

Figure 2.23: Single particle XEDS analysis of the larger core-shell CdSe-CdS nanocrystals. (a, c, e) HAADF-STEM images with regions of interest signified by red rectangles. (b, d, f) Corresponding XEDS spectra demonstrating the presence of Cd, Se and S with the respective measured atomic compositions listed as insets. Quantitative XEDS analysis was performed using the standardless Cliff-Lorimer method assuming no X-ray absorption.

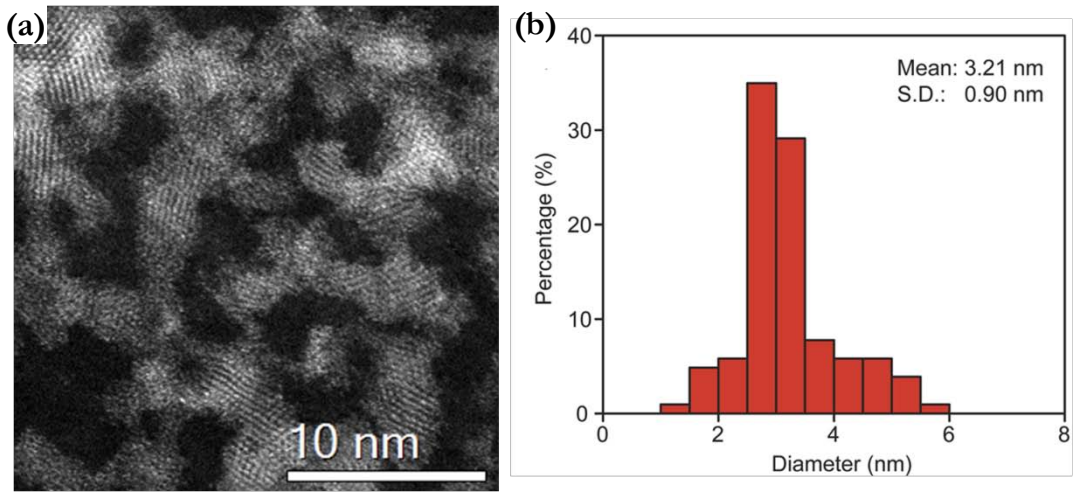

Figure 2.24: HAADF-STEM image (a) and corresponding particle size distribution histogram from 100 particles (b) of biomineralized CdSe-CdS core-shell nanocrystals with the CdSe core grown for 20 min.

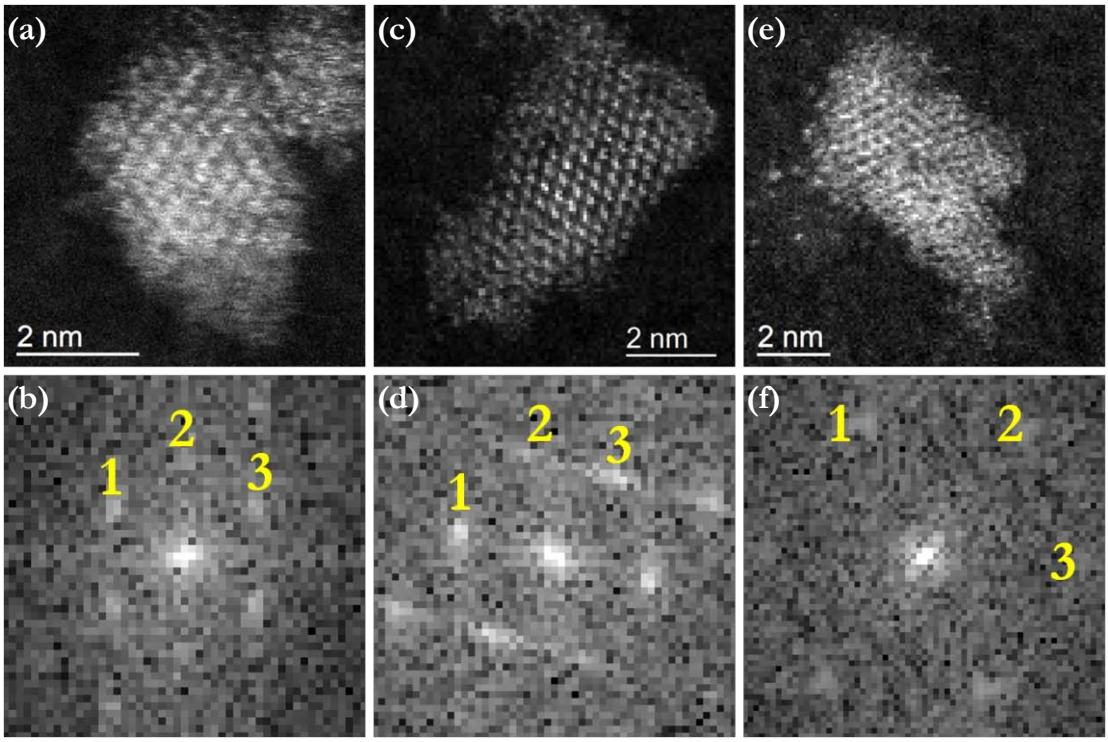

Figure 2.25: HAADF-STEM images (a, c, e) of individual CdSe-CdS core-shell nanocrystals after 20 min incubation of the CdSe cores with the corresponding FFT diagrams (b, d, f) demonstrating the formation of both zinc-blende (a) and wurtzite (c, e) CdSe cores.

Table 2.8: Lattice fringe analysis based on HAADF-STEM images of CdSe-CdS core-shell nanocrystals after 20 min incubation of the CdSe cores shown in Figure 2.25 demonstrating the formation of both zinc-blende and wurtzite type CdSe cores.

	Fig. 2.25 (a): [$1\bar{1}0$]		Fig. 2.25 (c): [010] or [011]			Fig. 2.25 (e): [001]	
	Measured	Zinc-blende	Measured	Wurtzite	Wurtzite	Measured	Wurtzite
Plane 1	3.6 Å	3.5 Å (111)	3.6 Å	3.5 Å (002)	3.7 Å (100)	3.8 Å	3.7 Å (100)
Plane 2	3.2 Å	3.0 Å (002)	3.3 Å	3.3 Å (101)	3.3 Å ($01\bar{1}$)	3.5 Å	3.7 Å ($1\bar{1}0$)
Plane 3	3.5 Å	3.5 Å ($11\bar{1}$)	3.4 Å	3.3 Å ($10\bar{1}$)	3.3 Å ($1\bar{1}1$)	3.6 Å	3.7 Å (010)
<1, 2>	58.9°	54.7°	59.1°	62.0°	63.8°	63.4°	60.0°
<2, 3>	52.3°	54.7°	56.1°	55.9°	52.4°	54.2°	60.0°
<3, 1>	68.8°	70.5°	64.8°	62.0°	63.8°	62.4°	60.0°

Nanostructural investigation of the smaller core-shell particles derived from the CdSe QDs incubated for 20 min revealed good crystallinity, albeit with asymmetric nanocrystal shapes (Figure 2.24 (a)). The particles grew by an average of 0.47 nm in diameter to 3.21 ± 0.90 nm upon shell coverage, consistent with that shown by the larger core-shell nanocrystals with the same shell growth period of 24 h. This size increase suggests 0.7 monolayer of CdS. Identification of the nanocrystal structure shows the co-existence of both zinc-blende and wurtzite CdSe cores (Figure 2.25, Table 2.8). XEDS analysis again validates the co-existence of Cd, Se and S in each nanocrystal, suggesting formation of a shell commensurate with 1.1 monolayer of CdS (Figure 2.26), which is close to the value of particle size increase revealed by HAADF imaging.

2.4.3 Correlations of nanostructure, optical properties and the biosynthesis process

As demonstrated in Section 2.3, we propose that the enzyme smCSE herein functions as a catalyst inducing CdSe and CdSe-CdS core-shell structure biomineralization, while templating the growth of the nanocrystals. CdSe biomineralization occurs via enzymatic decomposition of seleno-L-cystine to produce reactive H_2Se which could then immobilize Cd^{2+} cations to generate CdSe. However, unlike the monomer L-cysteine, the selenium analogue, seleno-L-cystine, is added to solution as a dimeric species. Therefore, H_2Se formation through seleno-L-cystine decomposition requires an additional dimer cleavage step.

As described in Section 2.3, both L-cysteine and smCSE are effective in directing CdS nanocrystal growth during biomineralization. This combined control facilitates the formation of relatively spherical nanocrystals. This contrasts with the more irregular shape noted for biomineralized CdSe particles here, which most likely results from the relatively limited availability of capping ligands during growth, as dimeric selenocystine could hardly bind to the nanocrystal surface. Hence, control over crystallite growth relies solely on smCSE, leading to non-spherical, irregular nanocrystals.

The low fluorescence efficiency for the CdSe core-only materials might be attributable to the irregularity in nanocrystal shape and potential aggregation of nanocrystals due to insufficient surface capping. We eschewed the use of L-cysteine or glutathione capping agents during CdSe QD preparation, because the addition of either would trigger unwanted CdS growth.

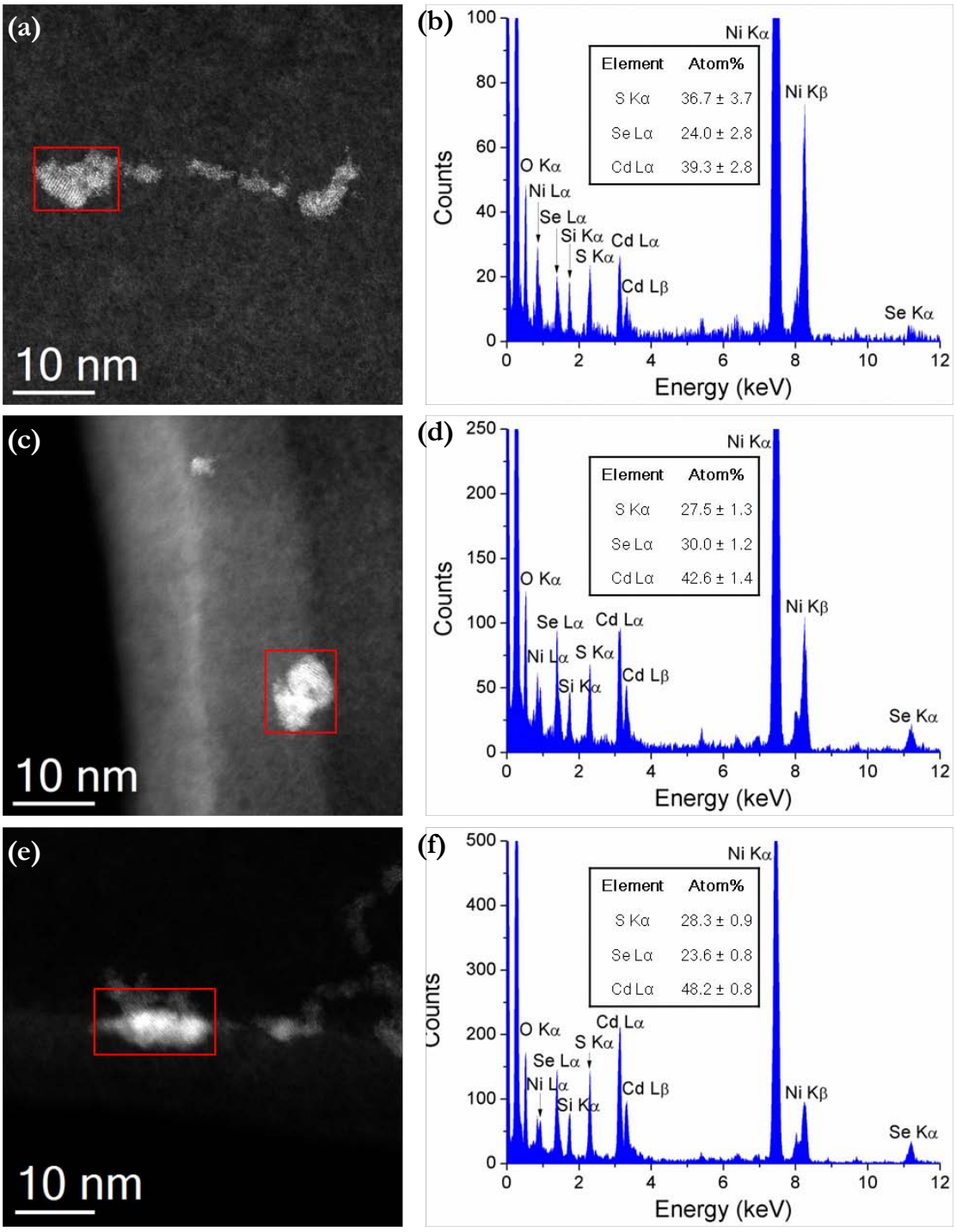

Figure 2.26: Single particle XEDS analysis of the smaller core-shell CdSe-CdS nanocrystals. (a, c, e) HAADF-STEM images with regions of interest signified by red rectangles. (b, d, f) Corresponding XEDS spectra demonstrating the presence of Cd, Se and S with the respective measured atomic compositions listed as insets. Quantitative XEDS analysis was performed using the standardless Cliff-Lorimer method assuming no X-ray absorption.

Given that the core-shell configuration could not be directly identified via imaging, we have

resorted to collating indirect evidence for the heterostructure. The considerably enhanced QY results from successful passivation of the CdSe nanocrystal surfaces through the epitaxial growth of the CdS shell.[44-45] The detection of Cd, Se and S elements in single particle XEDS analysis (Figures 2.21 (c), 2.23 and 2.26) adds further weight to the formation of core-shell nanocrystals, suggesting sequential mineralization of CdSe and CdS within a single nanocrystal rather than secondary nucleation of CdS particles. A significant separate CdS population would have led to a distinguishable additional characteristic absorption edge at ~375 nm, and would not have yielded such an improvement in QY. While small secondary peaks around this position appear in the absorption spectra for the smaller CdSe-CdS sample, these peaks also show up in those of the CdSe core-only samples and are due to additional absorption peaks in the quantum confined core nanocrystals.[46] Furthermore, the diameter increases determined from particle size distribution measurements for both the smaller and larger CdSe cores following shell growth are approximately commensurate with the shell thickness inferred from the XEDS compositional measurements.

One peculiarity noted for the CdSe 24 h growth and CdSe-CdS 24 h core growth samples is that the crystal structure of CdSe seems to be exclusively wurtzite, as revealed by lattice fringe analysis (Figures 2.15 (c, d), 2.16, 2.22, and Tables 2.5, 2.7). When the incubation time of CdSe biomineralization is reduced for both samples, both wurtzite and zinc-blende CdSe polymorphs were identifiable. This may originate from the difficulty of nanocrystal growth to reach thermodynamic equilibrium within a short time frame under such mild growth conditions. The temporal evolution of CdSe structure towards wurtzite implies a reversion in relative polytypic stability, as zinc-blende is generally considered as the preferred CdSe polymorph at lower

temperatures (*e.g.*, 350 °C).[47] However, the temperature employed in the current study (37 °C) is still much lower than the referenced temperature. It is also possible that the enzyme-induced crystallization and selenol binding characteristics could contribute to determining the favored crystal structure.

A possible explanation for the incomplete CdS shell coverage noted is that the Cd-deficient precursor solution for synthesizing the CdSe core (nominal molar ratio Cd/Se = 1/16) might lead to a Se-rich core surface which, upon addition of another Cd-deficient precursor solution for shell growth (nominal molar ratio Cd/S = 1/8), would likely inhibit the growth of the first shell monolayer.

A very significant QY improvement was achieved in spite of the envisaged partial coverage of the CdS shell over the CdSe core. While relatively thick CdS shells would substantially red-shift the absorbance and emission peak positions, incomplete or single monolayers are inadequate to markedly affect the band gap.[43, 48] The QYs we obtained are similar to those reported during the early years of organic phase chemical synthesis of metal chalcogenide QDs. For instance, Peng *et al.*[43] studied the QYs as a function of CdS coverage on CdSe cores, and reported QY values in organic solvents of 14% for 0.77 CdS monolayer coverage of 2.3 nm CdSe cores and 8% for 0.54 monolayer coverage on 3.0 nm CdSe cores. This compares well with the 12% QY measured for our biomineralized 2.74 nm CdSe cores with 0.7 monolayer of CdS shell.

2.4.4 Deliberation over the most appropriate method of particle size measurement

For semiconductor nanocrystals, the particle size distribution is a crucial parameter in controlling their optical properties as it dictates the band gap of the materials through the quantum confinement effect. Electron microscopy provides the most straightforward tool to visualize the particle size through 2-D projection of 3-D objects. The conventional way of particle size determination utilizing electron microscopy is to measure the area enclosed by the outline of the particle and deduce the spherical equivalent diameter assuming a circular shape for the 2-D projected particle.

However, this method produces over-estimated diameter values when applied to our irregularly shaped CdSe-based QDs. This is because quantum confinement of QDs is primarily governed by the shortest length within the particles. Alivisatos *et al.*[49] reported the band gaps of CdSe nanorods with varying widths and lengths. After acquiring fluorescence data for CdSe nanorods with varying widths ranging from 3.0 to 6.5 nm and lengths from 7.5 to 40 nm, they proposed a polynomial fit for the band gap (E_g, eV) as a function of width (W, nm) and length (L, nm):

$$E_{\mathrm{g}} = 1.8563 - 2.0835 * L^{-2} + 4.5507 * W^{-2} - 0.0018 * (L/W)^2 + 0.0001 * (L/W)^3 + 10.5824 * L^{-3} - 0.3833 * W^{-3}$$

The standard deviation of this fit is merely ~30 meV, slightly greater than the thermal energy at room temperature. The fit indicates a tendency for the band gap to decrease with an increase in either width or length.

To further assess the relative influence of the width and length on the band gap, we have calculated the partial derivatives of E_g dependence on W and L:

$$\frac{\partial E_{\mathrm{g}}}{\partial L/L} = 4.167 * L^{-2} - 0.0036 * (L/W)^2 + 0.0003 * (L/W)^3 - 31.7472 * L^{-3}$$

$$\frac{\partial E_{\mathrm{g}}}{\partial W/W} = -9.1014 * W^{-2} + 0.0036 * (L/W)^2 - 0.0003 * (L/W)^3 + 1.1499 * W^{-3}$$

The comparison of the sensitivity of E_g to W and L variation could be approached by taking the ratio (denoted by k) of $\frac{\partial E_g}{\partial W/W}$ to $\frac{\partial E_g}{\partial L/L}$: $k = \left|\frac{\partial E_g}{\partial W/W} / \frac{\partial E_g}{\partial L/L}\right|$. If $k = 1$, then W and L are equally exerting influence upon E_g; a higher k value means W is playing a larger role than L, and vice versa. A 3-D plot of k, W and L (Figure 2.27) shows $k >> 1$ in most combinations of W and L values. Thus, in most cases E_g is much more strongly affected by W than by L.

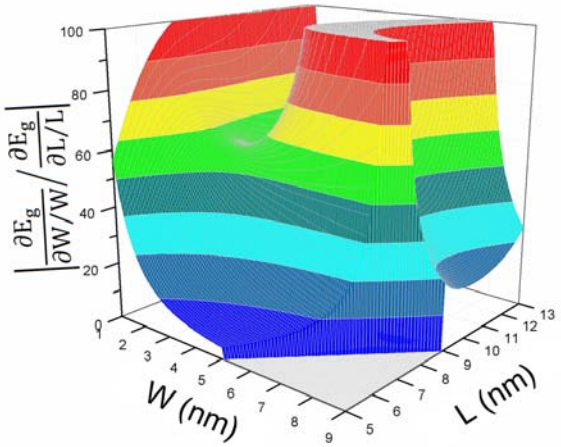

Figure 2.27: The colored 3-D surface plot showing the relationship of k, W and L. The W value ranges from 1 to 9 nm; the L value ranges from 5 to 13 nm. Only the data for the case of $L > W$ are considered. For clarity of display, the plot is cut off at an upper limit of $k = 100$.

This finding could shed light on the particle size analysis of our irregularly shaped CdSe and CdSe-CdS core-shell nanocrystals: the shortest dimension within a particle largely determines the band gap of the nanocrystals. Therefore, we propose that, and have used, the diameter of the largest circle enclosed by the projected outline of a particle as the most appropriate estimate of particle size.

2.5 Summary and Outlook

In this chapter, several biomineralized cadmium chalcogenide nanocrystal systems have been investigated and characterized. We demonstrated that the engineered SMCD1 bacteria and the

recombinant enzyme smCSE excreted by SMCD1 are capable of biomineralizing of CdS and CdSe nanocrystals in the aqueous phase under ambient conditions, using low-cost precursors and capping agents. The mean nanocrystal size could be tailored within the quantum confinement regime by varying the growth time, as verified by both optical spectroscopy and electron microscopy imaging experiments.

The SMCD1 bacteria have been shown to enable extracellular production of CdS nanocrystals, most likely via a CSE catalyzed conversion of L-cysteine to H_2S. For the enzymatic route, we confirmed the dual role of smCSE in both inducing particle growth by generating reactive S or Se species, and controlling the structure of the nanocrystals within the quantization regime. In the case of CdSe nanocrystal biomineralization, the smCSE enzyme has further been used to mineralize a shell of CdS onto the CdSe core, significantly improving the QY to 12% through surface passivation.

From the nanoscopic point of view, the employment of microscopic imaging and compositional analysis have unveiled key structural details on the nanocrystals and deepened our understanding of the biomineralization process through correlations of structures, properties and the biomineralization processes. Lattice fringe analysis revealed the coexistence of wurtzite and zinc-blende type CdS in both cellularly and enzymatically produced CdS nanocrystal samples. Similar polymorphism was also observed in the CdSe and CdSe-CdS core-shell nanocrystals with 20 min CdSe incubation; however, at an extended growth time of 24 h, wurtzite type CdSe seemed to have become the sole phase present. The apparent association of crystal structure with growth time could inspire further exploration into the crystallization process during biomineralization. XEDS-STEM analysis has allowed us to probe individual nanocrystals in the

CdSe-CdS core-shell materials and has consistently proven the co-existence of Cd, Se and S within single particles, pointing indirectly to the formation of a core-shell structure. The irregular shapes of the CdSe-based nanocrystals have prompted us to develop a new protocol for more appropriate particle size measurement when making meaningful correlations with optical properties. The shortest dimension within a particle has been proposed as the diameter which is considered to dominate the determination of the CdSe band gap.

In the future, the following aspects of this research area deserve further study:

(1) A more systematic study could be designed to comprehend what parameters could affect the crystal structure of the biomineralized CdS and CdSe QDs. As noted above, growth time probably plays a role in equilibrating the preferred polymorph. A series of reproducible experiments with more frequent growth time intervals over a longer incubation period could be conducted. The statistics of phase identification through high resolution electron microscopy could be improved by extensive examination of well resolved nanocrystals. Synchrotron X-ray diffraction with Rietveld refinement might be attempted to differentiate the two similar phases of wurtzite and zinc-blende on a global basis. Other parameters that might also impact the final crystal structures include, *e.g.*, growth temperature, choice of capping agent, precursor concentration ratio and pH value.

(2) As discussed in Section 2.4.3, the Cd-deficient precursor solution might have led to the incomplete shell coverage of CdS. Therefore, we might increase the cadmium precursor concentration with the aim of increasing the shell thickness to attain more complete coverage. With a thicker shell, we might be able to identify the core-shell configuration via XEDS-STEM. Extending the growth time might also give rise to increased thickness of the CdS shell.

(3) The nanocrystal growth mechanisms during single enzyme biomineralization need further clarification. We would also like to directly visualize the smCSE mediated nucleation and growth processes in real time in an *in-situ* liquid cell in (S)TEM. While we should bear in mind that the growth conditions will invariably be altered as the starting ingredients will be bombarded with energetic electrons, this *in-situ* microscopy observation may shed light on how nanocrystals are formed.

2.6 Acknowledgements

The work described in this chapter is in collaboration with the Biomineralization group led by Prof. Steven McIntosh and Prof. Bryan W. Berger in the Department of Chemical Engineering at Lehigh University. Their guidance and expert advice is much appreciated.

The biosynthetic QD sample preparation and optical property measurements were conducted by Dr. Zhou Yang (Sections 2.2 and 2.4) and Robert Dunleavy (Section 2.3). Their various important contributions to this work are gratefully acknowledged. The work described in Sections 2.2, 2.3 and 2.4 has been published in *Green Chemistry*[50], *Proceedings of the National Academy of Sciences*[51], and *ACS Applied Materials & Interfaces*[52], respectively.

2.7 References

1. Murray, C. B.; Kagan, C.; Bawendi, M., Synthesis and characterization of monodisperse nanocrystals and close-packed nanocrystal assemblies. *Annu. Rev. Mater. Sci.* **2000**, 30, 545-610.

2. Alivisatos, A. P., Perspectives on the physical chemistry of semiconductor nanocrystals. *J. Phys. Chem.* **1996**, 100, 13226-13239.

3. Klimov, V.; Mikhailovsky, A.; Xu, S.; Malko, A.; Hollingsworth, J.; Leatherdale, C.; Eisler, H.-J.; Bawendi, M., Optical gain and stimulated emission in nanocrystal quantum dots. *Science*

2000, 290, 314-317.

4. Han, M.; Gao, X.; Su, J. Z.; Nie, S., Quantum-dot-tagged microbeads for multiplexed optical coding of biomolecules. *Nat. Biotechnol.* **2001**, 19, 631-635.

5. Murray, C. B.; Norris, D. J.; Bawendi, M. G., Synthesis and characterization of nearly monodisperse CdE (E = sulfur, selenium, tellurium) semicondutor nanocrytallites. *J. Am. Chem. Soc.* **1993**, 115, 8706-8715.

6. Zhou, J.; Pu, C.; Jiao, T.; Hou, X.; Peng, X., A two-step synthetic strategy toward monodisperse colloidal CdSe and CdSe/CdS core/shell nanocrystals. *J. Am. Chem. Soc.* **2016**, 138, 6475-6483.

7. Dameron, C. T.; Reese, R. N.; Mehra, R. K.; Kortan, A. R.; Carroll, P. J.; Steigerwald, M. L.; Brus, L. E.; Winge, D. R., Biosynthesis of cadmium sulphide quantum semiconductor crystallites. *Nature* **1989**, 338, 596-597.

8. Li, Y.; Cui, R.; Zhang, P.; Chen, B.-B.; Tian, Z.-Q.; Li, L.; Hu, B.; Pang, D.-W.; Xie, Z.-X., Mechanism-oriented controllability of intracellular quantum dots formation: the role of glutathione metabolic pathway. *ACS Nano* **2013**, 7, 2240-2248.

9. Bao, H.; Hao, N.; Yang, Y.; Zhao, D., Biosynthesis of biocompatible cadmium telluride quantum dots using yeast cells. *Nano Res.* **2010**, 3, 481-489.

10. Bollet, C.; Davin-Regli, A.; De Micco, P., A simple method for selective isolation of Stenotrophomonas maltophilia from environmental samples. *Appl. Environ. Microbiol.* **1995**, 61, 1653-1654.

11. Alivisatos, A. P., Semiconductor clusters, nanocrystals, and quantum dots. *Science* **1996**, 271, 933-937.

12. Einevoll, G. T., Confinement of excitons in quantum dots. *Phys. Rev. B* **1992**, 45, 3410-3417.

13. Chatterjee, A.; Priyam, A.; Das, S. K.; Saha, A., Size tunable synthesis of cysteine-capped CdS nanoparticles by γ-irradiation. *J. Colloid Interface Sci.* **2006**, 294, 334-342.

14. Krupko, E. V.; Grodzyuk, G. Y.; Khalavka, Y. B.; Okrepka, G. M.; Shcherbak, L. P., Effect of the composition of the reaction mixture on the preparation of L-cysteine-stabilized CdS nanoparticles and their optical properties. *Theor. Exp. Chem.* **2011**, 47, 101-107.

15. Mullaugh, K. M.; Luther III, G. W., Growth kinetics and long-term stability of CdS nanoparticles in aqueous solution under ambient conditions. *J. Nanopart. Res.* **2011**, 13, 393-404.

16. Kang, S. H.; Bozhilov, K. N.; Myung, N. V.; Mulchandani, A.; Chen, W., Microbial synthesis of CdS nanocrystals in genetically engineered E. coli. *Angew. Chem. Int. Ed.* **2008**, 47, 5186-5189.

17. Cao, Y. C.; Wang, J., One-pot synthesis of high-quality zinc-blende CdS nanocrystals. *J. Am. Chem. Soc.* **2004**, 126, 14336-14337.

18. Moloney, M. P.; Gun'ko, Y. K.; Kelly, J. M., Chiral highly luminescent CdS quantum dots. *Chem. Commun.* **2007**, 3900-3902.

19. Negi, D. P. S.; Chanu, T. I., Surface-modified CdS nanoparticles as a fluorescent probe for the selective detection of cysteine. *Nanotechnology* **2008**, 19, 465503.

20. Tamang, S.; Beaune, G. g.; Texier, I.; Reiss, P., Aqueous phase transfer of InP/ZnS nanocrystals conserving fluorescence and high colloidal stability. *ACS Nano* **2011**, 5, 9392-9402.

21. Yu, W. W.; Qu, L.; Guo, W.; Peng, X., Experimental determination of the extinction coefficient of CdTe, CdSe, and CdS nanocrystals. *Chem. Mater.* **2003**, 15, 2854-2860.

22. Zhang, J.-Y.; Wang, X.-Y.; Xiao, M.; Qu, L.; Peng, X., Lattice contraction in free-standing CdSe nanocrystals. *Appl. Phys. Lett.* **2002**, 81, 2076-2078.

23. Dong, C.; Ren, J., Measurements for molar extinction coefficients of aqueous quantum dots. *Analyst* **2010**, 135, 1395-1399.

24. Beato-López, J. J.; Fernández-Ponce, C.; Blanco, E.; Barrera-Solano, C.; Ramírez-del-Solar, M.; Domínguez, M.; García-Cozar, F.; Litrán, R., Preparation and characterization of fluorescent CdS quantum dots used for the direct detection of GST fusion proteins. *Nanomater. Nanotechnol.* **2012**, 2, 1-10.

25. Mastronardi, M. L.; Maier-Flaig, F.; Faulkner, D.; Henderson, E. J.; Kübel, C.; Lemmer, U.; Ozin, G. A., Size-dependent absolute quantum yields for size-separated colloidally-stable silicon nanocrystals. *Nano Lett.* **2012**, 12, 337-342.

26. Mehra, R. K.; Winge, D. R., Metal ion resistance in fungi: molecular mechanisms and their regulated expression. *J. Cell. Biochem.* **1991**, 45, 30-40.

27. Deneke, S. M.; Fanburg, B. L., Regulation of cellular glutathione. *Am. J. Physiol. Lung Cell Mol. Physiol.* **1989**, 257, L163-L173.

28. Wang, C. L.; Lum, A. M.; Ozuna, S. C.; Clark, D. S.; Keasling, J. D., Aerobic sulfide production and cadmium precipitation by Escherichia coli expressing the Treponema denticola cysteine desulfhydrase gene. *Appl. Microbiol. Biotechnol.* **2001**, 56, 425-430.

29. Matsuo, Y.; Greenberg, D. M., A crystalline enzyme that cleaves homoserine and crystathionine. II. Prosthetic group. *J. Biol. Chem.* **1958**, 230, 561-571.

30. Sun, Q.; Collins, R.; Huang, S.; Holmberg-Schiavone, L.; Anand, G. S.; Tan, C.-H.; van-den-Berg, S.; Deng, L.-W.; Moore, P. K.; Karlberg, T.; Sivaraman, J., Structural basis for the inhibition mechanism of human cystathionine γ-lyase, an enzyme responsible for the production of H_2S. *J. Biol. Chem.* **2009**, 284, 3076-3085.

31. Yano, T.; Fukamachi, H.; Yamamoto, M.; Igarashi, T., Characterization of L‐cysteine desulfhydrase from Prevotella intermedia. *Oral Microbiol. Immunol.* **2009**, 24, 485-492.

32. Wei, S.-H.; Zhang, S. B., Structure stability and carrier localization in CdX (X= S, Se, Te) semiconductors. *Phys. Rev. B* **2000**, 62, 6944-6947.

33. Piven, N. G.; Khalavka, Y. B.; Shcherbak, L. P., Effect of SH-containing ligands on the growth of CdS nanoparticles. *Inorg. Mater.* **2008**, 44, 1047-1051.

34. Bae, W.; Mehra, R. K., Properties of glutathione- and phytochelatin-capped CdS bionanocrystallites. *J. Inorg. Biochem.* **1998**, 69, 33-43.

35. Thangadurai, P.; Balaji, S.; Manoharan, P. T., Surface modification of CdS quantum dots using thiols—structural and photophysical studies. *Nanotechnology* **2008**, 19, 435708-435716.

36. Collins, J. M.; Monty, K. J., The cysteine desulfhydrase of Salmonella typhimurium kinetic and catalytic properties. *J. Biol. Chem.* **1973**, 248, 5943-5949.

37. Winter, J. O.; Gomez, N.; Gatzert, S.; Schmidt, C. E.; Korgel, B. A., Variation of cadmium sulfide nanoparticle size and photoluminescence intensity with altered aqueous synthesis conditions. *Colloids Surf. Physicochem. Eng. Aspects* **2005**, 254, 147-157.

38. Spoerke, E. D.; Voigt, J. A., Influence of engineered peptides cadmium sulfide nanocrystals. *Adv. Funct. Mater.* **2007**, 17, 2031-2037.

39. Jiang, C.; Xu, S.; Yang, D.; Zhang, F.; Wang, W., Synthesis of glutathione‐capped CdS quantum dots and preliminary studies on protein detection and cell fluorescence image. *Luminescence* **2007**, 22, 430-437.

40. Aldana, J.; Wang, Y. A.; Peng, X., Photochemical instability of CdSe nanocrystals coated by hydrophilic thiols. *J. Am. Chem. Soc.* **2001**, 123, 8844-8850.

41. Rogach, A. L.; Kornowski, A.; Gao, M.; Eychmüller, A.; Weller, H., Synthesis and characterization of a size series of extremely small thiol-stabilized CdSe nanocrystals. *J. Phys.*

Chem. B **1999**, 103, 3065-3069.

42. Baskoutas, S.; Terzis, A. F., Size-dependent band gap of colloidal quantum dots. *J. Appl. Phys.* **2006**, 99, 013708.

43. Peng, X.; Schlamp, M. C.; Kadavanich, A. V.; Alivisatos, A. P., Epitaxial growth of highly luminescent CdSe/CdS core/shell nanocrystals with photostability and electronic accessibility. *J. Am. Chem. Soc.* **1997**, 119, 7019-7029.

44. Pu, C.; Peng, X., To battle surface traps on CdSe/CdS core/shell nanocrystals: shell isolation versus surface treatment. *J. Am. Chem. Soc.* **2016**, 138, 8134-8142.

45. Chen, O.; Zhao, J.; Chauhan, V. P.; Cui, J.; Wong, C.; Harris, D. K.; Wei, H.; Han, H.-S.; Fukumura, D.; Jain, R. K., Compact high-quality CdSe–CdS core–shell nanocrystals with narrow emission linewidths and suppressed blinking. *Nat. Mater.* **2013**, 12, 445-451.

46. Leatherdale, C. A.; Woo, W.-K.; Mikulec, F. V.; Bawendi, M. G., On the absorption cross section of CdSe nanocrystal quantum dots. *J. Phys. Chem. B* **2002**, 106, 7619-7622.

47. Rice, K. P.; Saunders, A. E.; Stoykovich, M. P., Seed-mediated growth of shape-controlled wurtzite CdSe nanocrystals: platelets, cubes, and rods. *J. Am. Chem. Soc.* **2013**, 135, 6669-6676.

48. Li, J. J.; Wang, Y. A.; Guo, W.; Keay, J. C.; Mishima, T. D.; Johnson, M. B.; Peng, X., Large-scale synthesis of nearly monodisperse CdSe/CdS core/shell nanocrystals using air-stable reagents via successive ion layer adsorption and reaction. *J. Am. Chem. Soc.* **2003**, 125, 12567-12575.

49. Li, L.; Hu, J.; Yang, W.; Alivisatos, A. P., Band gap variation of size- and shape-controlled colloidal CdSe quantum rods. *Nano Lett.* **2001**, 1, 349-351.

50. Yang, Z.; Lu, L.; Berard, V. F.; He, Q.; Kiely, C. J.; Berger, B. W.; McIntosh, S., Biomanufacturing of CdS quantum dots. *Green Chem.* **2015**, 17, 3775-3782.

51. Dunleavy, R.; Lu, L.; Kiely, C. J.; McIntosh, S.; Berger, B. W., Single-enzyme biomineralization of cadmium sulfide nanocrystals with controlled optical properties. *Proc. Natl. Acad. Sci. U.S.A.* **2016**, 113, 5275-5280.

52. Yang, Z.; Lu, L.; Kiely, C. J.; Berger, B. W.; McIntosh, S., Single enzyme direct biomineralization of CdSe and CdSe-CdS core-shell quantum dots. *ACS Appl. Mater. Interfaces* **2017**, 9, 13430-13439.

Chapter 3

Biomineralized nanocrystals of other metal sulfides

3.1 Introduction

In the previous chapter, we have shown that biomineralization has allowed the production of functional CdS and CdSe-based nanocrystals. Herein, the material palette is further expanded to other metal sulfide nanocrystals, namely, PbS-based, ZnS-based and $CuInS_2$-based nanocrystals.

Compared to CdS, PbS nanocrystal QDs possess a relatively large Bohr radius (18-20 nm)[1] with an easily accessible size quantization regime, making them highly interesting for energy harvesting applications. Here we describe successful biomineralization of quantum confined PbS nanocrystals via a purely biological approach as opposed to the expensive conventional hot injection method,[2] by using the previously engineered SMCD1 bacterial strain that generates a putative cystathionine γ-lyase capable of catalyzing and templating nanocrystal growth. Further growth of a CdS shell has been realized in the presence of the recombinant cystathionine γ-lyase (smCSE) and the respective precursors for the passivation of surface states on the PbS core. The versatility of the engineered single enzyme smCSE has been further exploited for the synthesis of heavy-metal free sulfide nanocrystals, namely the ternary alloy $CuInS_2$, the quaternary alloy $(CuInZn)S_2$, and core-shell $CuInS_2$-ZnS, under ambient conditions. This obviates the use of elevated temperatures and manipulation of pH, or direct addition of a reactive chemical precursor, which is necessary for aqueous phase nanocrystal formation in other reports.[3-7]

Furthermore, this greener synthetic route endows the resultant nanocrystals with biocompatibility that allows them to be used in non-toxic bioimaging applications. Extensive electron microscopic investigation has been utilized for a comprehensive understanding of the nanostructures of these different metal sulfide QD systems.

3.2 PbS and PbS-CdS core-shell nanocrystals synthesized by SMCD1 and smCSE

In Chapter 2 (Section 2.2), we have shown the ability of the SMCD1 bacteria to mineralize size controlled CdS nanocrystals. The current work demonstrates the generality of our approach by employing the same strain of SMCD1 for the production of PbS nanocrystals with no further evolution. The secretion of the smCSE enzyme could further drive the growth of PbS QDs in the absence of the cells. In addition, replacing the lead precursor with the cadmium counterpart enables CdS shell biomineralization on a PbS core which leads to the expected blue-shift in optical properties as compared to pure PbS QDs.

3.2.1 Synthetic protocols for biomineralized PbS and PbS-CdS core-shell nanocrystals

The engineered strain of SMCD1 was sub-cultured into 100 mL of LB broth and incubated for 12 h at 37 °C with shaking. Cells were collected by centrifugation at 5000 rpm for 10 min and re-suspended in aqueous tris-HCl buffer (0.1 M, pH = 7.5). An aqueous solution of 1 mM lead acetate, 8 mM L-cysteine and tris-HCl buffer was placed on ice, followed by addition of re-suspended SMCD1 cells (OD_{600} = 0.5). After 5 min incubation on ice, the solution was

centrifuged at 8000 rpm for 5 min to remove the cells. Then the supernatant was kept at 18 °C for a series of prescribed time periods to allow further PbS particle growth induced by the cystathionine γ-lyase enzyme generated by SMCD1. Here we show that this enzyme is not only responsible for biomineralization of cadmium chalcogenide nanocrystals as confirmed in Chapter 2, but also is associated with PbS biomineralization.

The PbS nanocrystals in the aqueous phase were further centrifuged at 12000 rpm for 10 min, and subsequently re-suspended in an 8 mM L-cysteine solution. For CdS shell growth, 1 mM cadmium acetate and 5 mM tetramethylammonium hydroxide were introduced and the mixture was incubated at 37 °C for 18 h.

In order to eliminate the interference of water in the infra-red region of the optical absorption spectrum phase transfer of the as-synthesized PbS or PbS-CdS QDs from aqueous to organic solvents was carried out using the procedure previously described by Gaponik *et al.*[8] Here, 5 mL of 1-dodecanethiol (DDT) and 5 mL of acetone were sequentially added to a 5 mL QD aqueous solution placed in a glass vial, followed by agitation of the mixture for 15 min at 60 °C. The organic phase was then removed after phase transfer and mixed with an equal volume of toluene. Finally, the DDT capped nanocrystals were precipitated with methanol and then re-suspended in chloroform or tetrachloroethylene for subsequent optical property and electron microscopy measurements.

3.2.2 Optical and structural characterization of PbS and PbS-CdS core-shell nanocrystals

The centrifuged and dried solid precipitated from the aqueous solution of lead acetate, L-cysteine

and strain SMCD1 after 3 h incubation consists of PbS crystallites having the cubic rock salt structure, as evidenced by XRD analysis (Figure 3.1). This precipitate is only formed in the presence of SMCD1, lead acetate and L-cysteine in a buffered aqueous solution. Omission of any of these ingredients, including using unbuffered DI water, does not result in the formation of the brown precipitate. Without all components present the mixture appears turbid due to the optical density of the cell suspension (Table 3.1). The absence of L-cysteine, a metal complexing agent, increases the opacity of the suspension by forming a white precipitate, most likely $Pb(OH)_2$. Note that no centrifugation was applied to the cells from any of the samples displayed in Table 3.1 during PbS growth. As described in Chapter 2, this biomineralization process is most likely driven by expression of the smCSE enzyme, which could generate reactive H_2S for PbS production. The use of excess L-cysteine provides both a sulfur source and a convenient nanocrystal capping agent.

The average crystallite size determined by the Scherrer equation for the XRD data (Figure 3.1) is ~7 nm. The synthesis procedure needed to be adjusted further for producing smaller PbS QDs that exhibit strong quantum confinement effects in the desirable near-IR region .[9] Drawing inspiration from an earlier report[10] which suggested that a lower rate of H_2S infusion could reduce PbS nanocrystal size, we tried slowing down the biomineralization process by decreasing the rate of H_2S generation by the putative smCSE enzyme. To achieve this, the solution was chilled on ice during the initial nanocrystal nucleation phase, and the SMCD1 cells were centrifuged from solution after 5 min of growth in order to arrest further enzyme secretion and thus curb particle growth. The aqueous centrifuged supernatant was buffered at pH = 7.5 and contained residual lead acetate, L-cysteine and any enzyme generated by the cells during the first

5 min of growth. Subsequent nanocrystal growth was then maintained at 18 °C for different time periods.

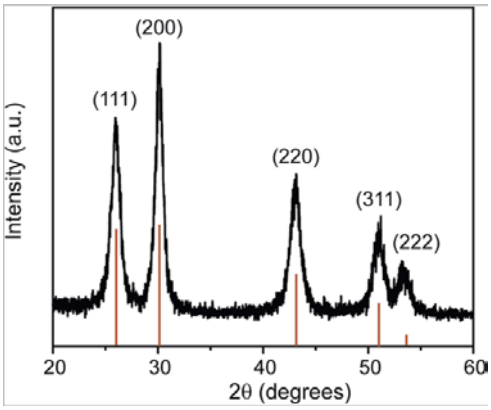

Figure 3.1: XRD pattern obtained from the precipitate formed after 3 h at 37 °C in a tris-HCl buffered aqueous solution (pH = 7.5) of lead acetate, L-cysteine and strain SMCD1. *Courtesy of Leah C. Spangler.*

Table 3.1: Comparison of different growth conditions for PbS QD formation. *Courtesy of Leah C. Spangler.*

Ingredient	Sample 1	Sample 2	Sample 3	Sample 4	Sample 5
SMCD1 (OD_{600})	0.5	0.5	0.5	0.5	-
$Pb(Ac)_2$ (mmol)	1	-	1	1	1
L-cysteine (mmol)	8	8	-	8	8
Growth media	Tris Buffer	Tris Buffer	Tris Buffer	DI water	Tris Buffer
Photographs of suspensions					

After centrifugation and cell withdrawal, the aqueous PbS nanocrystal solution exhibits a systematic red-shift in the photoluminescence peak with increasing incubation time, from 1040 nm after 15 min to 1135 nm after 95 min (Figure 3.2 (a)). However, the true maximum of the fluorescence peak is confused by the overlapping absorption profile of water (Figure 3.2 (a),

shown as a dotted line). Such interference of water plus the low concentration of PbS QDs present precluded us from obtaining the temporal evolution data of the corresponding absorbance spectra. Nevertheless, the red-shift of the peak luminescence positions with longer incubation time is still in accord with the expected gradual increase in the mean PbS particle size with increasing growth time.[1, 11-12] Despite our inability to pinpoint the absorbance maximum position to determine the direct band gap, calculating a band gap and thus nanocrystal size from the emission peak wavelengths of 1040 nm (1.2 eV) and 1135 nm (1.1 eV) gave us ballpark values of ~3.5 nm and ~4.0 nm for their respective maximum mean particle diameters.

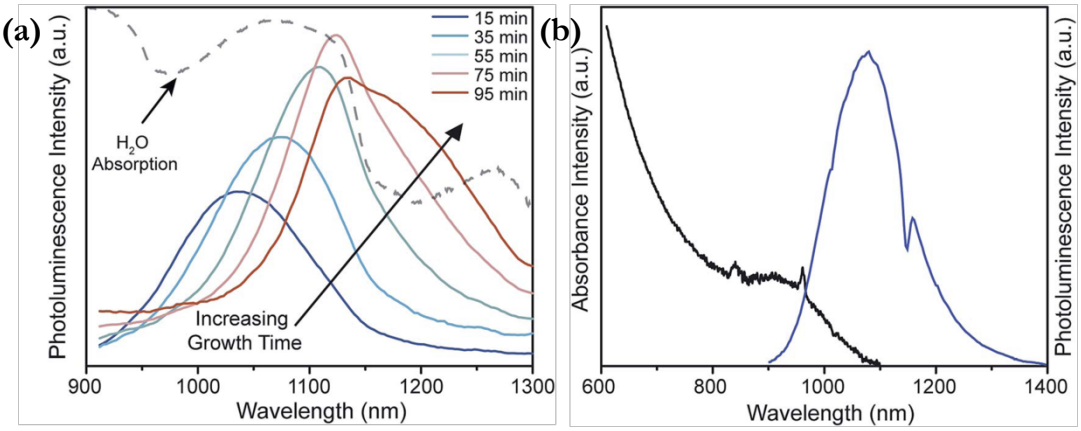

Figure 3.2: Optical spectra of biomineralized PbS nanocrystals. (a) Photoluminescence spectra of aqueous PbS nanocrystals as a function of incubation time at 18 °C. The dotted line indicates the expected absorption profile for water. (b) Absorbance (black curve) and corresponding photoluminescence (blue curve) spectra of PbS nanocrystals grown in the aqueous phase for 30 min followed by ligand and phase transfer into chloroform. The spikes in the absorbance spectrum at 820 and 980 nm are artifacts from the instrument detector switch and DDT ligands, respectively. The dip in the emission spectrum at 1150 nm is caused by an absorbance from chloroform. *Courtesy of Leah C. Spangler.*

Our biomineralized PbS nanocrystals were formed within 1 h, which is much faster than any previous reports of PbS biomineralization, which typically took 1-2 days at physiological temperature.[13-15] This is because these prior studies relied solely upon utilizing the natural

abundance of reactive sulfur generated in the cells in response to lead exposure. In our case, however, the enzyme actively catalyzes H_2S production from the excess L-cysteine, causing a much more rapid biomineralization response.

The nanocrystals after 30 min growth in the aqueous phase were phase transferred into chloroform with DDT as capping agent, so that the absorption spectra could be measured. The resultant absorption and photoluminescence spectra in the organic solution show maxima at 910 nm and 1080 nm, respectively (Figure 3.2 (b)), which are fully consistent with that expected for quantum confined PbS nanocrystals of ~3.0 nm in size.[1, 11-12] The full-width-at-half-maximum (FWHM) for the photoluminescence peak from our biomineralized PbS nanocrystals was determined to be 144 nm, close to the FWHM values in prior reports for bio-templated PbS QDs.[16-17] As a comparison, without any size-selective precipitation procedure, pure chemical synthesis of PbS QDs in the organic phase usually give a FWHM of ~100 nm.[18-19]

The PbS nanocrystals after phase transfer exhibited QY values that varied amongst synthesis batches from 16% to 45%, in agreement with the typical QY range of 20% to 80% for PbS QDs produced from chemically reactive precursors through traditional high temperature approaches.[12, 18-22] To date, the QY of 45% for our PbS nanocrystals is the highest ever reported for any biomineralized PbS QDs.

Electron microscopy examination of the PbS nanocrystals grown for 30 min revealed the formation of well crystalline particles with lattice spacings and intersection angles fitting well with rock salt PbS structure (Figure 3.3 (a-d), Table 3.2). The nanocrystals are somewhat irregularly shaped and typically around 4.0-4.5 nm in diameter, consistent with the PbS particle size inferred from the optical spectra of the same PbS nanocrystals (Figure 3.2 (b)). The presence

of Pb within an isolated particle was verified by detection of the Pb L_α and Pb L_β signals in XEDS analysis of an individual nanocrystal (Figure 3.3 (e)). Nevertheless, we could not unambiguously prove the existence of sulfur in the QD because the Pb M (2346 eV) and S K (2308 eV) peaks are too closely situated to be resolved using our XEDS spectrometer.

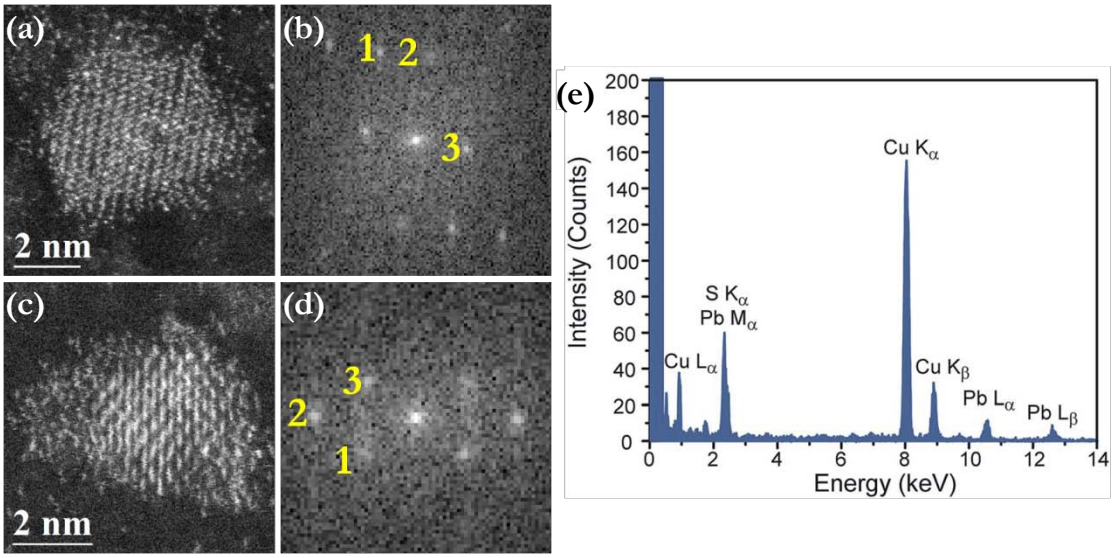

Figure 3.3: STEM characterization of biomineralized PbS nanocrystals. (a, c) HAADF-STEM images and (b, d) corresponding FFT diagrams of 4.5 nm and 4.0 nm PbS nanocrystals viewed along the $[1\bar{1}\bar{2}]$ and $[1\bar{1}0]$ projections respectively. (e) A representative XEDS spectrum acquired from a single biomineralized PbS nanocrystal.

Table 3.2: Lattice fringe analysis of the PbS nanocrystals shown in Figure 3.3 (a, c).

Rock salt PbS	Fig. 3.3 (a): $[1\bar{1}\bar{2}]$		Fig. 3.3 (c): $[1\bar{1}0]$	
	Measured	Matching	Measured	Matching
Plane 1	1.9 Å	1.8 Å (311)	3.5 Å	3.4 Å (111)
Plane 2	2.1 Å	2.1 Å (220)	2.1 Å	2.1 Å (220)
Plane 3	3.5 Å	3.4 Å $(1\bar{1}1)$	3.6 Å	3.4 Å $(11\bar{1})$
<1, 2>	32.2°	31.5°	36.0°	35.3°
<2, 3>	89.9°	90.0°	35.9°	35.3°
<3, 1>	57.9°	58.5°	71.9°	70.5°

Having established a parallelism between the biomineralization mechanism of PbS and CdS nanocrystals using SMCD1, we further sought to grow a thin CdS shell on the PbS core via a sequential biomineralization process. During the shell growth period, the photoluminescence maximum of the core-shell nanocrystals underwent a progressive blue-shift (Figure 3.4 (a)), consistent with the expected shift in optical properties engendered by the cumulative growth of a thin CdS shell onto the PbS core.[23-24] Shell biomineralization was induced by the residual smCSE enzyme alone, with no SMCD1 cells involved. The low enzyme concentration in the sequential growth phase allowed CdS mineralization to proceed in a slow, controllable rate so that only a thin CdS shell was deposited on the PbS core at the expense of a relatively long synthesis time.

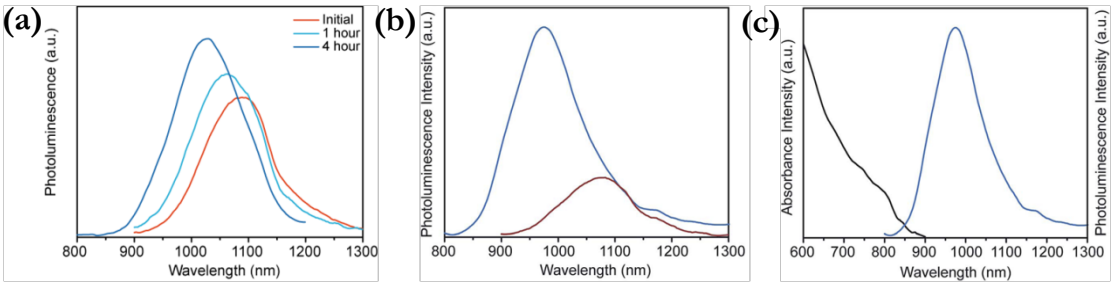

Figure 3.4: Optical spectra of biomineralized PbS-CdS core-shell nanocrystals. (a) Photoluminescence spectra of PbS-CdS core-shell nanocrystals as a function of shell growth time. (b) Photoluminescence spectra of biomineralized PbS (red curve) and PbS-CdS (blue curve) core-shell nanocrystals after 18 h incubation in the cadmium acetate solution. (c) Absorbance (black curve) and photoluminescence (blue curve) spectra of PbS-CdS core-shell nanocrystals after 18 h shell growth. The samples in (b) and (c) were phase transferred into chloroform. *Courtesy of Leah C. Spangler.*

Compared to the bare PbS nanocrystals, the core-shell nanocrystals after shell growth and then phase transferred exhibited a blue-shift in photoluminescence (Figure 3.4 (b)), characteristic of CdS shell growth on a PbS core.[21, 23, 25] The blue-shift of 100 nm suggests a 0.4 nm-thick CdSe shell,[26] which amounts to just one or two CdS monolayers. Similarly, the absorbance spectrum of the PbS-CdS core-shell nanocrystals was also blue-shifted relative to that of the

pure PbS nanocrystals (Figure 3.4 (c)), again indicating deposition of a thin CdS shell onto the PbS core. After shell coverage, the QY value dropped to 9%, which is probably attributable to the well-known quenching effect of the DDT capping agent on the luminescence of CdS QDs.[27]

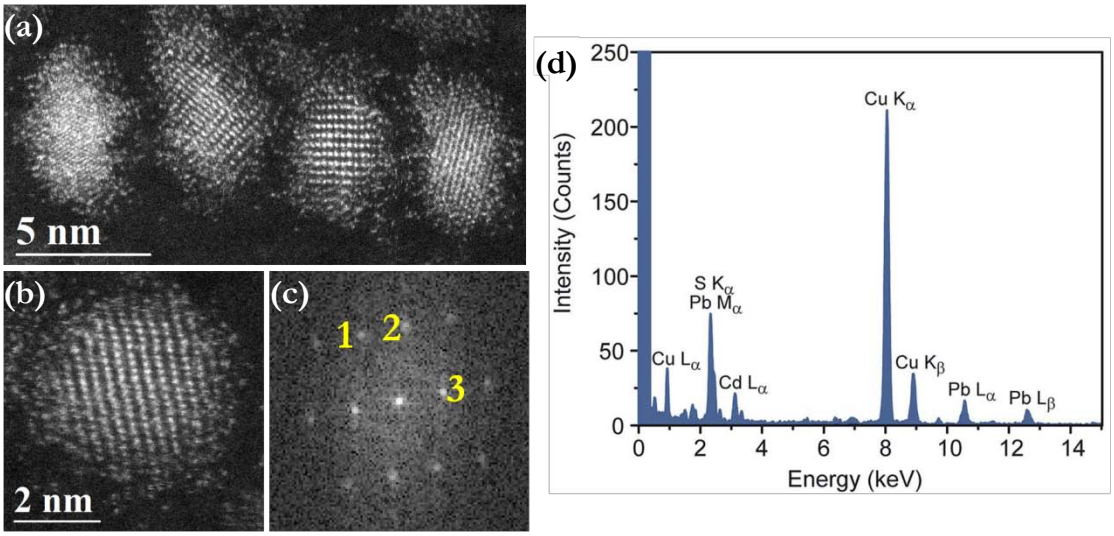

Figure 3.5: STEM characterization of biomineralized PbS-CdS core-shell nanocrystals. (a) HAADF-STEM image of several typical core-shell nanoparticles. (b) HAADF-STEM image and (c) corresponding FFT diagram from an individual core-shell morphology particle viewed along the [031] zone axis of rock salt PbS. (d) Representative XEDS spectrum collected from a single PbS-CdS core-shell nanocrystal.

Table 3.3: Lattice fringe analysis of the PbS-CdS core-shell nanocrystal shown in Figure 3.5 (b).

Rock salt PbS	Fig. 3.5 (b): [031]	
	Measured	Matching
Plane 1	1.8 Å	1.8 Å ($11\bar{3}$)
Plane 2	1.8 Å	1.8 Å ($1\bar{1}3$)
Plane 3	3.0 Å	3.0 Å (200)
<1, 2>	34.5°	35.1°
<2, 3>	73.7°	72.5°
<3, 1>	71.8°	72.5°

As revealed by HAADF-STEM imaging, the PbS-CdS nanocrystals have a well-defined

crystalline core and a somewhat more disordered shell (Figure 3.5 (a, b)), which is possibly related to the dissimilarity of the PbS and CdS crystal structures. The shell was found to be ~0.5 nm thick, close to that inferred from the blue-shift noted in Figure 3.4 (b). The interior regions of the PbS-CdS nanoparticles maintain their intrinsic crystalline nature and display lattice spacings and interplanar angles that match the rock salt structure of PbS (Figure 3.5 (b, c), Table 3.3). Compositional analysis of a single isolated nanoparticle demonstrates the co-existence of Pb and Cd in one particle, substantiating the formation of a PbS-CdS core-shell morphology. Efforts to perform XEDS line-scans on individual core-shell nanoparticles led to inconclusive elemental distributions, because of the small size of the particles and their electron beam sensitivity.

There are other possible explanations for the optical blue-shift that occurs upon addition of cadmium acetate. For example, a decrease of ~0.8 nm in PbS core diameter would theoretically cause a blue-shift of ~150 nm. Yet, this scenario is refuted by the consistent size of PbS seed particles before and after CdS growth as observed from the HAADF-STEM images (Figures 3.3 (a, c) and 3.5 (a, b)). Another hypothesis is the formation of a $Pb_{1-x}Cd_xS$ solid solution via interdiffusion of the two cations within a particle during synthesis. The rapid and progressive blue-shift during continuous incubation with cadmium acetate (Figure 3.4 (a)) suggests that such interdiffusion would need to occur very quickly in spite of the low synthesis temperature of 37 °C. As a reference, chemical synthesis of CdS shells on PbS nanocrystals carried out at significantly higher temperatures, can yield PbS-CdS core-shell heterostructured particles with no notable cation interdiffusion.[21, 23, 28-29] Therefore, the blue-shift in optical properties should be ascribed to the presence of PbS-CdS core-shell morphology rather than any size erosion of the PbS cores or by $Pb_{1-x}Cd_xS$ alloy formation.

While thicker shells (usually >2 nm) could be directly imaged[25, 30] or detected as slight peak shifts in XRD analysis,[23] proof for ultra-thin shells relies on observing optical shifts according to previous research.[31-32] In this regard, the possible role of the well-known cation exchange reaction[26, 33-36] in CdS shell growth cannot be completely ruled out. Pietryga *et al.*[34] noted a 50 nm blue-shift as a result of cation exchange between Pb and Cd in the organic phase at room temperature, which is in line with our data.

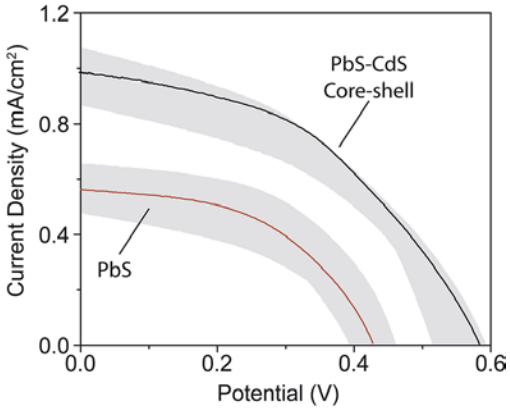

Figure 3.6: Current density as a function of cell potential of biomineralized PbS and PbS-CdS core-shell QD nanocrystal sensitized solar cells under AM 1.5 illumination. The shaded regions represent the reproducibility range achieved between four cells of each type. *Courtesy of Leah C. Spangler.*

Our biomineralized PbS and PbS-CdS core-shell QDs exhibit useful functional properties, as demonstrated by their successful incorporation into QD sensitized solar cell structures. The PbS-CdS core-shell QDs improved the open circuit potential (V_{OC}) to 0.59 V from 0.43 V measured from the PbS-only counterpart (Figure 3.6), which probably stemmed from passivation of PbS surface defects by CdS shell deposition. The V_{OC} values are entirely consistent with other reports for chemically prepared PbS-CdS core-shell QD sensitized solar cells.[24, 37-38]

3.3 $CuInS_2$, $(CuInZn)S_2$ and $CuInS_2$-ZnS core-shell

nanocrystals synthesized by smCSE

Herein, we have further explored the capability of the smCSE enzyme in biomineralizing non-toxic ternary and quaternary metal sulfide nanocrystals. Quantum confined $CuInS_2$, $(CuInZn)S_2$, and $CuInS_2$-ZnS core-shell nanocrystals have been successfully synthesized by the enzymatic turnover of L-cysteine to form reactive H_2S which then reacts with metal salts in solution. The biocompatibility of the enzyme-mineralized nanocrystals is illustrated by their use in the bioimaging of THP-1 leukemia cells.

3.3.1 Biomineralized $CuInS_2$ nanocrystals

Incubation of smCSE with a buffered solution of copper acetate and L-cysteine gave rise to the appearance of an absorbance peak, indicative of the formation of $Cu_{2-x}S$ nanocrystals (Figure 3.7 (a)). As described in Chapter 2 and Section 3.2 in this chapter, biomineralization takes place as L-cysteine is converted by smCSE to reactive H_2S, which then interacts with the metal salt in solution to produce the metal sulfide. This is comparable to the pure chemical approach towards aqueous phase sulfide mineralization wherein reactive Na_2S is used to catalyze mineralization of, for instance, $Cu_{2-x}S$.[39] The formation of nanoparticles rather than bulk materials is due to the presence of excess L-cysteine functioning as a capping agent,[40-41] and the templating ability of the smCSE enzyme itself. However, the corresponding fluorescence from this material was too low to be detected, which is commonly encountered with $Cu_{2-x}S$ nanocrystals. This could originate from surface oxidation of as-synthesized stoichiometric Cu_2S nanocrystals creating non-fluorescent Cu-deficient $Cu_{2-x}S$ QDs that promote exciton recombination.[42] Hence, little comparable fluorescence data is available from previous literature. To the best of our knowledge,

only two groups have published such data for $Cu_{2-x}S$ materials which were prepared under an inert atmosphere.[42-43]

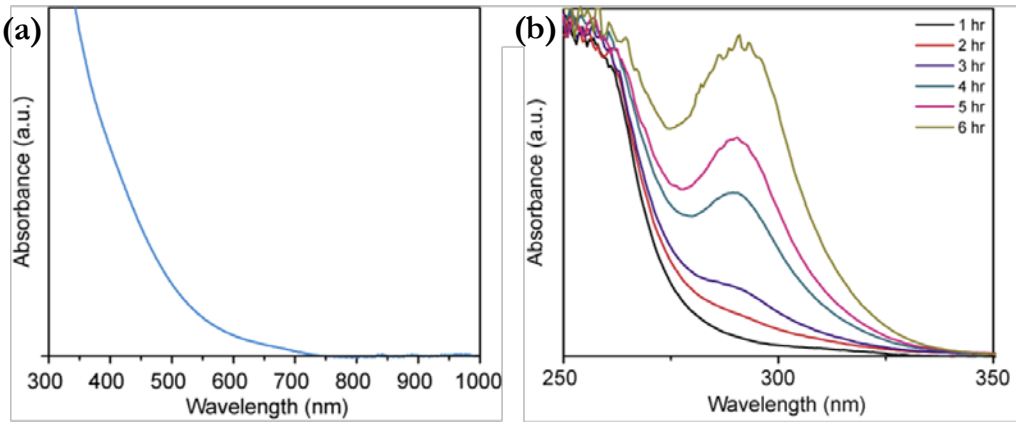

Figure 3.7: Absorbance spectra of (a) $Cu_{2-x}S$ nanoparticles and (b) In-S complex solutions as a function of time when synthesized by incubation of 0.1 mg mL^{-1} smCSE, 16 mL L-cysteine and 4 mM copper acetate or 2 mM indium nitrate, respectively. *Courtesy of Leah C. Spangler.*

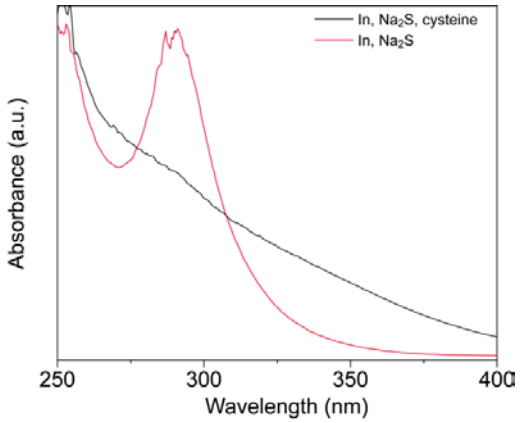

Figure 3.8: Absorbance spectra of a buffered solution of 4 mM indium nitrate, 8 mM Na_2S with 8 mM L-cysteine (red curve) and without L-cysteine (black curve). *Courtesy of Leah C. Spangler.*

Similar incubation of smCSE in a buffered solution of indium nitrate resulted in the emergence of an absorbance peak at 290 nm that intensified with increasing incubation time (Figure 3.7 (b)). A peak located at the same wavelength was visible when indium, Na_2S and L-cysteine were mixed (Figure 3.8). Yet the absence of L-cysteine led to the occurrence of a cloudy suspension with no strong peak at 290 nm (Figure 3.8), pointing to the formation of bulk

indium sulfide and indium hydroxide which would precipitate at neutral and basic pH.[44] The peak position at 290 nm agrees well with previous studies and is indicative of the presence of sub-nm molecular indium sulfide clusters.[45-48] The growth in absorbance peak intensity with synthesis time suggests an increasing concentration of these complexes. To lend additional support to this concept, the concentrations of L-cysteine and smCSE were doubled to 32 mM and 0.2 mg mL^{-1}, respectively, and the absorbance peak intensification was accelerated (Figure 3.9), indicating an increased production rate of the In-S clusters. Thus, while bulk solids precipitate during reaction with transition metals,[49] ultra-small soluble clusters are formed during reaction with indium.

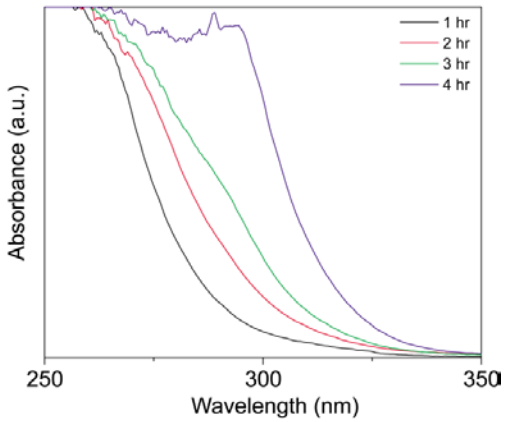

Figure 3.9: Absorbance spectra of a buffered solution of 4 mM indium nitrate, 0.2 mg mL^{-1} smCSE and 32 mM L-cysteine with different incubation times. *Courtesy of Leah C. Spangler.*

$CuInS_2$ nanocrystals were grown for 2-6 h at 37 °C in 0.1 mM tris-HCl buffer (pH = 7.5) containing 4 mM indium nitrate, 16 or 32 mM L-cysteine, and 0.1 or 0.2 mg mL^{-1} of smCSE. Upon the appearance of a 290 nm absorbance peak indicating the formation of sub-nm indium sulfide complexes, 2 mM copper acetate was introduced into the mixture, leading to an immediate solution color change to yellow, orange or red (Figure 3.10 (a)). This biomineralization strategy is slightly more complex than the straightforward direct biomineralization from buffered solutions of metal salt, cysteine and smCSE demonstrated for CdS and PbS nanocrystals

described previously, which will directly form a metal sulfide solid upon reaction with reactive sulfur. Both the solution color and absorption spectra (Figure 3.10 (b)) signify the formation of $CuInS_2$ nanocrystals, and compare well with previously reported data for $CuInS_2$ prepared via conventional chemical methods.[50-54] Consecutive addition of indium and copper precursors is essential to avoid the nucleation of a secondary population of $Cu_{2-x}S$ nanoparticles, as manifested by the modified absorbance peak shape and formation of a brown solution (Figure 3.11). A red-shift in the absorbance peak of the $CuInS_2$ nanocrystal suspension was observed with longer incubation time and higher L-cysteine concentration (Figure 3.10 (b)), corresponding to an increase in particle size with increasing In-S cluster concentration. The band gap values of these solutions was determined using a Tauc plot and ranged from 2.35 to 1.93 eV (Table 3.4), demonstrating the expected production of quantum confined nanocrystals of $CuInS_2$, which in bulk form would have a band gap of 1.53 eV.[55]

These $CuInS_2$ QDs give low fluorescence (Figure 3.10 (c)), probably suppressed due to the presence of surface defect sites induced by the mild synthesis conditions at low temperature in the aqueous phase.[7] For nanocrystals prepared with 16 mM L-cysteine, photoluminescence maxima were obfuscated by characteristic emission from the enzyme. Nonetheless, a small shoulder could still be recognized at ~600 nm for the sample with a 4 h indium incubation (Figure 3.10 (c)). Solutions starting with 32 mM L-cysteine show a peak shift in photoluminescence from 615 nm at 2 h to 650 nm at 4 h indium incubation, while further incubation for another 2 h caused no further shift of the emission peak but attenuated its intensity, evidencing saturation of In-S clusters after 4 h indium incubation which prevented further nanocrystal growth.

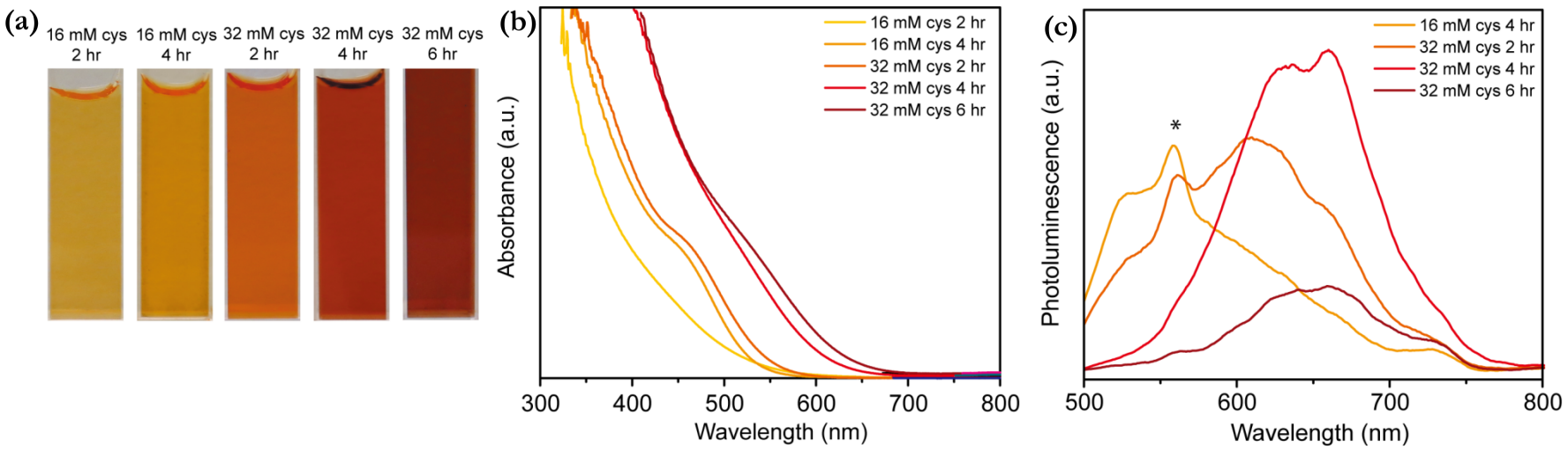

Figure 3.10: Optical properties of solutions upon addition of 2 mM copper acetate to solutions of smCSE, L-cysteine and indium nitrate previously incubated for the time period indicated and with the specified L-cysteine precursor concentrations. (a) Photographs of solutions. (b) Corresponding absorbance and (c) photoluminescence spectra of the solutions. * in (c) denotes the Raman peak for water which is not part of the QD fluorescence. *Courtesy of Leah C. Spangler.*

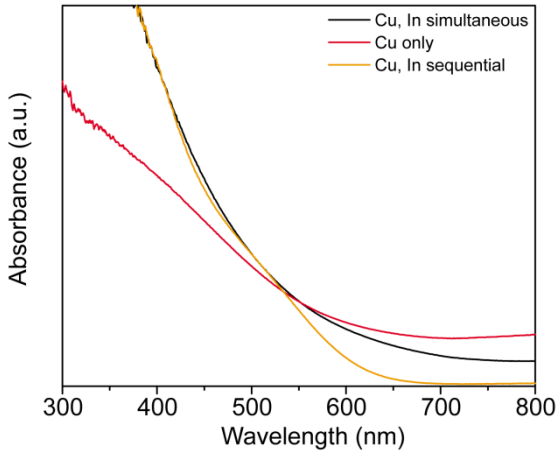

Figure 3.11: Absorbance spectra from a buffered solution of 0.2 mg mL^{-1} smCSE and 32 mM L-cysteine with copper and indium precursors incubated together, compared to solutions incubated with only copper or pre-incubated with indium for 2 h before adding copper. *Courtesy of Leah C. Spangler.*

Table 3.4: Calculated band gap values from Tauc plot analysis for the various sols shown in Figure 3.10. *Courtesy of Leah C. Spangler.*

Sample	Band gap (eV)
16 mM cys 2 h	2.35
16 mM cys 4 h	2.33
32 mM cys 2 h	2.26
32 mM cys 4 h	2.04
32 mM cys 6 h	1.93

It has been reported before[56-58] that relative compositional variations of Cu and In could shift the optical spectra of $CuInS_2$ QDs. For $CuInS_2$ solutions synthesized with 16 mM L-cysteine after 4 h indium incubation, the Cu/In atomic ratio as determined from quantitative XEDS-SEM analysis using ZAF correction was 1.60 ± 0.09; when 32 mM L-cysteine was used with indium incubation for 4 or 6 h, the Cu/In atomic ratios were 0.70 ± 0.04 and 0.60 ± 0.04, respectively. The higher Cu/In ratio associated with the 16 mM L-cysteine sample is in line with expectations as a smaller amount of L-cysteine would reduce the population of In-S complexes

(Figures 3.7 (b) and 3.9).

When more In-S complexes are formed, the $CuInS_2$ nanocrystals become Cu-deficient. Typically, such Cu-deficient $CuInS_2$ nanocrystals are expected to have a higher band gap relative to their stoichiometric counterpart,[59] but our nanocrystal solutions with 32 mM L-cysteine continued to shift towards a longer wavelength in absorbance as compared to the 16 mM L-cysteine sample. This seeming discrepancy could be caused by competing quantum confinement effects emanating from particle size variations.[53, 60]

Phase contrast imaging of the $CuInS_2$ QDs from the 32 mM L-cysteine sample after 4 h indium incubation reveals well dispersed nanocrystals with diameters of ~2.5 nm (Figure 3.12 (a, b)), corresponding to an expected photoluminescence peak at ~650 nm when referring to prior reports for chemically prepared $CuInS_2$ nanocrystals with a Cu/In atomic ratio of 0.7.[52] As anticipated, our nanocrystals had blue-shifted optical properties in comparison to chemically synthesized stoichiometric $CuInS_2$ nanocrystals with a mean diameter of 2.7 nm, which display a fluorescence peak at ~700 nm.[60] The nanocrystal in Figure 3.12 (b) could be indexed to the $[10\bar{3}]$ zone axis of tetragonal chalcopyrite $CuInS_2$ by analyzing the corresponding FFT diagram (Figure 3.12 (c), Table 3.5). Furthermore XEDS-STEM analysis verifies the presence of Cu, In and S within a single nanoparticle (Figure 3.12 (d)).

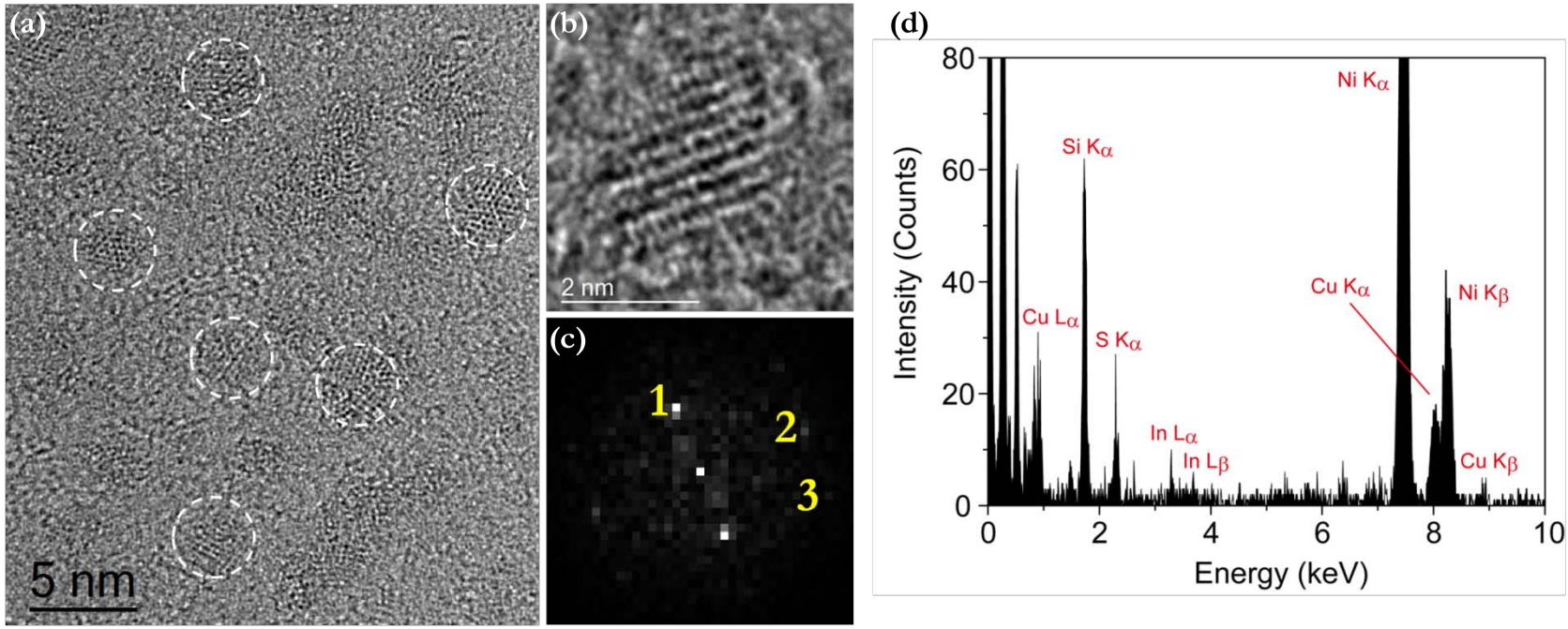

Figure 3.12: Electron microscopy characterization of $CuInS_2$ nanocrystals with 32 mM L-cysteine in incubation for 4 h. (a) HR-TEM image showing a number of $CuInS_2$ nanocrystals (marked by dashed circles) with diameters of ~2.5 nm. (b) Representative HR-TEM image of a $CuInS_2$ nanocrystal. (c) The FFT diagram of the particle in (b). (d) XEDS-STEM analysis of a single nanocrystal.

Table 3.5: Lattice fringe analysis of the $CuInS_2$ nanocrystal shown in Figure 3.12 (b).

Chalcopyrite $CuInS_2$	Fig. 3.12 (b): $[10\bar{3}]$	
	Measured	Matching
Plane 1	2.9 Å	2.8 Å (020)
Plane 2	1.7 Å	1.8 Å (301)
Plane 3	1.5 Å	1.5 Å (321)
<1, 2>	89.1°	90.9°
<2, 3>	31.6°	33.3°
<3, 1>	57.5°	56.7°

3.3.2 Biomineralized core-shell $CuInS_2$-ZnS and $(CuInZn)S_2$ nanocrystals

Enhanced photoluminescence has been previously observed upon growth of a ZnS shell onto $CuInS_2$ QDs.[59, 61-62] Incubation of smCSE in a buffered solution containing zinc acetate and L-cysteine led to an absorption peak at 280 nm (Figure 3.13), implying the generation of ZnS nanoparticles.[63-65] Accordingly we adapted our previously demonstrated protocol to incubate pre-formed $CuInS_2$ core nanoparticles in the presence of zinc acetate, L-cysteine and smCSE in a buffered solution. Although the peak positions in the resultant absorbance spectrum remained relatively unchanged except at the longest growth time, the photoluminescence performance improved remarkably over time (Figure 3.14). A small blue-shift in photoluminescence is discernible with respect to the $CuInS_2$ core nanocrystals, suggesting the overcoating of a ZnS shell. While core-shell QDs usually red-shift the optical spectra from the original core materials, a blue-shift with $CuInS_2$-ZnS core-shell nanocrystals has been previously noted by many groups and was considered to be the result of an etching effect which slightly reduced the $CuInS_2$ core

size during shell growth.[60, 66]

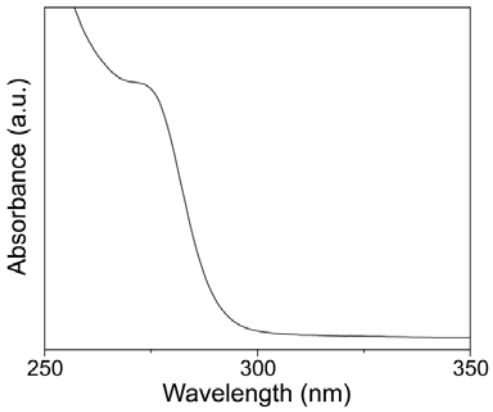

Figure 3.13: Absorbance spectrum of a buffered solution of 1 mM zinc acetate, 8 mM L-cysteine, and 0.05 mg mL^{-1} smCSE, showing an absorbance peak at 280 nm. *Courtesy of Leah C. Spangler.*

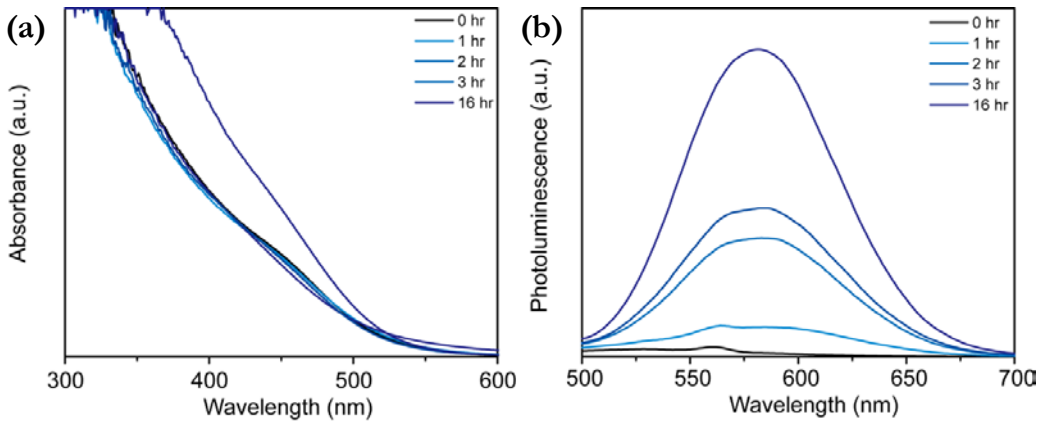

Figure 3.14: Absorbance (a) and photoluminescence (b) spectra of $CuInS_2$-ZnS core-shell nanocrystals grown with increasing incubation time at room temperature. *Courtesy of Leah C. Spangler.*

Well dispersed nanocrystals were present in the $CuInS_2$-ZnS core-shell sample, as revealed by HR-TEM imaging (Figure 3.15 (a-c)). The particles were ~4.0 nm in diameter, larger than the typical corresponding core $CuInS_2$ nanocrystals (Figure 3.12 (a, b)), corroborating the concept of shell coverage on the original $CuInS_2$ nanocrystals. Based on analysis of the FFT data from HR-TEM images (Figure 3.15 (b-e), Table 3.6), we could confirm the existence of tetragonal chalcopyrite $CuInS_2$ as the core. The $CuInS_2$ cores of these nanocrystals should be approximately

2.0-2.5 nm in size, as derived from the measured photoluminescence maxima of 630 nm.[3, 60] Assuming no intermixing between the core and shell materials, the increase in overall size of the observed nanocrystals indicates the deposition of a ~0.75 nm thick ZnS shell onto a ~2.5 nm diameter core. Given the lattice constant of 0.58 nm for zinc-blende ZnS, the shell thickness corresponds to ~1.5 monolayers. The growth of such an epitaxial shell is in accord with previous literature on chemically synthesized $CuInS_2$-ZnS core-shell nanoparticles,[66-67] and is expected for this system because of the small lattice mismatch (< 2%) between chalcopyrite $CuInS_2$ and zinc-blende ZnS.[68] Characteristic X-ray signals for Cu, In, Zn and S were all detected within an individual particle by XEDS-STEM (Figure 3.15 (f)), confirming the presence of all the constituent elements expected for a core-shell nanocrystal. However, a contrast difference between the core and shell regions was not readily distinguishable by either HR-TEM or HAADF-STEM imaging.

For the $CuInS_2$-ZnS core-shell nanocrystals, the average Cu/In atomic ratio was found to be 1.46 ± 0.18 and the Zn/In ratio was 2.30 ± 0.29, determined by a quantitative XEDS-SEM survey over several hundred particles. The higher Cu/In ratio compared to the original core sample (0.70 ± 0.04) could be ascribed to preferential substitution of zinc for indium cations in the crystal lattice, as no extra copper was introduced during ZnS shell growth. Such a phenomenon of lowered indium content in $CuInS_2$-ZnS core-shell nanocrystals has been previously observed in an aerobic, aqueous phase synthesized system in which the starting $CuInS_2$ core QDs had Cu/In atomic ratios less than unity.[7]

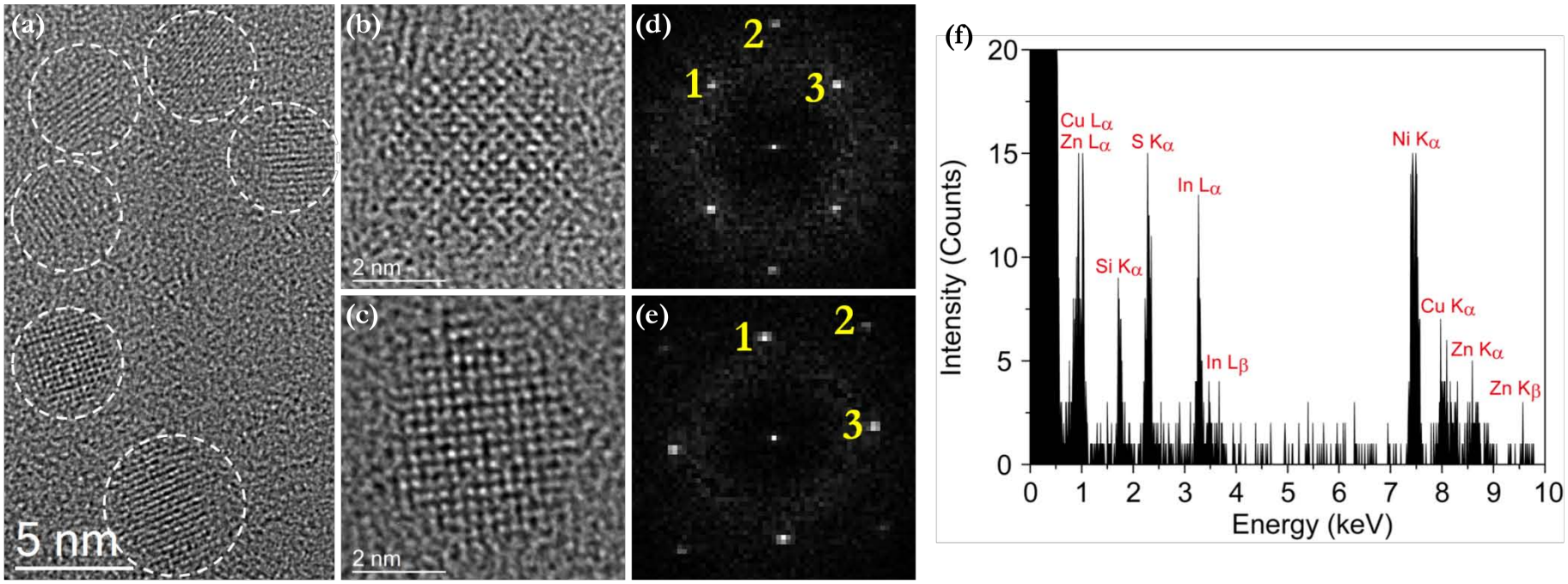

Figure 3.15: Electron microscopy characterization of $CuInS_2$-ZnS core-shell nanocrystals prepared from core $CuInS_2$ formed after 4 h pre-incubation of 32 mM L-cysteine, 4 mM indium nitrate and 0.2 mg mL^{-1} smCSE, followed by 12 h incubation with zinc acetate. (a) HR-TEM image showing a number of $CuInS_2$-ZnS core-shell nanocrystals (marked by dashed circles) with diameters of ~4.0 nm. (b, c) Representative HR-TEM images of $CuInS_2$-ZnS nanocrystals. (d, e) Corresponding FFT diagrams of the particle in (b) and (c), respectively. (f) XEDS-STEM analysis of a single nanocrystal.

Table 3.6: Lattice fringe analysis of the $CuInS_2$-ZnS core-shell nanocrystals shown in Figure 3.15 (b, c).

Chalcopyrite $CuInS_2$	Fig. 3.15 (b): [001]		Fig. 3.15 (c): [001]	
	Measured	Matching	Measured	Matching
Plane 1	2.8 Å	2.8 Å (200)	2.8 Å	2.8 Å (200)
Plane 2	2.0 Å	2.0 Å (220)	2.0 Å	2.0 Å (220)
Plane 3	2.8 Å	2.8 Å (020)	2.8 Å	2.8 Å (020)
<1, 2>	45.6°	45.0°	44.4°	45.0°
<2, 3>	44.7°	45.0°	44.4°	45.0°
<3, 1>	89.6°	90.0°	88.8°	90.0°

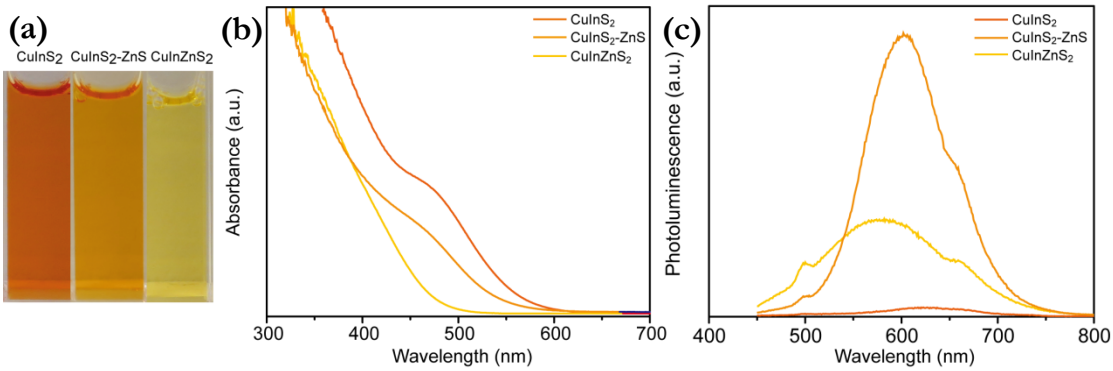

Figure 3.16: Optical properties of solutions of the original $CuInS_2$, core-shell $CuInS_2$-ZnS and $(CuInZn)S_2$ nanocrystals. (a) Light images. (b) Absorbance spectra. (c) Fluorescence spectra. *Courtesy of Leah C. Spangler.*

The fabrication of mixed quaternary $(CuInZn)S_2$ alloy nanocrystals is also of interest because of their potential of enhanced photoluminescence properties over $CuInS_2$ nanocrystals.[69-71] The capability of smCSE to biomineralize a quaternary alloy was assessed by concurrent addition of 4 mM zinc acetate and 2 mM copper acetate to a solution of 4 mM indium nitrate, 32 mM L-cysteine, and 0.2 mg mL^{-1} smCSE which had been subjected to 4 h incubation. The resultant solution had a more yellowish coloration compared to solutions of the

original $CuInS_2$ and core-shell $CuInS_2$-ZnS nanocrystals (Figure 3.16 (a)). Blue-shifts are visible in both the absorbance and fluorescence peaks of the $(CuInZn)_2S$ material when compared to the $CuInS_2$ nanocrystals mineralized from the same In-S complex solution (Figure 3.16 (b, c)), which is consistent with the expected optical properties for quaternary alloy QDs.[71-72] In addition, the fluorescence was significantly enhanced after Zn alloying, but still could not reach the level achieved by the core-shell QDs (Figure 3.16 (c)). The differing optical properties between the quaternary alloy and core-shell nanocrystals provides indirect evidence that adding zinc and copper together effectively produces an intimately mixed quaternary alloy, while adding zinc after the formation of $CuInS_2$ nanocrystals creates a more core-shell type heterostructure.

The $(CuInZn)_2S$ nanocrystals were ~5 nm in size and had higher shape irregularity than either the $CuInS_2$ or $CuInS_2$-ZnS core-shell nanocrystals (Figure 3.17 (a)). Its fluorescence peak at 575 nm is blue-shifted compared to other reports for 4-5 nm $(CuInZn)_2S$ QDs with a nominal 1:1:1 stoichiometry of Cu:In:Zn cations. Yet the cationic ratio measured by XEDS-SEM was 1.84 $\pm$ 0.13 for Cu/In and 2.07 $\pm$ 0.14 for Cu/Zn, similar to the case of the $CuInS_2$-ZnS core-shell nanocrystals wherein the Cu/In ratio increased markedly upon incorporation of zinc into the $CuInS_2$ nanocrystal system. Quaternary alloy $(CuInZn)_2S$ nanocrystals with a low indium content relative to zinc have been reported to induce a significant optical blue-shift.[69] In this instance, the low indium content paired with high zinc content might dominate the determination of the optical properties as opposed to the size quantization effect. As for the $CuInS_2$ and core-shell nanocrystals, the $(CuInZn)_2S$ QDs again exhibit a chalcopyrite structure analogous to $CuInS_2$ (Figure 3.17 (a, b), Table 3.7). The alloying of Cu, In, Zn and S within individual nanoparticles has been verified by XEDS-STEM analysis from a single nanocrystal (Figure 3.17 (c)).

Furthermore, no separate nucleation of $Cu_{2-x}S$, In_2S_3 or ZnS particles was discovered from XEDS analysis.

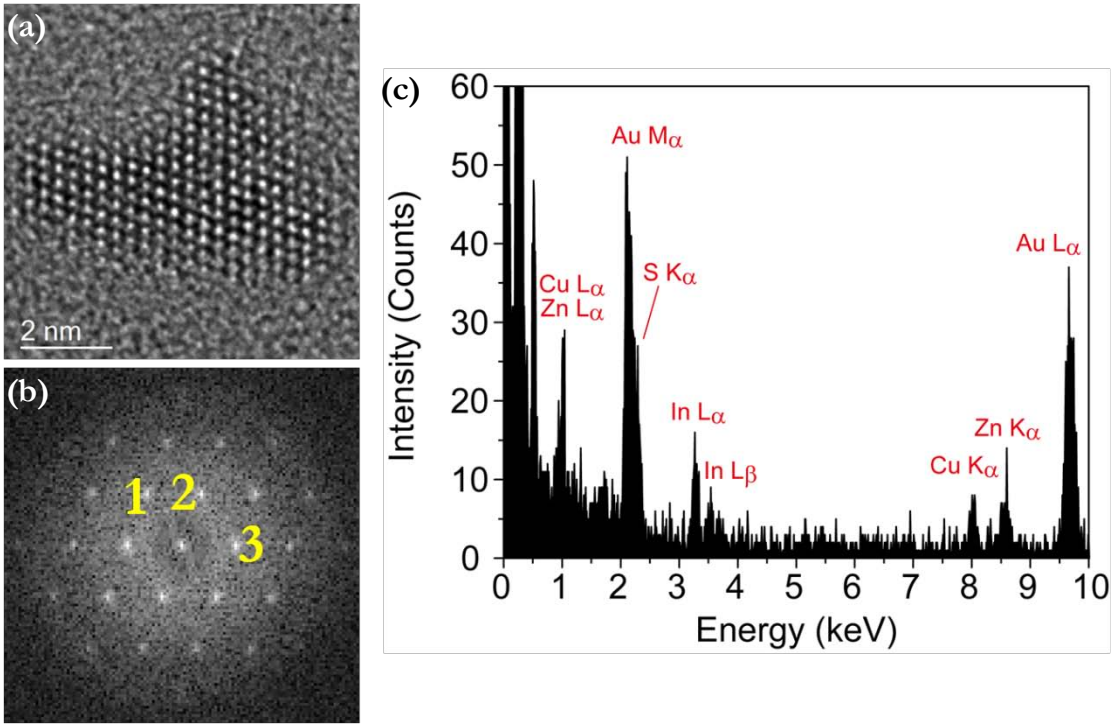

Figure 3.17: Electron microscopy characterization of quaternary alloy $(CuInZn)_2S$ nanocrystals. (a) HR-TEM image of a representative 5 nm particle. (b) The corresponding FFT diagram of (a). (c) Representative XEDS-STEM spectrum from a single nanocrystal.

Table 3.7: Lattice fringe analysis of the $(CuInZn)_2S$ nanocrystal shown in Figure 3.17 (a).

Chalcopyrite $CuInS_2$	Fig. 3.12 (b): $[02\bar{1}]$	
	Measured	Matching
Plane 1	2.8 Å	2.8 Å (200)
Plane 2	3.1 Å	3.2 Å (112)
Plane 3	3.2 Å	3.2 Å $(1\bar{1}\bar{2})$
<1, 2>	54.5°	54.6°
<2, 3>	69.4°	70.7°
<3, 1>	56.1°	54.6°

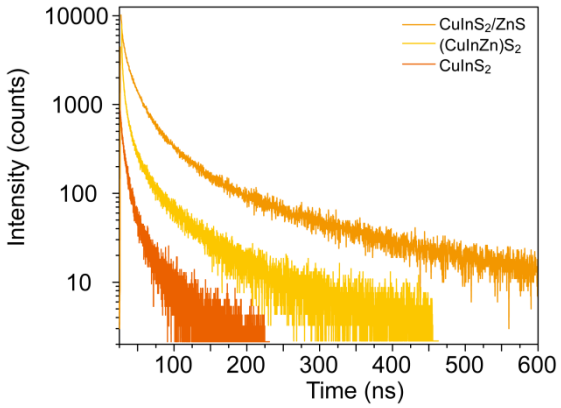

Figure 3.18: Time-resolved photoluminescence decay curves for $CuInS_2$ core-only nanocrystals, $(CuInZn)_2S$ quaternary alloy nanocrystals and $CuInS_2$-ZnS core-shell nanocrystals. *Courtesy of Leah C. Spangler.*

Photoluminescence lifetime measurements were conducted to further investigate core-shell and quaternary alloy formation. Typically $CuInS_2$ particles display two decay lifetimes: a short lifetime of ~10-50 ns and a longer lifetime of ~100-500 ns, assigned to non-radiative and radiative decay processes, respectively.[50, 73] However, because of the poor fluorescence characteristics of our $CuInS_2$ core-only nanocrystals, shorter overall lifetimes of 2.4 ns and 13.9 ns were obtained for these two processes. The quaternary alloy sample extended both lifetimes moderately to 2.8 ns and 31 ns, respectively, probably attributable to slight passivation of donor defects within the crystal lattice.[71] In contrast, the $CuInS_2$-ZnS core-shell material exhibited considerably longer lifetime values of 9.4 ns and 74.5 ns respectively, consistent with the expected surface passivation upon shell coverage of the core nanocrystals.[73]

The broad emission and relatively short photoluminescence lifetimes of $CuInS_2$ and $(CuInZn)S_2$ nanocrystals most likely arise from an abundance of intrinsic defects, although the exact decay mechanism is still the subject of much debate.[50] This leads to relatively large FWHM of ~300 meV, even with size selective precipitation, and a large Stokes shift of ~450 meV.[53, 73-74] Our aqueous phase, room temperature biosynthesized nanocrystals give similar FWHM values of

300, 590 and 430 meV, and Stokes shifts of 400, 300 and 650 meV, for the $CuInS_2$, $(CuInZn)S_2$ and $CuInS_2$-ZnS particle variants respectively. In addition, our Stokes shift values are slightly higher than those reported for analogous chemically prepared materials. For instance, a Stokes shift of ~400 meV has been measured for $CuInS_2$-ZnS QDs produced via a chemical route in the aqueous solution at 95 °C.[7] The FWHM value for the biomineralized quaternary alloy particles is significantly higher as a possible result of their irregular shapes.[69]

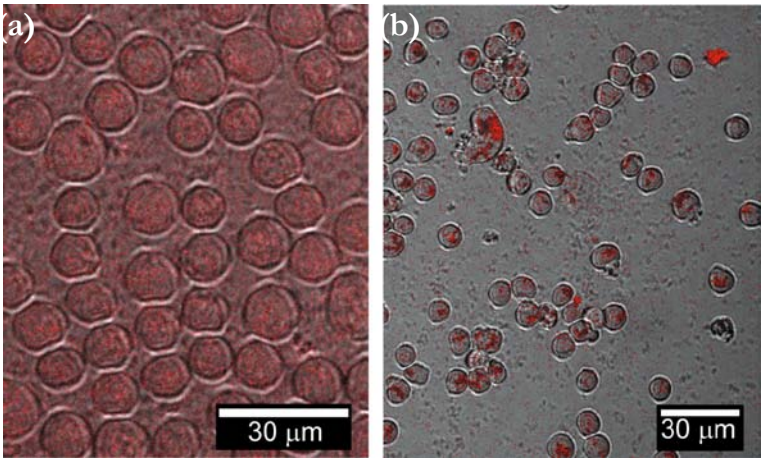

Figure 3.19: Light optical confocal microscopy images of THP-1 cells incubated in solution with $CuInS_2$-ZnS QDs with or without IgG antibody tagging. (a) No IgG antibody tagging. (b) With IgG antibody tagging. The red coloration corresponds to QD fluorescence, and is only site specific when the IgG antibody on the THP-1 leukemia cells are conjugated to the $CuInS_2$-ZnS nanocrystals. *Courtesy of Leah C. Spangler.*

To exploit the potential of our biomineralized $CuInS_2$-ZnS core-shell nanocrystals in bio-labeling, the as-prepared QDs were conjugated to IgG antibodies using EDC/NHS cross-linkers, which then bound to the epidermal growth factor receptor (EGFR) of the THP-1 leukemia cells. Confocal microscopy imaging of THP-1 cells incubated with $CuInS_2$-ZnS nanocrystals without IgG antibody tagging shows an evenly distributed fluorescence pattern, pointing to lack of site specificity in fluorescence inside the cells (Figure 3.19 (a)). This indicates that the $CuInS_2$-ZnS nanocrystals did not enter the cells via already existent endocytosis or

phagocytosis pathways, as opposed to prior reports for small nanocrystals.[75-76] However, when $CuInS_2$-ZnS nanocrystals were tagged with IgG and incubated for 1 h followed by removal of unbound QDs through washing twice, the fluorescence from confocal microscopy became localized to patches on the cell surfaces (Figure 3.19 (b)). A similar pattern of EGFR clustering at cell walls has been described before owing to dimer-dependent activation of EGFR.[77-78] To study the toxicity of the nanocrystals, a Trypan blue assay was employed to determine the percentage of dead THP-1 cells after incubation with the $CuInS_2$-ZnS QD solution. Over a duration of 6 h, the cells maintained a high survival rate averaged at 95.5% ± 2.6%, suggesting little or no toxic effect of the QDs on the target THP-1 cells.

Bioimaging applications generally require stable, aqueous phase nanocrystals that can be functionalized with a biological marker such as an antibody. Whereas $CuInS_2$ and $(CuInZn)S_2$ nanocrystals are usually chemically prepared utilizing organic solvents, they then need to be transferred into water through ligand exchange, or more commonly, encapsulation in a polymer shell.[66] Yet the QY is typically lowered after phase transfer,[66-67] and ligand exchange also negatively affects QD stability.[79] Polymer encapsulation would inevitably give rise to much larger nanocrystals than the initial nominal size.[80] In contrast, our biomineralized nanocrystals are produced in biological relevant aqueous buffers, and have high stability while still retaining an ultra-small size. With no additional processing steps required post synthesis, they could be conjugated to antibodies directly from the synthesis solution posing no detrimental effect on cell-surface binding properties.

3.4 Summary and Outlook

In this chapter, biomineralization of metal sulfide nanocrystals other than CdS has been achieved, and the optical and structural properties of the resultant QDs have been evaluated and correlated in detail. The smCSE enzyme exhibited its efficacy of both inducing and templating the growth of PbS, core-shell PbS-CdS, $CuInS_2$, $(CuInZn)S_2$ and core-shell $CuInS_2$-ZnS nanocrystals in the aqueous solution at low temperatures, with L-cysteine playing a dual role of capping agent and sulfur source.

Analogous to the cell-induced biomineralization of CdS QDs, simple PbS QDs could also be mineralized by the SMCD1 strain. Persistent particle growth after cell removal reflected the catalyzing ability of the secreted enzyme cystathionine γ-lyase. Growth time and temperature proved to be useful parameters in enabling nanocrystal size control. Mineralization of a thin CdS shell onto the PbS core yielded blue-shifts in both absorbance and photoluminescence spectra. Electron microscopy analysis confirmed that both the original PbS nanocrystals and the PbS cores in the core-shell material possessed the expected rock salt structure of PbS, and that the sizes of the two types of nanocrystals were both well within the strong quantum confinement regime. Compositional analysis using XEDS-STEM verified the coexistence of Pb and Cd within individual nanoparticles, supporting the notion that a core-shell morphology had been created. After shell growth, the nanocrystals also demonstrated a higher open circuit potential in comparison to the initial PbS nanocrystals when used in QD sensitized solar cells, indicating successful passivation of the PbS surface.

The work on the associated $CuInS_2$-based nanocrystals exemplified the ability of this single enzyme to manage more complex metal sulfide QD biomineralization. A two-step nucleation process was adopted; the first step generates soluble In-S clusters stabilized by L-cysteine, while

the second step immediately mineralize $CuInS_2$ or $(CuInZn)S_2$ nanocrystals upon addition of the respective non-indium precursor(s). Subsequent ZnS shell growth was also driven by smCSE after the introduction of zinc acetate to the preformed $CuInS_2$ QDs, which gave rise to significantly improved photoluminescence properties. The presence of the expected chalcopyrite structured nanocrystals in the $CuInS_2$, $(CuInZn)S_2$, and $CuInS_2$-ZnS core-shell samples was all proven via lattice fringe analysis of nanocrystals in HR-TEM images. Individual nanoparticles from the three $CuInS_2$-based materials contained all the necessary constituent elements, as revealed by XEDS-STEM analysis of single nanocrystals. Quantitative elemental analysis from XEDS-SEM using ZAF correction showed that after zinc incorporation in both the core-shell and quaternary alloy cases, the optical spectra blue-shifted and the Cu/In cationic ratio increases markedly, suggesting preferential substitution of zinc for indium which lowered the indium content considerably. The excellent biocompatibility of our biomineralized $CuInS_2$-ZnS core-shell nanocrystals was showcased through specific tagging of EFGR receptors on THP-1 leukemia cells after conjugation to an IgG antibody. The toxicity of our nanocrystals was quite low as a high survival rate for the cells was achieved.

We might further advance our understanding of the current metal sulfide systems via the following additional studies:

(1) For both the PbS-based and $CuInS_2$-based nanocrystal systems, a more comprehensive correlation of particle size and optical properties could be established if we were to carry out representative particle size distribution measurements of the different types of nanocrystals present, with the help of high resolution electron microscopy. Such measurements have been attempted but were impeded by insufficient numbers of well-defined nanocrystals collected

either due to massive particle overlap or the presence of residual precursors. Thus, better nanocrystal purification and dispersion can help to obtain good statistics for the size distribution.

(2) Quantitative XEDS-SEM analysis was conducted on the three $CuInS_2$-based samples showing different cationic ratios among the variants. However, the cationic ratios given by XEDS-SEM was global information of the samples and did not probe compositions at the individual particle level. One might therefore consider employing quantitative XEDS-STEM analysis from numerous individual particles in order to determine the cationic ratios within single nanocrystals. As mentioned above, this would require the preparation of purer, better dispersed nanocrystal samples. In this case, local compositional variations from particle-to-particle could be quantified and such single particle cationic ratios might aid in developing a deeper understanding of the respective growth mechanisms for the quaternary alloy and core-shell nanocrystals.

(3) Despite the fact that the quaternary alloy $(CuInZn)S_2$ and $CuInS_2$-ZnS core-shell nanocrystals displayed distinct optical properties which supported our deduction that they had very different elemental distribution within the particles, direct evidence for the core-shell structure is still missing, probably due to the small size of the QDs leading to insufficient amounts of X-ray signals from XEDS. Thus, it would be desirable for us to generate a thicker shell and if possible a larger core by raising the precursor concentration and/or extending incubation time, so that we might be able to perform more detailed XEDS-STEM analysis of the elemental distribution within single particles using either elemental mapping or X-ray linescans.

3.5 Acknowledgements

This part of work in Chapter 3 is in collaboration with the Biomineralization group led by Prof.

Steven McIntosh and Prof. Bryan W. Berger in the Department of Chemical Engineering at Lehigh University. Their guidance and advice is gratefully acknowledged.

The QD preparation, optical property measurements, solar cell production and XEDS-SEM analysis reported in Chapter 3 were carried out by Leah Spangler. Evan Koufus from the Brown lab was responsible for culturing THP-1 cells, helping plan the cell tagging experiments, and performing confocal microscopy. Their various contributions are much appreciated and fully acknowledged. The work described in Section 3.2 has been published in *Journal of Materials Chemistry A*[81], and the work in Section 3.3 has been published in *Nanoscale*[82].

3.6 References

1. Wise, F. W., Lead salt quantum dots: the limit of strong quantum confinement. *Acc. Chem. Res.* **2000**, 33, 773-780.

2. de Mello Donegά, C.; Liljeroth, P.; Vanmaekelbergh, D., Physicochemical evaluation of the hot‐injection method, a synthesis route for monodisperse nanocrystals. *Small* **2005**, 1, 1152-1162.

3. Liu, S.; Zhang, H.; Qiao, Y.; Su, X., One-pot synthesis of ternary $CuInS_2$ quantum dots with near-infrared fluorescence in aqueous solution. *RSC Adv.* **2012**, 2, 819-825.

4. Arshad, A.; Chen, H.; Bai, X.; Xu, S.; Wang, L., One-pot aqueous synthesis of highly biocompatible near infrared $CuInS_2$ quantum dots for target cell imaging. *Chin. J. Chem* . **2016**, 34, 576-582.

5. Gao, X.; Liu, Z.; Lin, Z.; Su, X., $CuInS_2$ quantum dots/poly(L-glutamic acid)–drug conjugates for drug delivery and cell imaging. *Analyst* **2014**, 139, 831-836.

6. Xiong, W.-W.; Yang, G.-H.; Wu, X.-C.; Zhu, J.-J., Aqueous synthesis of color-tunable $CuInS_2$/ZnS nanocrystals for the detection of human interleukin 6. *ACS Appl. Mater. Interfaces* **2013**, 5, 8210-8216.

7. Chen, Y.; Li, S.; Huang, L.; Pan, D., Green and facile synthesis of water-soluble Cu–In–S/ZnS core/shell quantum dots. *Inorg. Chem.* **2013**, 52, 7819-7821.

8. Gaponik, N.; Talapin, D. V.; Rogach, A. L.; Eychmüller, A.; Weller, H., Efficient phase transfer of luminescent thiol-capped nanocrystals: from water to nonpolar organic solvents. *Nano Lett.* **2002**, 2, 803-806.

9. van Veggel, F. C. J. M., Near-infrared quantum dots and their delicate synthesis, challenging characterization, and exciting potential applications. *Chem. Mater.* **2013**, 26, 111-222.

10. Zhao, X. K.; Yang, J.; McCormick, L. D.; Fendler, J. H., Epitaxial formation of PbS crystals under arachidic acid monolayers. *J. Phys. Chem.* **1992**, 96, 9933-9939.

11. Kang, I.; Wise, F. W., Electronic structure and optical properties of PbS and PbSe quantum dots. *J. Opt. Soc. Am. B* **1997**, 14, 1632-1646.

12. Moreels, I.; Lambert, K.; Smeets, D.; De Muynck, D.; Nollet, T.; Martins, J. C.; Vanhaecke, F.; Vantomme, A.; Delerue, C.; Allan, G.; Hens, Z., Size-dependent optical properties of colloidal PbS quantum dots. *ACS Nano* **2009**, 3, 3023-3030.

13. Seshadri, S.; Saranya, K.; Kowshik, M., Green synthesis of lead sulfide nanoparticles by the lead resistant marine yeast, Rhodosporidium diobovatum. *Biotechnol. Progr.* **2011**, 27, 1464-1469.

14. Bai, H.-J.; Zhang, Z.-M., Microbial synthesis of semiconductor lead sulfide nanoparticles using immobilized Rhodobacter sphaeroides. *Mater. Lett.* **2009**, 63, 764-766.

15. Senapati, S.; Syed, A.; Khan, S.; Pasricha, R.; Khan, M. I.; Kumar, R.; Ahmad, A., Extracellular biosynthesis of metal sulfide nanoparticles using the fungus Fusarium oxysporum. *Curr. Nanosci.* **2014**, 10, 588-595.

16. Ma, N.; Marshall, A. F.; Rao, J., Near-infrared light emitting luciferase via biomineralization. *J. Am. Chem. Soc.* **2010**, 132, 6884-6885.

17. Levina, L.; Sukhovatkin, V.; Musikhin, S.; Cauchi, S.; Nisman, R.; Bazett-Jones, D. P.; Sargent, E. H., Efficient infrared-emitting PbS quantum dots grown on DNA and stable in aqueous solution and blood plasma. *Adv. Mater.* **2005**, 17, 1854-1857.

18. Deng, D.; Xia, J.; Cao, J.; Qu, L.; Tian, J.; Qian, Z.; Gu, Y.; Gu, Z., Forming highly fluorescent near-infrared emitting PbS quantum dots in water using glutathione as surface-modifying molecule. *J. Colloid Interface Sci.* **2012**, 367, 234-240.

19. Hines, M. A.; Scholes, G. D., Colloidal PbS nanocrystals with size - tunable near - infrared emission: observation of post - synthesis self - narrowing of the particle size distribution. *Adv. Mater.* **2003**, 15, 1844-1849.

20. Weidman, M. C.; Beck, M. E.; Hoffman, R. S.; Prins, F.; Tisdale, W. A., Monodisperse, air-stable PbS nanocrystals via precursor stoichiometry control. *ACS Nano* **2014**, 8, 6363-6371.

21. Justo, Y.; Geiregat, P.; Hoecke, K. V.; Vanhaecke, F.; De Mello Donega, C.; Hens, Z., Optical properties of PbS/CdS core/shell quantum dots. *J. Phys. Chem. C* **2013**, 117, 20171-20177.

22. Moreels, I.; Justo, Y.; De Geyter, B.; Haustraete, K.; Martins, J. C.; Hens, Z., Size-tunable, bright, and stable PbS quantum dots: a surface chemistry study. *ACS Nano* **2011**, 5, 2004-2012.

23. Neo, M. S.; Venkatram, N.; Li, G. S.; Chin, W. S.; Ji, W., Synthesis of PbS/CdS core-shell QDs and their nonlinear optical properties. *J. Phys. Chem. C* **2010**, 114, 18037-18044.

24. Supran, G. J.; Song, K. W.; Hwang, G. W.; Correa, R. E.; Scherer, J.; Dauler, E. A.; Shirasaki, Y.; Bawendi, M. G.; Bulović, V., High‐performance shortwave‐infrared light‐emitting devices using core-shell (PbS-CdS) colloidal quantum dots. *Adv. Mater.* **2015**, 27, 1437-1442.

25. Zhao, H.; Chaker, M.; Wu, N.; Ma, D., Towards controlled synthesis and better understanding of highly luminescent PbS/CdS core/shell quantum dots. *J. Mater. Chem.* **2011**, 21, 8898-8904.

26. Zhao, H.; Chaker, M.; Ma, D., Effect of CdS shell thickness on the optical properties of water-soluble, amphiphilic polymer-encapsulated PbS/CdS core/shell quantum dots. *J. Mater. Chem.* **2011**, 21, 17483-17491.

27. Niu, J.; Xu, W.; Shen, H.; Li, S.; Wang, H.; Li, L. S., Synthesis of CdS, ZnS, and CdS/ZnS core/shell nanocrystals using dodecanethiol. *Bull. Korean Chem. Soc.* **2012**, 33, 393-397.

28. Lai, L.-H.; Protesescu, L.; Kovalenko, M. V.; Loi, M. A., Sensitized solar cells with colloidal PbS-CdS core-shell quantum dots. *Phys. Chem. Chem. Phys.* **2014**, 16, 736-742.

29. Kovalenko, M. V.; Schaller, R. D.; Jarzab, D.; Loi, M. A.; Talapin, D. V., Inorganically functionalized PbS-CdS colloidal nanocrystals: integration into amorphous chalcogenide glass and luminescent properties. *J. Am. Chem. Soc.* **2012**, 134, 2457-2460.

30. Abel, K. A.; FitzGerald, P. A.; Wang, T.-Y.; Regier, T. Z.; Raudsepp, M.; Ringer, S. P.; Warr, G. G.; van Veggel, F. C. J. M., Probing the structure of colloidal core/shell quantum dots formed by cation exchange. *J. Phys. Chem. C* **2012**, 116, 3968-3978.

31. Zhao, H.; Liang, H.; Vidal, F. o.; Rosei, F.; Vomiero, A.; Ma, D., Size dependence of temperature-related optical properties of PbS and PbS/CdS core/shell quantum dots. *J. Phys. Chem. C* **2014**, 118, 20585-20593.

32. Pietryga, J. M.; Werder, D. J.; Williams, D. J.; Casson, J. L.; Schaller, R. D.; Klimov, V. I.; Hollingsworth, J. A., Utilizing the lability of lead selenide to produce heterostructured nanocrystals with bright, stable infrared emission. *J. Am. Chem. Soc.* **2008**, 130, 4879-4885.

33. Zhou, H. S.; Honma, I.; Komiyama, H.; Haus, J. W., Coated semiconductor nanoparticles: the cadmium sulfide/lead sulfide system's synthesis and properties. *J. Phys. Chem.* **1993**, 97, 895-901.

34. Lin, Q.; Makarov, N. S.; Koh, W.-k.; Velizhanin, K. A.; Cirloganu, C. M.; Luo, H.; Klimov, V. I.; Pietryga, J. M., Design and synthesis of heterostructured quantum dots with dual emission in the visible and infrared. *ACS Nano* **2014**, 9, 539-547.

35. Abel, K. A.; Qiao, H.; Young, J. F.; van Veggel, F. C. J. M., Four-fold enhancement of the activation energy for nonradiative decay of excitons in PbSe/CdSe core/shell versus PbSe colloidal quantum dots. *J. Phys. Chem. Lett.* **2010**, 1, 2334-2338.

36. Lechner, R. T.; Fritz-Popovski, G.; Yarema, M.; Heiss, W.; Hoell, A.; Schülli, T. U.; Primetzhofer, D.; Eibelhuber, M.; Paris, O., Crystal phase transitions in the shell of PbS/CdS core/shell nanocrystals influences photoluminescence intensity. *Chem. Mater.* **2014**, 26, 5914-5922.

37. Speirs, M. J.; Balazs, D. M.; Fang, H.-H.; Lai, L.-H.; Protesescu, L.; Kovalenko, M. V.; Loi, M. A., Origin of the increased open circuit voltage in PbS–CdS core–shell quantum dot solar cells. *J. Mater. Chem. A* **2015**, 3, 1450-1457.

38. Gonfa, B. A.; Zhao, H.; Li, J.; Qiu, J.; Saidani, M.; Zhang, S.; Izquierdo, R.; Wu, N.; El Khakani, M. A.; Ma, D., Air-processed depleted bulk heterojunction solar cells based on PbS/CdS core–shell quantum dots and TiO_2 nanorod arrays. *Sol. Energy Mater. Sol. Cells* **2014**, 124, 67-74.

39. Kore, R. H.; Kulkarni, J. S.; Haram, S. K., Effect of nonionic surfactants on the kinetics of disproportion of copper sulfide nanoparticles in the aqueous sols. *Chem. Mater.* **2001**, 13, 1789-1793.

40. Liu, X.; Li, B.; Fu, F.; Xu, K.; Zou, R.; Wang, Q.; Zhang, B.; Chen, Z.; Hu, J., Facile synthesis of biocompatible cysteine-coated CuS nanoparticles with high photothermal conversion efficiency for cancer therapy. *Dalton Trans.* **2014**, 43, 11709-11715.

41. Prasanth, S.; Raj, D. R.; Vineeshkumar, T. V.; Thomas, R. K.; Sudarsanakumar, C., Exploring the interaction of L-cysteine capped CuS nanoparticles with bovine serum albumin (BSA): a spectroscopic study. *RSC Adv.* **2016**, 6, 58288-58295.

42. Kriegel, I.; Jiang, C.; Rodríguez-Fernández, J.; Schaller, R. D.; Talapin, D. V.; da Como, E.; Feldmann, J., Tuning the excitonic and plasmonic properties of copper chalcogenide nanocrystals.

J. Am. Chem. Soc. **2012**, 134, 1583-1590.

43. Wu, Y.; Wadia, C.; Ma, W.; Sadtler, B.; Alivisatos, A. P., Synthesis and photovoltaic application of copper(I) sulfide nanocrystals. *Nano Lett.* **2008**, 8, 2551-2555.

44. Kumta, P. N.; Phule, P. P.; Risbud, S. H., Low-temperature wet-chemical synthesis of amorphous indium sulfide powders. *Mater. Lett.* **1987**, 5, 401-404.

45. Ivanchenko, M. V.; Rayevska, O. E.; Stroyuk, O. L.; Kuchmiy, S. Y. In *Colloidal indium sulfide quantum dots in water: synthesis and optical properties*, MRS Proceedings, Cambridge Univ Press: 2013; pp 163-169.

46. Kamat, P. V.; Dimitrijevic, N. M.; Fessenden, R. W., Photoelectrochemistry in particulate systems. 7. Electron-transfer reactions of indium sulfide semiconductor colloids. *J. Phys. Chem.* **1988**, 92, 2324-2329.

47. Nosaka, Y.; Ohta, N.; Miyama, H., Photochemical kinetics of ultrasmall semiconductor particles in solution: effect of size on the quantum yield of electron transfer. *J. Phys. Chem.* **1990**, 94, 3752-3755.

48. Nagesha, D. K.; Liang, X.; Mamedov, A. A.; Gainer, G.; Eastman, M. A.; Giersig, M.; Song, J.-J.; Ni, T.; Kotov, N. A., In_2S_3 nanocolloids with excitonic emission: In_2S_3 vs CdS comparative study of optical and structural characteristics. *J. Phys. Chem. B* **2001**, 105, 7490-7498.

49. Lokhande, C. D., Chemical deposition of metal chalcogenide thin films. *Mater. Chem. Phys.* **1991**, 27, 1-43.

50. Leach, A. D. P.; Macdonald, J. E., Optoelectronic properties of $CuInS_2$ nanocrystals and their origin. *J. Phys. Chem. Lett.* **2016**, 7, 572-583.

51. So, D.; Konstantatos, G., Thiol-free synthesized copper indium sulfide nanocrystals as optoelectronic quantum dot solids. *Chem. Mater.* **2015**, 27, 8424-8432.

52. van der Stam, W.; Berends, A. C.; Rabouw, F. T.; Willhammar, T.; Ke, X.; Meeldijk, J. D.; Bals, S.; de Mello Donega, C., Luminescent $CuInS_2$ quantum dots by partial cation exchange in $Cu_{2-x}S$ nanocrystals. *Chem. Mater.* **2015**, 27, 621-628.

53. Zhong, H.; Zhou, Y.; Ye, M.; He, Y.; Ye, J.; He, C.; Yang, C.; Li, Y., Controlled synthesis and optical properties of colloidal ternary chalcogenide $CuInS_2$ nanocrystals. *Chem. Mater.* **2008**, 20, 6434-6443.

54. Jara, D. H.; Yoon, S. J.; Stamplecoskie, K. G.; Kamat, P. V., Size-dependent photovoltaic

performance of $CuInS_2$ quantum dot-sensitized solar cells. *Chem. Mater.* **2014**, 26, 7221-7228.

55. Omata, T.; Nose, K.; Otsuka-Yao-Matsuo, S., Size dependent optical band gap of ternary I-III-VI_2 semiconductor nanocrystals. *J. Appl. Phys.* **2009**, 105, 073106.

56. Kim, Y.-K.; Ahn, S.-H.; Chung, K.; Cho, Y.-S.; Choi, C.-J., The photoluminescence of $CuInS_2$ nanocrystals: effect of non-stoichiometry and surface modification. *J. Mater. Chem.* **2012**, 22, 1516-1520.

57. Uehara, M.; Watanabe, K.; Tajiri, Y.; Nakamura, H.; Maeda, H., Synthesis of $CuInS_2$ fluorescent nanocrystals and enhancement of fluorescence by controlling crystal defect. *J. Chem. Phys.* **2008**, 129, 134709.

58. Wang, X.; Swihart, M. T., Controlling the size, shape, phase, band gap, and localized surface plasmon resonance of $Cu_{2-x}S$ and Cu_xIn_yS nanocrystals. *Chem. Mater.* **2015**, 27, 1786-1791.

59. Nam, D.-E.; Song, W.-S.; Yang, H., Noninjection, one-pot synthesis of Cu-deficient $CuInS_2$/ZnS core/shell quantum dots and their fluorescent properties. *J. Colloid Interface Sci.* **2011**, 361, 491-496.

60. Li, L.; Pandey, A.; Werder, D. J.; Khanal, B. P.; Pietryga, J. M.; Klimov, V. I., Efficient synthesis of highly luminescent copper indium sulfide-based core/shell nanocrystals with surprisingly long-lived emission. *J. Am. Chem. Soc.* **2011**, 133, 1176-1179.

61. Kim, H.; Han, J. Y.; Kang, D. S.; Kim, S. W.; Jang, D. S.; Suh, M.; Kirakosyan, A.; Jeon, D. Y., Characteristics of $CuInS_2$/ZnS quantum dots and its application on LED. *J. Cryst. Growth* **2011**, 326, 90-93.

62. Kuo, K.-T.; Chen, S.-Y.; Cheng, B.-M.; Lin, C.-C., Synthesis and characterization of highly luminescent $CuInS_2$ and $CuInS_2$/ZnS (core/shell) nanocrystals. *Thin Solid Films* **2008**, 517, 1257-1261.

63. Ghatak, A.; Debnath, G. H.; Mandal, M.; Mukherjee, P., Lanthanide cation-induced tuning of surface capping properties in zinc sulfide nanoparticles: an infrared absorption study. *RSC Adv.* **2015**, 5, 32920-32932.

64. Kumbhojkar, N.; Nikesh, V. V.; Kshirsagar, A.; Mahamuni, S., Photophysical properties of ZnS nanoclusters. *J. Appl. Phys.* **2000**, 88, 6260-6264.

65. Li, L. S.; Pradhan, N.; Wang, Y.; Peng, X., High quality ZnSe and ZnS nanocrystals formed by activating zinc carboxylate precursors. *Nano Lett.* **2004**, 4, 2261-2264.

66. Deng, D.; Chen, Y.; Cao, J.; Tian, J.; Qian, Z.; Achilefu, S.; Gu, Y., High-quality $CuInS_2$/ZnS quantum dots for in vitro and in vivo bioimaging. *Chem. Mater.* **2012**, 24, 3029-3037.

67. Pons, T.; Pic, E.; Lequeux, N.; Cassette, E.; Bezdetnaya, L.; Guillemin, F.; Marchal, F.; Dubertret, B., Cadmium-free $CuInS_2$/ZnS quantum dots for sentinel lymph node imaging with reduced toxicity. *ACS Nano* **2010**, 4, 2531-2538.

68. Li, L.; Daou, T. J.; Texier, I.; Kim Chi, T. T.; Liem, N. Q.; Reiss, P., Highly luminescent $CuInS_2$/ZnS core/shell nanocrystals: cadmium-free quantum dots for in vivo imaging. *Chem. Mater.* **2009**, 21, 2422-2429.

69. Jiang, T.; Song, J.; Wang, H.; Ye, X.; Wang, H.; Zhang, W.; Yang, M.; Xia, R.; Zhu, L.; Xu, X., Aqueous synthesis of color tunable Cu doped Zn–In–S/ZnS nanoparticles in the whole visible region for cellular imaging. *J. Mater. Chem. B* **2015**, 3, 2402-2410.

70. Zhang, J.; Xie, R.; Yang, W., A simple route for highly luminescent quaternary Cu-Zn-In-S nanocrystal emitters. *Chem. Mater.* **2011**, 23, 3357-3361.

71. De Trizio, L.; Prato, M.; Genovese, A.; Casu, A.; Povia, M.; Simonutti, R.; Alcocer, M. J. P.; D'Andrea, C.; Tassone, F.; Manna, L., Strongly fluorescent quaternary Cu–In–Zn–S nanocrystals prepared from $Cu_{1-x}InS_2$ nanocrystals by partial cation exchange. *Chem. Mater.* **2012**, 24, 2400-2406.

72. Akkerman, Q. A.; Genovese, A.; George, C.; Prato, M.; Moreels, I.; Casu, A.; Marras, S.; Curcio, A.; Scarpellini, A.; Pellegrino, T., From binary Cu_2S to ternary Cu–In–S and quaternary Cu–In–Zn–S nanocrystals with tunable composition via partial cation exchange. *ACS Nano* **2015**, 9, 521-531.

73. Berends, A. C.; Rabouw, F. T.; Spoor, F. C. M.; Bladt, E.; Grozema, F. C.; Houtepen, A. J.; Siebbeles, L. D. A.; de Mello Donegá, C., Radiative and nonradiative recombination in $CuInS_2$ nanocrystals and $CuInS_2$-Based core/shell nanocrystals. *J. Phys. Chem. Lett.* **2016**, 7, 3503-3509.

74. Zhong, H.; Lo, S. S.; Mirkovic, T.; Li, Y.; Ding, Y.; Li, Y.; Scholes, G. D., Noninjection gram-scale synthesis of monodisperse pyramidal $CuInS_2$ nanocrystals and their size-dependent properties. *ACS Nano* **2010**, 4, 5253-5262.

75. Parak, W. J.; Boudreau, R.; Le Gros, M.; Gerion, D.; Zanchet, D.; Micheel, C. M.; Williams, S. C.; Alivisatos, A. P.; Larabell, C., Cell motility and metastatic potential studies based on quantum dot imaging of phagokinetic tracks. *Adv. Mater.* **2002**, 14, 882-885.

76. Feliu, N.; Hühn, J.; Zyuzin, M. V.; Ashraf, S.; Valdeperez, D.; Masood, A.; Said, A. H.; Escudero, A.; Pelaz, B.; Gonzalez, E., Quantitative uptake of colloidal particles by cell cultures. *Sci. Total Environ.* **2016**, 568, 819-828.

77. Choi, S. H.; Mendrola, J. M.; Lemmon, M. A., EGF-independent activation of cell-surface EGF receptors harboring mutations found in gefitinib-sensitive lung cancer. *Oncogene* **2007**, 26, 1567-1576.

78. Ichinose, J.; Murata, M.; Yanagida, T.; Sako, Y., EGF signalling amplification induced by dynamic clustering of EGFR. *Biochem. Biophys. Res. Commun.* **2004**, 324, 1143-1149.

79. Parak, W. J.; Gerion, D.; Pellegrino, T.; Zanchet, D.; Micheel, C.; Williams, S. C.; Boudreau, R.; Le Gros, M. A.; Larabell, C. A.; Alivisatos, A. P., Biological applications of colloidal nanocrystals. *Nanotechnology* **2003**, 14, R15-R27.

80. Erathodiyil, N.; Ying, J. Y., Functionalization of inorganic nanoparticles for bioimaging applications. *Acc. Chem. Res.* **2011**, 44, 925-935.

81. Spangler, L. C.; Lu, L.; Kiely, C. J.; Berger, B. W.; McIntosh, S., Biomineralization of PbS and PbS-CdS core-shell nanocrystals and their application in quantum dot sensitized solar cells. *J. Mater. Chem. A* **2016**, 4, 6107-6115.

82. Spangler, L. C.; Chu, R.; Lu, L.; Kiely, C. J.; Berger, B. W.; McIntosh, S., Enzymatic biomineralization of biocompatible $CuInS_2$, $(CuInZn)S_2$ and $CuInS_2/ZnS$ core/shell nanocrystals for bioimaging. *Nanoscale* **2017**, 9, 9340-9351.

Chapter 4

Biomineralized metal oxide nanocrystals

4.1 Introduction

In Chapters 2 and 3, we have demonstrated successful biomineralization of a number of metal sulfide and metal selenide nanocrystals driven by either the SMCD1 bacterial strain or SMCD1-associated enzyme cystathionine γ-lyase. Herein we show that nanocrystals of metal oxides, in this case ceria (CeO_{2-x}) and ceria-zirconia ($Ce_{1-y}Zr_yO_{2-x}$), could also be biomineralized employing another single enzyme, namely a modified form of silicatein (rCeSi).

Ceria and ceria-zirconia nanoparticles are of functional interest owing to their multifarious emerging and commercial applications in environmental catalysis,[1] fuels cells,[2] biomedicine,[3] and chemical mechanical planarization abrasives.[4] Ceria-based materials are widely utilized in automotive exhaust catalysis as oxygen storage media for their facile redox behavior which allows the reversible transformation between Ce(III) and Ce(IV). This redox pair also makes ceria and ceria-zirconia mixed oxide active oxidation catalysts and catalyst supports for a variety of oxidation reactions.[5-7] The doping of zirconium cations into the ceria matrix facilitates the formation of oxygen defects within the nanocrystals to improve catalytic activity and thermal stability of the materials.[8-9] Conventionally, ceria and ceria-zirconia nanomaterials are synthesized by flame pyrolysis,[10] co-precipitation,[11] or hydrothermal routes,[12] all of which require elevated temperatures, and most typically, the use of a base to induce precipitation from the precursor solution. As an alternative approach, biomineralization offers a feasible and green pathway to the

production of ceria and ceria-zirconia nanocrystals which are functionally equivalent to their chemically prepared counterparts.

Natural biomineralization processes[13-14] usually create amorphous structural materials, for example, calcium carbonate-biopolymer composite mollusk shells,[15] and structural spicules of silica in sea sponges.[16] The lack of structural control during biomineralization produces materials with irregular size, shape, structure, and composition, rather than well-defined functional nanomaterials. On the other hand, precipitation solely depending on supersaturation of a solution following a biotemplating route restricts the materials palette only to certain thermodynamically allowed reactions. Therefore, it is highly desirable to manufacture functional materials via a biomineralization strategy that integrates metabolic precursor turnover and biotemplating in a single biological system.

Biotemplated ceria synthesis has been demonstrated before,[17] wherein mineralization was initiated by a base followed by the use of an apoferritin cage as a template yielding CeO_2 nanoparticles ~5 nm in size. However, this method required multiple separation steps to sort out bulky ceria aggregates produced by reaction of the precipitant with the non-templated ceria precursor. In contrast, the combined enzymatic mineralization and templating approach described herein exclusively generates ceria nanocrystals with no need for post-synthesis size selection.

The single enzyme utilized in our approach was derived from silicatein, first identified by Morse *et al.*[18] as responsible for mineralization of silica spicules in the marine sponge *Tethya aurantia*. Native or recombinant forms of silicatein have been applied to biomineralization of silica,[19] titania,[20] gallium trioxide,[21] tin dioxide,[22] and barium titanate oxyfluoride[23] particles. Yet

silicatein and its derivatives have not been reported to directly mineralize catalytic oxides. Herein, we present a single enzyme, *i.e.*, a recombinant silicatein rCeSi, capable of direct biomineralization of structurally controlled cerium oxide and cerium-zirconium oxide solid solution nanocrystals active for CO oxidation. The structural analysis of the resultant biomineralized oxide nanocrystals was carried out using advanced electron microscopy and other complementary characterization techniques such as XRD and XPS.

4.2 Synthesis, characterization and catalytic testing of rCeSi mineralized ceria and ceria-zirconia nanocrystals

4.2.1 Biosynthetic protocols for ceria and ceria-zirconia nanocrystals

Silicatein originally derived from *Petrosia ficiformis* (NCBI accession number Q6YD92.1) was codon-optimized with the N- and C-terminal truncated to enhance expression yield from *E. coli*. A truncated sequence was identified to contain amino acids 124-217 and a C-terminal hexahistidine tag that showed consistently high expression from *E. coli* (rCeSi). The recombinant enzyme was purified using immobilized metal affinity chromatography (IMAC) followed by dialysis against DI water to remove residual salts.

Nanocrystal formation was induced by introduction of either (i) 2 mM cerium ammonium nitrate (CAN), (ii) 2 mM zirconium dinitrate oxide hydrate (ZDO), or (iii) a mixture of 1 mM CAN and 1 mM ZDO, to 4 μM rCeSi enzyme solution. Sample incubation proceeded on an orbital shaker at room temperature for 24 h, followed by centrifugation and resuspension of the pellet in 2 mM nitric acid solution. After five repetitions of this washing process, the samples were centrifuged and dried under vacuum. Control samples with only the rCeSi enzyme absent

were subjected to synthesis procedures identical to the primary samples. No sign of particle formation or color change was observed within 48 h.

4.2.2 Characterization of the biomineralized ceria and ceria-zirconia nanocrystals

Incubation of rCeSi with the CAN precursor in the aqueous phase for 24 h resulted in an opaque, yellow solution that displayed the Tyndall effect under laser light irradiation, indicating the formation of a fine suspension of nanocrystals (Figure 4.1). In contrast, in the absence of the rCeSi enzyme no color change or colloid formation occurred, illustrating the stability of aqueous CAN solutions against spontaneous oxidation to form nanocrystals within this time period at this pH and temperature.

Figure 4.1: Photographs of the CAN precursor solution with and without rCeSi (a) under natural light, and (b) with red laser illumination. *Courtesy of Christopher D. Curran.*

Synchrotron XRD analysis of the solid pellet collected from this opaque solution displays peak positions and peak broadening corresponding to CeO_2 nanocrystallites with the fluorite structure (Figure 4.2). Rietveld refinement of the XRD pattern further determined a lattice constant of 5.449(1) Å and a mean crystallite size of 22.1 ± 0.2 Å, estimated from the Lorentzian

crystallite size broadening parameter.[24]

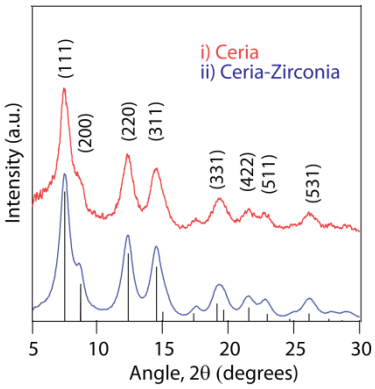

Figure 4.2: Synchrotron XRD patterns of the dried as-synthesized product of incubation of rCeSi with either CAN alone (red line) or an equimolar mixture of CAN and ZDO (blue line). *Courtesy of Christopher D. Curran.*

HR-TEM imaging of the centrifuged and dried pure ceria sample reveals the formation of highly faceted individual crystalline nanoparticles (Figure 4.3 (a)). Lattice fringe analysis based on their FFT patterns confirmed the presence of fluorite type CeO_2 (Figure 4.3 (a), Table 4.1). The as-prepared ceria nanocrystals possess a narrow size distribution of 2.56 ± 0.38 nm (Figure 4.3 (b)), agreeing with the crystallite size derived from XRD. No crystallites larger than 4 nm or amorphous particles were observed. In addition, the presence of only cerium and oxygen was verified by XEDS analysis of the pure ceria sample (Figure 4.3 (c)).

Hence, the enzyme biologically catalyzes ceria mineralization, in comparison to biological templating during chemically induced mineralization.[17] It is worth noting that distinct from other preparation methods, our ceria nanocrystals were formed in the aqueous phase without the need of a base, elevated temperature or an explicit chemical structure-directing agent. The direct biomineralization route yielded ceria nanoparticles that are amongst the smallest reported in the literature.[25-26] In contrast, the elevated temperatures utilized in most chemical approaches to ceria

nanoparticle formation, usually accelerate particle growth and sintering.[6]

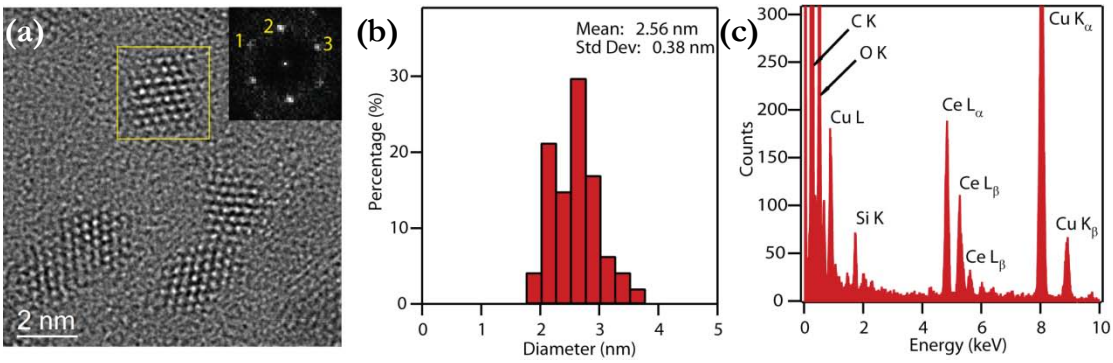

Figure 4.3: Electron microscopy characterization of the biomineralized ceria nanocrystals. (a) Representative HR-TEM image of some ceria nanocrystals. The inset is the FFT diagram from the nanocrystal in the yellow box. (b) Corresponding spherical equivalent particle size distribution histogram. (c) XEDS spectrum of the ceria nanocrystals.

Table 4.1: Lattice fringe analysis of the CeO_2 nanocrystal shown in Figure 4.3 (a).

Fluorite CeO_2	Fig. 4.3 (a): $[1\bar{1}0]$	
	Measured	Matching
Plane 1	2.8 Å	2.7 Å (002)
Plane 2	3.2 Å	3.1 Å (111)
Plane 3	3.1 Å	3.1 Å ($11\bar{1}$)
<1, 2>	54.6°	54.7°
<2, 3>	70.6°	70.5°
<3, 1>	54.8°	54.7°

Incubation of the ZDO precursor alone with rCeSi produced a solid zirconia phase consisting primarily of larger (5-10 nm) disordered species with only a small number of crystalline tetragonal ZrO_2 nanocrystals being present (Figure 4.4, Table 4.2). This situation is analogous to previous reports of biomineralization of amorphous silica,[19] titania,[20] and gallium(III) oxide.[21]

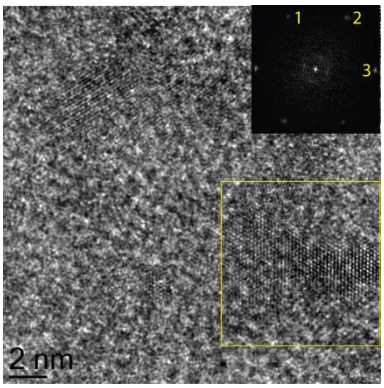

Figure 4.4: HR-TEM image of representative biomineralized pure zirconia nanoparticles. The inset is the FFT diagram from the nanocrystal in the yellow box.

Table 4.2: Lattice fringe analysis of the ZrO_2 nanocrystal in Figure 4.4.

Tetragonal ZrO_2	Fig. 4.4: $[02\bar{1}]$	
	Measured	Matching
Plane 1	1.8 Å	1.8 Å ($1\bar{1}\bar{2}$)
Plane 2	1.8 Å	1.8 Å (200)
Plane 3	1.8 Å	1.8 Å (112)
<1, 2>	59.1°	59.6°
<2, 3>	59.0°	59.6°
<3, 1>	61.9°	60.8°

When a 1:1 mixture of CAN and ZDO was added to an aqueous solution of rCeSi, an opaque sol was observed after 24 h, just as in the case of pure ceria synthesis. Also similarly XRD analysis identified the phase of the resultant nanocrystals as the fluorite structure in a ceria matrix (Figure 4.2). This phase identification conclusion was further supported by lattice fringe analysis of single nanocrystals (Figure 4.5 (a), Table 4.3). Rietveld refinement determines a lattice constant of 5.437(2) Å and a mean crystallite size of 24.53 ± 0.1 Å. The slight contraction in lattice parameter compared to that of pure ceria sample is consistent with the formation of a

ceria-zirconia solid solution,[8, 27-28] as Zr cations are smaller than Ce cations.

The formation of dispersed nanocrystals was confirmed by HAADF-STEM imaging (Figure 4.5 (a)). These particles also have a small average size of 2.41 ± 0.43 nm (Figure 4.5 (b)), in good accord with that calculated from XRD. No larger particles or disordered species were detected under microscopic examination.

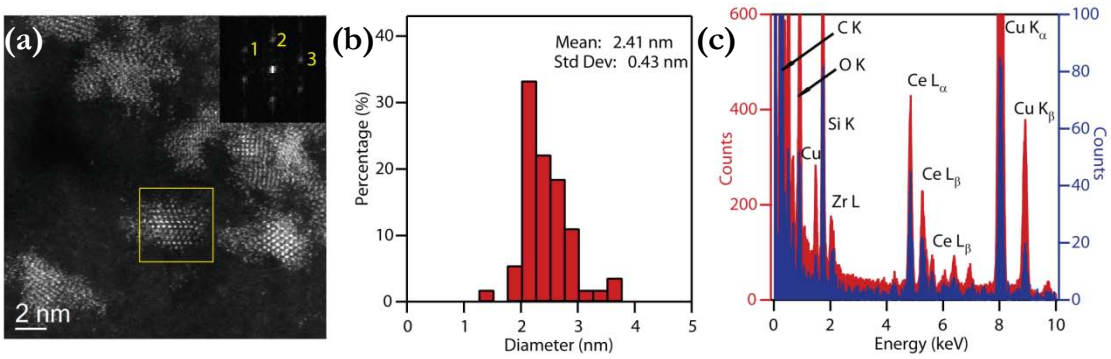

Figure 4.5: Electron microscopy characterization of the biomineralized ceria-zirconia nanocrystals. (a) Representative HR-TEM image of ceria-zirconia nanocrystals. The inset is the FFT pattern from the nanocrystal in the yellow box. (b) Corresponding spherical equivalent particle size distribution histogram. (c) XEDS spectrum of a single nanoparticle (blue) and the summation of 10 spectra from extended area nanocrystal groupings (red).

Table 4.3: Lattice fringe analysis of the ceria-zirconia nanocrystal in Figure 4.5 (a).

Fluorite CeO_2	Fig. 4.5 (a): $[1\bar{1}0]$	
	Measured	Matching
Plane 1	2.9 Å	2.7 Å ($00\mathbf{2}$)
Plane 2	3.3 Å	3.1 Å ($\mathbf{111}$)
Plane 3	3.3 Å	3.1 Å ($\mathbf{11\bar{1}}$)
<1, 2>	55.3°	54.7°
<2, 3>	69.2°	70.5°
<3, 1>	55.5°	54.7°

XEDS-STEM analysis of single particles was attempted, which often resulted in collection

of a statistically insignificant number of X-ray signals before irreversible damage of nanoparticles by electron bombardment. Alternatively, spectra could be more feasibly collected from groups of two or three nanocrystals, and analysis of many such nanoparticle groupings gave similar XEDS spectra. The summation of 10 such groupings or nanocrystals, and one spectrum of a single nanocrystal both point to the co-existence of Ce and Zr, (Figure 4.5 (c)) validating the expected formation of ceria-zirconia solid solution nanoparticles through incubation in the presence of rCeSi. The statistically significant number of X-ray counts from each spectrum enabled meaningful quantitative XEDS analysis using the standardless Cliff-Lorimer method assuming no absorption or fluorescence. The relative atomic ratio of Zr:Ce averaged from multiple spectra was determined to be approximately 21%:79%, in good agreement with the Ce-dominant fluorite structure identified by lattice image analysis of alloyed nanocrystals. Actually, the relative Ce cationic concentration measured from the 10 spectra ranges from 60% to 95%, all of which indicate a Ce-dominant mixture. As with the case of pure ceria, this represents the first report of biomineralized mixed ceria-zirconia nanocrystals, and once again they are amongst the smallest reported to date by any synthesis method.[29]

Interestingly, any attempt to increase the ratio of Zr:Ce in the mixed oxide by adjusting the CAN to ZDO precursor concentrations in the synthesis step did not seem to change the cationic ratio of the as-prepared nanocrystals. Samples synthesized with nominal Zr:Ce ratios of 2:1 and 4:1 in solution, at the same total precursor concentration as the other materials in this study, yielded particles with Zr:Ce cationic ratios of 17%:83% and 19%:81%, respectively, as measured by quantitative XEDS analysis (Figure 4.6). This relative insensitivity to increased Zr content in solution might arise from the intrinsic enzymatic biomineralization turnover kinetics of cerium

versus zirconium that is not substantially affected within the current range of precursor concentrations used here. In comparison, using pure chemical synthesis routes it is feasible to raise the zirconium content in fluorite structured nanocrystals by adding higher proportions of zirconium precursors.[30-31]

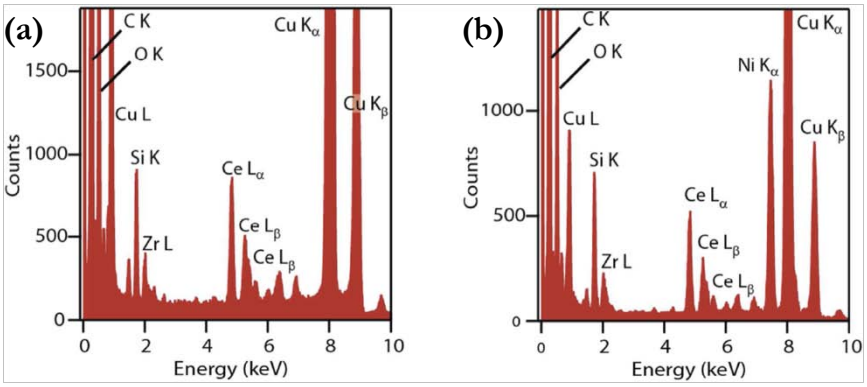

Figure 4.6: XEDS spectra of ceria-zirconia nanocrystals synthesized with different nominal Zr:Ce precursor ratios. The XEDS spectra are summed from data acquired from several extended area nanocrystal groupings for samples prepared with (a) 2:1 ratio and (b) 4:1 ratio of zirconium and cerium precursors.

Therefore, the rCeSi enzyme has been shown to be active in biological induction and control of mineralization of crystalline pure ceria, amorphous pure zirconia, and crystalline mixed cerium-zirconium oxide nanoparticles under ambient conditions. The catalytic pathway of both ceria and zirconia biomineralization by rCeSi is likely to follow that previously proposed for native silicatein.[16] The resultant rCeSi from N- and C-terminal truncations is similar to the mature, protease-resistant fragment of *P. ficiformis* silicatein isolated directly from spicules.[32] Despite the current debate on the exact structure of the CAN precursor, most recent studies agree that it exists as a dimeric entity with bridging Ce-O-Ce bonds.[33-34] While the nature of the six-coordinating species around each cerium atom in the dimeric entity varies between reports, most likely due to the different solvent pH values used, for simple dissolution of the precursor in

water, the coordinating species are probably a mixture of $(NO_3)^-$, OH^-, and H_2O.[33] Herein, a hydrolysis mechanism has been suggested that is analogous to that proposed previously for silicatein-mineralized silica,[19] titania[20] and gallium oxide[21] (Figure 4.7). The number of hydrolysis steps for oxide formation depends upon the nature or number of the coordinating ligands surrounding the Ce-O-Ce dimeric structure in the solvated precursor. Interestingly, the use of a Ce(III)-type precursor, Ce(III) nitrate, led to no observable mineralization, implying the importance of the precursor coordination environment or valence state to the biomineralization process.

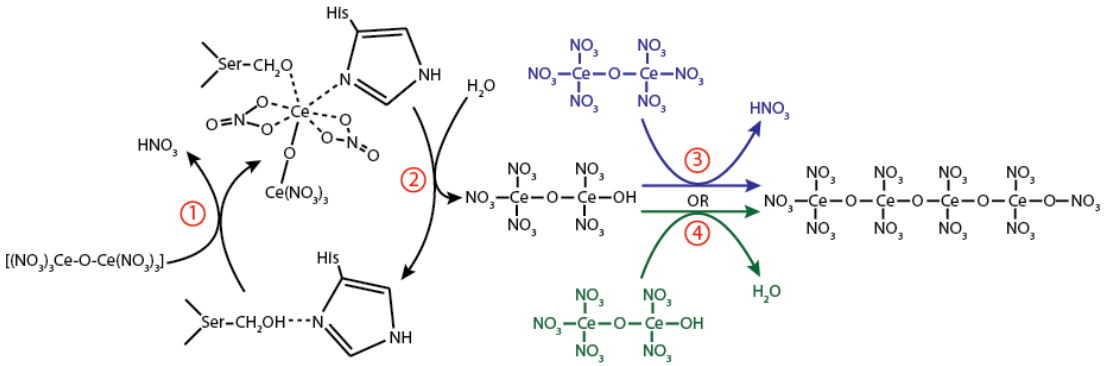

Figure 4.7: Proposed mechanism for the formation of ceria nanocrystals from CAN: (1) dissociative binding of the precursor to the active site of rCeSi, (2) hydrolysis of the precursor, and *either* (3) subsequent condensation of a precursor molecule and a hydrolyzed molecule *or* (4) dehydration of two hydrolyzed precursor species. *Courtesy of Christopher D. Curran.*

This proposed mechanism, whereby hydrolysis of the precursor is induced by an acid/base pair consisting of a serine and histidine pair within the enzymatic active site, draws upon the sequence and structural similarities between the α-form of native silicatein and the hydrolytic enzyme cathepsin L.[19] The hydrolyzed precursor subsequently undergoes condensation or nitrate removal to form ceria. The formation of crystalline ceria instead of crystalline cerium hydroxide or an amorphous phase, is likely due to templating by hydrogen-bonding interactions between

hydroxyls on the rCeSi and the hydrolyzed precursors.

In contrast to the case of pure zirconia, no particles larger than 4 nm or amorphous domains were found in the ceria and ceria-zirconia samples, suggesting an intimate intermixing of the two cations rather than separate mineralization of ceria and zirconia. The notable specificity of rCeSi toward templated biomineralization of Ce-rich nanocrystals is consistent with the previously demonstrated requirement to engineer material-specific variants to selectively biomineralize crystalline silica and titania.[35] This is further supported by the disparity in the commonly adopted crystal structures between monoclinic or tetragonal zirconia, and cubic ceria and Ce-rich ceria-zirconia mixed oxides.

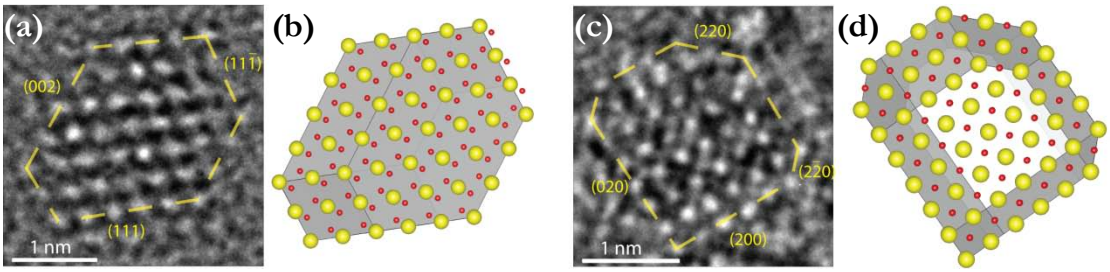

Figure 4.8: Faceting of biomineralized ceria nanocrystals. (a, c) Representative HR-TEM images of biomineralized ceria having polyhedral and truncated cubic morphology nanocrystals. (b, d) Plausible schematic reconstructions of the nanocrystals in (a) and (c), respectively.

Both polyhedral and cuboid morphologies were adopted by the biomineralized ceria nanocrystals (Figure 4.8), with the polyhedral being the dominant shape. The exposure of {111}- and {200}-type facet terminations forms the polyhedral shape, while predominant {200} surface faceting leads to cuboid-like nanocrystals. These morphologies are commonly found in ceria and ceria-zirconia materials synthesized by more conventional chemical approaches using elevated temperature,[36] demonstrating that whereas ceria mineralization is induced and controlled by the enzyme rCeSi, the resulting surface facet distributions do not deviate much from the typically

expected distribution. The polyhedral shape was more commonly observed in the biomineralized materials, just as in the ceria nanocrystals prepared in chemical routes, which probably results from the comparable surface energies of {111} and {200} facets.[5] Similarly, polyhedral and cuboid morphologies are also found in the alloyed ceria-zirconia sample, with the former being the majority type (Figure 4.9).

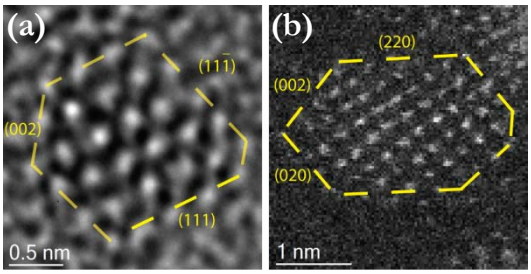

Figure 4.9: Faceting of biomineralized ceria-zirconia nanocrystals. (a) HR-TEM image of a polyhedral nanocrystal. (b) HAADF-STEM image of a truncated cubic nanocrystals.

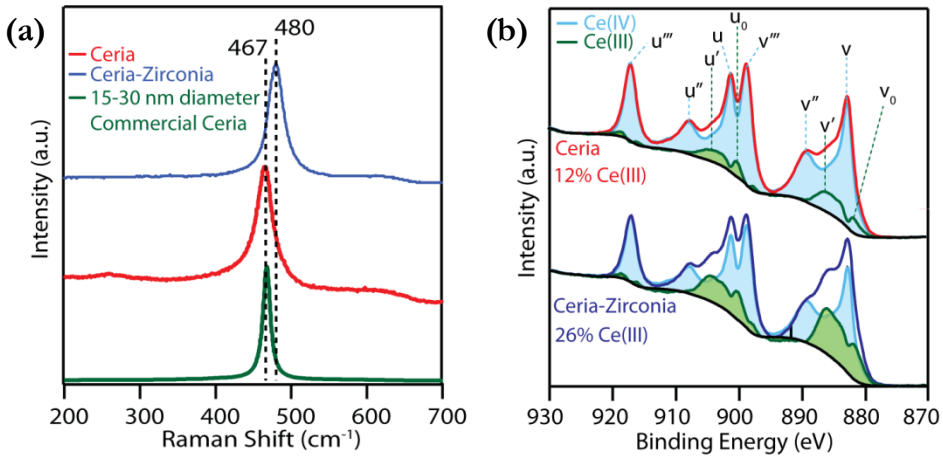

Figure 4.10: Raman and X-ray photoelectron spectroscopic analysis. (a) Raman spectra collected on as-prepared samples of biomineralized ceria and ceria-zirconia and from the commercially obtained reference sample of ceria. (b) X-ray photoelectron spectra of the Ce(3d) region of the biomineralized ceria and ceria-zirconia samples after annealing at 500 °C for 20 min in air. *Courtesy of Christopher D. Curran.*

When characterized by Raman spectroscopy, the pure ceria sample should exhibit, a Raman shift at ~462 cm^{-1}, indicative of the Ce-O bond within the fluorite structure.[37-38] Incorporation

of Zr cations is known to shift the Ce-O bond vibrational frequency to a higher wavenumber.[37-39] The Raman spectra of both our biomineralized and a commercial pure ceria display peaks at the expected position of 467 cm^{-1} (Figure 4.10 (a)). In comparison, the peak position for our biomineralized ceria-zirconia sample shifts to 480 cm^{-1}, further verifying the formation of ceria-zirconia solid solution nanoparticles.

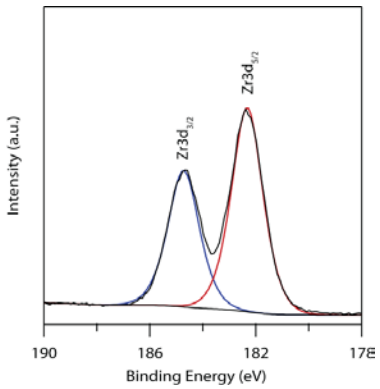

Figure 4.11: Zr(3d) XPS analysis of the biomineralized ceria-zirconia sample. *Courtesy of Christopher D. Curran.*

X-ray photoelectron spectroscopic (XPS) analysis reveals the co-existence of Ce(III) and Ce(IV) cations in both pure ceria and ceria-zirconia biomineralized samples (Figure 4.10 (b)). XPS peaks of U and V stand for the spin-orbit doublet $3d_{5/2}$ and $3d_{3/2}$ respectively.[40] The peaks u, v, u", v", u'" and v'" represent cerium in the 4+ oxidation state, while u^0, v^0, u", and v" correspond to cerium in the 3+ oxidation state. Upon annealing the Ce(III) content in the mixed oxide material reached 26% as compared to 12% Ce(III) in the pure ceria sample. This trend of a higher Ce(III) concentration after introduction of zirconium into the ceria lattice is in accord with previous reports,[8, 41] which could be ascribed to more facile oxygen vacancy formation aided by weakened electrostatic attraction of smaller Zr cations as compared to Ce cations.[42] The measured Ce(III) content is within the range of previous reports.[43-45] High resolution XPS

analysis of the Zr(3d) region from the mixed ceria-zirconia biomineralized sample shows the spin orbital doublet Zr $3d_{5/2}$-Zr $3d_{3/2}$ with binding energies of 182.4 and 184.8 eV respectively (Figure 4.11). This confirms the existence of zirconium in the mixed sample solely in the 4+ oxidation state.

4.2.3 Catalytic testing of the biomineralized ceria and ceria-zirconia nanocrystals

The direct optical band gap values derived from UV-vis spectroscopy for our biomineralized ceria and ceria-zirconia materials and a commercial ceria sample consisting of 15-30 nm particles were 3.55(3), 3.57(3) and 3.22(3) eV, respectively (Figure 4.12 (a)). The larger band gap for the biomineralized ceria compared with the commercial ceria indicates the presence of quantum confined nanocrystals in our biomineralized ceria sample. According to Vegard's law assuming a linear relationship between alloy composition and band gap, increased zirconium content should lead to a larger band gap, since the band gap of bulk cubic zirconia is 6-7 eV.[46] But it has been reported[47-48] that higher concentrations of Ce(III) cations and oxygen vacancies in $Ce_{1-y}Zr_yO_{2-x}$ would give rise to the formation of a partially occupied $4f^1$ band that actually *decreases* the band gap of oxygen deficient ceria. Thus, after Zr doping the increase in the band gap due to higher zirconium content might have been canceled out by the increased oxygen vacancy concentration, resulting in similar band gap values of pure ceria and mixed ceria-zirconia biomineralized nanocrystals. Additionally, the band gap might also be impacted by a number of subtle factors including the chemical environment and attachment of capping ligands.

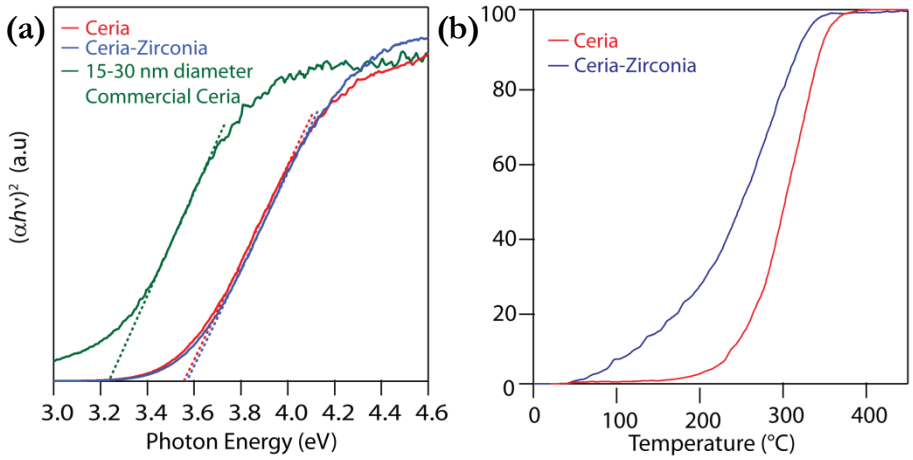

Figure 4.12: Optical properties and catalytic activity toward CO oxidation. (a) Optical band gap determination for the as-synthesized biomineralized ceria and ceria-zirconia nanocrystals compared to larger grained (15-30 nm) commercial ceria. (b) CO conversion as a function of temperature for comparing the catalytic activity of biomineralized ceria and ceria-zirconia nanocrystals. *Courtesy of Christopher D. Curran.*

The rationale of adding zirconium atoms into ceria is to improve the thermal stability, oxygen storage capacity, and associated catalytic activity of the material relative to that of pure ceria. Herein, CO oxidation was chosen as a test reaction to evaluate the catalytic performance of our biomineralized nanocrystals. After heating in air at 500 ˚C, the ceria and ceria-zirconia samples were dispersed (10 wt%) onto 110 μm γ-Al_2O_3 particles by mixing in ethanol. 70 mg supported catalyst was packed into a 4 mm diameter quartz reactor. The reactor was purged with pure O_2 before reaction with a temperature ramp of 10 ˚C/min from 30 ˚C to 500 ˚C. CO light-off curves demonstrate enhanced catalytic activity of the biomineralized ceria-zirconia sample, which is illustrated by a 52 ˚C lowering in the temperature (from 304 ± 5 ˚C down to 252 ± 5 ˚C) to reach 50% CO conversion (Figure 4.12 (b)). Under identical reaction conditions a commercial ceria sample (with a 15-30 nm particle size) arrived at 50% CO conversion at 293 ± 5 ˚C, close to the light-off temperature exhibited by our biomineralized pure ceria sample.

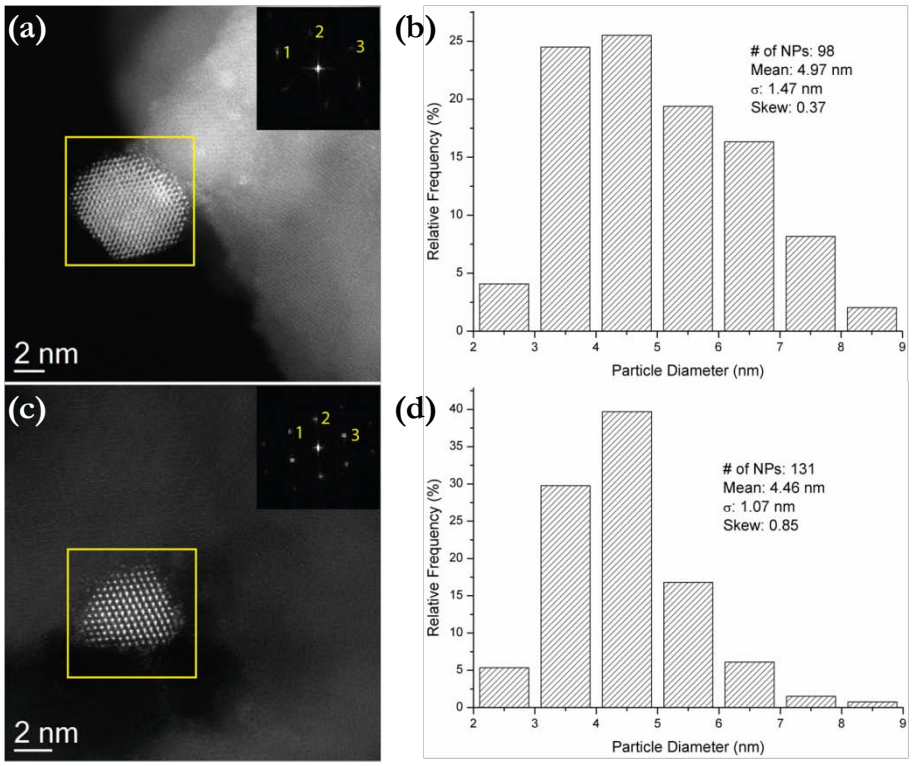

Figure 4.13: HAADF-STEM images of biomineralized ceria and ceria-zirconia supported on alumina after catalysis and respective PSD histograms. (a) Representative HAADF-STEM image of a nanocrystal of ceria and (b) corresponding PSD histogram. (c) Representative HAADF-STEM image of a nanocrystal of ceria-zirconia and (d) corresponding PSD histogram. Insets in (a) and (c) are the FFT diagrams of the respective nanocrystals.

Table 4.4: Lattice fringe analysis of the ceria and ceria-zirconia nanocrystals shown in Figure 4.13 (a, c).

Fluorite CeO_2	Fig. 4.13 (a): $[1\bar{1}0]$		Fig. 4.13 (c): $[1\bar{1}0]$	
	Measured	Matching	Measured	Matching
Plane 1	2.9 Å	2.7 Å (002)	2.8 Å	2.7 Å (002)
Plane 2	3.3 Å	3.1 Å (111)	3.2 Å	3.1 Å (111)
Plane 3	3.2 Å	3.1 Å ($11\bar{1}$)	3.3 Å	3.1 Å ($11\bar{1}$)
<1, 2>	56.9°	54.7°	55.1°	54.7°
<2, 3>	69.1°	70.5°	69.8°	70.5°
<3, 1>	54.0°	54.7°	55.1°	54.7°

After the CO oxidation reaction, both biomineralized samples retained nanocrystals

matching the fluorite-type CeO_2 crystal structure (Figure 4.13 (a, c), Table 4.4). Limited particle growth was noted for both samples compared to the as-prepared nanocrystals before any heat treatment (Figure 4.13 (b, d)). In particular, the ceria-zirconia particles (4.46 ± 1.07 nm) experienced less significant growth than their pure ceria counterparts (4.97 ± 1.47 nm), validating the expected improved thermal stability of ceria upon doping with zirconium.[8]

4.3 Summary and Outlook

In this chapter, we have described a facile biomineralization process for the production of quantum confined, sub-3 nm ceria and ceria-zirconia mixed oxide nanocrystals that are amongst the smallest ever reported. This process utilized a specially engineered single enzyme rCeSi derived from native silicatein which could play a dual role of both catalyzing turnover of the reactants and templating the nanocrystal structure and size. The successful formation of ceria and ceria-zirconia nanocrystals has been verified by analytical electron microscopy analysis. Both samples contained nanocrystals with the cubic fluorite-type CeO_2 crystal structure. XEDS-STEM analysis on single nanoparticles from the mixed oxide sample has unambiguously established the formation of Ce-dominant ceria-zirconia solid solution within individual nanocrystals. The incorporation of zirconium into ceria has enhanced the reducibility, CO oxidation activity and thermal stability of the biomineralized nanocrystals.

In the future, it would be fruitful to perform further studies on the biomineralized ceria-based nanocrystal system from the following perspectives:

(1) As shown in this chapter, even in the presence of excess Zr precursor, the mixed oxide nanocrystals harvested were always Ce-rich. We suspect that Zr cations might have reached their

solubility limit in the fluorite matrix under current experimental conditions. Different synthesis temperatures might be employed to either substantiate or refute this hypothesis. Preliminary results from the quantitative XEDS-STEM analysis of ceria-zirconia nanocrystals show that groups of just a few mixed oxide nanocrystals synthesized with a CAN/ZDO ratio of 2 mM/8 mM at 4 °C had a Ce:Zr atomic ratio of around 91%:9%. If the growth temperature was raised to room temperature while maintaining the same precursor concentrations, the Ce:Zr ratio became 63%:37%. This trend in the compositional change could be observed based on multiple examples from each sample. This XEDS result seems to suggest that if we were to further increase the temperature, we might be able to incorporate more zirconium into the solid solution by raising the zirconium solubility limit.

(2) Another possible scenario for the formation of Ce-rich nanocrystals is the preferential mineralization of the CAN precursor due to higher affinity of rCeSi for CAN as compared to ZDO. Hence if we were to further extend the growth time, the residual ZDO precursor might get incorporated into the nanocrystal matrix by interacting with rCeSi. It would also be interesting to see whether or not Zr-rich nanocrystals with the tetragonal or monoclinic structure could form. Another nanocrystal parameter worth monitoring is the possible systematic variation of the mean particle size with growth time.

(3) Besides zirconium, other transition metals such as copper, cobalt and yttrium have also been used as a dopant to enhance the chemical and electronic properties of pure ceria.[6, 49] One might seek to explore the possibility of biomineralizing other ceria-based mixed oxide nanocrystals using the rCeSi enzyme. The incubation of appropriate precursors of these metal elements with the CAN precursor in the presence of rCeSi may effectively incorporate the

cations into ceria. Such an attempt could also help us better understand the specificity of the rCeSi enzyme.

4.4 Acknowledgements

The work described in this chapter is in collaboration with the Biomineralization group led by Prof. Steven McIntosh and Prof. Bryan W. Berger in the Department of Chemical Engineering at Lehigh University. Their guidance and expert advice is acknowledged.

The sample preparation, macroscopic spectroscopic measurements, and catalyst testing were performed by Christopher D. Curran and Yue Jia. Their various contributions to this work are gratefully appreciated. The work described in this chapter has been published in *ACS Nano*[50].

4.5 References

1. Yao, H. C.; Yao, Y. Y., Ceria in automotive exhaust catalysts: I. oxygen storage. *J. Catal.* **1984**, 86, 254-265.

2. McIntosh, S.; Gorte, R. J., Direct hydrocarbon solid oxide fuel cells. *Chem. Rev.* **2004**, 104, 4845-4866.

3. Celardo, I.; Pedersen, J. Z.; Traversa, E.; Ghibelli, L., Pharmacological potential of cerium oxide nanoparticles. *Nanoscale* **2011**, 3, 1411-1420.

4. Krishnan, M.; Nalaskowski, J. W.; Cook, L. M., Chemical mechanical planarization: slurry chemistry, materials, and mechanisms. *Chem. Rev.* **2009**, 110, 178-204.

5. Zhou, K.; Wang, X.; Sun, X.; Peng, Q.; Li, Y., Enhanced catalytic activity of ceria nanorods from well-defined reactive crystal planes. *J. Catal.* **2005**, 229, 206-212.

6. Sun, C.; Li, H.; Chen, L., Nanostructured ceria-based materials: synthesis, properties, and applications. *Energy Environ. Sci.* **2012**, 5, 8475-8505.

7. Si, R.; Flytzani‐Stephanopoulos, M., Shape and crystal‐plane effects of nanoscale ceria

on the activity of Au - CeO_2 catalysts for the water-gas shift reaction. *Angew. Chem. Int. Ed.* **2008**, 47, 2884-2887.

8. Mamontov, E.; Egami, T.; Brezny, R.; Koranne, M.; Tyagi, S., Lattice defects and oxygen storage capacity of nanocrystalline ceria and ceria-zirconia. *J. Phys. Chem. B* **2000**, 104, 11110-11116.

9. Bunluesin, T.; Gorte, R. J.; Graham, G. W., CO oxidation for the characterization of reducibility in oxygen storage components of three-way automotive catalysts. *Appl. Catal., B* **1997**, 14, 105-115.

10. Stark, W. J.; Mädler, L.; Maciejewski, M.; Pratsinis, S. E.; Baiker, A., Flame synthesis of nanocrystalline ceria–zirconia: effect of carrier liquid. *Chem. Commun.* **2003**, 588-589.

11. Escribano, V. S.; López, E. F.; Panizza, M.; Resini, C.; Amores, J. M. G.; Busca, G., Characterization of cubic ceria–zirconia powders by X-ray diffraction and vibrational and electronic spectroscopy. *Solid State Sci.* **2003**, 5, 1369-1376.

12. Lee, J.-S.; Choi, S.-C., Crystallization behavior of nano-ceria powders by hydrothermal synthesis using a mixture of H_2O_2 and NH_4OH. *Mater. Lett.* **2004**, 58, 390-393.

13. Heuer, A. H.; Fink, D. J.; Laraia, V. J.; Arias, J. L.; Calvert, P. D.; Kendall, K.; Messing, G. L.; Blackwell, J.; Rieke, P. C.; Thompson, D. H.; Wheeler, A. P.; Veis, A.; Caplan, A. I., Innovative materials processing strategies: a biomimetic approach. *Science* **1992**, 255, 1098-1105.

14. Nudelman, F.; Sommerdijk, N. A., Biomineralization as an inspiration for materials chemistry. *Angew. Chem. Int. Ed.* **2012**, 51, 6582-6596.

15. Addadi, L.; Raz, S.; Weiner, S., Taking advantage of disorder: amorphous calcium carbonate and its roles in biomineralization. *Adv. Mater.* **2003**, 15, 959-970.

16. Cha, J. N.; Shimizu, K.; Zhou, Y.; Christiansen, S. C.; Chmelka, B. F.; Stucky, G. D.; Morse, D. E., Silicatein filaments and subunits from a marine sponge direct the polymerization of silica and silicones in vitro. *Proc. Natl. Acad. Sci. U. S. A.* **1999**, 96, 361-365.

17. Okuda, M.; Suzumoto, Y.; Yamashita, I., Bioinspired synthesis of homogenous cerium oxide nanoparticles and two-or three-dimensional nanoparticle arrays using protein supramolecules. *Cryst. Growth Des.* **2011**, 11, 2540-2545.

18. Shimizu, K.; Cha, J.; Stucky, G. D.; Morse, D. E., Silicatein α: cathepsin L-like protein in sponge biosilica. *Proc. Natl. Acad. Sci. U. S. A.* **1998**, 95, 6234-6238.

19. Brutchey, R. L.; Morse, D. E., Silicatein and the translation of its molecular mechanism of biosilicification into low temperature nanomaterial synthesis. *Chem. Rev.* **2008**, 108, 4915-4934.

20. Sumerel, J. L.; Yang, W.; Kisailus, D.; Weaver, J. C.; Choi, J. H.; Morse, D. E., Biocatalytically templated synthesis of titanium dioxide. *Chem. Mater.* **2003**, 15, 4804-4809.

21. Kisailus, D.; Choi, J. H.; Weaver, J. C.; Yang, W.; Morse, D. E., Enzymatic synthesis and nanostructural control of gallium oxide at low temperature. *Adv. Mater.* **2005**, 17, 314-318.

22. André, R.; Tahir, M. N.; Schröder, H. C. C.; Müller, W. E. G.; Tremel, W., Enzymatic synthesis and surface deposition of tin dioxide using silicatein-α. *Chem. Mater.* **2011**, 23, 5358-5365.

23. Brutchey, R. L.; Yoo, E. S.; Morse, D. E., Biocatalytic synthesis of a nanostructured and crystalline bimetallic perovskite-like barium oxofluorotitanate at low temperature. *J. Am. Chem. Soc.* **2006**, 128, 10288-10294.

24. Larson, A.; Von Dreele, R., *General Structure Analysis System (GSAS)*; Los Alamos National Laboratory: Los Alamos, NM, 2004; Report LAUR 86-748.

25. Yu, T.; Lim, B.; Xia, Y., Aqueous-phase synthesis of single-crystal ceria nanosheets. *Angew. Chem. Int. Ed.* **2010**, 49, 4484-4487.

26. Depner, S. W.; Kort, K. R.; Jaye, C.; Fischer, D. A.; Banerjee, S., Nonhydrolytic synthesis and electronic structure of ligand-capped $CeO_{2-\delta}$ and CeOCl nanocrystals. *J. Phys. Chem. C* **2009**, 113, 14126-14134.

27. Yao, M. H.; Baird, R. J.; Kunz, F. W.; Hoost, T. E., An XRD and TEM investigation of the structure of alumina-supported ceria–zirconia. *J. Catal.* **1997**, 166, 67-74.

28. Hori, C. E.; Permana, H.; Ng, K. Y. S.; Brenner, A.; More, K.; Rahmoeller, K. M.; Belton, D., Thermal stability of oxygen storage properties in a mixed CeO_2-ZrO_2 system. *Appl. Catal., B* **1998**, 16, 105-117.

29. Zhang, H. T.; Wu, G.; Chen, X. H., Thermal stability and photoluminescence of $Zr_{1-x}Ce_xO_2$ ($0 \leqslant x \leqslant 1$) nanoparticles synthesized in a non-aqueous process. *Mater. Chem. Phys.* **2007**, 101, 415-422.

30. Duwez, P.; Odell, F., Phase relationships in the system zirconia-ceria. *J. Am. Ceram. Soc.* **1950**, 33, 274-283.

31. Hirano, M.; Miwa, T.; Inagaki, M., Low-temperature direct synthesis of nanoparticles of

fluorite-type ceria–zirconia solid solutions by "forced cohydrolysis" at 100°C. *J. Solid State Chem.* **2001**, 158, 112-117.

32. Armirotti, A.; Damonte, G.; Pozzolini, M.; Mussino, F.; Cerrano, C.; Salis, A.; Benatti, U.; Giovine, M., Primary structure and post-translational modifications of silicatein beta from the marine sponge Petrosia ficiformis (Poiret, 1789). *J. Proteome Res.* **2009**, 8, 3995-4004.

33. Guillou, N.; Auffredic, J. P.; Louër, M.; Louër, D., The crystal structure of hydronium cerium (III) nitrate hydrate, $Ce(NO_3)_5(H_3O)_2 \cdot H_2O$. *J. Solid State Chem.* **1993**, 106, 295-300.

34. Demars, T. J.; Bera, M. K.; Seifert, S.; Antonio, M. R.; Ellis, R. J., Revisiting the solution structure of ceric ammonium nitrate. *Angew. Chem. Int. Ed.* **2015**, 54, 7534-7538.

35. Bawazer, L. A.; Izumi, M.; Kolodin, D.; Neilson, J. R.; Schwenzer, B.; Morse, D. E., Evolutionary selection of enzymatically synthesized semiconductors from biomimetic mineralization vesicles. *Proc. Natl. Acad. Sci. U.S.A.* **2012**, 109, E1705-E1714.

36. Trovarelli, A.; Fornasiero, P., Catalysis by Ceria and Related Materials; World Scientific: Singapore, 2013.

37. Reddy, B. M.; Bharali, P.; Thrimurthulu, G.; Saikia, P.; Katta, L.; Park, S.-E., Catalytic efficiency of ceria–zirconia and ceria–hafnia nanocomposite oxides for soot oxidation. *Catal. Lett.* **2008**, 123, 327-333.

38. Katta, L.; Sudarsanam, P.; Thrimurthulu, G.; Reddy, B. M., Doped nanosized ceria solid solutions for low temperature soot oxidation: zirconium versus lanthanum promoters. *Appl. Catal., B* **2010**, 101, 101-108.

39. Luo, M.-F.; Yan, Z.-L.; Jin, L.-Y.; He, M., Raman spectroscopic study on the structure in the surface and the bulk shell of $Ce_xPr_{1-x}O_{2-\delta}$ mixed oxides. *J. Phys. Chem. B* **2006**, 110, 13068-13071.

40. Burroughs, P.; Hamnett, A.; Orchard, A. F.; Thornton, G., Satellite structure in the X-ray photoelectron spectra of some binary and mixed oxides of lanthanum and cerium. *J. Chem. Soc., Dalton Trans.* **1976**, 1686-1698.

41. Yang, Z.; Wei, Y.; Fu, Z.; Lu, Z.; Hermansson, K., Facilitated vacancy formation at Zr-doped ceria (111) surfaces. *Surf. Sci.* **2008**, 602, 1199-1206.

42. Yang, Z.; Woo, T. K.; Hermansson, K., Effects of Zr doping on stoichiometric and reduced ceria: a first-principles study. *J. Chem. Phys.* **2006**, 124, 224704.

43. Zhang, F.; Wang, P.; Koberstein, J.; Khalid, S.; Chan, S.-W., Cerium oxidation state in ceria

nanoparticles studied with X-ray photoelectron spectroscopy and absorption near edge spectroscopy. *Surf. Sci.* **2004**, 563, 74-82.

44. Tsunekawa, S.; Ishikawa, K.; Li, Z.-Q.; Kawazoe, Y.; Kasuya, A., Origin of anomalous lattice expansion in oxide nanoparticles. *Phys. Rev. Lett.* **2000**, 85, 3440-3443.

45. Zhang, C.; Grass, M. E.; McDaniel, A. H.; DeCaluwe, S. C.; El Gabaly, F.; Liu, Z.; McCarty, K. F.; Farrow, R. L.; Linne, M. A.; Hussain, Z.; Jackson, G. S.; Bluhm, H.; Eichhorn, B. W., Measuring fundamental properties in operating solid oxide electrochemical cells by using in situ X-ray photoelectron spectroscopy. *Nat. Mater.* **2010**, 9, 944-949.

46. French, R. H.; Glass, S. J.; Ohuchi, F. S.; Xu, Y.-N.; Ching, W. Y., Experimental and theoretical determination of the electronic structure and optical properties of three phases of ZrO_2. *Phys. Rev. B* **1994**, 49, 5133-5142.

47. Castleton, C. W. M.; Kullgren, J.; Hermansson, K., Tuning LDA + U for electron localization and structure at oxygen vacancies in ceria. *J. Chem. Phys.* **2007**, 127, 244704.

48. Nolan, M.; Parker, S. C.; Watson, G. W., The electronic structure of oxygen vacancy defects at the low index surfaces of ceria. *Surf. Sci.* **2005**, 595, 223-232.

49. Xie, S.; Wang, Z.; Cheng, F.; Zhang, P.; Mai, W.; Tong, Y., Ceria and ceria-based nanostructured materials for photoenergy applications. *Nano Energy* **2017**, 34, 313-337.

50. Curran, C. D.; Lu, L.; Jia, Y.; Kiely, C. J.; Berger, B. W.; McIntosh, S., Direct single-enzyme biomineralization of catalytically active ceria and ceria–zirconia nanocrystals. *ACS Nano* **2017**, 11, 3337-3346.

Chapter 5

Developing atomically dispersed Au catalysts for the hydrochlorination of acetylene

5.1 Introduction

At present, vinyl chloride monomer (VCM), a major commodity chemical in the manufacture of polyvinyl chloride (PVC), can be synthesized via acetylene hydrochlorination or ethylene oxychlorination. Acetylene hydrochlorination is an economically important process in locations with rich coal resources. However, the catalyst involved in this production route, $HgCl_2$, poses a severe threat to the environment and human health due to its toxicity and volatility. Thus, it is imperative to seek a mercury-free replacement in the acetylene hydrochlorination reaction.

Three decades ago, Hutchings predicted and experimentally confirmed that gold catalysts would be highly active for the hydrochlorination of acetylene.[1-2] In stark contrast to the supported $HgCl_2$ catalysts, supported gold catalysts can be very stable and do not leach metal.[2] Recently a supported gold catalyst has been successfully used in a pilot plant for several thousand hours with no notable deactivation.[3] In late 2015 the commercialization of a carbon-supported gold (Au/C) catalyst for VCM production was realized in China.[4-5]

The identity of the active gold species for the acetylene hydrochlorination reaction still remains a matter of some debate. Previous *ex-situ* spectroscopy and electron microscopy studies[6-9] have indicated the presence of gold nanoparticles and suggested a correlation between

cationic gold on the nanoparticle surface and the high catalytic activity.[6, 10] It has also been proposed that Au(I) and Au(III) cationic species are probably involved in acetylene hydrochlorination[11] and other reactions[12-13]. The notion of single gold cations as active sites is not new, but the catalysts previously reported[14-17] either suffered quick deactivation or generated considerable quantities of gold clusters or nanoparticles during reaction.

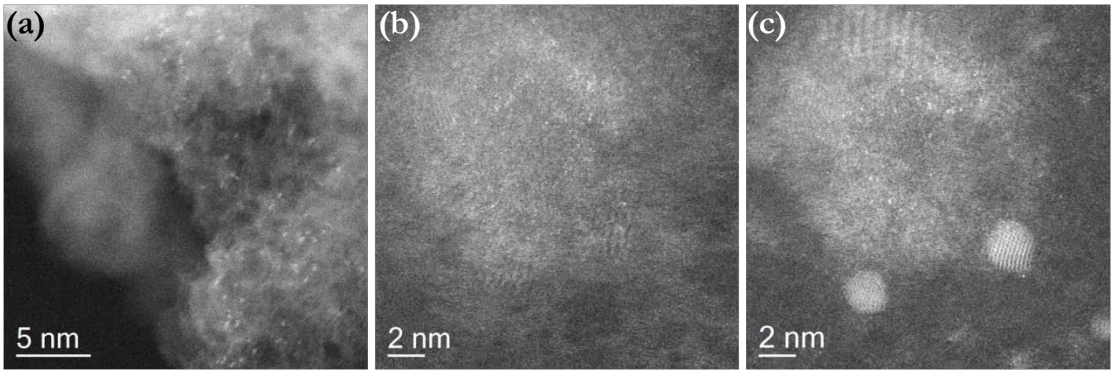

Figure 5.1: HAADF-STEM images of an unused *aqua regia* treated Au catalyst supported on an activated carbon extrudate. (a) Atomically dispersed Au over the support. (b, c) Au-containing thin films (b) which decomposed to form Au nanoparticles upon extended electron beam irradiation (c).[11]

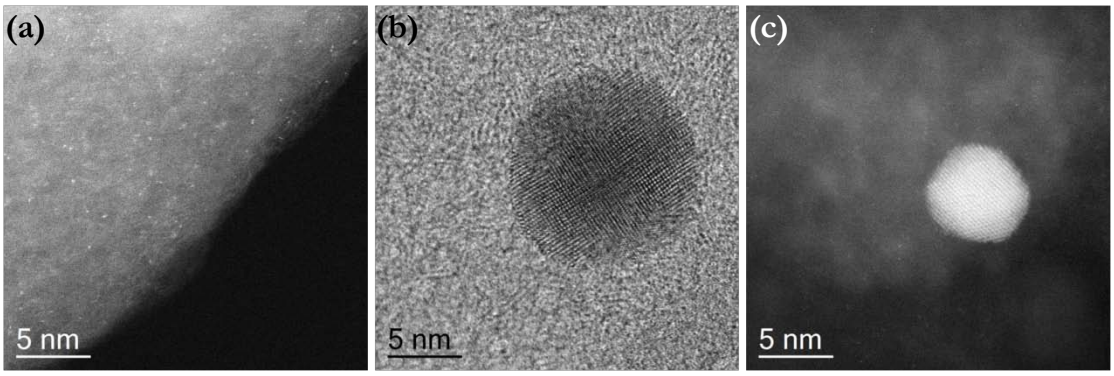

Figure 5.2: STEM images of the *aqua regia* treated Au/C catalyst after 30 min of use. (a) HAADF-STEM image of atomically dispersed Au over the support. (b) BF-STEM image of a nanoparticle whose lattice fringes are consistent with tetragonal AuCl viewed along the <001> projection. (c) HAADF-STEM image of some individual Au atoms and a AuCl nanoparticle viewed along the <111> projection.[11]

In our previous study[11], a 1 wt% Au catalyst supported on activated carbon extrudates was

synthesized by dissolving $HAuCl \cdot xH_2O$ in an *aqua regia* solution followed by drying at 110 °C. The catalyst before use contained an abundance of atomically dispersed Au species, while no discrete metallic Au particles were observed (Figure 5.1 (a)). Another feature noted in this sample was the presence of patches of unstable Au-containing thin films (Figure 5.1 (b)), which under electron beam irradiation decomposed to form Au nanoparticles (Figure 5.1 (c)).

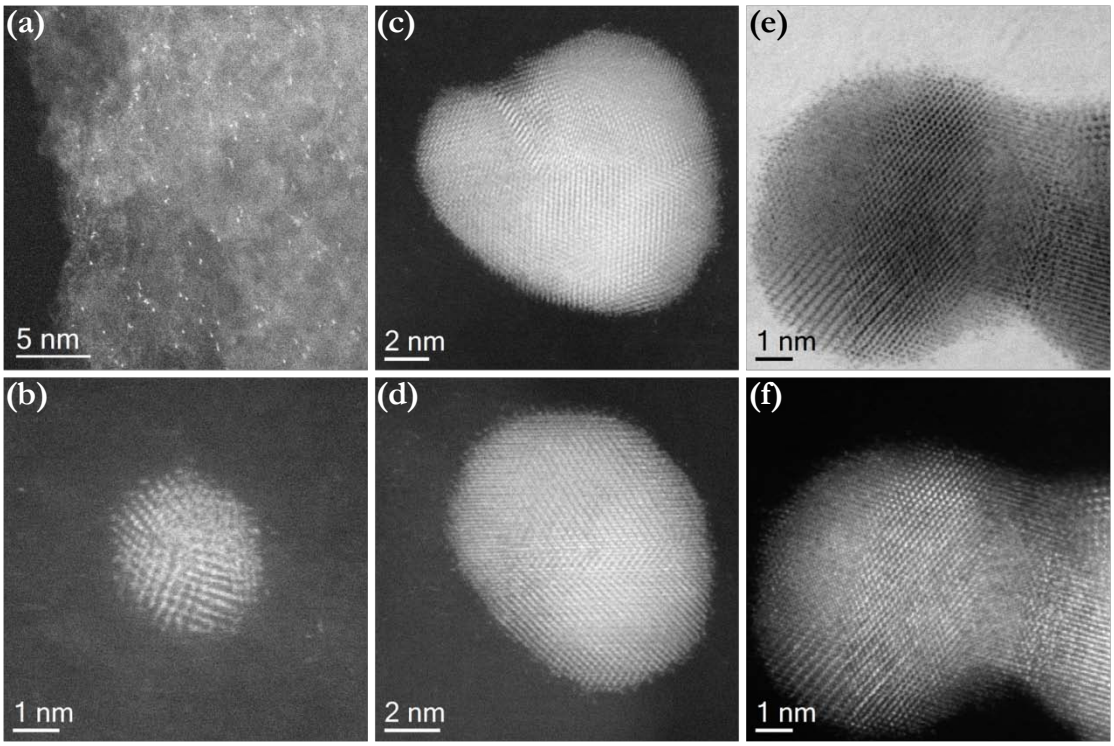

Figure 5.3: STEM images of the *aqua regia* treated Au/C catalyst after 60 min of use. (a) HAADF-STEM image showing discrete Au atoms decorating the support. (b) HAADF-STEM image of a Au nanoparticle. (c, d) HAADF-STEM images of sintered agglomerates of Au nanoparticles. (e, f) BF- and HAADF-STEM image pair of a sintered Au agglomerate.[11]

After 30 min reaction of acetylene hydrochlorination, atomically dispersed Au was still observed on the C support (Figure 5.2 (a)). The presence of beam sensitive Au-containing thin films was much less obvious. Sporadically particles containing both Au and Cl were detected. Two examples of such nanoparticles were displayed in Figure 5.2 (b, c) which exhibited crossed lattice fringes that match the crystal structure of tetragonal AuCl. When the same catalyst was

used for 60 min, there remained a population of isolated Au atoms on carbon (Figure 5.3 (a)). Few Au-containing thin films or AuCl particles were detected in this sample. Instead small (~2 nm) Au nanoparticles (Figure 5.3 (b)) and larger agglomerates of sintered Au particles (Figure 6 (c-f)) emerged. Notably these larger agglomerates appeared quite rounded and seemed to have unidentified atomic scale 'debris' decorating their surfaces, which could be adsorbed chloride species.

From this previous study, it became obvious that the atomically dispersed Au entities on the activated carbon extrudates were not very stable during the reaction, since they became mobile and sintered into larger particles. This is likely due to the low surface area of the carbon extrudates that led to a high density of atomic Au on the support surfaces in the as-prepared sample. In addition, the co-existence of many types of gold species in any given sample made the process of determining meaningful structure/function relationships rather ambiguous. Herein, we present a comparative study of gold on carbon catalysts prepared with different solvents and gold precursors, with the aim of identifying a route for making simpler catalyst materials, just containing atomically dispersed Au, which were stable under reaction conditions. In this follow-on study[11], the rather complex activated low surface area carbon extrudates have also been ground into fine powders with higher surface areas to serve as catalyst supports. To understand the nature of the active form of gold for acetylene hydrochlorination, a combination of aberration-corrected HAADF-STEM and *in-situ* X-ray absorption fine structure (XAFS) analysis has been performed, and we show that isolated atomically dispersed Au(I) cationic species present in the catalyst plays an important role in this reaction, and they function in a similar fashion to the single-site homogeneous catalysis afforded by Au(I) complexes.[18-19]

5.2 Preparation of the Au/C catalysts

All the catalysts in this study were prepared by a wet impregnation method. Activated carbon was initially ground to obtain a powder (100-140 mesh). The chloroauric acid gold precursor $HAuCl_4 \cdot xH_2O$ (Au 49%, 40 mg) was dissolved in 5.4 mL of solvent: namely either (i) *aqua regia* (3:1 HCl : HNO_3); or (ii) HNO_3 only; or (iii) deionized (DI) water. The solutions of gold precursor having the same nominal metal loadings of either 1 or 2 wt%, were then added drop-wise with stirring to the activated carbon powder (Norit ROX 0.8, 1.98 g). Stirring was continued at ambient temperature until NO_x production subsided after ~1 h. The product was then dried for 16 h at 140 °C under an N_2 flow. The series of catalysts prepared using *aqua regia*, HNO_3 or DI water as solvents were designated as Au/C-AR, Au/C-HNO_3, and Au/C-H_2O respectively. It is worth noting that this catalyst preparation procedure differs from that reported before[11], in that powdered carbon was employed as opposed to commercially used C extrudates. The use of a powdered support would give a much lower concentration of gold species on the carbon surface.

For comparative purposes, a 1 wt% Au/C catalyst prepared using Au(I)-thiosulfate as a precursor complex (labeled as Au/C-S_2O_3) was also made by mixing aqueous solutions of $HAuCl_4$ and $Na_2S_2O_3$. This mixture was then added in aliquots to the activated carbon powder with mixing for a pre-determined amount of time, followed by drying overnight at 110 °C.

5.3 Characterization and testing of the 1 wt% Au/C-AR catalysts

The presence of predominantly highly dispersed isolated Au species in the fresh 1 wt% Au/C-AR catalyst was revealed by HAADF-STEM imaging (Figure 5.4). Occasional Au dimers were also noted (Figure 5.4 (b), white circles). The projected distances of Au atoms in the dimeric species were typically in the 0.20-0.34 nm range, which is below the 0.34 nm Au-Au separation found in $AuCl_3$. Some other distinct nanoparticles were observed in the fresh sample (Figure 5.5 (a, c)). However, instead of being gold supported on carbon, XEDS showed that both the particles and the underlying support materials were impurities of Ru, Ti, P and Ca (Figure 5.5 (b, d)). The origin of these intrinsic impurities can be traced back to the crushed activated carbon extrudates (Norit ROX 0.8), which is a form of charcoal processed with steam and chemicals that is well known to suffer from adventitious contamination. The observation of atomic Au dispersion was substantiated by XRD analysis (Figure 5.6), where no reflections associated with metallic Au nanoparticles were detected. Extended X-ray absorption fine structure (EXAFS) analysis further corroborated the absence of long-range order (Figure 5.7 (a)), where once again no features with Au-Au characteristic distances were visible. Moreover, the EXAFS Fourier transform (FT) showed appreciable contributions from Au-Cl entities. *Ex-situ* Cl K-edge X-ray absorption near-edge structure (XANES) revealed the presence of Au-Cl bonding (Figure 5.7 (c)), while the average Au-Cl coordination number (CN) was fitted to 2.6 by EXAFS modeling (Table 5.1).

The normalized Au L_3-edge XANES can give even more information on Au speciation. The rising absorption edge shown at ~11,920 eV in the XANES region (Figure 5.7 (b)), also known as the white line feature, corresponds to the Au $2p_{3/2} \rightarrow 5d$ primary transition. A higher white-line intensity indicates a lower 5d electron occupancy and an increased Au oxidation

state.[20-21] Analysis of the white-line intensity during XANES measurements, when compared to appropriate standards, has been reported to give reliable identification of the Au oxidation state.[20, 22] The typical normalized white-line intensity values reported for cationic Au standards of Au(III) (*e.g.*, $KAuCl_4$/$[AuCl_4]^-$) and Au(I) (*e.g.*, $[AuCl_2]^-$) are 1.1 and 0.6, respectively, which is in good agreement with measured values from our chosen standard materials (Figure 5.7 (b)).[22-23] The fresh 1 wt% Au/C-AR catalyst gave a white-line intensity of 0.78 (Figure 5.7 (b)), suggesting a substantially oxidized Au speciation. Further linear combination fitting showed no contribution from Au(0) (within fitting error), 56% from $[AuCl_2]^-$, and the remaining 44% from $[AuCl_4]^-$.

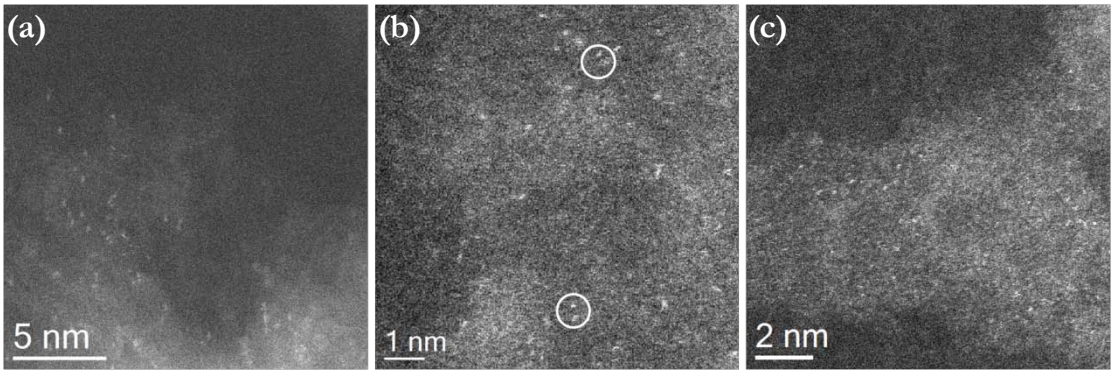

Figure 5.4: HAADF-STEM images of the fresh 1 wt% Au/C-AR catalyst showing isolated Au species and sporadic dimeric Au species (indicated by white circles in (b)).

Notably, in our study, XPS has not been relied upon for determination of Au oxidation states, because X-ray induced reduction of Au(III) would over-estimate the Au(0) content (Figure 5.8 (a)), a phenomenon that is well documented in the literature.[24-25] In contrast, the absence of photo-reduction during XAFS analysis is a result of the higher photon incident energy, which leads to a much lower interaction cross-section and hence photo-absorption probability (Figure 5.8 (b)).

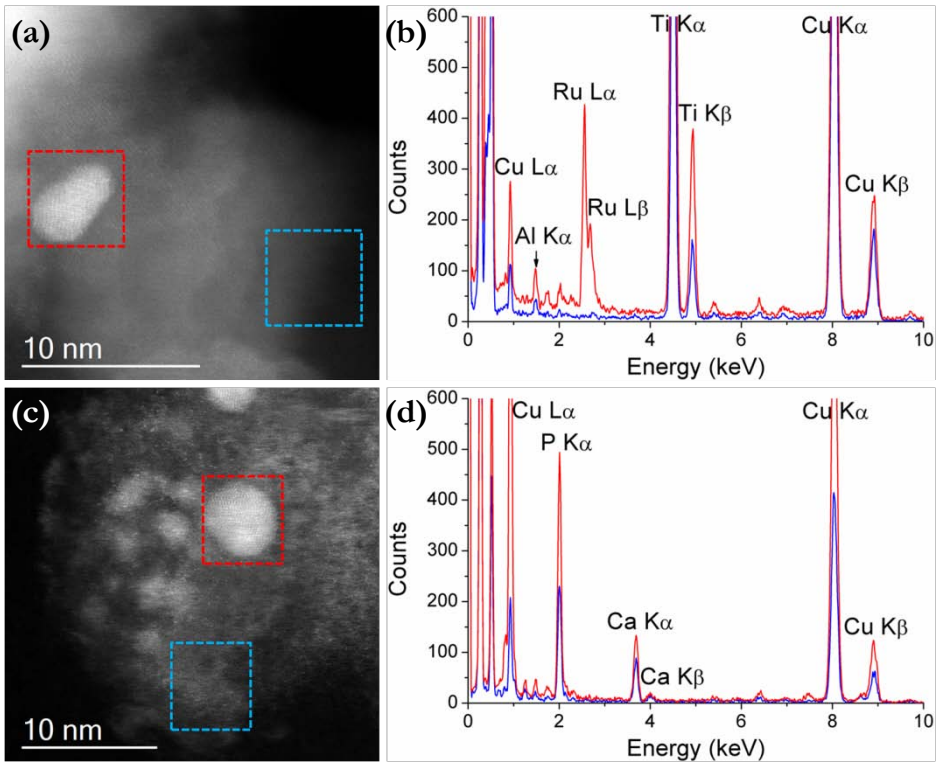

Figure 5.5: Impurities intrinsic to the activated carbon support in the fresh 1 wt% Au/C-AR catalyst. (a) HAADF-STEM image and (b) corresponding XEDS spectrum of a Ru-containing particle on Ti-containing agglomerates. (c) HAADF-STEM image and (d) corresponding XEDS spectrum of a P-containing particle on Ca- and P-containing agglomerates. Red and blue rectangles in (a, c) correspond to red and blue spectra in (b, d) respectively.

Catalytic performance studies of the 1 wt% Au/C-AR catalyst showed it to have an induction period of ~1 h, during which time the activity is suppressed, indicating the generation of active species under reaction conditions.[11] To identify the active form in the gold catalyst under *in-situ* acetylene hydrochlorination reaction conditions, a purpose-built micro-reactor was employed to carry out XAFS analysis while tracking the progress of the reaction by mass spectrometry. In the presence of dilute gas reactants (2.36% C_2H_2 and 2.40% HCl) required to ensure apparatus safety, a higher acetylene conversion was noted for increasing time-on-line (Figure 5.9 (a)). However, the more dilute conditions employed resulted in a longer induction period of 3 h (Figure 5.9 (a)). All of the 1 wt% Au/C catalysts tested were highly selective toward

VCM; no undesirable dichloroethene or chloroethane by-products were detected throughout the reaction process.

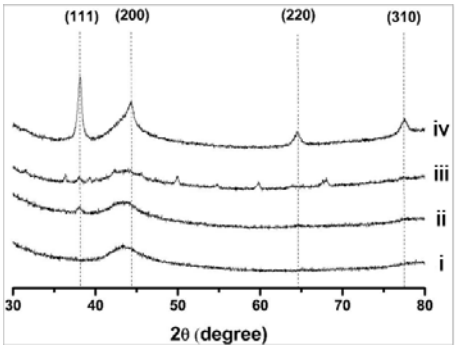

Figure 5.6: XRD patterns for different fresh Au/C catalysts. (i): 1 wt% Au/C-AR; (ii) 1 wt% Au/C-HNO_3; (iii) 1 wt% Au/C-S_2O_3; (iv) 1 wt% Au/C-H_2O. *Courtesy of Grazia Malta.*

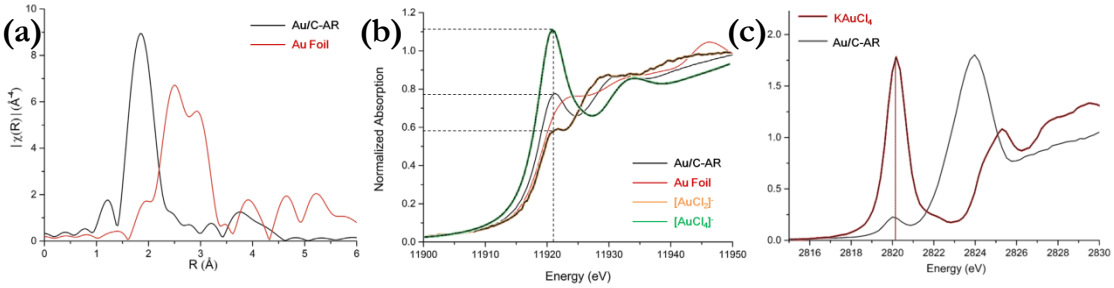

Figure 5.7: *Ex-situ* XAFS analysis of the fresh 1 wt% Au/C-AR catalyst and reference materials. (a) Fourier transform of k^3-weighted χ EXAFS data. Variation in magnitude of Fourier transform is plotted with distance *R* from the Au absorber. (b) Au L_3-edge normalized XANES. (c) Cl K-edge XANES. *Courtesy of Dr. Peter P. Wells.*

Prior to the introduction of reactants, *in-situ* XAFS was applied to analyze the 1 wt% Au/C-AR catalyst upon heating to reaction temperature of 200 °C under an Ar atmosphere. The white-line intensity decreased from 0.78 at 25 °C to 0.68 (Figure 5.9 (b)), reflecting a variation in Au speciation from a Au(III)/Au(I) chloride mixture to a Au(I) chloride-like species. This change corresponds well to the decomposition of $AuCl_3$ to AuCl that is known to occur at ~160 °C.[26] The white-line intensity remained constant at 0.68 during the 30 min isotherm at 200 °C before the addition of reactant gases (Figure 5.9 (b)).

Table 5.1: EXAFS modeling for the Au L_3-edge of the $KAuCl_4$ standard, 1 wt% Au/C-AR (fresh and *in-situ*) and 1 wt% Au/C-S_2O_3 (fresh and *in-situ*) samples at different times-on-line. *Courtesy of Dr. Peter P. Wells.*

Sample	Scattering path	CN	R (Å)	$2\sigma^2$ (Å^2)	S_0^2	E_f (eV)	R_{factor}
$KAuCl_4$ (Au^{3+} std)	Au-Cl1	4†	2.284(3)	0.001	0.75(3)	2.9(5)	0.014
Au/C-AR unused	Au-Cl1	2.58(8)	2.273(4)			2.8(7)	0.006
Au/C-AR 0 min *in-situ*	Au-Cl1	2.39(9)	2.268(6)			1(1)	0.008
Au/C-AR 20 min *in-situ*§	Au-Cl1	2.78(46)	2.297(18)	0.0037‡		1(1)	0.005
	Au-Cl2	0.54(37)	2.171(76)				0.005
	Combined	3.32(83)	2.277				-
Au/C-AR 240 min *in-situ*	Au-Cl1	2.46(9)	2.275(6)			1.2(9)	0.006
Au/C-S_2O_3 unused	Au-S(Cl)§	1.97(8)	2.269(5)	0.001		1.7(9)	0.010
Au/C-S_2O_3 0 min *in-situ*	Au-S(Cl)§	2.23(6)	2.264(7)	0.0037‡		1.3(6)	0.005
Au/C-S_2O_3 30 min *in-situ*	Au-S(Cl)§	2.61(9)	2.277(5)			2.0(8)	0.007

† $KAuCl_4$ standard was fitted with a fixed CN of 4 and used to determine the Debye-Waller factor (for samples at 25 °C) and also the amplitude reduction factor for all other fittings.

‡ Debye-Waller factor at 200 °C was calculated from literature values and the value calculated at 25 °C.

§ Due to comparable atomic numbers, S and Cl are indistinguishable via EXAFS analysis.

$ For the Au/C-AR catalyst after 20 min reaction time, two distinct Au-Cl scattering paths were observed.

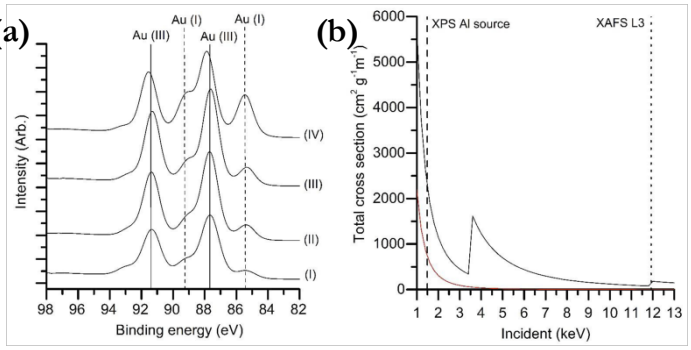

Figure 5.8: Photo-reduction of gold chloride species under X-ray illumination. (a) Photo-reduction of $KAuCl_4$ during Au(4f) XPS analysis for increasing X-ray exposure time (approximately 50 s per Au(4f) spectrum). (b) X-ray absorption cross-section with respect to incident energy for Au (black line) and C (red line). *Courtesy of Grazia Malta.*

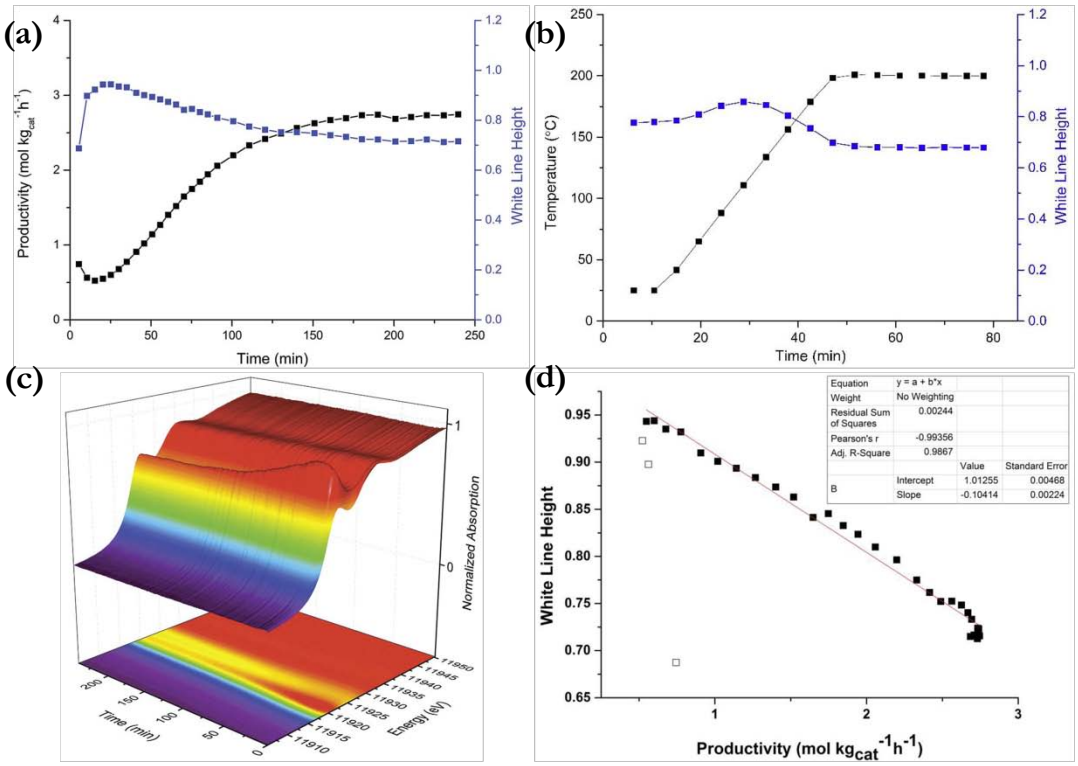

Figure 5.9: VCM productivity and *in-situ* characterization of the 1 wt% Au/C-AR catalyst as a function of time-on-line. (a) Catalytic performance as a function of time-on-line (black) and the change in normalized white-line intensity (blue) as a function of reaction time. (b) Au L_3-edge XANES during heating to reaction temperature under Ar atmosphere at 5 °C min^{-1}. (c) 3-D profile plot of successive Au L_3-edges from XANES spectra acquired *in-situ* as a function of reaction time. (d) Plot of VCM productivity and the corresponding normalized Au L_3-edge white-line intensity during the 240 min time-on-line. Open squares denote data acquired during the first the first 15 min of reaction, and solid squares are those collected between 15 and 240 min time-on-line. *Courtesy of Grazia Malta.*

Once the reactant gases were admitted into the reactor, an immediate change was observed in the Au L_3-edge XANES spectrum (Figure 5.9 (a, c)). The white-line intensity increased from 0.68 to 0.94 within the first 20 min time-on-line, and then steadily fell back to a stable value of 0.72 after ~180 min. The initial increase in the white-line intensity suggests oxidation of Au(I) chloride-like species to predominantly Au(III) chloride species; during the subsequent ~160 min of reaction, the average oxidation state of the Au species progressively moved back towards that of Au(I), and eventually leveled-off somewhere between the two extremes. When under steady

state reaction conditions (after the first 15 min time-on-line), a strong negative linear relationship could be established between the white-line intensity and the simultaneously recorded VCM productivity (Figure 5.9 (d)).

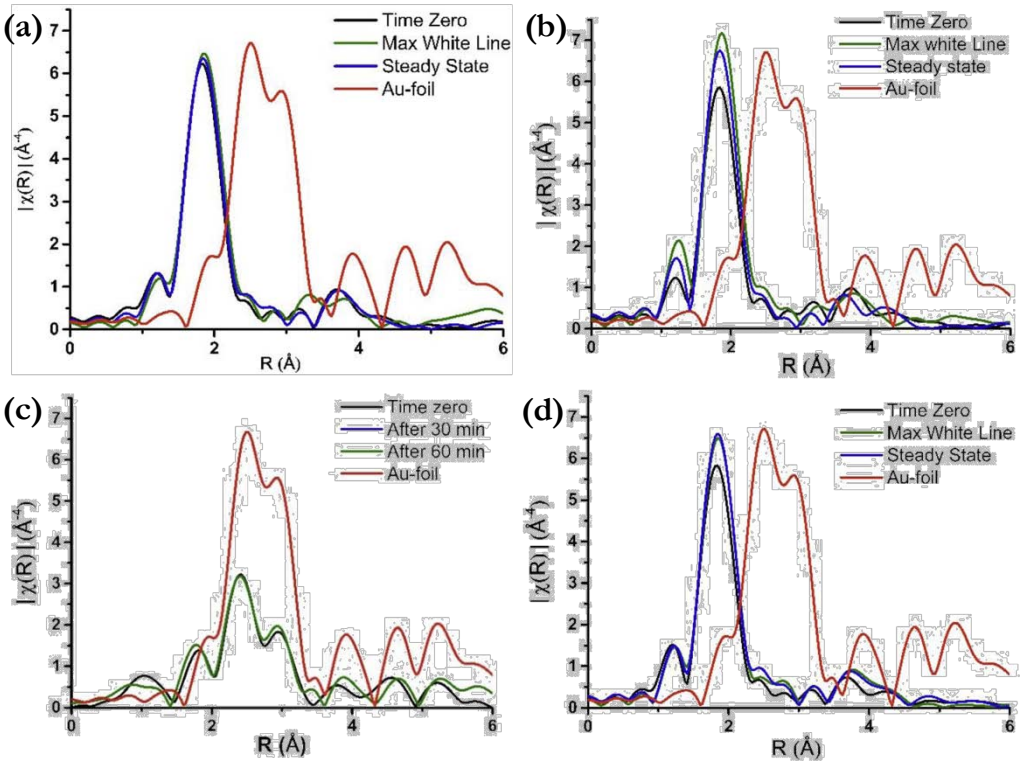

Figure 5.10: EXAFS data of the Au L_3-edge under reaction conditions for the four different 1 wt% Au/C catalysts at different times-on-line. (a) 1 wt% Au/C-AR. (b) 1 wt% Au/C-HNO_3. (c) 1 wt% Au/C-H_2O. (d) 1 wt% Au/C-S_2O_3. Reaction conditions: 200 °C, C_2H_2:HCl = 1:1.02, GHSV (total) = 14,000 h^{-1}, or 11,000 h^{-1} for the Au/C-S_2O_3 catalyst. *Courtesy of Dr. Peter P. Wells.*

Characteristic Au-Au distances were persistently absent from EXAFS during the entire reaction period (Figure 5.10 (a)), pointing to good stability of the highly dispersed Au species in the 1 wt% Au/C-AR catalyst. Linear combination fitting analysis of XANES spectral data for $[AuCl_4]^-$, $[AuCl_2]^-$ and Au foil standard presented a similar trend to that inferred from the white-line intensity measurements (Figure 5.11 (a)). However, the variations in the relative concentrations of $[AuCl_4]^-$ and $[AuCl_2]^-$ may not be the sole contributor to the XANES spectral

changes, as is implied by the poor *R*-factor fitting values in the linear combination fitting (Figure 5.12).

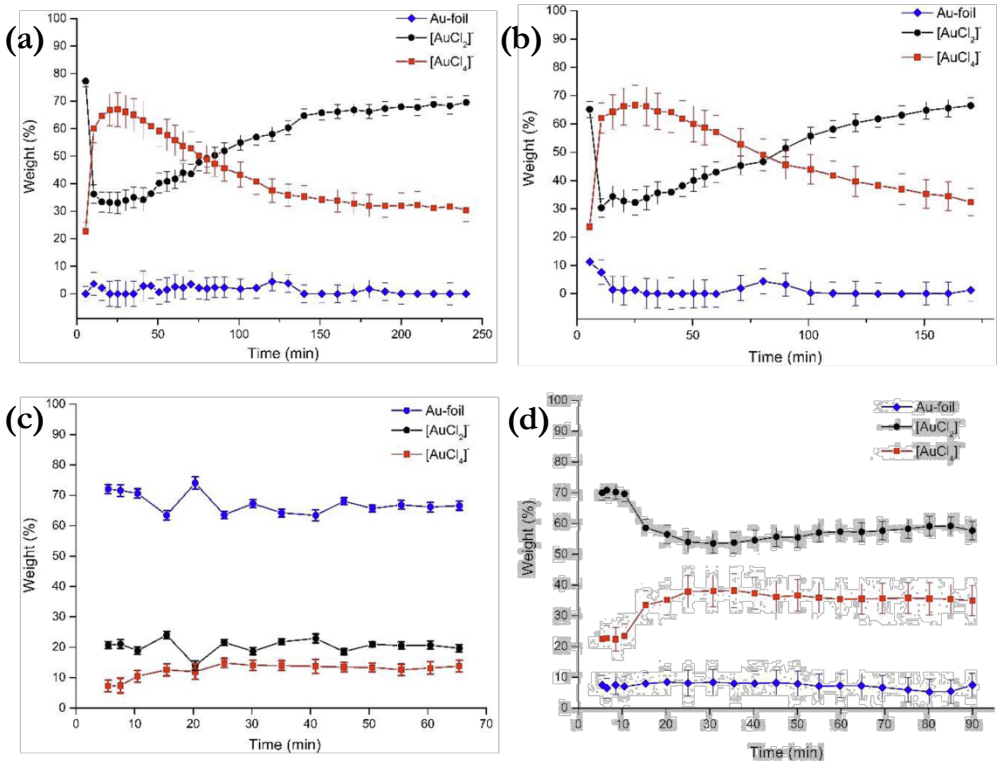

Figure 5.11: Linear combination fitting of the XANES data under reactions for four 1 wt% Au/C catalysts. (a) 1 wt% Au/C-AR. (b) 1 wt% Au/C-HNO_3. (c) 1 wt% Au/C-H_2O. (d) 1 wt% Au/C-S_2O_3. Reaction conditions: 200 °C, C_2H_2:HCl = 1:1.02, GHSV (total) = 14000 h^{-1}, or 11000 h^{-1} for the Au/C-S_2O_3 catalyst. *Courtesy of Dr. Peter P. Wells.*

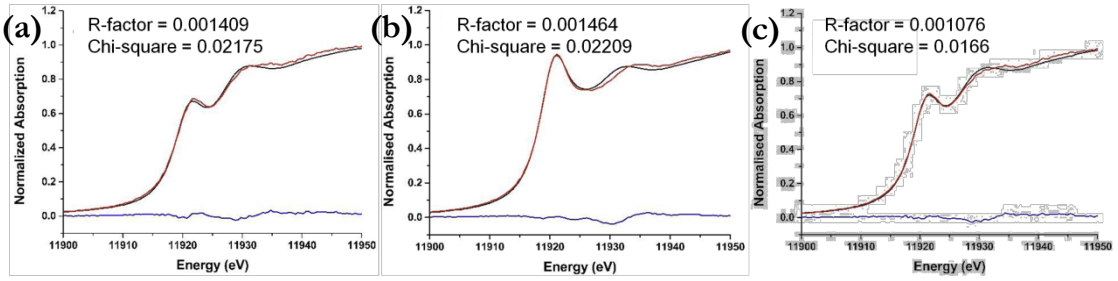

Figure 5.12: XANES data fitting for the 1 wt% Au/C-AR catalyst under reaction conditions at three different points in the induction cycle. (a) Time zero. (b) Maximum of the white-line intensity. (c) Steady state. Black line: experimental data; red line: fit; blue line: residual. Reaction conditions: 200 °C, C_2H_2:HCl = 1:1.02, GHSV (total) = 14,000 h^{-1}. *Courtesy of Dr. Peter P. Wells.*

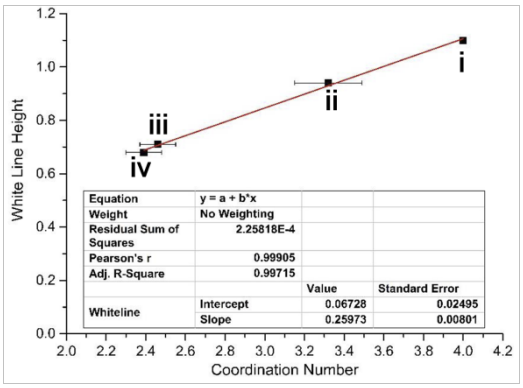

Figure 5.13: Linear correlation of relative Au L_3-edge white-line intensity with Au coordination number for the 1 wt% Au/C-AR catalyst under reaction conditions. (i): the Au(III) ($KAuCl_4$) standard; (ii) Au/C-AR at the maximum white-line intensity, after ~25 min of reaction; (iii) Au/C-AR at steady state, after 240 min of reaction; (iv) Au/C-AR at time zero. *Reaction conditions:* 200 °C, C_2H_2:HCl = 1:1.02, GHSV (total) = 14,000 h^{-1}. *Courtesy of Dr. Peter P. Wells.*

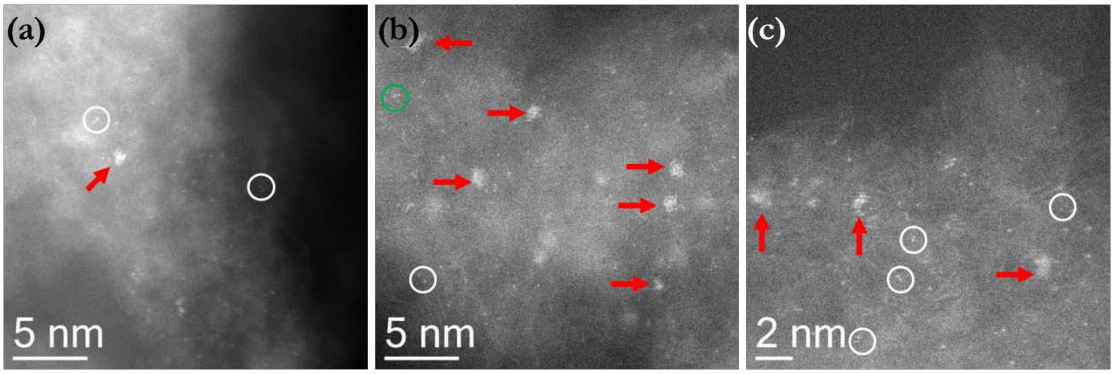

Figure 5.14: HAADF-STEM images of the 1 wt% Au/C-AR catalyst after use for 240 min showing atomically dispersed species, sub-nm clusters (red arrows), and a few dimeric (white circles) and trimeric (green circle) species.

XANES spectra can also be affected by the hybridization of substrate molecule and metal d-band orbitals[27-28] and by geometric changes in the metal speciation via interaction with the support[29]. Both of these complications are conceivable in this work, in the forms of (i) interactions between the acetylene π and Au(5d) orbitals and (ii) C-$AuCl_x$ geometric effects. Nevertheless, the white-line intensity was found to be linearly correlated to the EXAFS-derived Au-Cl CN over a range of reaction times (Figure 5.13), which validates the direct association of the white-line intensity with variations in the Au-Cl speciation. HAADF-STEM imaging (Figure

5.14) of the spent 1 wt% Au/C-AR catalyst confirmed the prevalence of atomically dispersed Au species, along with occasional dimeric and trimeric species, and sub-nm clusters, all of which ensured nearly 100% dispersion.

5.4 Characterization and testing of the 1 wt% Au/C-HNO_3 and 1 wt% Au/C-H_2O catalysts

To evaluate the solvent effect, comparable *in-situ* XAFS studies were performed on corresponding Au/C catalysts prepared with just nitric acid or water. The Au/C-HNO_3 catalyst has been shown to exhibit some activity and display an induction period analogous to that of the Au/C-AR catalyst,[11] which was also extended by dilution of the reactant gases. A trace of metallic Au particles showed up in the Au/C-HNO_3 sample according to *ex-situ* XRD characterization (Figure 5.6), implying lower Au dispersion relative to the Au/C-AR catalyst. However, *in-situ* EXAFS and XANES of Au/C-HNO_3 under reaction conditions indicated that cationic $AuCl_x$ species still dominated the active stable catalyst (Figures 5.10 (b) and 5.11 (b)). The same correlation as for the Au/C-AR catalyst was manifested between the white-line intensity and VCM productivity (Figure 5.15 (a, c)).

By comparison, the 1 wt% Au/C-H_2O catalyst exhibited consistently low activity throughout the reaction, as measured under more concentrated reactant mixtures[11]; this is well associated with its non-existent white-line intensity (Figure 5.15 (a)). XRD analysis of the 1 wt% Au/C-H_2O catalyst displayed distinct reflections characteristic of metallic Au (Figure 5.6). Indeed, only in this catalyst were discernible Au-Au scattering paths observable in the Fourier transform of the EXAFS data (Figure 5.15 (b)); in contrast, no characteristic Au-Cl distances were detected.

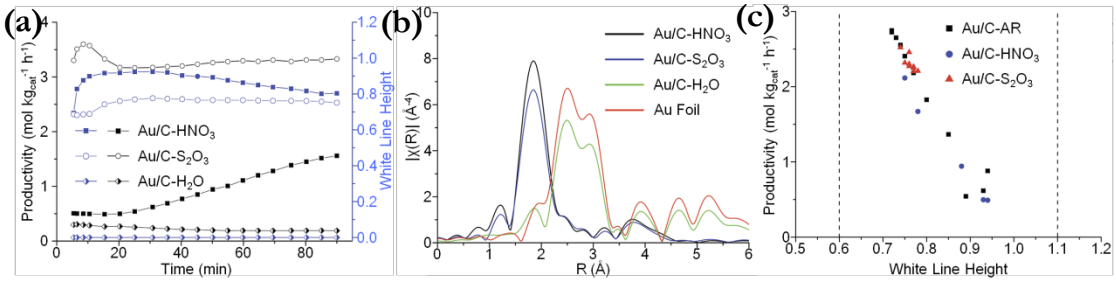

Figure 5.15: VCM productivity (first 90 min time-on-line) and *in-situ* XAFS analysis of 1 wt% Au/C catalysts using alternative solvents and precursors. (a) Catalytic activity (black lines) and the white-line intensity (blue lines) as a function of time-on-line for the catalysts prepared with nitric acid, thiosulfate, and water. (b) k^3-weighted χ EXAFS Fourier transform data for Au/C-HNO_3 (black), Au/C-S_2O_3 (blue), Au/C-H_2O (green), and reference gold foil (red). (c) Correlations between VCM productivity and the white-line intensity for Au/C-AR (black), Au/C-HNO_3 (blue), and Au/C-S_2O_3 (red). Dashed lines denote the white-line intensities of the Au(I) $[AuCl_2]^-$ standard (value of 0.6) and the Au(III) $KAuCl_4$ standard (value of 1.1). $[AuCl_2]^-$ standard from difference spectra calculated in Ref. 22. *Courtesy of Grazia Malta.*

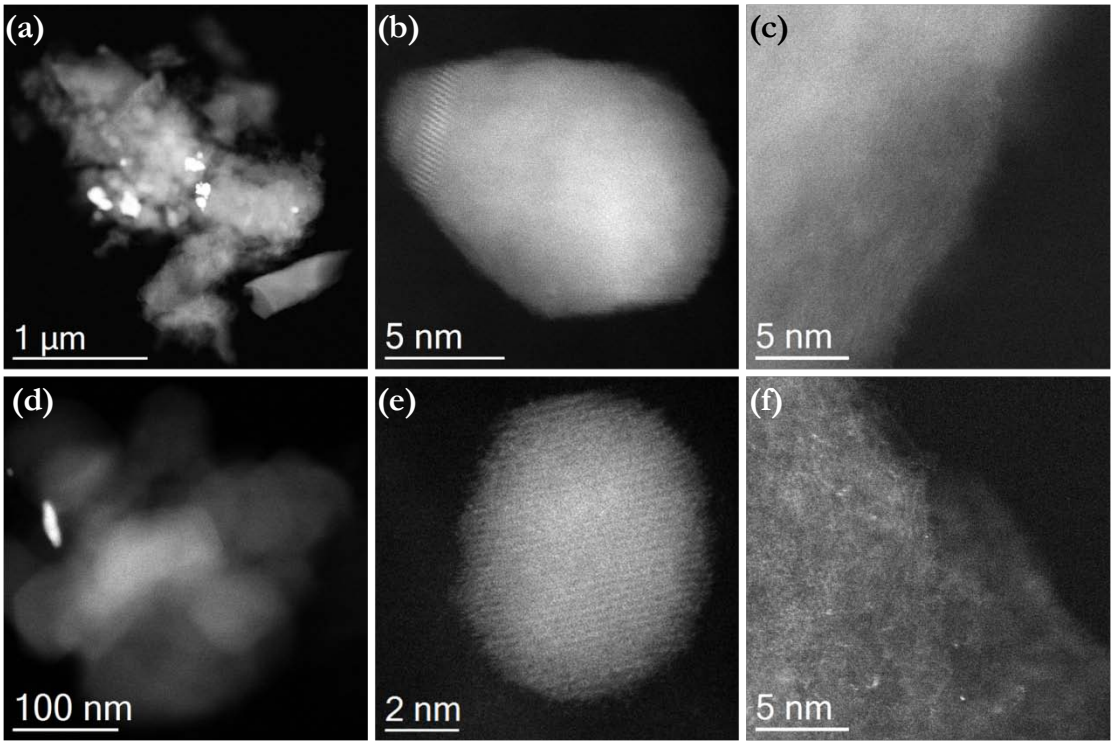

Figure 5.16: HAADF-STEM images of the Au/C-H_2O catalyst. (a-c) Before use. (d-f) After use. Before the reaction this catalyst consisted exclusively of supported Au particles in the 5-100 nm size range, with no atomically dispersed species found on the carbon support. After use the 5-100 nm particles were still present, while atomically dispersed Au entities were also occasionally observed.

During the reaction, there was very little change found in the *in-situ* XANES and EXAFS spectra (Figures 5.10 (c) and 5.11 (c)). This is also evidenced by HAADF-STEM imaging, which showed the Au species only in the form of 5-100 nm nanoparticles in the fresh Au/C-H_2O sample (Figure 5.16 (a, b)). This catalyst before use was totally devoid of any atomically dispersed Au species on the carbon support areas (Figure 5.16 (c)). After reaction, the Au nanoparticles were still visible (Figure 5.16 (d, e)), while atomically dispersed Au entities were now sporadically encountered (Figure 5.16 (f)). These observations strongly demonstrate that the Au/C catalyst prepared with water had a very low Au dispersion, in agreement with its very low catalytic activity and minimal white-line intensity.

5.5 Characterization and testing of the 1 wt% Au/C-S_2O_3 catalysts

An analogous 1 wt% Au/C catalyst was synthesized by using Au(I)-thiosulfate as a precursor complex (denoted as Au/C-S_2O_3) that was more stable and active under reaction conditions than those prepared with the $HAuCl_4$ precursor. It has been demonstrated that the use of a more stable cationic gold complex as the precursor prepared from a range of S-containing ligands such as thiosulfate would lead to highly active catalysts at low gold loadings.[4, 30] The Au/C-S_2O_3 catalyst showed catalytic activity similar to Au/C-AR in the steady state (Figure 5.15 (a)), except that it had no induction period. As in the cases of Au/C-AR and Au/C-HNO_3, the unused Au/C-S_2O_3 catalyst exhibited no Au-Au distances and a significant contribution from a scattering path involving Au and a low-atomic number neighbor in the EXAFS analysis (Figure 5.15 (b)). Au-Cl and Au-S scattering paths by EXAFS are hardly distinguishable, due to the similar nature

of Cl and S from an EXAFS perspective, and the close structural resemblance Au-thiosulfate complexes bear to $[AuCl_2]^-$, both of which form nearly linear molecular geometries with a Au cation bridging two anions (Cl or S). The CN for the fresh Au/C-S_2O_3 catalyst was fitted to 2.0 (±0.1) by EXAFS (Table 5.1), showing that the Au-bonded species was the Au-thiosulfate complex. This CN correlated well with the white-line intensity of 0.68, thus indicating the preponderance of Au(I) species in the unused sample (Figure 5.15 (a)). Upon interaction with the reactants, the Au/C-S_2O_3 material gave a slightly increased white-line intensity of 0.78 after 30 min, illustrating oxidation of some Au species to the Au(III) state (Figure 5.15 (a)). However, this increase in white-line intensity was much less pronounced than that for the corresponding 1 wt% Au/C-AR sample, which was in accord with the absence of an induction period in the Au/C-S_2O_3 catalyst. Meanwhile during the initial 30 min reaction, the Au-S(Cl) CN was increased from 2.0 to 2.6 (Table 5.1), suggesting the coordination of Cl to the Au-thiosulfate complex. In common with the Au/C-AR and Au/C-HNO_3 materials, the Au/C-S_2O_3 catalyst showed a consistent lack of Au-Au distances in the EXAFS spectra during the reaction (Figure 5.10 (d)), reflecting a high dispersion of the Au species. Closer inspection by HAADF-STEM demonstrated that atomically dispersed Au species were abundant in both the unused and used Au/C-S_2O_3 materials (Figure 5.17 (a-e)), which is similar to the case for Au/C-AR. Sub-nm Au clusters constituted the minority species in the fresh sample (Figure 5.17 (a, b)), while no Au nanoparticles were found. After the reaction, however, sparsely distributed Au nanoparticles were formed on the C support (Figure 5.17 (f)), but clusters were rarely observed. It seemed that Au clusters in the fresh sample had sintered into nanoparticles during reaction, while the catalytically desirable atomically dispersed Au species were largely retained.

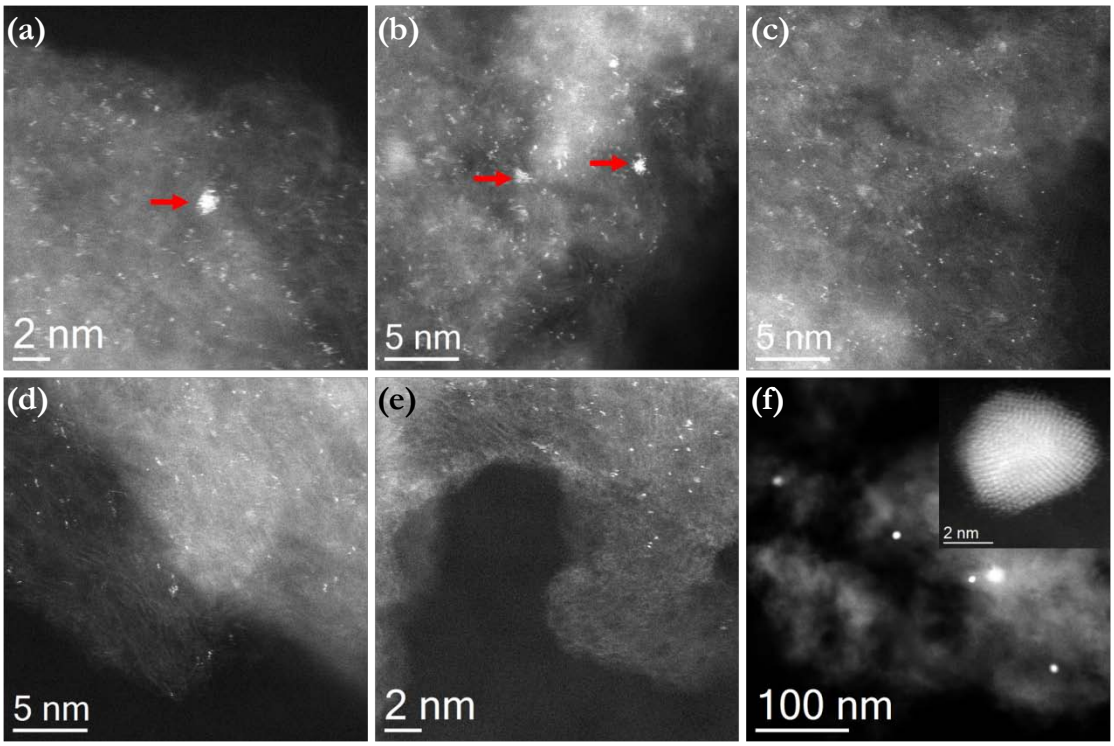

Figure 5.17: HAADF-STEM images of the Au/C-S_2O_3 catalyst. (a-c) Before use. (d-f) After use. Red arrows in (a, b) indicate sub-nm Au clusters. The inset in (f) is an enlarged Au nanoparticle.

5.6 Stability of atomic Au in the 2 wt% Au/C-AR catalysts

To further assess the stability of the atomically dispersed Au in the Au/C-AR catalyst, the Au loading was doubled to 2 wt%. Contrary to the trend exhibited by the 1 wt% Au/C-AR catalyst (Figure 5.9 (a)), the VCM productivity of the 2 wt% Au/C-AR catalyst decreased continuously after reaching a maximum at ~40 min (Figure 5.18 (a)). Concurrently, the white-line intensity measured from *in-situ* XANES plummeted shortly (~20 min) after the start of the reaction (Figure 5.18 (a)). These results can be associated with the transformation of Au(III) to Au(I) and Au(0) (Figure 5.18 (b)).

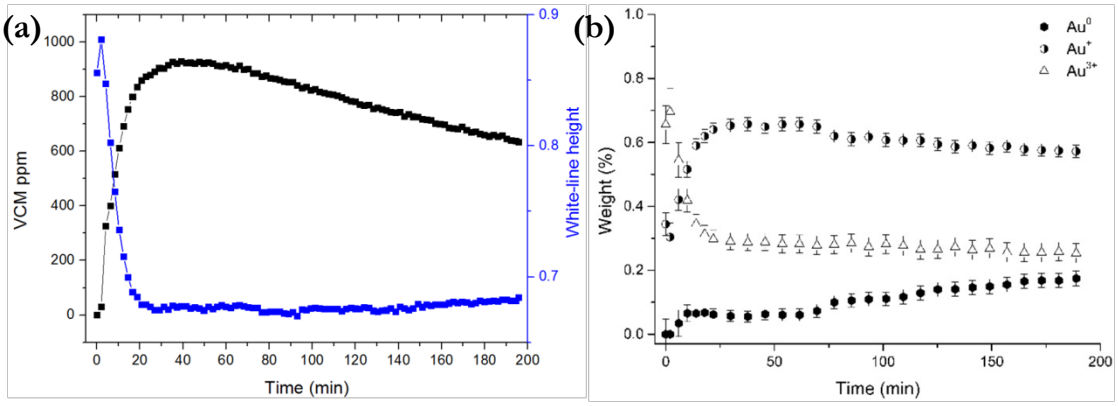

Figure 5.18: VCM productivity and *in-situ* characterization of the 2 wt% Au/C-AR catalyst as a function of time-on-line. (a) Catalytic performance as a function of time-on-line (black) and the change in normalized white-line intensity (blue) as a function of reaction time. (b) Linear combination fitting of the XANES data under reactions. *Courtesy of Grazia Malta.*

HAADF-STEM imaging shows that the fresh sample contained primarily atomically dispersed Au with the occasional occurrence of Au clusters (Figure 5.19), similar to the situation observed in the 1 wt% Au/C-AR analogue. After the reaction, in spite of the persistent presence of discrete Au atoms (Figure 5.20 (a, b)), quite a few very large Au particles were formed (Figure 5.20 (c, d)), indicating the sintering of atomic Au during exposure to C_2H_2 and HCl, which is in stark contrast to the exclusive presence of Au atoms and clusters observed in the used 1 wt% Au/C-AR sample (Figure 5.14). The presence of Au particles was consistent with the emergence of Au(0) signals in XANES during the reaction (Figure 5.18 (b)).

Counting the numbers of Au atoms over certain areas of the carbon support from several HAADF-STEM images gave estimated Au atom densities of 0.470 atoms/nm^2 and 0.154 atoms/nm^2 for the unused and used 2 wt% Au/C-AR catalysts respectively. This suggests that ~2/3 of atomic Au transformed into large Au particles during the reaction, leading to significantly decreased Au dispersion. Therefore, increasing the Au loading from 1 wt% to 2 wt% compromised the activity and stability of the Au/C-AR catalysts.

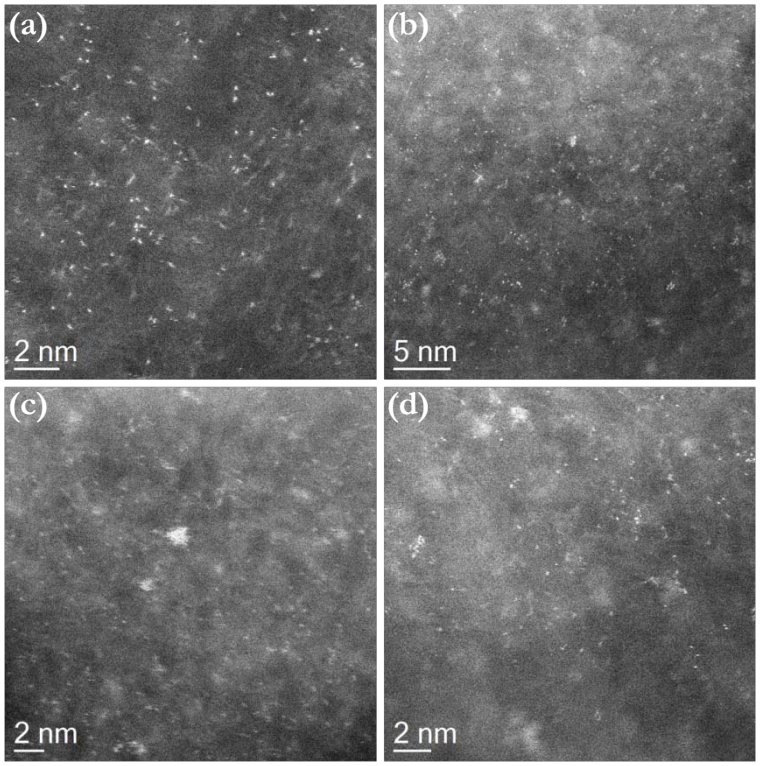

Figure 5.19: HAADF-STEM images of the 2 wt% Au/C-AR catalyst before use. Atomically dispersed Au could be easily seen, while a small number of sub-nm Au clusters were also present.

5.7 Theoretical modeling of acetylene hydrochlorination over a Au/C catalyst

For the three active catalysts, *i.e.*, Au/C-AR, Au/C-HNO_3, and Au/C-S_2O_3, the white-line intensity and VCM productivity could be linearly correlated throughout their induction periods and at steady states (Figure 5.15 (c)), indicating a significant role the highly dispersed Au(I) species plays in this reaction and that the activity of these catalyst systems is attributable to similar oxidation-state species. Notably, apart from the Au(I) species, a population of Au(III)-like species having high dispersion was also associated with all catalysts displaying high activity. This observation demonstrated that the Au(I)-Au(III) redox couple is a key feature of the active site of this catalyst, as originally predicted by Hutchings from correlations with standard electrode

potential.[1] A conjectural reaction pathway may start with the oxidative addition of HCl to Au chloride, followed by the addition of acetylene and reductive removal of VCM through a Au(I)-Au(III) redox couple. This mechanism has generally been disregarded, as it requires Au(I) rather than the more often observed Au(III).[31] However, we find the Au(I)/Au(III) ratio is ~1.5 at the steady state (Figure 5.11), and that activity can be associated with the presence of Au(I), as noted in several homogeneous systems.[32-33]

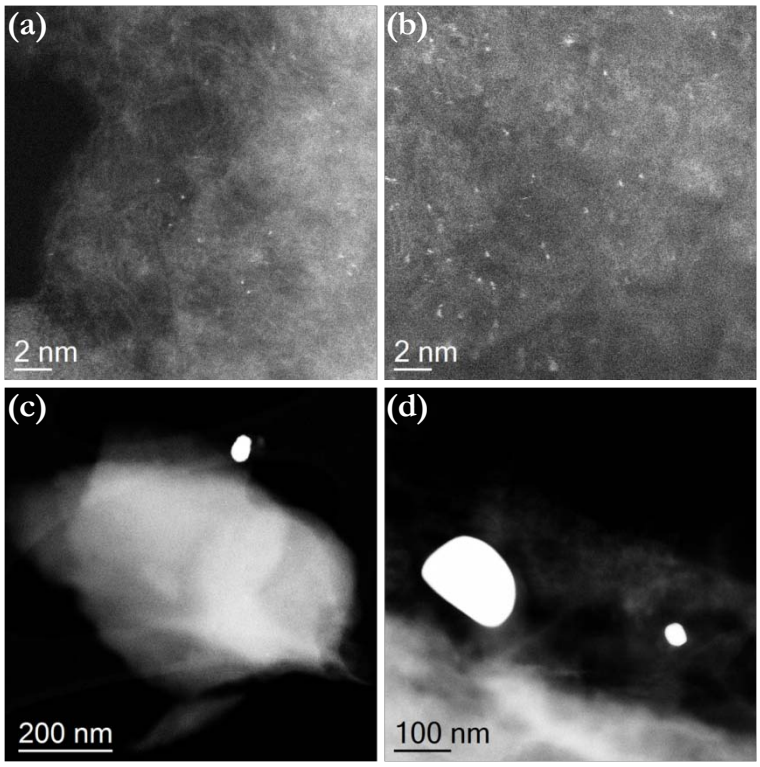

Figure 5.20: HAADF-STEM images of the 2 wt% Au/C-AR catalyst after use. (a, b) Atomically dispersed Au entities. (c, d) Large Au particles.

A density functional theory (DFT) calculation has been undertaken on the interaction of HCl with supported Au(I) in the form of AuCl to better understand the role of Au(I) (Figure 5.21). $AuCl_2H$ is formed from the combination of HCl and AuCl by overcoming a barrier of 98 kJ mol^{-1}. This species gives a Hirshfeld charge of 0.37e, nearly twice the value for AuCl (0.19e).

The former value is close to that for Au(III), which shows a charge of 0.41e when modeled as $AuCl_3$, implying a more Au(III)-like character for $AuCl_2H$. The most stable configuration for a HCl molecule interacting with AuCl has a binding energy of -131 kJ mol^{-1}, in comparison to -73 kJ mol^{-1} for $AuCl_2H$. The dissociation of HCl is hindered by hydrogen bonding. Furthermore, this site can easily be blocked by additional HCl, and other paths for dissociation are less favorable given the lower adsorption energy of -52 kJ mol^{-1} for HCl. The transfer of a hydrogen atom to C_2H_2 forms $AuCl_2(C_2H_3)$, which is more stable than $AuCl_2H(C_2H_2)$ with a binding energy of -224 kJ mol^{-1} compared to -128 kJ mol^{-1}. VCM is then generated by transfer of a chlorine atom to the (C_2H_3) group. This theoretical mechanism that describes a catalytic cycle where the interaction between cationic Au species and reactant molecules leads to VCM production, is fully compatible with the experimental data.

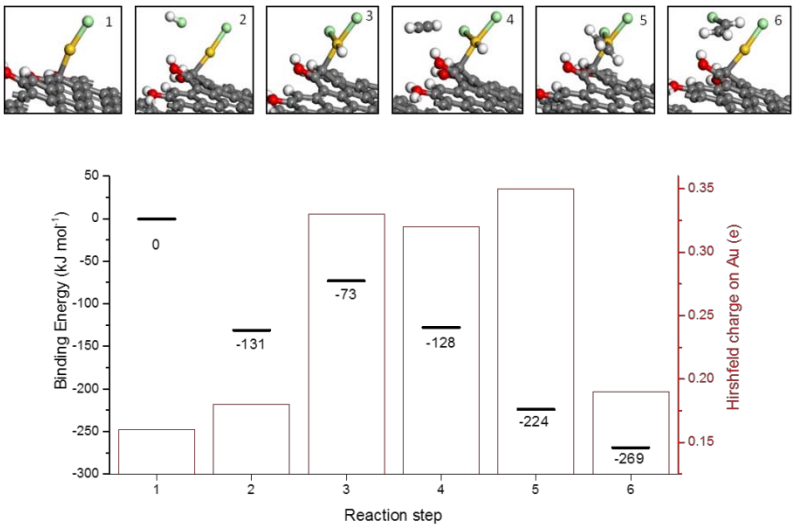

Figure 5.21: Mechanism for the transformation of AuCl to $AuCl_2H$ and formation of VCM reproducing AuCl. Gold: Au atoms; green: Cl atoms; white: H atoms; gray: C atoms; red: O atoms. The bar chart shows binding energies for each energy minima and the Hirshfeld charge on each Au atom. Energies are given with reference to the geometry-optimized configuration of AuCl on the C support and gas phase acetylene and HCl. *Courtesy of Adam Thetford.*

5.8 Summary and Outlook

This study has highlighted the importance of isolated cationic gold chloride species in facilitating a redox reaction mechanism for the industrially relevant hydrochlorination of acetylene. A combination of *in-situ* XAFS analysis under reaction conditions and *ex-situ* HAADF-STEM characterization confirmed the primary components of Au species in active Au/C catalysts to be isolated monomeric and dimeric gold cations. The nearly 100% Au dispersion achieved by judicious choice of solvent and precursor maximized the accessible sites to attain high activity for the catalysts. The active form of these catalysts is analogous to the homogeneous single site Au cations typically associated with liquid phase organic transformations of alkynes.[34-35] The finding that single site supported Au catalysts can be successfully applied to high temperature reactions opens up research avenues where heterogeneous and homogeneous catalysis can work together to create new classes of materials for these industrially important reactions.

The microstructure-based studies on atomically dispersed Au/C catalysts can be further expanded in the following directions:

(1) In principle, if a suitable systematic set of samples were to be prepared, the proportions of atomic Au, dimers (and trimers), clusters and nanoparticles could be statistically determined at different stages of the reaction. Since acetylene hydrochlorination is a gas phase reaction, the loss of metal components by leaching is not an issue. Thus, the evolution of different Au species may be monitored and correlated to the activity and white-line intensity during the reaction.

(2) *In-situ* STEM characterization in a windowed cell system could be applied to dynamically observe the changes occurring in the Au/C catalysts. Although resolving individual Au atoms under a gas environment might be challenging, aberration corrected HAADF imaging can

potentially identify Au clusters and nanoparticles. In the case where no clusters or nanoparticles are observed, the presence of atomically dispersed Au species only may be inferred, which should be further verified by *ex-situ* HAADF imaging.

5.9 Acknowledgements

The work presented in this chapter is in collaboration with a number of institutions and researchers, including Cardiff Catalysis Institute in Cardiff University led by Prof. Graham J. Hutchings, UK Catalysis Hub in Rutherford Appleton Laboratory led by Prof. C. Richard A. Catlow, and Dr. Peter Johnson from Johnson Matthey. Their guidance and support are much appreciated.

The Au/C catalyst syntheses, testing and *ex-situ* characterizations of XRD and XPS were carried out by Grazia Malta, Dr. Simon A. Kondrat, Dr. Simon J. Freakley, and Dr. David J. Morgan at Cardiff University. The *in-situ* XAFS analysis and interpretation were performed by Dr. Simon J. Freakley, Dr. Simon A. Kondrat, Grazia Malta and Dr. Peter P. Wells. The DFT study was conducted by Dr. Adam Thetford. Their various contributions to this work are gratefully acknowledged. This work has been published in *Science*[36].

5.10 References

1. Hutchings, G. J., Vapor phase hydrochlorination of acetylene: correlation of catalytic activity of supported metal chloride catalysts. *J. Catal.* **1985**, 96, 292-295.

2. Nkosi, B.; Coville, N. J.; Hutchings, G. J., Vapour phase hydrochlorination of acetylene with group VIII and IB metal chloride catalysts. *Appl. Catal.* **1988**, 43, 33-39.

3. Zhou, K.; Jia, J.; Li, C.; Xu, H.; Zhou, J.; Luo, G.; Wei, F., A low content Au-based catalyst for hydrochlorination of C_2H_2 and its industrial scale-up for future PVC processes. *Green Chem.*

2015, 17, 356-364.

4. Johnston, P.; Carthey, N.; Hutchings, G. J., Discovery, development, and commercialization of gold catalysts for acetylene hydrochlorination. *J. Am. Chem. Soc.* **2015**, 137, 14548-14557.

5. Ciriminna, R.; Falletta, E.; Della Pina, C.; Teles, J. H.; Pagliaro, M., Industrial applications of gold catalysis. *Angew. Chem. Int. Ed.* **2016**, 55, 14210-14217.

6. Nkosi, B.; Coville, N. J.; Hutchings, G. J.; Adams, M. D.; Friedl, J.; Wagner, F. E., Hydrochlorination of acetylene using gold catalysts: a study of catalyst deactivation. *J. Catal.* **1991**, 128, 366-377.

7. Hong, G.; Tian, X.; Jiang, B.; Liao, Z.; Wang, J.; Yang, Y.; Zheng, J., Improvement of performance of a Au–Cu/AC catalyst using thiol for acetylene hydrochlorination reaction. *RSC Adv.* **2016**, 6, 3806-3814.

8. Zhu, M.; Wang, Q.; Chen, K.; Wang, Y.; Huang, C.; Dai, H.; Yu, F.; Kang, L.; Dai, B., Development of a heterogeneous non-mercury catalyst for acetylene hydrochlorination. *ACS Catal.* **2015**, 5, 5306-5316.

9. Tian, X.; Hong, G.; Jiang, B.; Lu, F.; Liao, Z.; Wang, J.; Yang, Y., Efficient Au^0/C catalyst synthesized by a new method for acetylene hydrochlorination. *RSC Adv.* **2015**, 5, 46366-46371.

10. Nkosi, B.; Adams, M. D.; Coville, N. J.; Hutchings, G. J., Hydrochlorination of acetylene using carbon-supported gold catalysts: a study of catalyst reactivation. *J. Catal.* **1991**, 128, 378-386.

11. Liu, X.; Conte, M.; Elias, D.; Lu, L.; Morgan, D. J.; Freakley, S. J.; Johnston, P.; Kiely, C. J.; Hutchings, G. J., Investigation of the active species in the carbon-supported gold catalyst for acetylene hydrochlorination. *Catal. Sci. Technol.* **2016**, 6, 5144-5153.

12. Carrettin, S.; Blanco, M. C.; Corma, A.; Hashmi, A. S. K., Heterogeneous gold ‐ catalysed synthesis of phenols. *Adv. Synth. Catal.* **2006**, 348, 1283-1288.

13. Huang, L.; Rudolph, M.; Rominger, F.; Hashmi, A. S. K., Photosensitizer ‐ free visible ‐ light ‐ mediated gold ‐ catalyzed 1, 2 ‐ difunctionalization of alkynes. *Angew. Chem. Int. Ed.* **2016**, 55, 4808-4813.

14. Flytzani-Stephanopoulos, M., Gold atoms stabilized on various supports catalyze the water–gas shift reaction. *Acc. Chem. Res.* **2013**, 47, 783-792.

15. Deng, W.; Frenkel, A. I.; Si, R.; Flytzani-Stephanopoulos, M., Reaction-relevant gold

structures in the low temperature water-gas shift reaction on Au-CeO_2. *J. Phys. Chem. C* **2008**, 112, 12834-12840.

16. Fierro-Gonzalez, J. C.; Gates, B. C., Mononuclear Au^{III} and Au^{I} complexes bonded to zeolite NaY: catalysts for CO oxidation at 298 K. *J. Phys. Chem. B* **2004**, 108, 16999-17002.

17. Lu, J.; Aydin, C.; Browning, N. D.; Gates, B. C., Imaging isolated gold atom catalytic sites in zeolite NaY. *Angew. Chem. Int. Ed.* **2012**, 24, 5842-5846.

18. Blanco Jaimes, M. C.; Böhling, C.; Serrano‐Becerra, J. M.; Hashmi, A. S. K., Highly active mononuclear NAC–gold (I) catalysts. *Angew. Chem. Int. Ed.* **2013**, 52, 7963-7966.

19. Blanco Jaimes, M. C.; Rominger, F.; Pereira, M. M.; Carrilho, R. M. B.; Carabineiro, S. A. C.; Hashmi, A. S. K., Highly active phosphite gold(I) catalysts for intramolecular hydroalkoxylation, enyne cyclization and furanyne cyclization. *Chem. Commun.* **2014**, 50, 4937-4940.

20. Pantelouris, A.; Kueper, G.; Hormes, J.; Feldmann, C.; Jansen, M., Anionic gold in Cs_3AuO and Rb_3AuO established by X-ray absorption spectroscopy. *J. Am. Chem. Soc.* **1995**, 117, 11749-11753.

21. Tibiletti, D.; Fonseca, A. A.-.; Burch, R.; Chen, Y.; Fisher, J. M.; Goguet, A.; Hardacre, C.; Hu, P.; Thompsett, D., DFT and in situ EXAFS investigation of gold/ceria low-temperature water gas shift catalysts: identification of the nature of the active form of gold. *J. Phys. Chem. B* **2005**, 109, 22553-22559.

22. Chang, S.-Y.; Uehara, A.; Booth, S. G.; Ignatyev, K.; Mosselmans, J. F. W.; Dryfe, R. A. W.; Schroeder, S. L. M., Structure and bonding in Au(I) chloride species: a critical examination of X-ray absorption spectroscopy (XAS) data. *RSC Adv.* **2015**, 5, 6912-6918.

23. Berrodier, I.; Farges, F.; Benedetti, M.; Winterer, M.; Brown, G. E.; Deveughèle, M., Adsorption mechanisms of trivalent gold on iron- and aluminum-(oxy)hydroxides. Part 1: X-ray absorption and Raman scattering spectroscopic studies of Au(III) adsorbed on ferrihydrite, goethite, and boehmite. *Geochim. Cosmochim. Acta* **2004**, 68, 3019-3042.

24. Kitagawa, H.; Kojima, N.; Matsushita, N.; Ban, T.; Tsujikawa, I., Studies of mixed-valence states in three-dimensional halogen-bridged gold compounds, $Cs_2Au^{I}Au^{III}X_6$ (X = Cl, Br or I). Part 1. Synthesis, X-ray powder diffraction, and electron spin resonance studies of $CsAu_{0.6}Br_{2.6}$. *J. Chem. Soc., Dalton Trans.* **1991**, 3115-3119.

25. Kitagawa, H.; Kojima, N.; Nakajima, T., Studies of mixed-valence states in three-dimensional halogen-bridged gold compounds, $Cs_2Au^{I}Au^{III}X_6$, (X = Cl, Br or I). Part 2. X-ray photoelectron spectroscopic study. *J. Chem. Soc., Dalton Trans.* **1991**, 3121-3125.

26. Glemser, O.; Sauer, H. *Handbook of preparative inorganic chemistry*; Academic Press: New York, 1965.

27. Hu, P.; Duchesne, P. N.; Song, Y.; Zhang, P.; Chen, S., Self-assembly and chemical reactivity of alkenes on platinum nanoparticles. *Langmuir* **2015**, 31, 522-528.

28. Weiher, N.; Beesley, A. M.; Tsapatsaris, N.; Delannoy, L.; Louis, C.; van Bokhoven, J. A.; Schroeder, S. L. M., Activation of oxygen by metallic gold in Au/TiO_2 catalysts. *J. Am. Chem. Soc.* **2007**, 129, 2240-2241.

29. Fernández-García, M., XANES analysis of catalytic systems under reaction conditions. *Cat. Rev. - Sci. Eng.* **2002**, 44, 59-121.

30. Bishop, P. T.; Carthey, N. A.; Johnston, P. Catalyst comprising gold and a sulphur containing ligand on a support and method for its preparation. US Patent WO2013008004 A3, May 16, 2013.

31. Conte, M.; Carley, A. F.; Heirene, C.; Willock, D. J.; Johnston, P.; Herzing, A. A.; Kiely, C. J.; Hutchings, G. J., Hydrochlorination of acetylene using a supported gold catalyst: a study of the reaction mechanism. *J. Catal.* **2007**, 250, 231-239.

32. Pernpointner, M.; Hashmi, A. S. K., Fully relativistic, comparative investigation of gold and platinum alkyne complexes of relevance for the catalysis of nucleophilic additions to alkynes. *J. Chem. Theory Comput.* **2009**, 5, 2717-2725.

33. Hashmi, A. S. K., Fire and ice: a gold(III) monohydride. *Angew. Chem. Int. Ed.* **2012**, 51, 12935-12936.

34. Zhang, G.; Peng, Y.; Cui, L.; Zhang, L., Gold - catalyzed homogeneous oxidative cross - coupling reactions. *Angew. Chem. Int. Ed.* **2009**, 48, 3112-3115.

35. Hashmi, A. S. K.; Hutchings, G. J., Gold catalysis. *Angew. Chem. Int. Ed.* **2006**, 45, 7896-7936.

36. Malta, G.; Kondrat, S. A.; Freakley, S. J.; Davies, C. J.; Lu, L.; Dawson, S.; Thetford, A.; Gibson, E. K.; Morgan, D. J.; Jones, W., Identification of single-site gold catalysis in acetylene hydrochlorination. *Science* **2017**, 355, 1399-1403.

Chapter 6

Preferential atomic Pt re-dispersion over Co particles by heat treatment in CO_2 methanation catalysts

6.1 Introduction

There has been growing research interest in the reduction of carbon dioxide (CO_2) as a route to alleviate the impact of greenhouse gases on global climate.[1-2] CO_2 methanation can effectively convert CO_2 emissions into a substitute hydrocarbon fuel,[3] potentially building a sustainable closed carbon cycle. This process may also enable large-scale storage of renewable energy by utilizing hydrogen generated from electrolysis to transform CO_2 to methane fuel, which can then be stored in existing natural gas facilities. Nanostructured cobalt-based catalysts have been identified as active for hydrogenation,[4-7] especially when promoted by separate particles of platinum and other precious metals.[8-9]

Kinetic studies by Somorjai's group on CO_2 and CO hydrogenation employing size- and morphology-controlled Co and Pt nanoparticles supported on mesoporous silica have focused on investigating the reaction mechanism, the effect of catalyst particle size, and the introduction of a promoter such as Pt.[10-12] These studies showed that a mixture of size-controlled nanoparticles of pure Co and Pt produced remarkably higher CO_2 methanation rates than Co-Pt bimetallic nanoparticles. A cooperation was proposed to exist between the two metals during reaction, wherein CO_2 dissociated on the Co particles, and H_2 dissociated on Pt. Hydrogen

spillover was thought to occur from the Pt nanoparticles onto the oxide support, followed by surface migration of H atoms to the Co nanoparticles and subsequent generation of CH_4. The significant lowering of apparent activation energy noted upon the introduction of the Pt nanoparticles suggested that the rate-determining step is the surface hydrogen transport from Pt to Co.[12]

Acceptor-doped $BaZrO_3$ and $BaCeO_3$ ceramics have been used as proton conducting materials for solid oxide fuel cell electrolytes,[13] in which mobile protons are incorporated into the bulk of these perovskite structured oxides. The potential application of this class of materials as oxide supports for metal-catalyzed hydrogenation and dehydrogenation reactions is therefore of considerable interest. It has been previously observed[14] that in Cr-catalyzed non-oxidative ethane dehydrogenation perovskite structured $BaZrO_3$ and $BaCeO_3$ supports provided more than one order of magnitude higher ethylene formation rate compared to γ-Al_2O_3, which could be rationalized by possible proton incorporation in the perovskite supports via hydrogen spillover from chromium.[15]

Herein, we present a study involving the use of Co nanoparticles with Pt decoration for CO_2 methanation, in which pure and yttria-doped $BaZrO_3$ supports are shown to promote the activity and selectivity of the catalyst when compared to the γ-Al_2O_3 support. Extensive HAADF-STEM analysis reveals surface migration and atomic dispersion of the Pt species onto Co particles caused by heat treatment that is expected to facilitate hydrogen spillover. It also demonstrated that different strengths in metal-support interaction could give rise to the significant increase in reaction rate we measure on $BaZrO_3$ relative to γ-Al_2O_3.

6.2 Preparation of Co and Pt nanoparticles and supported Co-Pt catalysts

Co nanoparticles were synthesized using a Schlenk technique under Ar atmosphere following a previously described procedure.[10] In an N_2-filled glovebox 1.025 g of cobalt carbonyl was dissolved in 6 mL of 1,2-dichlorobenzene (DCB). Then 0.3 mL of oleic acid and 30 mL of DCB were mixed in a three-neck flask, followed by 20 min degassing and another 20 min stirring under Ar prior to heating to 170 °C. The $Co_2(CO)_8$ in DCB was rapidly injected under vigorous stirring conditions, causing an immediate color change to black, indicative of the formation of colloidal Co nanoparticles. After 20 min heating at 170 °C and then cooling to 50 °C, the solution was mixed with 20 mL of DCB and 40 mL of 2-proponal. Subsequent centrifugation (8000 rpm) led to the precipitation of Co nanoparticles, which was re-dispersed and stored in chloroform for use.

The preparation of Pt nanoparticles followed a method reported by Sun *et al.*[16] whereby 80 mg of platinum(II) acetylacetonate ($Pt(acac)_2$) was introduced to 10 mL of 1-octadecene mixed with 1 mL of oleic acid and 1 mL of oleylamine. The solution was degassed for 20 min and then stirred under an Ar atmosphere for another 20 min. Vigorous stirring continued as the solution was gradually heated to 120 °C and held there for 30 min to dissolve the $Pt(acac)_2$. A further temperature increase to 200 °C turned the solution to black, suggesting the formation of Pt nanoparticles. After maintaining at 200 °C for 30 min and subsequent cooling to room temperature, 20 mL of acetone and 20 mL of methanol were added to the solution prior to centrifugation (8000 rpm), resulting in the precipitation of Pt nanoparticles. The precipitated solid was re-dispersed and stored in chloroform until required for use.

The support materials $BaZrO_3$, $BaZr_{0.95}Y_{0.05}O_{3-\delta}$, and $BaZr_{0.8}Y_{0.2}O_{3-\delta}$ were synthesized with a modified Pechini method. Aqueous solutions of $Ba(NO_3)_2$, $Zr(NO_3)_2$, and $Y(NO_3)_2$ were prepared with metal concentrations determined by redox titration. The chelating agent EDTA and citric acid monohydrate were added to the metal precursor solutions in stoichiometric mixtures matching the desired compositions. The pH was adjusted to >8.5 by adding ammonium hydroxide. After the evaporation of excess water, the resultant homogeneous gel was calcined in an oven at 300 °C, generating a powder which was then sintered at 1300 °C for 4 h. The incipient wetness approach[15, 17] was applied with chloroform as the solvent to deposit colloidally prepared metal nanoparticles onto the synthesized pure oxide (either 1.0 wt% Co, 1.0 wt% Pt, or 1.0 wt% Co +0.2 wt% Pt, respectively designated as 1Co, 1Pt, or 0.2Pt1Co hereafter). These samples were placed in a muffle furnace in air and heated at 500 °C for 1 h before use. For comparative purposes, Co and Pt supported on γ-Al_2O_3 were also prepared using incipient wetness.

6.3 Catalytic testing of supported Co-Pt catalysts

The catalytic activities of the supported Co-only and Co-Pt catalysts (0.2 g) were tested between 200 and 350 °C (Figure 6.1 (a)), with the CH_4 formation rate normalized by the total catalyst mass. It should therefore be noted that normalization based on support surface area would give an even greater rate enhancement for the lower surface area $BaZrO_3$ support. The specific surface areas of the γ-Al_2O_3 and $BaZrO_3$ materials were measured as 54 and 2 $m^2\ g^{-1}$, respectively. During the catalytic test, the 0.2Pt1Co/$BaZrO_3$ and 0.2Pt1Co/γ-Al_2O_3 catalysts both exhibited remarkably higher CH_4 production rates than their respective Co-only counterparts with the same support material (Figure 6.1 (a)). This is in good agreement with a cooperative methanation

reaction mechanism[12, 18] whereby H_2 and CO_2 dissociate on Pt and Co respectively. The spillover of H atoms from the Pt onto the Co is then required to form CH_4. The use of a Co-free $1Pt/BaZrO_3$ catalyst led to no CH_4 formation and only minimal CO formation, substantiating the key role played by the Co phase in CO_2 activation. The change from γ-Al_2O_3 to $BaZrO_3$ as the support for the bimetallic catalyst provided a more than 6-fold increase in CH_4 formation rate at 325 °C.

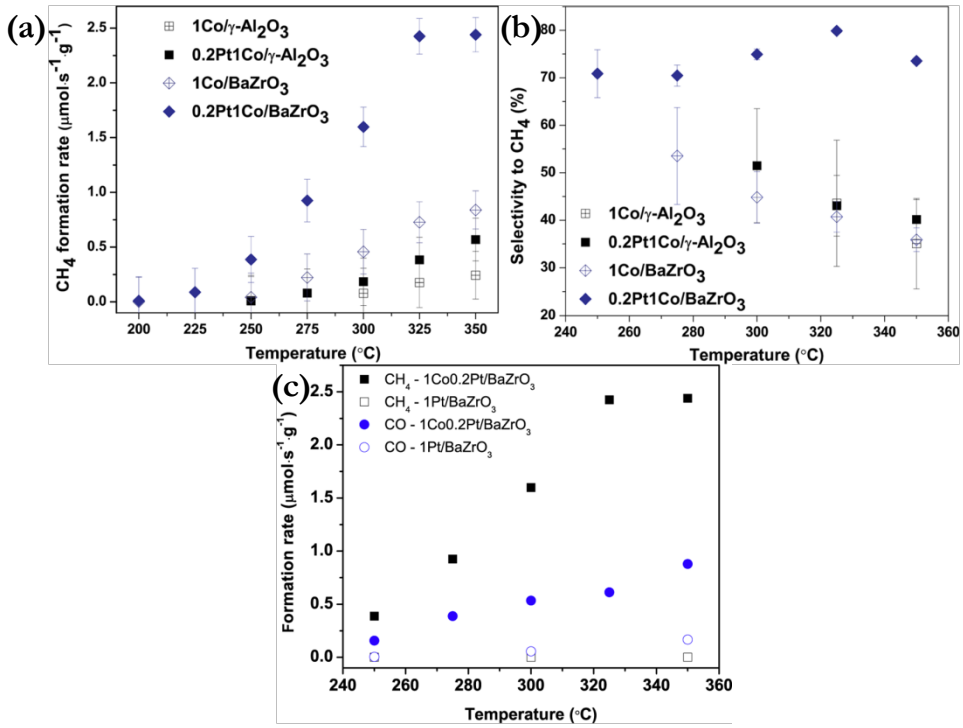

Figure 6.1: Catalytic performance of the supported metal catalysts as a function of reaction temperature. (a) CH_4 formation rate and (b) selectivity to CH_4 of the $1Co/\gamma$-Al_2O_3, $0.2Pt1Co/\gamma$-Al_2O_3, $1Co/BaZrO_3$, and $0.2Pt1Co/BaZrO_3$ catalysts. (c) CH_4 and CO formation rates of the $1Pt/BaZrO_3$ and $0.2Pt1Co/BaZrO_3$ catalysts. *Courtesy of Dr. Hyun Ho Shin.*

Gas-phase selectivity to CH_4 was measured for each catalyst after 10 min on stream, and the only gas-phase species detected were CH_4, CO_2, CO, H_2, and H_2O. For the γ-Al_2O_3 supported and $1Co/BaZrO_3$ catalysts, the selectivity to CH_4 decreased with increasing temperature (Figure 6.1 (b)). However, the $0.2Pt1Co/BaZrO_3$ catalyst was able to maintain a high CH_4 selectivity

(>70%) over the 250-350 ˚C temperature range, reaching a maximum of 80% at 325 ˚C which was double the measured selectivity of 43% over γ-Al_2O_3.

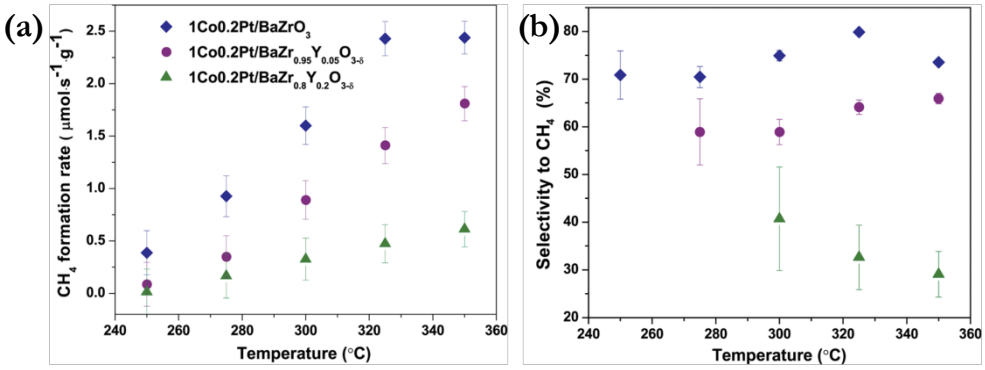

Figure 6.2: Influence of Y doping of $BaZrO_3$ on the catalytic performance of supported 1Co0.2Pt catalysts. (a) CH_4 formation rate. (b) Selectivity to CH_4. *Courtesy of Dr. Hyun Ho Shin.*

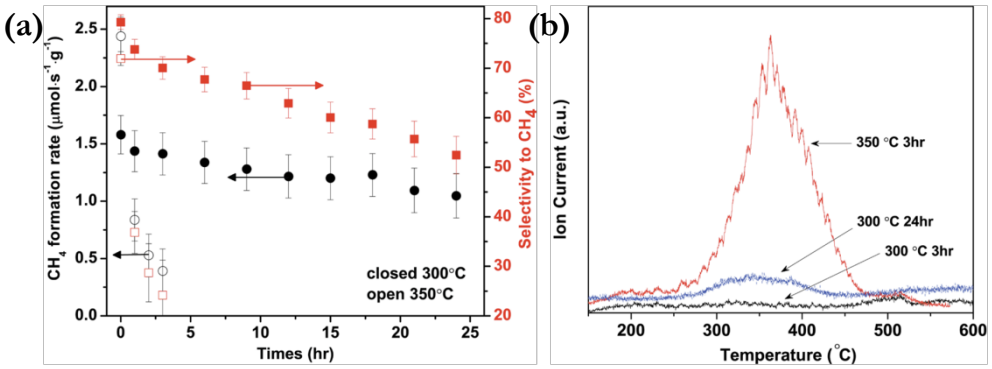

Figure 6.3: Evaluation of catalyst stability. (a) Temporal evolution of CH_4 formation rate and selectivity for the 0.2Pt1Co/$BaZrO_3$ catalyst at 300 and 350 ˚C. (b) Temperature-programmed oxidation of the 0.2Pt1Co/$BaZrO_3$ catalyst after testing for 3 and 24 h at 300 ˚C and for 3 h at 350 ˚C. *Courtesy of Dr. Hyun Ho Shin.*

The possible role of bulk proton incorporation in these catalysts was investigated by substituting 5 and 20 at% of the Zr sites with Y doping of the $BaZrO_3$ support in the 1Co0.2Pt catalysts. In principle, proton incorporation into the lattice should neutralize the charge imbalance induced by Y doping.[19] Higher Y doping levels gave a lower CH_4 formation rate and selectivity (Figure 6.2), although all the catalysts with Y-doped $BaZrO_3$ displayed higher activities than those observed for the γ-Al_2O_3 variants. The CH_4 formation rates were 2.4, 1.8, and 0.5 ×

10^{-6} mol s^{-1} g^{-1} for 0.2Pt1Co supported on $BaZrO_3$, $BaZr_{0.95}Y_{0.05}O_{3-\delta}$, and $BaZr_{0.8}Y_{0.2}O_{3-\delta}$, respectively, at 325 °C, all of which were higher than the 0.4 × 10^{-6} mol s^{-1} g^{-1} obtained for the 0.2Pt1Co/γ-Al_2O_3 catalyst.

The catalytic stability of the 0.2Pt1Co/$BaZrO_3$ catalyst was evaluated at 300 °C for 24 h and 350 °C for 3 h, respectively. Over a reaction time of 24 h at 300 °C, the catalyst performance gradually degraded to 66.6% of the initial CH_4 formation rate and 65.8% of the initial selectivity to CH_4 (Figure 6.3 (a)). When the temperature was raised to 350 °C, the CH_4 formation rate and selectivity rapidly dropped to 25.9% and 42.5% of their initial values respectively within 3 h (Figure 6.3 (a)). Temperature-programmed oxidation (TPO) of the 0.2Pt1Co/$BaZrO_3$, catalyst tested at 350 °C for 3 h caused CO_2 evolution which occurred as a single peak centered at 380 °C (Figure 6.3 (b)). In contrast, the catalyst working at 300 °C for 3 h exhibited no CO_2 evolution during TPO, while after a longer reaction time of 24 h at 300 °C, a relatively small peak for CO_2 evolution started to appear at ~360 °C (Figure 6.3 (b)). These TPO experiments pointed to carbon deposition as a potential cause for catalyst deactivation at 300 and 350 °C. In addition, the low oxidation temperature of the deposited carbon suggested that this carbon was not graphitic in character. During the 3 h reaction at 350 °C, the number of deposited C atoms per Co atom was measured to be 0.4, which, assuming a constant deposition rate, would give an estimated carbon deposition rate of 1.5 × 10^{-2} μmol s^{-1} g^{-1}, which is much lower than the observed reaction rates. This deactivation via carbon deposition is in accord with the constantly declining CH_4 production rate observed for the 0.2Pt1Co/$BaZrO_3$ catalyst between 300 and 350 °C (Figure 6.3 (a)).

6.4 Structural characterization of supported Co-Pt catalysts

STEM examination of as-prepared colloidal Pt and Co nanoparticles evidenced the formation of well-dispersed nanocrystals with relatively uniform sizes of ~2.5 nm and ~12 nm, respectively (Figures 6.4 and 6.5). The Pt nanoparticles were highly crystalline (Figure 6.4), with Figure 6.4 (c, d) showing a pair of HAADF- and BF-STEM images of a nanoparticle viewed along the <110> projection of face-centered cubic (fcc) Pt. Within the Co particles a core-shell structure is readily discernible with a sharp transition from a lower intensity shell to a brighter core in the HAADF-STEM imaging mode, suggesting the presence of a 6 nm diameter hexagonal close packed (hcp) metallic Co core enclosed by a 3 nm thick Co oxide shell (Figure 6.5). Additional proof for this proposed core-shell configuration is provided by the appearance of Moiré fringes in the core region of a particle (Figure 6.5 (b)), indicative of overlapping crystalline grains. This oxidation is probably a result of the aerobic transfer of the catalyst sample into the electron microscope.

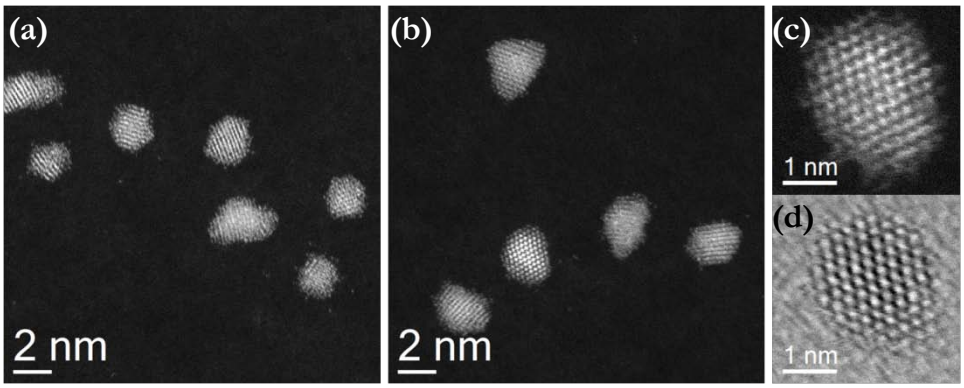

Figure 6.4: STEM images of as-prepared Pt nanoparticles. (a, b) Lower magnification HAADF-STEM images exhibiting well dispersed Pt nanoparticles with a uniform size of ~2.5 nm. (c, d) Higher magnification HAADF- and BF-STEM image pair of a Pt nanoparticle with the expected fcc crystal structure.

These colloidally prepared metal nanoparticles were deposited onto either a γ-Al_2O_3 or

$BaZrO_3$ support. Prior to microscopy observation or catalytic testing, the catalyst materials were subjected to a calcination treatment in air at 500 °C to eliminate moisture and contaminants, followed by reduction in dilute H_2 (10 vol%) at 450 °C in an effort to reduce cobalt oxide to cobalt metal.[18] In common with the bare Co particles, supported Co particles also exhibited a characteristic Co-CoO_x core-shell structure (Figures 6.6 (a-c), 6.7 (a-c)), again probably due to oxidation in air during sample transfer. Lattice fringe analysis of the oxide shell in the Co particles supported on γ-Al_2O_3 and $BaZrO_3$ identified the shell as a mixture of cubic spinel Co_3O_4, cubic rock salt CoO, and hexagonal Co_2O_3 phases (Figure 6.8 (a-c, g-i), Table 6.1). Similar analysis of the particle cores in the $BaZrO_3$ support sample verified our initial judgment that the inner cores were metallic Co in the hcp structure (Figure 6.8 (d-f, j-l), Table 6.2).

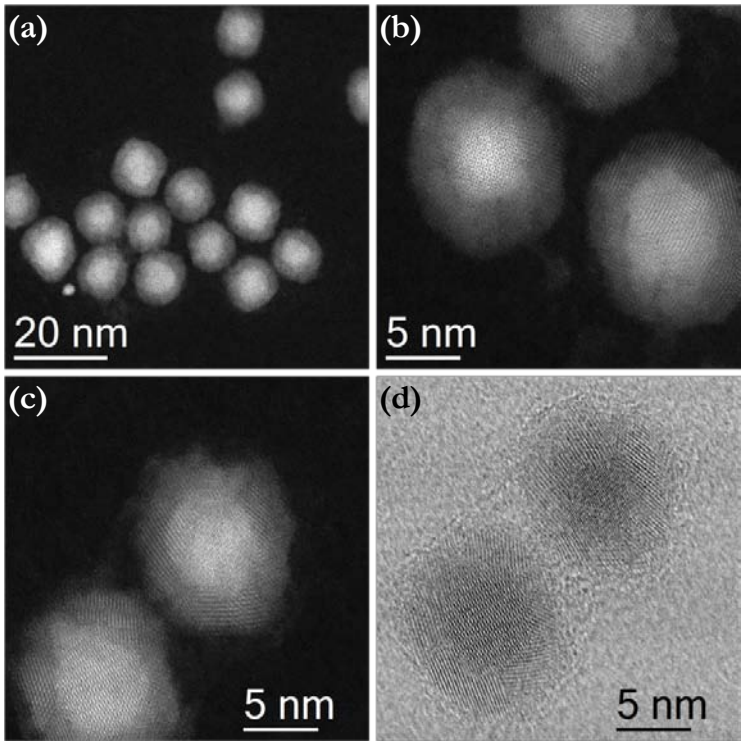

Figure 6.5: HAADF- and BF-STEM images of as-prepared Co nanoparticles. (a) Lower magnification HAADF-STEM image showing well dispersed spherical Co particles with core-shell structures. (b-d) Higher magnification STEM images of Co particles displaying different lattice fringe patterns in the core and shell regions.

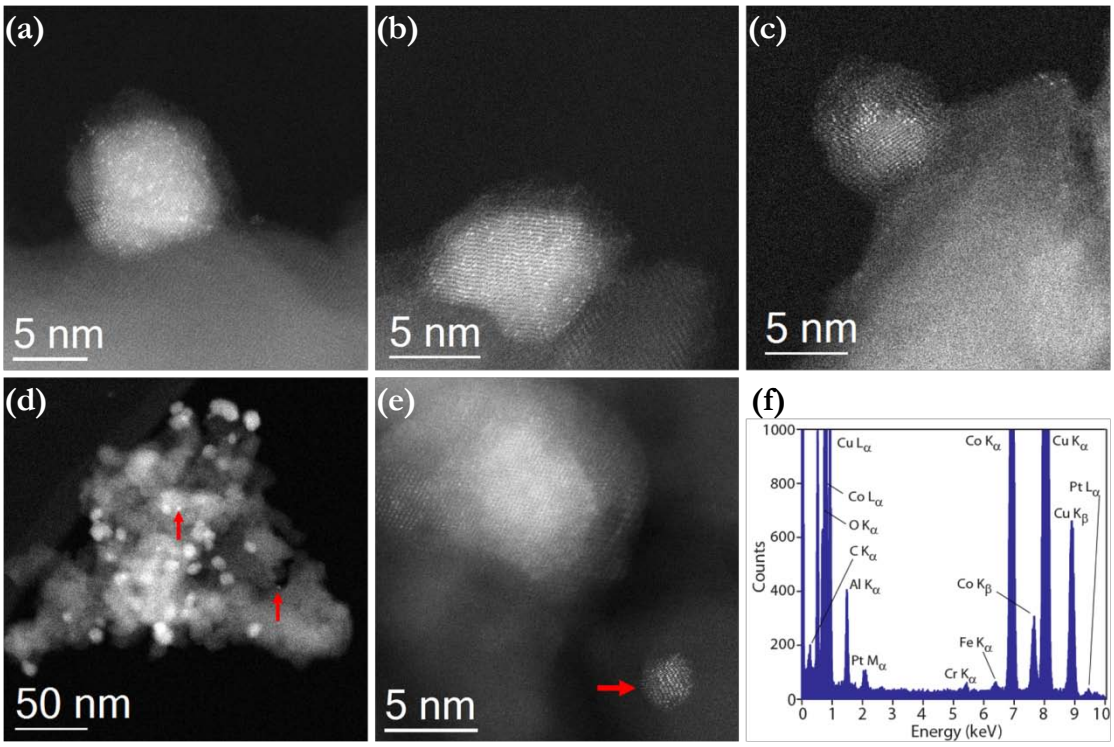

Figure 6.6: STEM characterization of the 0.2Pt1Co/Al_2O_3 catalyst. (a-e) HAADF-STEM images. (f) XEDS spectrum from a single Co particle. Red arrows in (d) and (e) mark Pt nanoparticles.

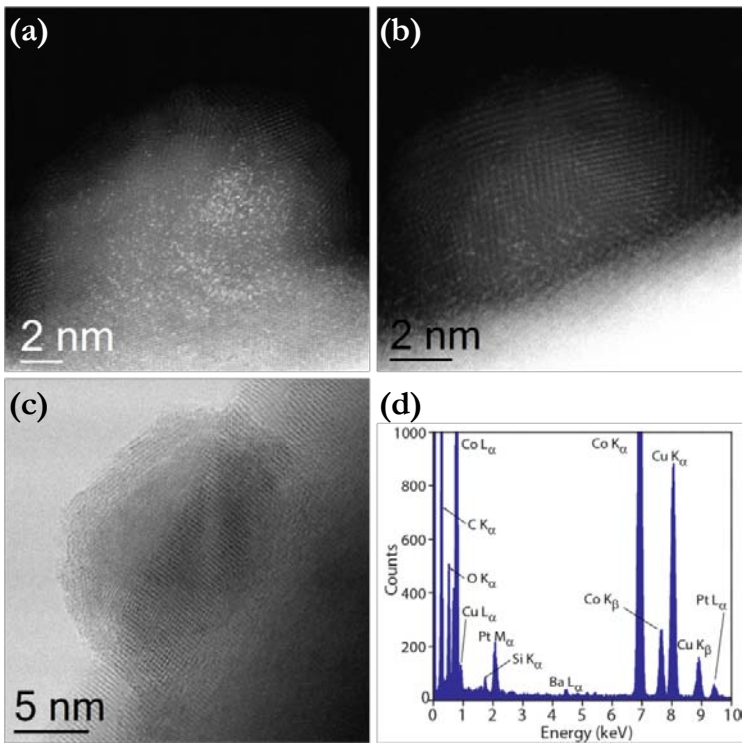

Figure 6.7: STEM characterization of the 0.2Pt1Co/$BaZrO_3$ catalyst. (a, b) HAADF- and (c) BF-STEM images. (d) XEDS spectrum from a single Co particle.

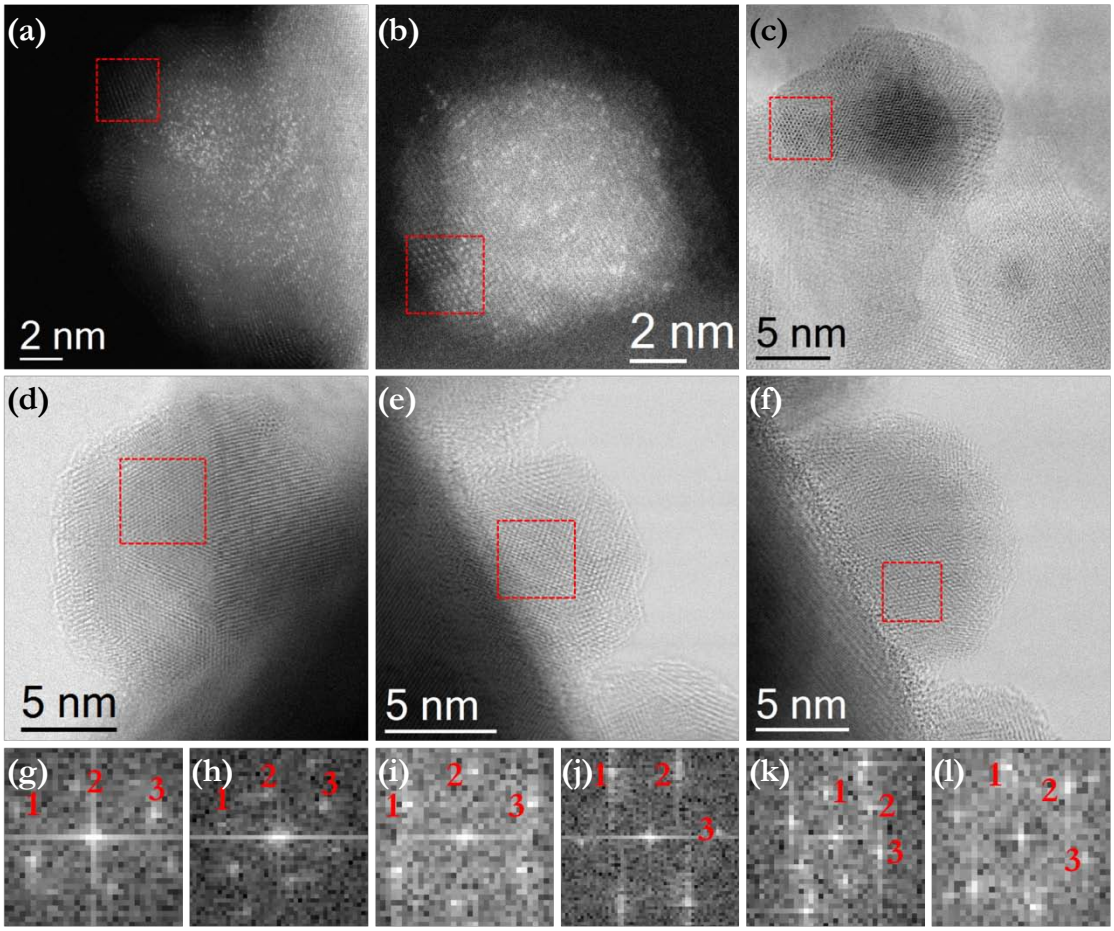

Figure 6.8: Phase analysis of Co-CoO_x core-shell particles in the supported catalysts. (a-c) Regions of interest in the shells of Co particles on $BaZrO_3$ (a) and γ-Al_2O_3 (b, c), and (g-i) the corresponding FFTs. (d-f) Regions of interest in the cores of Co particles on $BaZrO_3$, and (j-l) the corresponding FFTs. Red squares in (a-f) indicate the regions of interest for FFT analysis.

Table 6.1: Lattice fringe analysis of oxide shells in Co particles shown in Figure 6.8 (a-c).

Oxide shells	(a): hexagonal Co_2O_3 $[1\bar{1}0]$		(b): cubic Co_3O_4 [114]		(c): cubic CoO $[1\bar{1}0]$	
	Measured	Matching	Measured	Matching	Measured	Matching
Plane 1	1.6 Å	1.6 Å (116)	2.3 Å	2.4 Å $(31\bar{1})$	2.5 Å	2.5 Å (111)
Plane 2	2.5 Å	2.4 Å (110)	2.9 Å	2.9 Å $(2\bar{2}0)$	2.5 Å	2.5 Å $(11\bar{1})$
Plane 3	2.1 Å	2.2 Å (006)	2.4 Å	2.4 Å $(13\bar{1})$	2.2 Å	2.1 Å (002)
<1, 2>	50.8°	47.9°	62.0°	64.8°	68.2°	70.5°
<2, 3>	89.1°	90.0°	69.8°	64.8°	55.2°	54.7°
<3, 1>	40.2°	42.1°	48.2°	50.5°	56.6°	55.7°

Table 6.2: Lattice fringe analysis of metallic cores in Co particles shown in Figure 6.8 (d-f).

Metallic cores	(d): hexagonal Co [$10\bar{1}$]		(e): hexagonal Co [001]		(f): hexagonal Co [100]	
	Measured	Matching	Measured	Matching	Measured	Matching
Plane 1	2.0 Å	1.9 Å (101)	2.2 Å	2.2 Å (100)	2.0 Å	1.9 Å (011)
Plane 2	2.1 Å	1.9 Å ($1\bar{1}1$)	2.2 Å	2.2 Å (010)	2.0 Å	1.9 Å ($01\bar{1}$)
Plane 3	2.2 Å	2.2 Å (010)	2.1 Å	2.2 Å ($1\bar{1}0$)	2.1 Å	2.0 Å (002)
<1, 2>	54.0°	52.3°	61.9°	60.0°	53.8°	56.5°
<2, 3>	62.7°	63.9°	59.1°	60.0°	65.8°	61.8°
<3, 1>	63.3°	63.9°	59.0°	60.0°	60.4°	61.8°

Contrary to the expected co-existence of individual Pt and Co nanoparticles in the supported catalysts, the majority of the Pt species were actually found to exist as an atomic dispersion on the Co particles, as revealed by HAADF-STEM imaging (Figure 6.6 (a-e), Figure 6.7 (a, b)). The Pt atoms were preferentially located at the Co/CoO_x interface, probably because the grain boundaries and oxygen vacancies in the polycrystalline shell accommodated facile inward diffusion of atomic Pt, whose further advance would be interrupted by the more tightly packed array of the hcp Co atoms making up the core. The distribution of Pt atoms on the Co surface distinguishes this structure from a homogeneous Co-Pt alloy.

The co-existence of Co and Pt within individual particles was confirmed by local XEDS analysis in both the γ-Al_2O_3 and $BaZrO_3$ supported catalysts (Figures 6.6 (f), 6.7 (d)). In the case of 0.2Pt1Co/Al_2O_3 catalyst, there were sporadic appearances of Pt nanoparticles, while atomic Pt was rarely detected on the γ-Al_2O_3 support (Figure 6.6 (a-e)). Such observations over the $BaZrO_3$ support were quite challenging, because in both HAADF- and BF-STEM modes, the considerable thickness and high atomic number composition of $BaZrO_3$ would very likely

overshadow contributions from Pt nanoparticles and Pt atoms (if any) located on the support. However, the possible presence of the two types of Pt species over $BaZrO_3$ could not be excluded.

The observation of Co and Pt species suggests that while isolated Pt and Co particles might exist in the as-prepared samples, the subsequent pre-treatment has mobilized Pt to decorate the Co surface. Counting the individual Pt atoms visible on a number of Co particles over the two supports yielded values between ~50 and 450 atoms. Re-assembling these Pt atoms could form spherical particles of between ~1.1 and 2.35 nm in diameter. Since some out-of-focus atoms would not be counted, the populations of Pt atoms per Co particle approximately match the expected number of Pt atoms within individual nanoparticles initially deposited onto the support. Judging from the counting of individual Pt atoms, this decoration probably originated from Pt nanoparticles initially in close proximity to, or even on, the Co phase.

It should be noted that a 2-3 nm Pt nanoparticle will melt at between 950 and 1438 °C depending on the method of parameter estimation,[20] taking into account the melting-point depression effect on smaller particles.[21] Thus, the temperatures of 500 °C and 450 °C used for catalyst activation are between one-third and one-half of the melting point for the Pt nanoparticles (*i.e.*, above the Hüttig temperature for surface diffusion, but below the Tammann temperature for bulk diffusion), corroborating the idea that the high-temperature pre-treatment caused Pt migration. For the larger Co particles, similar calculations yielded estimated melting points of 1370-1382 °C, explaining their relative stability against high temperature treatment. Notably, while previous literature[22] studied the role of 1.8 nm Pt nanoparticles in reducing Co, only rates and mechanisms for 12 nm Pt particles were reported. These larger Pt particles would

no doubt be much more stable during any catalyst pre-treatment step.

A peculiarity of the mobile Pt species is that they did not tend to agglomerate, but instead further adjusted their size to individual atoms. This might imply a relatively weak interaction between Pt and both support materials that allowed free motion of Pt, as compared to the strong anchoring effect on the metallic Co surface that created a shortcut to bring adsorbed hydrogen into intimate contact with dissociated CO_2 on the Co particles. The observed Pt decoration here does not necessarily invalidate the previously proposed mechanism of hydrogen diffusion from spatially separated Pt to Co nanoparticles. However, the atomically dispersed Pt could certainly provide enhanced availability of hydrogen in intimate contact with the dissociated CO_2 on the Co surface.

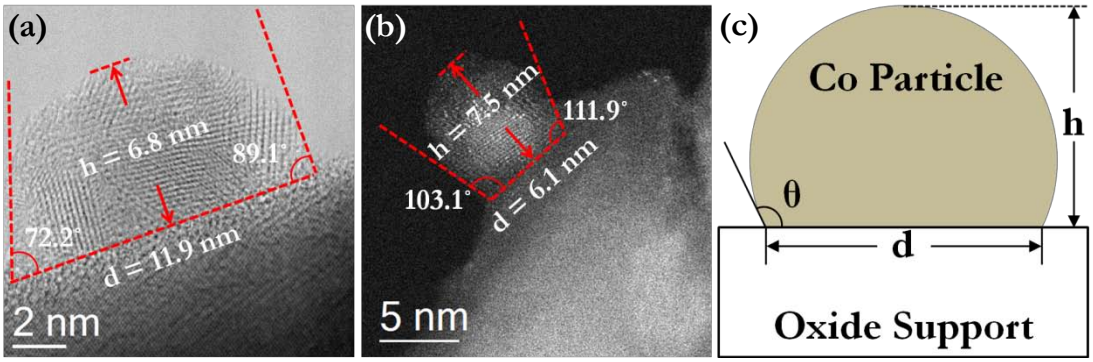

Figure 6.9: Measurements of wetting behaviors of Co particles. (a) Wetting of Co on $BaZrO_3$. (b) Wetting of Co on γ-Al_2O_3. (c) Schematic of a Co particle wetting the oxide support.

The intimate decoration of Co with Pt might explain the detrimental effects of Y doping of $BaZrO_3$ on catalyst performance, which is perhaps in contrast to the previous proposals[10-12] that H transport between Co and Pt is an essential step in the reaction. The direct contact of atomically dispersed Pt with Co particles circumvents the need for longer range hydrogen transport, as it enables direct spillover from Pt to Co. Another possible explanation is that any

hydrogen available for the reaction was rapidly depleted due to bulk proton incorporation into the support.

There were marked improvements in both CH_4 formation rate and selectivity to CH_4 in the reaction when the $BaZrO_3$ type supports were used, as compared to the γ-Al_2O_3 support (Figure 6.1 (a, b)). The Pt decoration of the Co nanoparticles did not seem to appear to vary with support identity. STEM analysis indicated that the interaction between the Co particles and the respective oxide support might have contributed to the significantly improved catalytic performance associated with the $BaZrO_3$ support relative to γ-Al_2O_3 (Figures 6.6, 6.7). While there was limited wetting of Co particles on the γ-Al_2O_3 grains, Co formed a low contact angle interface with $BaZrO_3$. The validity of the heuristics could be further assessed by systematic evaluation of the wetting behaviors of Co particles over the two supports. Apart from the concept of contact angle θ, the ratio d/h, of the base diameter d to the particle height h, reflective of the particle shape, serves as another parameter characterizing Co wettability (Figure 6.9). Measurements of contact angles and the d/h ratios of a number of supported Co particles were performed based on STEM images. For $BaZrO_3$, the mean contact angle was $84^\circ \pm 22^\circ$, and the mean d/h ratio was 1.66 ± 0.38; for γ-Al_2O_3, the mean contact angle was $106^\circ \pm 14^\circ$, and the mean d/h ratio was 0.82 ± 0.22. Representative examples of measurements for both supports are provided in Figure 6.9 (a, b). The lower contact angle and higher d/h ratio associated with $BaZrO_3$ support suggested that Co particles in contact with $BaZrO_3$ were more flattened and thus could expose more surface area and possess a longer perimeter at the metal/oxide interface per unit volume to serve as active catalytic sites. More Pt atoms might also be attached to the Co surface. This stronger interaction between Co and the $BaZrO_3$ support could positively affect the

activity and selectivity in the Pt-Co catalyst. Both CO_2 dissociation over Co and H_2 dissociation over Pt atoms would most likely benefit from this effect.

Such support-dependent particle wetting behaviors can be classified into a type of metal-support interaction, which has been frequently demonstrated to appreciably influence the catalytic performance of supported metal catalysts.[23-27] A number of factors are generally considered to contribute to the change in activity: (i) particle morphological changes, (ii) electronic interactions between metal and support, and (iii) the creation of active sites at the metal-support interface. With direct relevance to the current work, more significant spreading of Co on TiO_2 was noted compared to that of Co on a SiO_2 support,[28] which was proposed to lead to a higher activity of Co/TiO_2 than Co/SiO_2 towards CO_2 hydrogenation.[18] In a recent report by Zhao *et al.*[29], analytical electron microscopy was employed to identify flattening of Ir particles supported on TiO_2 as being responsible for a 20-fold increase in activity for propene hydrogenation. As with this previous report, herein we are not able to unambiguously decide whether the beneficial effect on activity in our system was purely morphological or if it was also impacted by electronic interactions. However, we can conclude that both atomic dispersion of Pt over Co and wetting of Co on the support contribute in a positive manner to promoting catalytic activity and selectivity in CO_2 methanation.

6.5 Summary and Outlook

The $BaZrO_3$ support brought remarkable improvements to a Pt and Co nanoparticle co-operative catalytic mechanism for CO_2 hydrogenation. The most active catalyst structure comprised Co nanoparticles supported on $BaZrO_3$, with the Co surface decorated with highly

dispersed Pt atoms. The Pt species in atomic dispersion provided sites for hydrogen dissociation, while Co was responsible for dissociating CO_2. Heat-induced diffusion and spreading of Pt atoms from small (~2.5 nm) Pt nanoparticles led to their decoration over the Co particles. The wettability of Co particles on $BaZrO_3$ and γ-Al_2O_3 was also quantitatively compared, which indicated that $BaZrO_3$ led to smaller contact angles and more flattened particle shapes, reflecting a stronger metal-support interaction. This catalyst sextupled the CH_4 formation rate and provided higher CH_4 selectivity when compared to an analogous Co-Pt catalyst supported on γ-Al_2O_3. Carbon deposition was considered to be the primary cause of catalyst deactivation as suggested by TPO experiments.

Studies to further advance this current work include:

(1) It would be worth examining the supported Co-Pt catalysts after the reaction using STEM. By doing this, we would determine whether or not the Pt species remained atomically dispersed on the Co particles. Possible modifications of the wetting behaviors of Co particles over $BaZrO_3$ and γ-Al_2O_3 after use could also be evaluated. In addition, such experiments could aid in the direct visualization of any carbonaceous deposits that might form during methanation.

(2) *In-situ* microscopy observation would be of interest to directly monitor the changes in catalyst structure under reaction conditions. Under exposure to H_2 and CO_2 gases, the Co particles should get progressively more reduced, allowing us to visualize the real-time interactions between the Co particles and the support. While *in-situ* conditions might degrade the spatial resolution of HAADF-STEM, it should still be sufficiently capable of capturing the shrinkage of Pt nanoparticles and the diffusion of Pt atoms on a light element support such as Al_2O_3.

6.6 Acknowledgements

The content described in this chapter is in collaboration with Prof. Steven McIntosh's group from the Department of Chemical Engineering at Lehigh University. His insightful guidance and advice is gratefully acknowledged.

The catalyst preparation, testing and TPO analysis were performed by Dr. Hyun Ho Shin and Dr. Zhou Yang. Their contributions to this work are much appreciated and fully acknowledged. The work described in Chapter 6 has been published in *ACS Catalysis*[30].

6.7 References

1. Ritter, S. K., What can we do with carbon dioxide. *Chem. Eng. News* **2007**, 85, 11-17.

2. Schwartz, S. E., Uncertainty in climate sensitivity: causes, consequences, challenges. *Energy Environ. Sci.* **2008**, 1, 430-453.

3. Centi, G.; Quadrelli, E. A.; Perathoner, S., Catalysis for CO_2 conversion: a key technology for rapid introduction of renewable energy in the value chain of chemical industries. *Energy Environ. Sci.* **2013**, 6, 1711-1731.

4. Alayoglu, S.; Beaumont, S. K.; Zheng, F.; Pushkarev, V. V.; Zheng, H.; Iablokov, V.; Liu, Z.; Guo, J.; Kruse, N.; Somorjai, G. A., CO_2 hydrogenation studies on Co and CoPt bimetallic nanoparticles under reaction conditions using TEM, XPS and NEXAFS. *Top. Catal.* **2011**, 54, 778-785.

5. Melaet, G.; Ralston, W. T.; Li, C.-S.; Alayoglu, S.; An, K.; Musselwhite, N.; Kalkan, B.; Somorjai, G. A., Evidence of highly active cobalt oxide catalyst for the Fischer–Tropsch synthesis and CO_2 hydrogenation. *J. Am. Chem. Soc.* **2014**, 136, 2260-2263.

6. Zhang, Y.; Jacobs, G.; Sparks, D. E.; Dry, M. E.; Davis, B. H., CO and CO_2 hydrogenation study on supported cobalt Fischer–Tropsch synthesis catalysts. *Catal. Today* **2002**, 71, 411-418.

7. Wang, W.; Wang, S.; Ma, X.; Gong, J., Recent advances in catalytic hydrogenation of carbon dioxide. *Chem. Soc. Rev.* **2011**, 40, 3703-3727.

8. Khodakov, A. Y.; Chu, W.; Fongarland, P., Advances in the development of novel cobalt

Fischer−Tropsch catalysts for synthesis of long-chain hydrocarbons and clean fuels. *Chem. Rev.* **2007**, 107, 1692-1744.

9. Schanke, D.; Vada, S.; Blekkan, E. A.; Hilmen, A. M.; Hoff, A.; Holmen, A., Study of Pt-promoted cobalt CO hydrogenation catalysts. *J. Catal.* **1995**, 156, 85-95.

10. Iablokov, V.; Beaumont, S. K.; Alayoglu, S.; Pushkarev, V. V.; Specht, C.; Gao, J.; Alivisatos, A. P.; Kruse, N.; Somorjai, G. A., Size-controlled model Co nanoparticle catalysts for CO_2 hydrogenation: synthesis, characterization, and catalytic reactions. *Nano Lett.* **2012**, 12, 3091-3096.

11. Beaumont, S. K.; Alayoglu, S.; Specht, C.; Michalak, W. D.; Pushkarev, V. V.; Guo, J.; Kruse, N.; Somorjai, G. A., Combining in situ NEXAFS spectroscopy and CO_2 methanation kinetics to study Pt and Co nanoparticle catalysts reveals key insights into the role of platinum in promoted cobalt catalysis. *J. Am. Chem. Soc.* **2014**, 136, 9898-9901.

12. Beaumont, S. K.; Alayoglu, S.; Specht, C.; Kruse, N.; Somorjai, G. A., A nanoscale demonstration of hydrogen atom spillover and surface diffusion across silica using the kinetics of CO_2 methanation catalyzed on spatially separate Pt and Co nanoparticles. *Nano Lett.* **2014**, 14, 4792-4796.

13. Iwahara, H.; Yajima, T.; Hibino, T.; Ozaki, K.; Suzuki, H., Protonic conduction in calcium, strontium and barium zirconates. *Solid State Ion.* **1993**, 61, 65-69.

14. Shin, H. H.; McIntosh, S., Proton-conducting perovskites as supports for Cr catalysts in short contact time ethane dehydrogenation. *ACS Catal.* **2014**, 5, 95-103.

15. Shin, H. H.; McIntosh, S., On the H_2/D_2 isotopic exchange rate of proton conducting barium cerates and zirconates. *J. Mater. Chem. A* **2013**, 1, 7639-7647.

16. Wang, C.; Daimon, H.; Lee, Y.; Kim, J.; Sun, S., Synthesis of monodisperse Pt nanocubes and their enhanced catalysis for oxygen reduction. *J. Am. Chem. Soc.* **2007**, 129, 6974-6975.

17. Levy, P.-J.; Primet, M., States of hydrogen adsorption on platinum-alumina and platinum-ceria catalysts: a temperature-programmed desorption study. *Appl. Catal.* **1991**, 70, 263-276.

18. Melaet, G. r. m.; Ralston, W. T.; Li, C.-S.; Alayoglu, S.; An, K.; Musselwhite, N.; Kalkan, B.; Somorjai, G. A., Evidence of highly active cobalt oxide catalyst for the Fischer-Tropsch synthesis and CO_2 hydrogenation. *J. Am. Chem. Soc.* **2014**, 136, 2260-2263.

19. Kreuer, K. D., Proton-conducting oxides. *Annu. Rev. Mater. Res.* **2003**, 33, 333-359.

20. Nanda, K. K.; Sahu, S. N.; Behera, S. N., Liquid-drop model for the size-dependent melting of low-dimensional systems. *Phys. Rev. A* **2002**, 66, 013208.

21. Buffat, P.; Borel, J. P., Size effect on the melting temperature of gold particles. *Phys. Rev. A* **1976**, 13, 2287.

22. Thomas, J. M.; Raja, R.; Lewis, D. W., Single - site heterogeneous catalysts. *Angew. Chem. Int. Ed.* **2005**, 44, 6456-6482.

23. Tauster, S. J.; Fung, S. C.; Baker, R. T. K.; Horsley, J. A., Strong interactions in supported-metal catalysts. *Science* **1981**, 211, 1121-1125.

24. Stakheev, A. Y.; Kustov, L. M., Effects of the support on the morphology and electronic properties of supported metal clusters: modern concepts and progress in 1990s. *Appl. Catal., A* **1999**, 188, 3-35.

25. Gonzalez-DelaCruz, V. M.; Holgado, J. P.; Pereñíguez, R.; Caballero, A., Morphology changes induced by strong metal–support interaction on a Ni–ceria catalytic system. *J. Catal.* **2008**, 257, 307-314.

26. Farmer, J. A.; Campbell, C. T., Ceria maintains smaller metal catalyst particles by strong metal-support bonding. *Science* **2010**, 329, 933-936.

27. Tauster, S. J., Strong metal-support interactions. *Acc. Chem. Res.* **1987**, 20, 389-394.

28. Riva, R.; Miessner, H.; Vitali, R.; Del Piero, G., Metal–support interaction in Co/SiO_2 and Co/TiO_2. *Appl. Catal., A* **2000**, 196, 111-123.

29. Zhao, E. W.; Zheng, H.; Ludden, K.; Xin, Y.; Hagelin-Weaver, H. E.; Bowers, C. R., Strong metal–support interactions enhance the pairwise selectivity of parahydrogen addition over Ir/TiO_2. *ACS Catal.* **2016**, 6, 974-978.

30. Shin, H. H.; Lu, L.; Yang, Z.; Kiely, C. J.; McIntosh, S., Cobalt catalysts decorated with platinum atoms supported on barium zirconate provide enhanced activity and selectivity for CO_2 Methanation. *ACS Catal.* **2016**, 6, 2811-2818.

Chapter 7

Controlling Ni dispersion on SiO_2 supports: An investigation of performance-size correlations in the CO_2 hydrogenation reaction

7.1 Introduction

As discussed in Chapter 6, the conversion of CO_2 into methane (CH_4) through hydrogenation has attracted considerable attention as a strategy to curb greenhouse gas emissions and meet the increasing demand for electricity storage in the form of chemical energy. In general, the methanation reaction is catalyzed by the metals from groups 8 to 10 of the periodic table, amongst which nickel is the most commonly utilized active metal catalyst for commercial methanation applications.[1] Compared to the cobalt based catalyst described in the previous chapter, nickel is more selective with a high activity towards CH_4 production and has a lower price.[2]

Advances in catalysis and nanotechnology have enabled us to manufacture ever smaller and catalytically more active metal particles. While smaller particles expose higher proportions of surface atoms to reactant gases, they do not necessarily linearly correspond to higher catalytic activity.[3-5] This phenomenon, wherein surface atoms in a supported metal catalyst are not equally active, is referred to as structure sensitivity and is likely to depend on the specific lattice plane terminations for π bond activation in CO_2, or σ bond activation in H_2 dissociation and C-H bond

formation.[3, 6] Different particle sizes affect the relative proportions and accessibility of stepped (less coordinated) and terrace (more coordinated) sites on the surface of supported catalyst nanoparticles. For example, atomic geometries are deemed incapable of accommodating π-bond activation when the particle dimension falls below 2 nm.[3] Despite numerous studies on the role of particle size and dispersion in CO hydrogenation over Co,[5, 7] such structure sensitivity effects for these critical particle sizes are poorly understood given the difficulty of synthesizing sub-2 nm particles of the first row transition metals of interest (*i.e.*, Co, Fe and Ni). Herein, a series of silica supported Ni nanoparticles with mean diameters ranging from 1-7 nm has been fabricated and used to demonstrate a distinct particle size effect that deepens our understanding of the structure sensitivity of CO_2 hydrogenation over Ni as a model structure sensitive reaction.

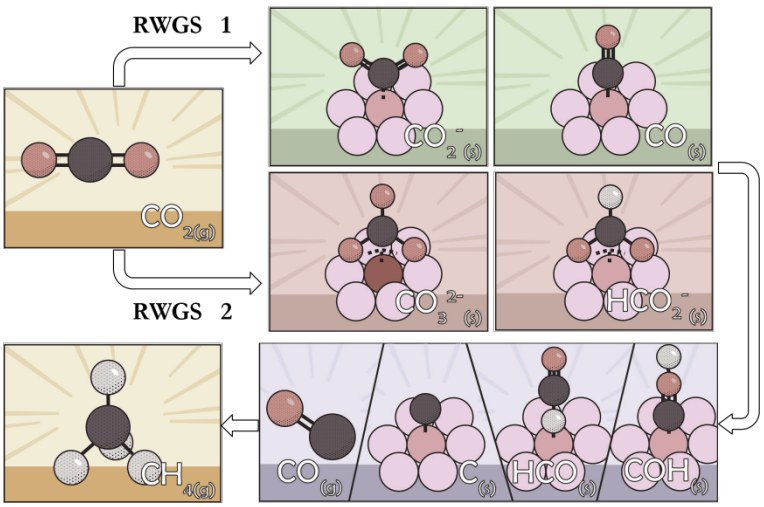

Figure 7.1: Proposed mechanisms of catalytic CO_2 hydrogenation over Ni. The two reaction pathways for the reverse water gas shift reaction are shown in the green and brown boxes. In pathway 1, CO_2 is directly dissociated to CO via a CO_2^- ion; the alternative pathway 2 depicts the reduction of CO_2 to a formate species. The subsequent purple panels indicate certain non-rate determining steps (RDS), where CO, C, HCO and COH species are formed during either CO dissociation and hydrogenation or the hydrogenation of $HCOO^-$. *Courtesy of Charlotte Vogt.*

CO_2 hydrogenation over Ni has been generally considered to proceed via a two-step

Langmuir-Hinshelwood mechanism,[8] wherein CO_2 dissociatively adsorbs with H_2 to form CO and H_2O via the reverse water gas shift (RWGS) reaction, followed by subsequent CO hydrogenation or initial dissociation to atomic C_{ads} and then subsequent hydrogenation (Figure 7.1). However, recent experimental and theoretical studies indicate that this reaction mechanism, especially on surfaces of non-model catalysts, is not well understood.[9-13] The RWGS reaction is believed to follow either of two possible mechanisms: firstly, the direct dissociation of CO_2 to CO via a CO_2^- ion (Figure 7.1, RWGS pathway 1), and secondly, transformation of a surface bound carbonate ion to a formate species (Figure 7.1, RWGS pathway 2). Ongoing debate in the literature largely originates from the direct comparison between model and non-model surface studies. Herein structure sensitivity is hypothesized to be associated with the reaction mechanism.

In this work, advanced electron microscopy is coupled with operando FT-IR analysis and quick X-ray absorption spectroscopy (XAS) to evaluate the impact of different atomic co-ordinations in metal nanoclusters on the activation of different bond types, and to enable quantification of the availability of active surface sites and their respective participation in the different reaction pathways.

7.2 Preparation and determination of particle size distributions in Ni/SiO_2 catalysts

Silica-supported Ni nanoparticles with varying Ni loadings (*i.e.,* 0.95, 1.7, 4.7, 5.0, 6.7, 11.8, 19.5, and 60.0 wt%) were prepared via homogeneous deposition precipitation.[14] Dispersed nickel hydroxide was precipitated from nickel nitrate mixed with an aqueous ammonia solution. The precipitate was filtered out, washed with water to remove ammonium nitrate and dried in air at

110 ˚C. Subsequent calcination of the hydroxide in flowing air at 250 ˚C for 1 h led to the formation of hydrated nickel oxide. The Ni/SiO_2 systems were prepared by impregnating nickel oxide with tetraethoxysilane followed by drying at room temperature and then at 150 ˚C. Samples were reduced in a flow quartz reactor and cooled to room temperature.

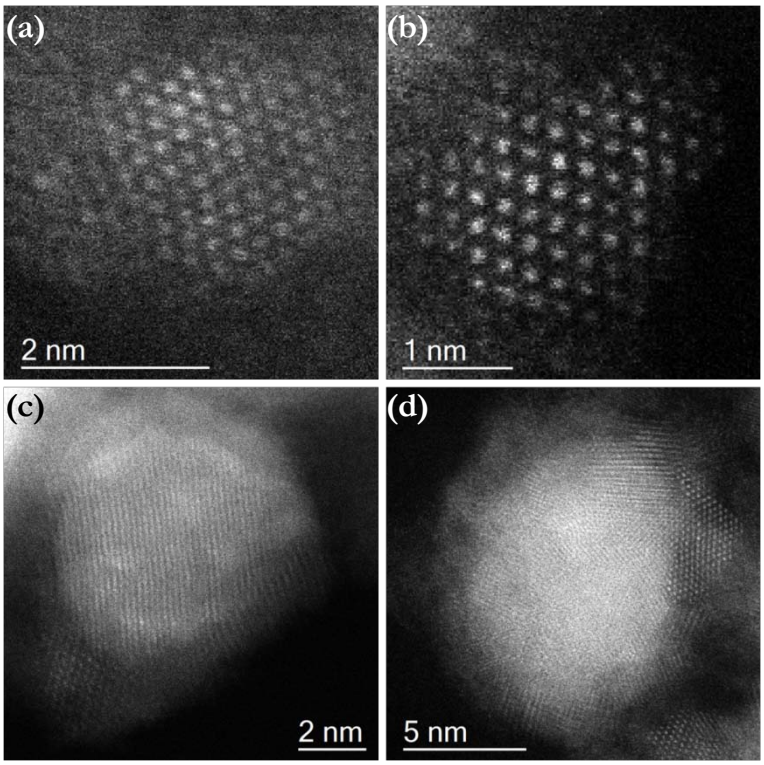

Figure 7.2: Representative HAADF-STEM images of (a, b) fully oxidized NiO particles (both viewed from the [110] projection of cubic NiO), and (c, d) partially oxidized Ni particles. (a) 11.8% Ni/SiO_2; (b, c) 19.5% Ni/SiO_2; (d) 60% Ni/SiO_2.

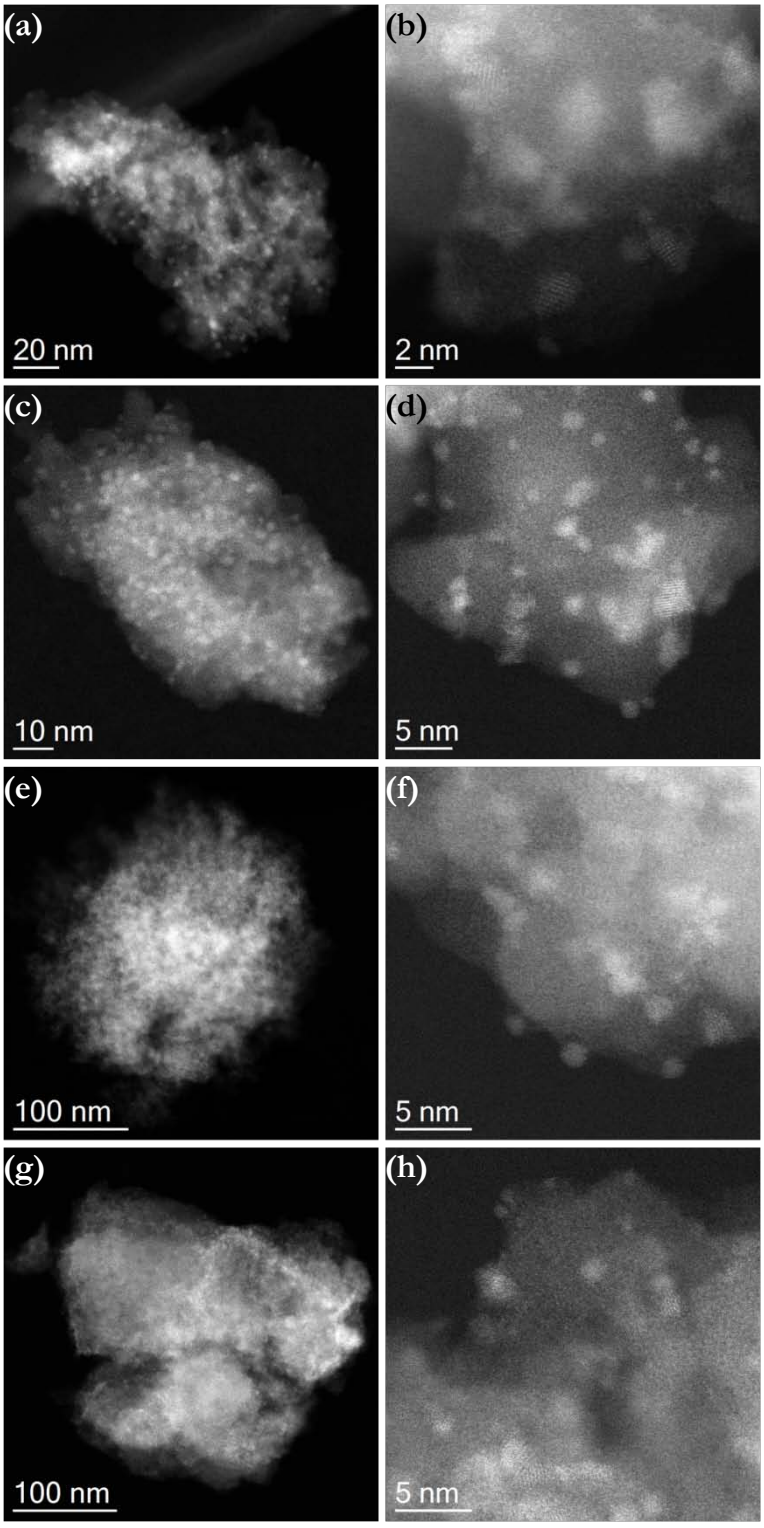

Figure 7.3: Representative HAADF-STEM images of the fresh Ni/SiO_2 catalyst samples after their respective reduction steps, and consecutive re-oxidation under ambient conditions. (a, b) 0.95% Ni/SiO_2; (c, d) 5.0% Ni/SiO_2; (e, f) 4.7% Ni/SiO_2; (g, h) 6.7% Ni/SiO_2.

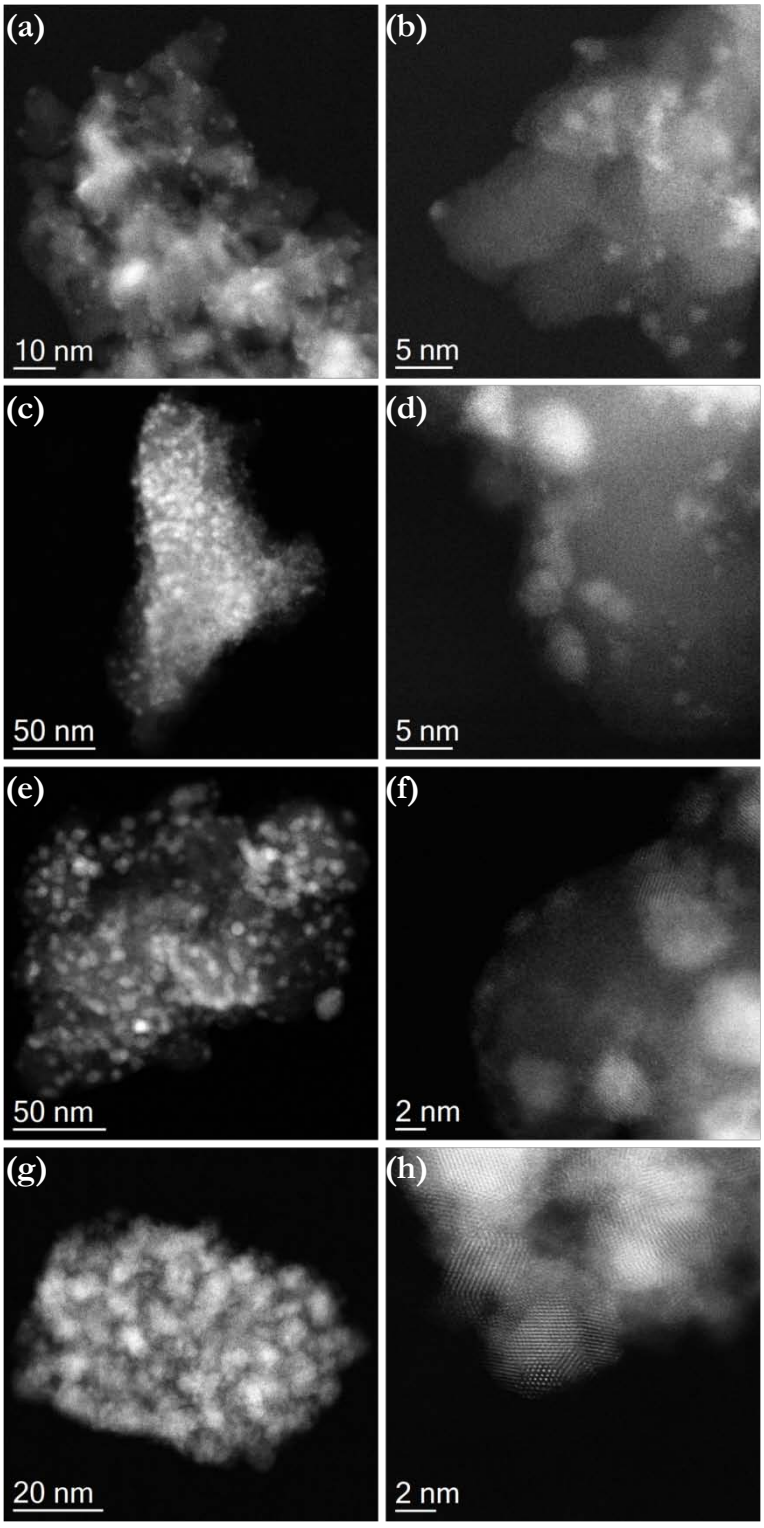

Figure 7.4: Representative HAADF-STEM images of the fresh Ni/SiO_2 catalyst samples after their respective reduction steps, and consecutive re-oxidation under ambient conditions. (a, b) 1.7% Ni/SiO_2; (c, d) 11.8% Ni/SiO_2; (e, f) 19.5% Ni/SiO_2; (g, h) 60.0% Ni/SiO_2.

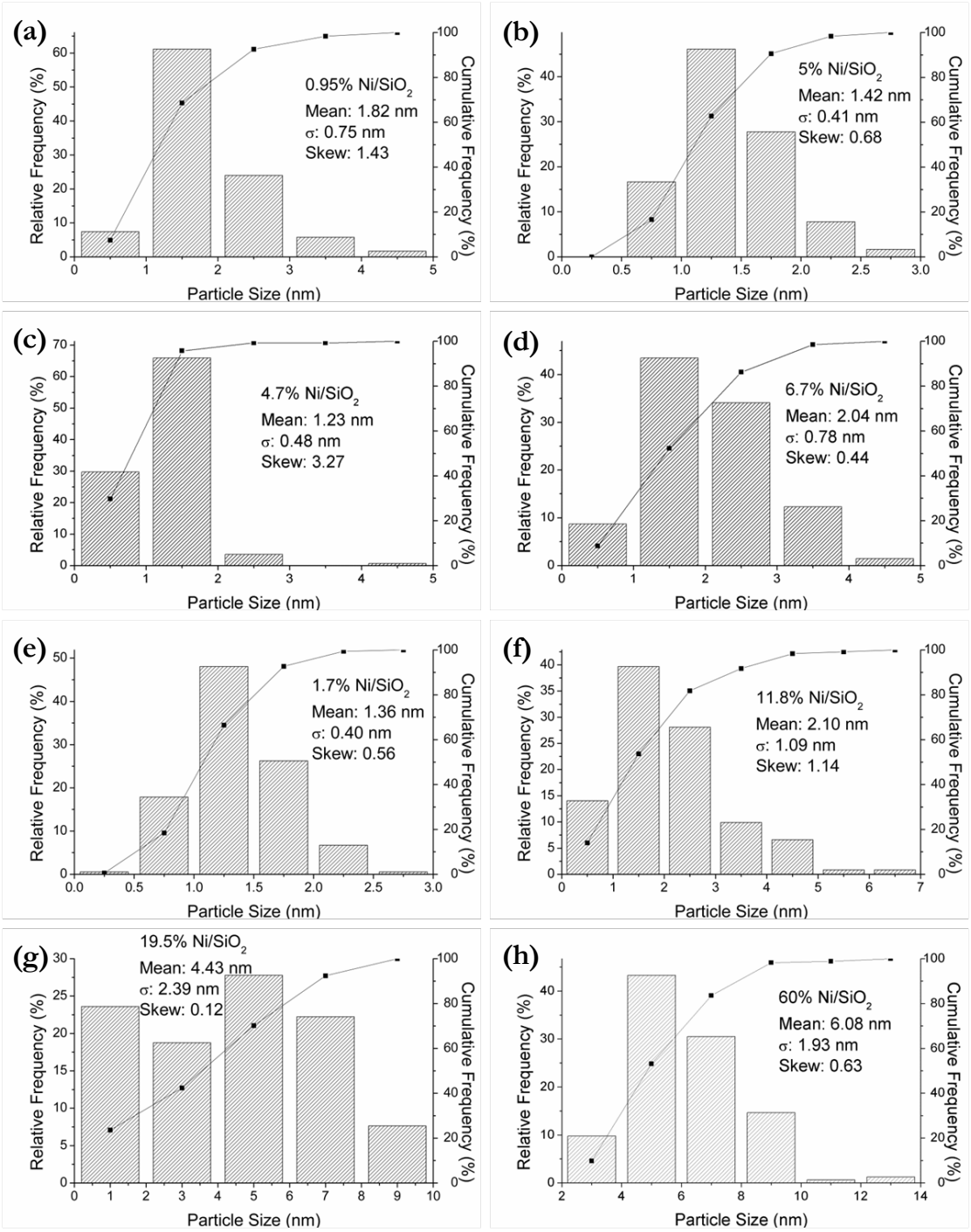

Figure 7.5: Particle size distributions of the fresh Ni/SiO_2 catalyst samples after their respective reduction steps and consecutive re-oxidation under ambient conditions. These histograms have been corrected to take into account the full or partial oxidation of Ni particles, thus representing the original Ni particle sizes. (a) 0.95% Ni/SiO_2; (b) 5.0% Ni/SiO_2; (c) 4.7% Ni/SiO_2; (d) 6.7% Ni/SiO_2; (e) 1.7% Ni/SiO_2; (f) 11.8% Ni/SiO_2; (g) 19.5% Ni/SiO_2; (h) 60.0% Ni/SiO_2.

In this non-model catalyst system, the evaluation of structure sensitivity relies greatly on accurate determination of the respective particle size distributions (PSDs) for samples with

different metal loadings. Aberration corrected STEM imaging provides direct and reliable evidence for particle size measurement. Although the fresh Ni/SiO_2 catalysts had underwent a reduction step prior to STEM analysis, exposure to air during storage and transfer into the microscope caused the Ni species to re-oxidize (Figure 7.2). The extent of Ni re-oxidization could be correlated to the size of Ni particles: smaller particles (*i.e.*, below ~3 nm in diameter) were found to be fully oxidized to cubic NiO (Figure 7.2 (a, b)); larger particles (*i.e.*, above ~3 nm in diameter), on the other hand, exhibited a metallic Ni core enclosed by an oxidized shell (Figure 7.2 (c, d)). The NiO shell thickness in the larger particles were relatively uniform, irrespective of their diameter, with a mean thickness value of 1.36 ± 0.24 nm.

Employing *ex-situ* characterization techniques such as (S)TEM and XRD for particle size measurement inevitably involves sampling of Ni particles after their complete or partial oxidization to NiO. However, such particle size changes in our STEM data can be corrected by back calculating the size of the original Ni particle that would give rise to a fully oxidized NiO particle or partially transformed Ni/NiO core-shell particle of a certain dimension. Thus, histograms more representative of the actual size distributions of the reduced Ni particles can be produced, which are be more relevant to the Ni catalyst size that would be found under RWGS reaction conditions. The corrected sizes could be then applied in the determination of activity and turnover frequency (TOF) values of the Ni/SiO_2 catalysts.

The mean shell thickness t was taken as 1.36 nm. The diameter of the whole particle measured as the equivalent spherical diameter was denoted as $d_{measured}$. The lattice constants of cubic Ni and cubic NiO structures are a_{Ni} = 0.353 nm and a_{NiO} = 0.418 nm, respectively. Thus, the diameter of the original metallic Ni particle could be deduced as follows:

Fully oxidized particle ($d_{\text{whole}} \leq 2t$): $d_{\text{original}} = d_{\text{measured}} \times (a_{\text{Ni}}/a_{\text{NiO}})$ **Eq. 7.1**

Partially oxidized particle ($d_{\text{whole}} > 2t$): $d_{\text{original}} = (d_{\text{measured}} - 2t) + 2t \times (a_{\text{Ni}}/a_{\text{NiO}})$ **Eq. 7.2**

Using this correction method, the PSDs characterizing the original metal nanoparticle sizes was deduced for a series of Ni/SiO_2 catalysts in which the Ni weight loadings was varied from 0.95% to 60.0% (Figure 7.5). Our PSDs derived from HAADF-STEM imaging experiments on these Ni/SiO_2 catalysts show that at low Ni loadings (0.95-11.8%) the Ni particles were generally around 1-2 nm in diameter, while at higher Ni loadings (19.5-60.0%) the Ni particles grew considerably in size (Figures 7.3-7.5).

Mean particle sizes and coordination numbers of the catalysts were measured using multiple *ex-situ* techniques including HAADF-STEM, BF-TEM, XAS and XRD (Table 7.1). During the catalytic reaction the Ni particles experienced limited size changes, as substantiated by comparing the mean sizes of the oxidized Ni particles before and after use (Table 7.1). It should be noted that there is some discrepancy in the mean particle size values measured by HAADF-STEM and XRD. One of the limitations of XRD is that it only measures the average crystallite size as opposed to the size of particles that might be polycrystalline. Further complications would arise from the probable oxidation of Ni particles prior to or during *ex-situ* XRD analysis.

7.3 Assessment of structure sensitivity for CO_2 hydrogenation over Ni/SiO_2 catalysts with different metal particle sizes

The catalysts with different mean sizes were systematically investigated in an operando transmission FT-IR spectroscopy set-up where on-line activities toward methane formation in CO_2 hydrogenation were acquired (Figure 7.6). All the catalysts maintained high catalytic stability over the 150 min duration of the reaction duration. The initial methane production onset

temperature, which is associated with the apparent activation energy, generally decreased with an increasing Ni loading (except for sample F with 11.8% Ni loading), suggesting that increased availability of the Ni species facilitated the methanation process (Figure 7.6 (a)). While in the extensively investigated Co catalyst system for CO hydrogenation, the TOF is relatively insensitive to variations in particle size larger than 6 nm[5, 7], a maximum activity could be noted at a mean size of ~2.0 nm for CO_2 hydrogenation over Ni at 400 °C (Figure 7.6 (b, c)). Thus, by using a set of well-defined catalyst samples a particle size effect has been established whereby the surface specific activity of catalytic CO_2 hydrogenation over Ni changes with mean Ni particle size.

Operando FT-IR spectroscopy was applied to correlate the particle size, or structure sensitivity effects to surface species and processes (Figure 7.7). Difference FT-IR spectra between 2250-1400 cm^{-1}, in which the first spectrum of the series is subtracted from subsequent spectra, exhibit intermediate triple bond C≡O to single bond C─O stretching vibrations[15-18] as shown in Figure 7.7 (a, b). In addition, signals arising from framework silica were also observed at 1932, 1866 and 1635 cm^{-1}.

Three important reaction intermediates were observed from the operando FT-IR data. Firstly, two distinct features between 2060-1900 cm^{-1} both representing adsorbed CO species (CO_{ads}) were noted: namely a set of peaks at 2060 cm^{-1} with a shoulder at 2019 cm^{-1}, and a peak at 1903 cm^{-1} (Figure 7.7). The former set corresponds to terminally adsorbed CO atop a single Ni atom, where vibrations can occur anywhere between 2060-2019 cm^{-1}, depending on the oxidation state of nickel[15-18]. The band at 1903 cm^{-1} describes bridged carbonyl species, where a CO molecule binds to three adjacent Ni atoms. The second relevant reaction intermediate,

gaseous CO, gives a symmetrical broad band with maxima at 2180 cm^{-1} and 2095 cm^{-1}. The third intermediate is surface formate that leads to a peak at 1591 cm^{-1}. Thus, the FT-IR analysis detected reaction intermediates expected from RWGS pathway 1 as well as pathway 2 on supported Ni catalysts. Relatively few bands in the CO_{ads} region show up in catalyst A which has a high Ni dispersion, whereas catalyst H consisting of the largest Ni nanoparticles gives more pronounced peaks in this CO_{ads} region (Figure 7.7 (a, b)), suggesting a more dominant role of pathway 1 with increasing Ni particle size.

Table 7.1: Characterization of the set of Ni/SiO_2 catalysts (A-H) by HAADF-STEM, TEM, XAS and XRD. The particle size measured from STEM was for the original metallic Ni particles; all the other size values were based on the Ni particles after re-oxidation under ambient conditions.

Sample	Ni loading (wt%)	Mean Ni particle size from STEM (fresh, nm)	Mean Ni particle size from TEM (spent, nm)	Ni co-ordination number from XAS (fresh)	Mean NiO particle size from XRD (fresh, nm)
A	0.95	1.82 ± 0.75 (2.13)†	1.1 ± 0.4	6.4 ± 1.2 (1 nm)‡	1.0 ± 0.9
B	5.0	1.42 ± 0.41 (1.68)	1.6 ± 0.3	7.3 ± 1.2 (2 nm)	1.2 ± 0.6
C	4.7	1.23 ± 0.48 (1.45)	1.6 ± 0.7	7.1 ± 1.5 (1.5 nm)	1.2 ± 1.0
D	6.7	2.04 ± 0.78 (2.38)	2.5 ± 0.7	7.6 ± 1.3 (2 nm)	0.9 ± 0.2
E	1.7	1.36 ± 0.40 (1.61)	2.6 ± 0.5	5.8 ± 3.1 (1 nm)	1.9 ± 0.4
F	11.8	2.10 ± 1.09 (2.42)	3.5 ± 0.6	7.3 ± 2.1 (2 nm)	2.3 ± 1.2
G	19.5	4.43 ± 2.39 (4.81)	5.0 ± 1.4	7.4 ± 1.3 (2 nm)	4.2 ± 1.6
H	60.0	6.08 ± 1.93 (6.50)	6.9 ± 1.9	8.8 ± 1.1 (6 nm)	5.2 ± 2.6

† The number between parentheses denotes the measured mean Ni particle size (nm) without correction for the oxidation effect.

‡ The value between parentheses denotes the Ni particle size derived from first shell analysis in EXAFS.

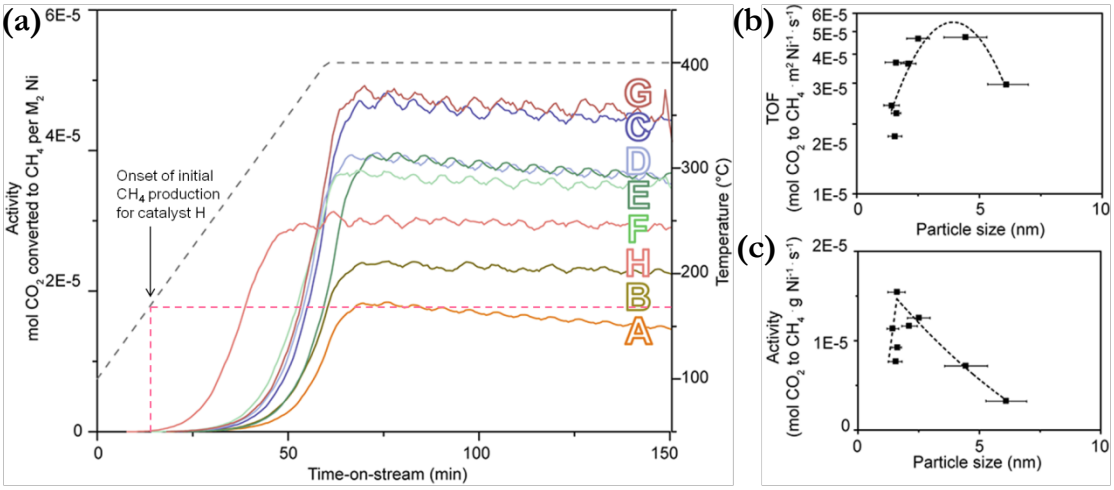

Figure 7.6: Activity measurements of the Ni/SiO_2 catalysts (H_2/CO_2 =4, 1 bar). (a) Methane activity profiles normalized to the Ni surface area (assuming hemispherical particles) for catalyst samples A-H. The dashed grey line denotes the temperature profile; the dashed pink line denotes the onset of initial CH_4 production for catalyst H. (b) The correlation of Ni mean particle size with the TOF value (400 °C). (c) The correlation of Ni mean particle size with activity normalized to the Ni loading (400 °C). *Courtesy of Charlotte Vogt.*

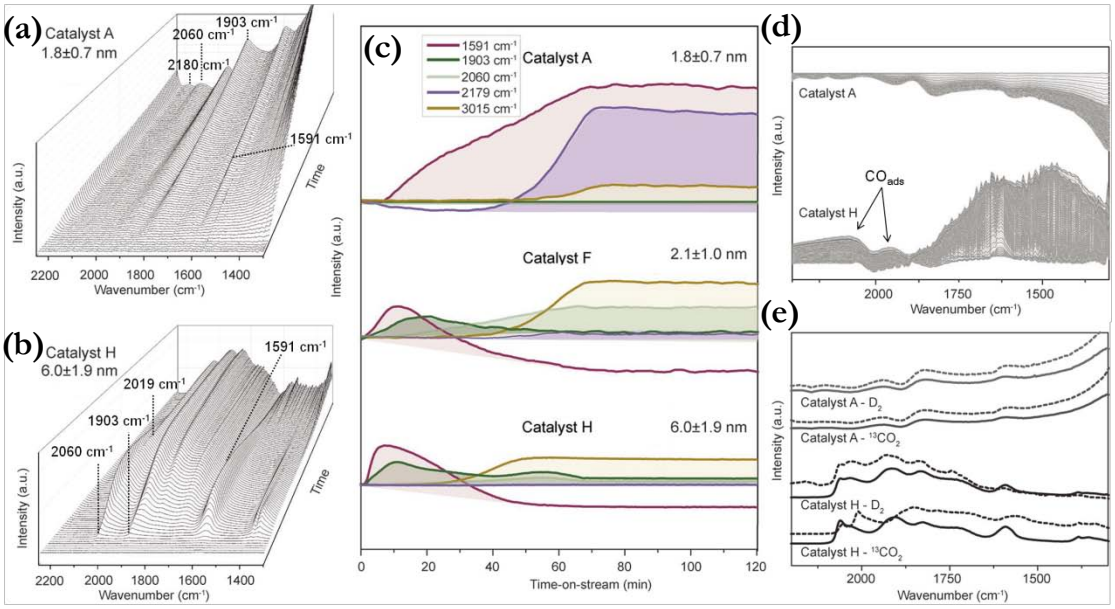

Figure 7.7: Operando FT-IR measurements. (a, b) Consecutive FT-IR spectra of the CO stretching absorption region plotted against time-on-stream for catalysts A and H, respectively. (c) Integrated FT-IR peak areas as a function of time-on-stream. (d) Consecutive operando FT-IR spectra of catalysts A and H recorded during post-reaction flushing with N_2. The CO_{ads} signals attenuated in catalyst A, but persisted in catalyst H in exposure to N_2. (e) Operando FT-IR spectra recorded during CO_2 hydrogenation experiments pulsed with labeled feedstocks. Solid lines denote non-pulsed feedstock, while dotted lines denote subsequent pulses of either $^{13}CO_2$ or D_2. *Courtesy of Charlotte Vogt.*

Integrated FT-IR peak areas as a function of time-on-stream (Figure 7.7 (c)) show a positive correlation between the intensity of the absorption bands in the CO_{ads} stretching region during CO_2 hydrogenation and mean Ni particle size. Notably, the contributions from gaseous CO decreased with larger particle sizes and this species is only present for catalyst A which had lower TOF values. Moreover, since CO_{ads} atop a single nickel atom (2060-2019 cm^{-1}) possesses a weaker Ni-C bond than CO adsorbed in a tri-fold bridge position (1903 cm^{-1}), the FT-IR data also illustrate the particle size dependence of Sabatier's general principle for catalysis, where optimal catalyst activity is attained with intermediate adsorption strength, which is achieved in this case by Ni particles within the 2-3 nm size range. Flushing the spent catalysts with N_2 caused the desorption of the CO species from the smaller Ni particles, while CO_{ads} on the larger particles remained as bridged carbonyl or carboxylate species (Figure 7.7 (d)).

While both RWGS pathways seemed to be involved given the detection of both formate and CO_{ads} species by FT-IR, the intermediate species for each pathway exhibited distinct adsorption properties for different particle sizes. The formate species was observed regardless of particle size, but only for the smaller Ni particle sizes (catalyst A) was there no signal attenuation for formate (Figure 7.7 (c)). The introduction of isotopically labeled gas feedstocks ($^{13}CO_2$ and D_2) did not seem to alter the FT-IR spectra for catalyst A, indicating a lack of interplay between ^{12}C and ^{13}C, and between H and D in the formate species for small Ni particle sizes (Figure 7.7 (e)). On the other hand, for the larger Ni particle sizes, both D_2 and $^{13}CO_2$ pulses shifted the formate band. While the surface of larger Ni particles was dominated by intermediate CO_{ads} species, in catalyst A which had the smaller Ni nanoparticles, formate was the dominant species and gaseous CO was also detected.

Further assessment of the structure sensitivity effects was carried out by operando quick X-ray absorption spectroscopy (Q-XAS) which allows determination of the percentage of metallic Ni with time-on-stream for different Ni particle sizes while minimizing the exposure of the samples to X-ray irradiation. Catalysts A, B and F were subjected to pulses of 100 s CO_2 and H_2 alternated by 30 s N_2. All the three catalyst samples contained ultra-small Ni particles that theoretically exposed more than 50% of Ni atoms which contributed significantly to bulk Q-XAS signals for the detection of surface changes[19-20] (Figure 7.5 (a, b, f), Table 7.1). By using the clustering and least squares fitting approach the content of metallic nickel as opposed to oxidized nickel species could be quantified with time-on-stream (Figure 7.8).

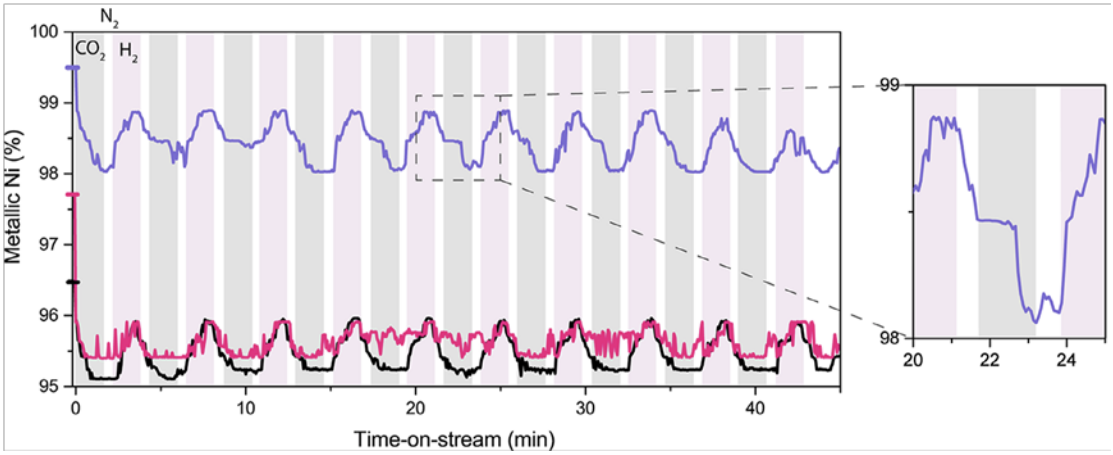

Figure 7.8: Quick X-ray absorption spectroscopy of three Ni/SiO_2 catalysts with different mean Ni particle sizes. Pulses of 100 s CO_2 and H_2 alternated by 30 s N_2 were applied to the catalysts. Pink curve: catalyst A; black curve: catalyst B; purple curve: catalyst F. *Courtesy of Charlotte Vogt.*

For all Ni particle sizes, the initial oxidation process was direct as evidenced by the immediate drop in the percentage of metallic nickel upon the introduction of CO_2 at the start; but the second slope initiated at the same level of Ni(0) content that subsequent H_2 pulses reduced to (Figure 7.8). This implies the presence of slower and faster mechanisms for CO_2 activation that takes place on different catalytic sites. In addition, as indicated by a plateau during

the CO_2 pulse, a two-step re-oxidation process was noted for catalyst F with larger particles (Figure 7.8). This suggests the existence of a second, slower and less favorable mechanism involving either H_2 or CO_{ads} on specific sites for the RWGS reaction on larger particles. This plateau feature was less pronounced for catalysts with smaller Ni particles that offered fewer terrace sites. These results agree well with the assignment of more coordinately saturated sites to the less active RWGS pathway 2 (Figure 7.1).

The maximum changes in the degree of reduction for catalysts A, B and F were 2.3% (from 97.7 to 95.4%), 1.5% (from 96.6 to 95.1%), and 1.5% (from 99.5 to 98.0%), respectively (Figure 7.8). The extent of surface changes is an important parameter in evaluating the fraction of active sites for CO_2 activation. On average a Ni particle in catalyst B (1.42 ± 0.41 nm) contains ~136 Ni atoms, of which approximately 68% inhabit surface sites. If all the 92 surface atoms were active in CO_2 dissociation during a CO_2 pulse, half the surface atoms (~46 atoms) would bind to oxygen atoms and could potentially be oxidized, leaving the other half covered in CO_{ads}. A 1.5% change in the extent of reduction corresponds to 2 atoms that changed the oxidation state, indicating that ~4.4% of the surface atoms that were available for oxidation (~46 atoms) were actually oxidized. For catalysts A and F, the same calculation method yields 8.1% and 5.9%, respectively as the proportions of oxidizable surface atoms that were oxidized. These derivations, based on data acquired from HAADF-STEM imaging and Q-XAS analysis, provide some new insights into the likely restructuring effects illustrated by catalysts with such small Ni particle sizes, as demonstrated by the presence of the atomic co-ordinations, albeit in small quantities, capable of cleaving π-bonds under working conditions.

Operando FT-IR spectroscopy analysis has indicated that the CO species had a high surface

coverage over Ni/SiO_2 catalysts with larger Ni particles, where gaseous CO was absent. In comparison, gaseous CO was observed on catalysts with high Ni dispersion, along with lower amounts of CO_{ads} species. Apparently, the reactivity or stability of intermediate CO relies greatly on the mean Ni particle size. More specifically, the interactions between the catalyst and the substrate (CO_{ads}) should be neither too strong nor too weak. Too strong an interaction with the larger Ni particles produces a monolayer of CO_{ads} in a highly stable bridge conformation. Conversely easy desorption was facilitated for CO_{ads} that was very weakly bound to the smallest Ni particles. It appears that a large proportion of linearly adsorbed CO gives rise to high catalytic activity for the CO_2 methanation reaction. Hence the rate-determining step in CO_2 hydrogenation is not CO_2 activation or CO dissociation, but rather relates to the propensity of the adsorbed intermediate CO species for hydrogenation and the availability of adjacent H_{ads} sites to hydrogenate the CO_{ads} molecule. Theoretically this activity should improve with smaller particle sizes, but such a trend is weakened or even reversed by the slow removal of oxidizing or charged surface species in the very smallest nanoclusters. The more localized energy levels in the electronic band structure of smaller Ni particles promotes the stability of oxidizing or charged species. Contrary to the previously reported inability of sub-2 nm particles to cleave π-bonds,[3] gaseous CO and methane were formed on the ultra-small Ni particles examined in the current study. These results point to the direct dissociation of CO_2 (pathway 1) as the major reaction mechanism in RWGS over Ni at 400 °C.

7.4 Summary and Outlook

In summary, by combining HAADF-STEM, operando FT-IR and Q-XAS techniques, the

structure sensitivity effect in Ni/SiO_2 catalysts with different particle sizes has been shown to relate to Ni size-dependent reaction pathways in CO_2 activation. Three factors have been identified that might have contributed to the structure sensitivity of methanation over supported Ni catalysts. Firstly, the variations of activity with different sites within a narrow PSD has been demonstrated by operando experiments coupled with HAADF-STEM observations. Secondly, active sites were formed, particularly for sub-2 nm Ni particles, that facilitated CO_2 hydrogenation. Thirdly, the lower d-band energy or higher electron localization for sub-2 nm particles significantly influenced their catalytic activity due to the higher stability of oxidizing or charged species on the surface. Thus, structure sensitivity effects have been demonstrated in non-model Ni/SiO_2 catalysts that depend on the interplay between a number of physical phenomena. On the other hand, model catalyst systems, such as single crystal facet studies, would perhaps lack control over any electronic effects that can contribute to structure sensitivity. Therefore, it is necessary to study non-model systems if seeking a fuller understanding of structure sensitivity.

In this work, the effect of Ni particle size on stability and reactivity of reaction intermediates in CO_2 methanation has been evaluated using HAADF-STEM and operando spectroscopy techniques. To more accurately determine the size of metallic Ni particles under reaction conditions, surface oxidation of Ni particles due to exposure to air was taken into account and statistical thickness measurements of oxidized layers were applied in order to deduce the original particle size from the *ex-situ* HAADF-STEM data. The current study not only deepens the understanding of the Ni particle size effects on CO_2 hydrogenation and activation, but also shines light on the reactivity of intermediate CO with direct practical interest, for

instance in the Fischer-Tropsch synthesis of hydrocarbons.

Further experiments should be attempted to further probe the following aspects:

(1) The influence of catalyst support on Ni particle size and reaction kinetics has not been addressed in this study, as SiO_2 is a relatively inert support material. It might be of interest to carry out a comparative study that investigates the structure sensitivity effects using other common support materials, such as TiO_2 and Al_2O_3.

(2) In this work, the control over Ni particle size was achieved by varying the nominal Ni loading. In the 60% Ni/SiO_2 sample (catalyst H), the high metal loading led to significant overlap of large Ni particles. Despite extreme caution exercised during particle size measurement using STEM imaging, errors in determining the particle shape outlines could not be completely eliminated. Perhaps another approach to modify the Ni particle size is to systematically change the calcination temperature in the last heat treatment step during catalyst preparation. Thus, we can study how the Ni particle size changes with the calcination temperature. It might be possible to obtain larger but non-overlapping Ni particles supported by SiO_2 by applying a higher calcination temperature while maintaining a relatively low Ni loading. Therefore, the size distribution for larger Ni particles can be measured with higher accuracy.

(3) All the STEM-derived PSDs for the Ni particles were from the fresh samples, while PSDs for the used catalysts were acquired from TEM (FEI Tecnai 12 at 120 keV) which does not have as good resolution as the aberration-corrected STEM. Therefore, it would be desirable to measure PSDs for the used catalysts from STEM and apply the same back-calculation method to determine the original metallic Ni particle sizes.

(4) Direct measurements of reduced Ni particle sizes may be conducted in *in-situ* TEM

under a reducing atmosphere. This circumvents the need for correcting the sizes for oxidized particles.

(5) As illustrated by HAADF-STEM, the partially oxidized Ni particles have a relatively uniform oxide shell thickness of 1.36 ± 0.24 nm, which suggests that NiO shells with this thickness formed a passivating layer[21] that prevented further oxidation in air. To understand the oxidation process that led to this characteristic shell thickness, two approaches can be attempted. First, it has been reported before[21-22] that heating unsupported Ni particles in air could increase the oxide shell thickness. Thus, we may treat our Ni/SiO_2 samples in air at different elevated temperatures for some pre-determined times and measure the corresponding mean shell thickness. A temperature-NiO thickness correlation might be developed which can help to elucidate the process of oxygen diffusion in Ni particles with heat-induced lattice strains. Second, the SiO_2 support may also play a role in forming the NiO shell through Ni-O-Si bonds.[23] This implies that the oxidation process could be support-dependent. Hence it might be of interest to use non-oxide (*e.g.*, C) or other oxide (*e.g.*, Al_2O_3, TiO_2) supports for the preparation of Ni catalysts and evaluate their influence on the thickness of NiO layers.

7.5 Acknowledgements

This work is in collaboration with several institutions and researchers, including Prof. Bert M. Weckhuysen's group in Utrecht University, Dr. Peter H. Berben's team at BASF Nederland B.V., and Dr. Maarten Nachtegaal from Paul Scherrer Institute. Their guidance and support are greatly appreciated.

The Ni/SiO_2 catalyst samples were prepared by Dr. Esther Groeneveld at BASF Nederland

B.V.; the operando spectroscopic experiments were carried out by Charlotte Vogt and Dr. Florian Meirer at Utrecht University. Their various contributions to this study are gratefully acknowledged.

This work has been accepted for publication in *Nature Catalysis*.

7.6 References

1. Rönsch, S.; Schneider, J.; Matthischke, S.; Schlüter, M.; Götz, M.; Lefebvre, J.; Prabhakaran, P.; Bajohr, S., Review on methanation–from fundamentals to current projects. *Fuel* **2016**, 166, 276-296.

2. Mills, G. A.; Steffgen, F. W., Catalytic methanation. *Cat. Rev. - Sci. Eng.* **1974**, 8, 159-210.

3. Van Santen, R. A., Complementary structure sensitive and insensitive catalytic relationships. *Acc. Chem. Res.* **2009**, 42, 57-66.

4. Van Hardeveld, R.; Van Montfoort, A., The influence of crystallite size on the adsorption of molecular nitrogen on nickel, palladium and platinum: an infrared and electron-microscopic study. *Surf. Sci.* **1966**, 4, 396-430.

5. Bezemer, G. L.; Bitter, J. H.; Kuipers, H. P. C. E.; Oosterbeek, H.; Holewijn, J. E.; Xu, X.; Kapteijn, F.; Van Dillen, A. J.; De Jong, K. P., Cobalt particle size effects in the Fischer−Tropsch reaction studied with carbon nanofiber supported catalysts. *J. Am. Chem. Soc.* **2006**, 128, 3956-3964.

6. Ren, J.; Guo, H.; Yang, J.; Qin, Z.; Lin, J.; Li, Z., Insights into the mechanisms of CO_2 methanation on Ni(111) surfaces by density functional theory. *Appl. Surf. Sci.* **2015**, 351, 504-516.

7. Den Breejen, J. P.; Radstake, P. B.; Bezemer, G. L.; Bitter, J. H.; Frøseth, V.; Holmen, A.; De Jong, K. P., On the origin of the cobalt particle size effects in Fischer−Tropsch catalysis. *J. Am. Chem. Soc.* **2009**, 131, 7197-7203.

8. Weatherbee, G. D.; Bartholomew, C. H., Hydrogenation of CO_2 on group VIII metals: II. Kinetics and mechanism of CO_2 hydrogenation on nickel. *J. Catal.* **1982**, 77, 460-472.

9. Heine, C.; Lechner, B. A. J.; Bluhm, H.; Salmeron, M., Recycling of CO_2: probing the chemical state of the Ni(111) surface during the methanation reaction with ambient-pressure X-ray photoelectron spectroscopy. *J. Am. Chem. Soc.* **2016**, 138, 13246-13252.

10. Czekaj, I.; Loviat, F.; Raimondi, F.; Wambach, J.; Biollaz, S.; Wokaun, A., Characterization of surface processes at the Ni-based catalyst during the methanation of biomass-derived synthesis gas: X-ray photoelectron spectroscopy (XPS). *Appl. Catal., A* **2007**, 329, 68-78.

11. Tao, F.; Grass, M. E.; Zhang, Y.; Butcher, D. R.; Renzas, J. R.; Liu, Z.; Chung, J. Y.; Mun, B. S.; Salmeron, M.; Somorjai, G. A., Reaction-driven restructuring of Rh-Pd and Pt-Pd core-shell nanoparticles. *Science* **2008**, 322, 932-934.

12. Tao, F.; Dag, S.; Wang, L.-W.; Liu, Z.; Butcher, D. R.; Bluhm, H.; Salmeron, M.; Somorjai, G. A., Break-up of stepped platinum catalyst surfaces by high CO coverage. *Science* **2010**, 327, 850-853.

13. Miao, D.; Cavusoglu, G.; Lichtenberg, H.; Yu, J.; Xu, H.; Grunwaldt, J.-D.; Goldbach, A., Water-gas shift reaction over platinum/strontium apatite catalysts. *Appl. Catal., B* **2017**, 202, 587-596.

14. Ermakova, M. A.; Ermakov, D. Y., High-loaded nickel–silica catalysts for hydrogenation, prepared by sol–gel route: structure and catalytic behavior. *Appl. Catal., A* **2003**, 245, 277-288.

15. Campuzano, J. C.; Greenler, R. G., The adsorption sites of CO on Ni(111) as determined by infrared reflection-absorption spectroscopy. *Surf. Sci.* **1979**, 83, 301-312.

16. Trenary, M.; Uram, K. J.; Yates, J. T., An infrared reflection-absorption study of CO chemisorbed on clean and sulfided Ni(111)—Evidence for local surface interactions. *Surf. Sci.* **1985**, 157, 512-538.

17. Layman, K. A.; Bussell, M. E., Infrared spectroscopic investigation of CO adsorption on silica-supported nickel phosphide catalysts. *J. Phys. Chem. B* **2004**, 108, 10930-10941.

18. Courtois, M.; Teichner, S. J., Infrared studies of CO, O_2, and CO_2 gases and their interaction products, chemically adsorbed on nickel oxide. *J. Catal.* **1962**, 1, 121-135.

19. Van Bokhoven, J. A.; Lamberti, C., Eds.; *X-ray absorption and X-ray emission spectroscopy: theory and applications*; John Wiley & Sons: New York, 2016.

20. Bordiga, S.; Groppo, E.; Agostini, G.; Van Bokhoven, J. A.; Lamberti, C., Reactivity of surface species in heterogeneous catalysts probed by in situ X-ray absorption techniques. *Chem. Rev.* **2013**, 113, 1736-1850.

21. Sakiyama, K.; Koga, K.; Seto, T.; Hirasawa, M.; Orii, T., Formation of size-selected Ni/NiO core−shell particles by pulsed laser ablation. *J. Phys. Chem. B* **2004**, 108, 523-529.

22. Johnston-Peck, A. C.; Wang, J.; Tracy, J. B., Synthesis and structural and magnetic characterization of Ni(core)/NiO(shell) nanoparticles. *ACS Nano* **2009**, 3, 1077-1084.

23. Umegaki, T.; Yan, J.-M.; Zhang, X.-B.; Shioyama, H.; Kuriyama, N.; Xu, Q., Hollow Ni–SiO_2 nanosphere-catalyzed hydrolytic dehydrogenation of ammonia borane for chemical hydrogen storage. *J. Power Sources* **2009**, 191, 209-216.

Appendix A

Publication lists

Journal papers

1. Alhumaimess, M.; Lin, Z.; He, Q.; Lu, L.; Dimitratos, N.; Dummer, N. F.; Conte, M.; Taylor, S. H.; Bartley, J. K.; Kiely, C. J.; Hutchings, G. J., Oxidation of benzyl alcohol and carbon monoxide using gold nanoparticles supported on MnO_2 nanowire microspheres. *Chem. Eur. J.* **2014**, 20, 1701-1710.

2. Edwards, J. K.; Pritchard, J.; Lu, L.; Piccinini, M.; Shaw, G.; Carley, A. F.; Morgan, D. J.; Kiely, C. J.; Hutchings, G. J., The direct synthesis of hydrogen peroxide using platinum-promoted gold–palladium catalysts. *Angew. Chem. Int. Ed.* **2014**, 53, 2381-2384.

3. Forde, M. M.; Armstrong, R. D.; McVicker, R.; Wells, P. P.; Dimitratos, N.; He, Q.; Lu, L.; Jenkins, R. L.; Hammond, C.; Lopez-Sanchez, J. A.; Kiely, C. J.; Hutchings, G. J., Light alkane oxidation using catalysts prepared by chemical vapour impregnation: tuning alcohol selectivity through catalyst pre-treatment. *Chem. Sci.* **2014**, 5, 3603-3616.

4. Kennedy, J.; Jones, W.; Morgan, D. J.; Bowker, M.; Lu, L.; Kiely, C. J.; Wells, P. P.; Dimitratos, N., Photocatalytic hydrogen production by reforming of methanol using Au/TiO_2, Ag/TiO_2 and $Au\text{-}Ag/TiO_2$ catalysts. *Catal. Struct. React.* **2015**, 1, 35-43.

5. Wang, J.; Kondrat, S. A.; Wang, Y.; Brett, G. L.; Giles, C.; Bartley, J. K.; Lu, L.; Liu, Q.; Kiely, C. J.; Hutchings, G. J., Au–Pd nanoparticles dispersed on composite titania/graphene oxide-supports as a highly active oxidation catalyst. *ACS Catal.* **2015**, 5, 3575-3587.

6. Yang, Z.; Lu, L.; Berard, V. F.; He, Q.; Kiely, C. J.; Berger, B. W.; McIntosh, S., Biomanufacturing of CdS quantum dots. *Green Chem.* **2015**, 17, 3775-3782.

7. Iqbal, S.; Kondrat, S. A.; Jones, D. R.; Schoenmakers, D. l. C.; Edwards, J. K.; Lu, L.; Yeo, B. R.; Wells, P. P.; Gibson, E. K.; Morgan, D. J.; Kiely, C. J.; Hutchings, G. J., Ruthenium nanoparticles supported on carbon: an active catalyst for the hydrogenation of lactic acid to 1, 2-propanediol. *ACS Catal.* **2015**, 5, 5047-5059.

8. Freakley, S. J.; He, Q.; Harrhy, J. H.; Lu, L.; Crole, D. A.; Morgan, D. J.; Ntainjua, E. N.; Edwards, J. K.; Carley, A. F.; Borisevich, A. Y.; Kiely, C. J.; Hutchings, G. J., Palladium-tin catalysts for the direct synthesis of H_2O_2 with high selectivity. *Science* **2016**, 351, 965-968.

9. Kondrat, S. A.; Smith, P. J.; Wells, P. P.; Chater, P. A.; Carter, J. H.; Morgan, D. J.; Fiordaliso, E. M.; Wagner, J. B.; Davies, T. E.; Lu, L.; Bartley, J. K.; Taylor, S. H.; Spencer, M. S.; Kiely, C. J.; Kelly, G. J.; Park, C. W.; Rosseinsky, M. J.; Hutchings, G. J., Stable amorphous georgeite as a precursor to a high-activity catalyst. *Nature* **2016**, 531, 83-87.

10. Liu, X.; Conte, M.; Elias, D.; Lu, L.; Morgan, D. J.; Freakley, S. J.; Johnston, P.; Kiely, C. J.; Hutchings, G. J., Investigation of the active species in the carbon-supported gold catalyst for acetylene hydrochlorination. *Catal. Sci. Technol.* **2016**, 6, 5144-5153.

11. Sankar, M.; He, Q.; Dawson, S.; Nowicka, E.; Lu, L.; Bruijnincx, P. C.; Beale, A. M.; Kiely, C. J.; Weckhuysen, B. M., Supported bimetallic nano-alloys as highly active catalysts for the one-pot tandem synthesis of imines and secondary amines from nitrobenzene and alcohols. *Catal. Sci. Technol.* **2016**, 6, 5473-5482.

12. Shin, H. H.; Lu, L.; Yang, Z.; Kiely, C. J.; McIntosh, S., Cobalt catalysts decorated with platinum atoms supported on barium zirconate provide enhanced activity and selectivity for CO_2 Methanation. *ACS Catal.* **2016**, 6, 2811-2818.

13. Spangler, L. C.; Lu, L.; Kiely, C. J.; Berger, B. W.; McIntosh, S., Biomineralization of PbS and PbS-CdS core-shell nanocrystals and their application in quantum dot sensitized solar cells. *J. Mater. Chem. A* **2016**, 4, 6107-6115.

14. Dunleavy, R.; Lu, L.; Kiely, C. J.; McIntosh, S.; Berger, B. W., Single-enzyme biomineralization of cadmium sulfide nanocrystals with controlled optical properties. *Proc. Natl. Acad. Sci. U.S.A.* **2016**, 113, 5275-5280.

15. Ftouni, J.; Muñoz-Murillo, A.; Goryachev, A.; Hofmann, J. P.; Hensen, E. J.; Lu, L.; Kiely, C. J.; Bruijnincx, P. C.; Weckhuysen, B. M., ZrO_2 is preferred over TiO_2 as support for the Ru-catalyzed hydrogenation of levulinic acid to γ-valerolactone. *ACS Catal.* **2016**, 6, 5462-5472.

16. Yang, Z.; Lu, L.; Kiely, C. J.; Berger, B. W.; McIntosh, S., Biomineralized CdS quantum dot nanocrystals: optimizing synthesis conditions and improving functional properties by surface modification. *Ind. Eng. Chem. Res.* **2016**, 55, 11235-11244.

17. Smith, P. J.; Kondrat, S. A.; Chater, P. A.; Yeo, B. R.; Shaw, G. M.; Lu, L.; Bartley, J. K.; Taylor, S. H.; Spencer, M. S.; Kiely, C. J.; Kelly, G. J.; Park, C. W.; Hutchings, G. J., A new class of Cu/ZnO catalysts derived from zincian georgeite precursors prepared by co-precipitation. *Chem. Sci.* **2017**, 8, 2436-2447.

18. Gregory, D. G.; Lu, L.; Kiely, C. J.; Snyder, M. A., Interfacial stabilization of metastable TiO_2 films. *J. Phys. Chem. C* **2017**, 121, 4434-4442.

19. Curran, C. D.; Lu, L.; Jia, Y.; Kiely, C. J.; Berger, B. W.; McIntosh, S., Direct single-enzyme

biomineralization of catalytically active ceria and ceria–zirconia nanocrystals. *ACS Nano* **2017**, 11, 3337-3346.

20. Yang, Z.; Lu, L.; Kiely, C. J.; Berger, B. W.; McIntosh, S., Single enzyme direct biomineralization of CdSe and CdSe-CdS core-shell quantum dots. *ACS Appl. Mater. Interfaces* **2017**, 9, 13430-13439.

21. Malta, G.; Kondrat, S. A.; Freakley, S. J.; Davies, C. J.; Lu, L.; Dawson, S.; Thetford, A.; Gibson, E. K.; Morgan, D. J.; Jones, W., Identification of single-site gold catalysis in acetylene hydrochlorination. *Science* **2017**, 355, 1399-1403.

22. Gregory, D. G.; Guo, Q.; Lu, L.; Kiely, C. J.; Snyder, M. A., Template-induced structuring and tunable polymorphism of three-dimensionally ordered mesoporous (3DOm) metal oxides. *Langmuir* **2017**, 33, 6601-6610.

23. Spangler, L. C.; Chu, R.; Lu, L.; Kiely, C. J.; Berger, B. W.; McIntosh, S., Enzymatic biomineralization of biocompatible $CuInS_2$, $(CuInZn)S_2$ and $CuInS_2$/ZnS core/shell nanocrystals for bioimaging. *Nanoscale* **2017**, 9, 9340-9351.

24. Yao, S.; Zhang, X.; Zhou, W.; Gao, R.; Xu, W.; Ye, Y.; Lin, L.; Wen, X.; Liu, P.; Chen, B.; Crumlin, E.; Guo, J.; Zuo, Z.; Li, W.; Xie, J.; Lu, L.; Kiely, C. J.; Gu, L.; Shi, C.; Rodriguez, J. A.; Ma, D., Atomic-layered Au clusters on α-MoC as catalysts for the low-temperature water-gas shift reaction. *Science* **2017**, 357, 389-393.

25. Sadeghnejad, A.; Lu, L.; Kiely, C. J.; Berger, B. W.; McIntosh, S., Single enzyme direct biomineralization of ZnS, $Zn_xCd_{1-x}S$ and $Zn_xCd_{1-x}S$–ZnS quantum confined nanocrystals. *RSC Adv.* **2017**, 7, 38490-38497.

26. Liu, K.; Pritchard, J.; Lu, L.; van Putten, R.; Verhoeven, M. W. G. M.; Schmitkamp, M.; Huang, X.; Lefort, L.; Kiely, C. J.; Hensen, E. J. M.; Pidko, E. A., Supported nickel–rhenium catalysts for selective hydrogenation of methyl esters to alcohols. *Chem. Commun.* **2017**, 53, 9761-9764.

Extended abstracts (selected)

1. Yang, Z.; Lu, L.; Berard, V. F.; Kiely, C. J.; Mcintosh, S.; Berger, B. W., Structural and optical characterization of biosynthesized CdS quantum dots. *Microsc. Microanal.* **2015**, 21, 1737-1738.

2. Lu, L.; Curran, C.; Kiely, C. J.; Berger, B. W.; Mcintosh, S., Morphology and composition of biomineralized ceria and ceria-zirconia nanocrystals. *Microsc. Microanal.* **2016**, 22, 250-251.

Vita

Li Lu was born to Huanhuan Lyu and Hongxia Zhao on September 14th, 1989 in Huzhou, Zhejiang Province, China. After graduating from Zhejiang Anji Senior High School in 2008, he entered Shanghai Jiao Tong University in Shanghai, China, where he received a bachelor's degree in Materials Science and Engineering in June 2012. He then joined Lehigh University in August 2012 to start his Ph.D. study in the Department of Materials Science and Engineering. Under the supervision of Professor Christopher J. Kiely, he has been working on the electron microscopy studies of biomineralized functional nanocrystals and heterogeneous catalysts.